NATIONAL INSTITUTE FOR FUSION SCIENCE

Proceeding of A3 Foresight Program Seminar on Critical Physics Issues Specific to Steady State Sustainment of High-Performance Plasmas
November 22-25, 2016, Jeju, Korea

Edited by Yeong-Kook OH, Shigeru MORITA and Liqun HU

(Received - Aug. 20. 2017)

NIFS-PROC-108

Jan. 11,. 2018

Proceeding of A3 Foresight Program Seminar on Critical Physics Issues Specific to Steady State Sustainment of High-Performance Plasmas

November 22-25, 2016, Jeju, Korea

Edited by

Yeong-Kook OH, Shigeru MORITA and Liqun HU

Abstract

The A3 Foresight Program titled by "Critical Physics Issues Specific to Steady State Sustainment of High-Performance Plasmas", based on the scientific collaboration among China, Japan and Korea in the field of plasma physics, has been started from August 2012 under the auspice of the Japan Society for the Promotion of Science (JSPS, Japan), the National Research Foundation of Korea (NRF, Korea) and the National Natural Science Foundation of China (NSFC, China). The main purpose of this project is to enhance joint experiments on three Asian advanced fully superconducting fusion devices (EAST in China, LHD in Japan and KSTAR in Korea) and other magnetic confinement devices to solve several key physics issues on steady state sustainment of high-performance plasmas. The 10th workshop of the A3 program was held in Jeju, Korea, 22-25 November 2016, as the 9th A3 seminar on the collaborative research, which was hosted by National Fusion Research Institute, to check and review on-going joint research activities including scientific results during past four years and to discuss the future plan. New proposals based on the A3 collaborative research and oral presentations by young scientists were also encouraged. The topics in the seminar include steady state sustainment of magnetic configurations, edge and divertor plasma control and confinement of alpha particles.

Key words: magnetically confined devices, toroidal plasmas, high performance plasmas, steady state operation, edge plasma, divertor plasma, edge stability, high-energy particle, alpha particle and fusion plasma simulation.

Organizing Committee

Yeong-Kook OH (National Fusion Research Institute, Korea)

Shigeru MORITA (National Institute for Fusion Science, Japan)

Liqun HU (Institute of Plasma Physics, Chinese Academy of Sciences, China)

Program Committee

Yeong-Kook OH (National Fusion Research Institute, Korea)

Shigeru MORITA (National Institute for Fusion Science, Japan)

Liqun HU (Institute of Plasma Physics, Chinese Academy of Sciences, China)

Youngmu JEON (National Fusion Research Institute, Korea)

Conference Secretariat

Noh-Yeong OH (National Fusion Research Institute, Korea)

Chihiro SAKO (National Institute for Fusion Science, Japan)
Shaohua Dong (Institute of Plasma Physics, Chinese Academy of Sciences, China)

Preface

Steady-state sustainment of high-performance plasmas is one of the crucial issues needed to be addressed for fusion reactor development. To enhance close collaborations among scientists in three Asian countries (China, Japan and Korea), A3 foresight program on Plasma Physics started from August 2012 under the auspice of JSPS (Japan), NRF (Korea) and NSFC (China). The main purpose of this project is to solve several key physics issues through joint experiments on three Asian advanced fully superconducting fusion devices (EAST in China, LHD in Japan, KSTAR in Korea) and other magnetic confinement devices to carry out multi-faceted and complementary physics researches.

The first meeting of A3 foresight program on Plasma Physics hosted by NFRI (Korea) was held in Jeju Island, Korea on 22nd August, 2012 as coordinator meeting to initiate the A3 program. As a result, the first seminar hosted by NIFS (Japan), the second seminar hosted by ASIPP (China), and the third seminar hosted by NFRI (Korea) were held in Kushiro, Japan during 22-25 January, in Beijing, China during 20-23 May, and in Gyeongju, Korea during 3-4 November, respectively, in 2013. Concrete planning of collaborative research was made and possible scientific progresses done in steady state sustainment of high-performance plasmas were discussed. Also, many young scientists were joined in these seminars. The fourth seminar hosted by NIFS (in Kagoshima, Japan during 23-26 June in 2014), the fifth seminar by ASIPP (in Nanning, China during 6-9 January in 2015), the sixth seminar by NFRI (in Chuncheon, Korea during 19-22 May in 2015), the seventh seminar by NIFS (in Gotemba, Japan during 1-4 December in 2015), and the eighth seminar by ASIPP (in Yinchuan, China during 17-20 May in 2016) were held successfully, to discuss achievements and summarize intermediate report within the A3 scientific framework.

The ninth seminar as the tenth meeting, hosted by NFRI (Korea), was held in Jeju, Korea during 22-25 November, 2016 to continuously report the progress and achievement in on-going A3 collaboration. In total 51 participants attended in this seminar (15 from China, 14 from Japan, and 22 from Korea) and 45 scientific reports were presented for five categories; I. Steady state sustainment of magnetic configurations, II. Edge and divertor plasma control (IIa. Transport of edge and divertor plasmas and IIb. Stability of edge plasma), III. Confinement of alpha particles and IV. Theory and simulation. Especially, there were special presentations on the project overview and tokamak theory; EAST overview (Prof. B. Wan), KSTAR overview (Dr. Y.K. Oh), JT60SA overview (Dr. A. Isayama), Transport theory (Prof. Y. Kishimoto), and physics from 2D imaging (Prof. H.K. Park).

The seminar was closed with great success, clarifying remarkable progress in researches along A3 program physics subjects and also contributing to the fostering of younger scientists. The organizing and program committees are deeply grateful to all participants and to strong and

continuous support from foundation of three countries (NSFC in China, JSPS in Japan, and NRF in Korea), with those support and corporation the seminar was smoothly and successfully concluded.

Yeong-Kook OH, Shigeru MORITA, and Liqun HU

Chairpersons of the Organizing Committee


10th A3 Foresight Program Workshop
Nov. 22nd - 25th, 2016, Jeju, Korea
NFRI 국가핵융합연구소
中国科学院等离子体物理研究所
核融合科学研究所
10th A3 Foresight Program Workshop
日中韓フォーサイト事業
A3 Foresight Program
日本学術振興会

,

Contents

◆Session 11

Status of the JT-60SA Project

A. Isayama[1] on behalf of the JT-60SA team

[1]National Institutes for Quantum and Radiological Science and Technology, Naka, Ibaraki 311-0193, Japan

Abstract

This paper describes recent progress in the JT-60SA project. After the disassembly of JT-60U in October 2012, the assembly of JT-60SA started in January 2013. Since then, the construction of the JT-60SA tokamak is steadily progressing. As of November 2016, 3 toroidal field coils, which were fabricated in France and Italy, have arrived at the Naka site. Component installation and subsequent commissioning by EU workers are also in progress. For example, commissioning of the quench protection circuit and the cryogenic system has been successfully completed. The development of auxiliary heating systems, which are the neutral beam injection system and the electron cyclotron range of frequency system, is also in progress, and the performance required in JT-60SA was achieved. Discussion on research items is also continuing by European and Japanese researchers, and the JT 60SA Research Plan is growing toward First Plasma. Dedicated experiments toward JT-60SA using existing tokamaks, such as cleaning of plasma-facing wall by electron cyclotron waves, were also conducted.

1. Introduction

The JT-60SA project is a combined project of the Japanese national fusion program and the JA-EU Satellite Tokamak Program in collaboration with European and Japanese fusion communities. The mission of JT-60SA is to contribute to the early realization of fusion energy by addressing key physics and engineering issues for ITER and DEMO [1]. The main objectives of JT-60SA is (1) to support research for ITER by starting experiment in 2019, which is 6 years before ITER's First Plasma, (2) to complement research for DEMO by demonstrating long-duration sustainment of high integrated performance plasmas, and (3) to foster scientists and engineers of next generations toward ITER and DEMO.

To achieve this goals, sustainment of high-beta plasmas above the no-wall limit for much longer than typical physics time scales, such as energy confinement time and current diffusion time, is planned by utilizing various heating systems, in-vessel coils, advanced fueling systems, and active divertor pumping. The JT-60SA device is under construction at the Naka site of the National Institutes for Quantum and Radiological Science and Technology (QST). The operation of JT-60U was completed in August 2008, and the disassembly of JT-60U was finished in October 2012. Since the start of assembly of JT-60SA in January 2013, the construction is steadily progressing [1].

The components for JT-60SA are procured both by Japan and EU as shown in Fig. 1. Fabrication of components is in progress, and first 3 toroidal field (TF) coils, which were fabricated in France and Italy, have arrived at the Naka site as of the end of November 2016. In addition to the delivery of components, installation and commissioning of the components are carried out by workers from EU.

2. Status of the construction of JT-60SA

2.1 Construction of JT-60SA tokamak

The construction of the JT-60SA tokamak started by installing the cryostat base fabricated in Spain. After the temporal installation of the 3 lower equilibrium field (EF) coils procured by Japan, installation and welding of the 340º vacuum vessel sectors was carried out and finished in 2015. After then the thermal shields were installed on the outer surface of the vacuum vessel, and this work was finished in November 2016. The next work is to insert the toroidal field coils one by one through the 20º spacing. The latest status of the JT-60SA tokamak and first 2 TF coils are shown in Fig. 2.

2.2 Fabrication, installation and commissioning of components

2.2.1 Poloidal field coils

The poloidal field coils are composed of 6 EF coils made of NbTi and 4 modules of central solenoids (CSs) made of NB_3Sn, which are procured by Japan.

The EF coils except the first small EF4 coil were fabricated in the Naka site because some of them are too large to transport through the public road. The fabrication of the 3 lower EF coils was finished in 2014. The fabrication of the 3 upper EF coils was subsequently started, and finished in August 2016. In spite of its size (12 m diameter for the largest one), the circularity was measured to be 0.2-1.3 mm, which is much smaller than the requirement (6-8 mm).

The CS of JT-60SA is composed of 4 identical modules. The fabrication of the CS modules is in progress, and the first module was completed in September 2016. This module was then sent to National Institute for Fusion Science in Toki for cold tests.

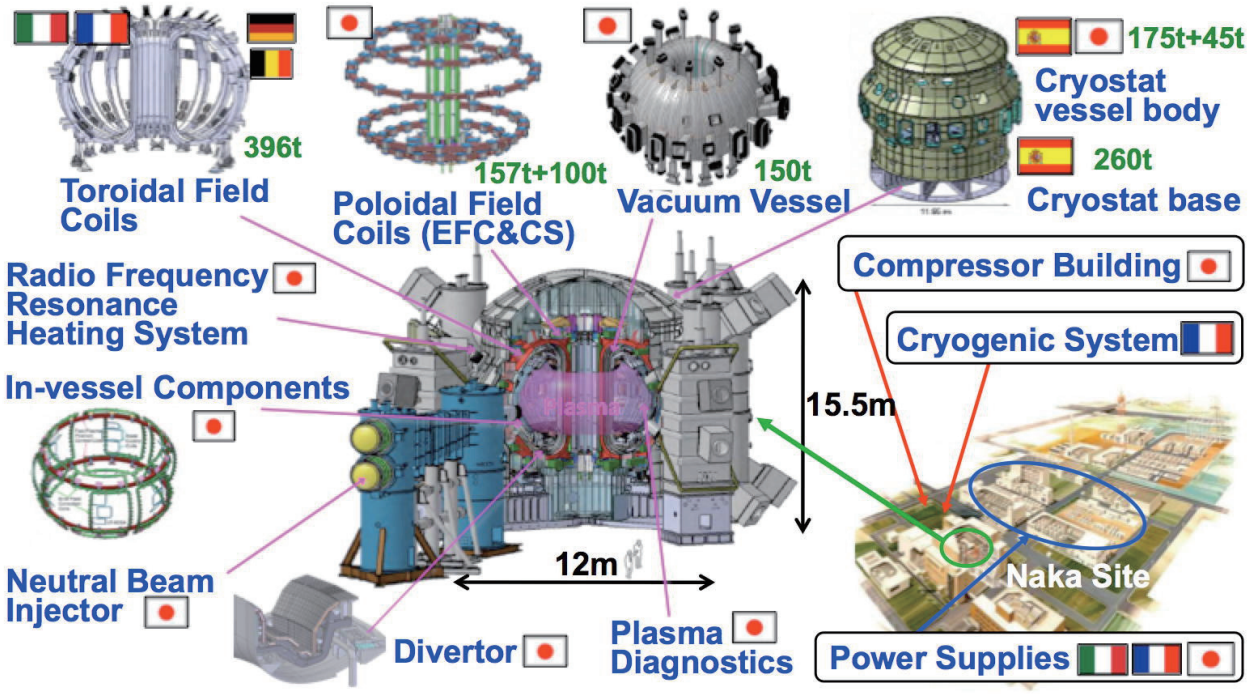

Fig. 1 Component sharing by EU and Japan.

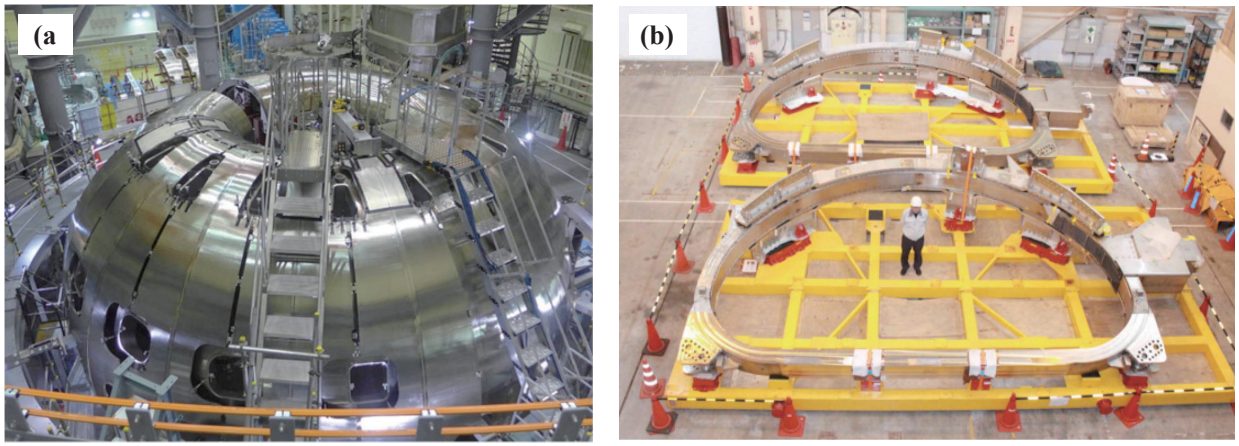

Fig. 2 (a) JT-60SA device in the torus hall, and (b) first 2 toroidal field coils arrived at the Naka site.

2.2.2 Toroidal field coils

The TF coils of JT-60SA are composed of 18 coils made of NbTi. The fabrication is conducted by CEA in France and ENEA in Italy. Both institutes are in charge of fabricating 10 TF coils (1 coil for spare). The manufacturing is in progress.

After successful cold tests at CEA Saclay including full current tests at 25.7 kA and quench tests, 2 coils from France, named "Annie" and "Brigitte" and 1 coil from Italy, named "Roberta", have already arrived at the Naka site. The next coil, fabricated in France and named "Cécile", is under shipment and will arrive at the Hitachi port in December 2016. Fabrication and testing of other coils are also in progress.

2.2.3 Vacuum vessel

The vacuum vessel (VV), which is procured by Japan, has a double-wall structure and is made of SUS316L with 18 mm thickness. The VV was composed of 10 components: seven 40º sector, two 30º sector and one 20º sector. Their parts were fabricated at the factory and jointed at the Naka site. After the first delivery of 40° inboard sector in April 2011, installation and welding works made good progress. Welding of the components was carried out by taking into account the deformation caused by welding. The welding of 340º torus was completed in 2015 with the displacement of +/–5 mm in the horizontal direction and –4 mm in the vertical direction, which is well within the requirement.

2.2.4 Cryostat

The cryostat of JT-60SA is composed of the cryostat base procured by EU, the cryostat vessel body procured by EU and the cryostat top lid procured by Japan. The cryostat base, whose diameter and height are ~12 m and ~3 m, respectively, was fabricated in Spain, delivered to the Naka site and installed at the torus hall in 2013. The cryostat vessel body, whose diameter is ~13.5 m, is under fabrication in Spain by dividing 12 sectors (Fig. 3). These sectors will be delivered to the Naka site in the middle of 2017. The design of the cryostat top lid was finished. The procurement arrangement will be concluded soon, and then fabrication will start.

Fig. 3 Cryostat vessel body cylindrical section under fabrication in Spain.

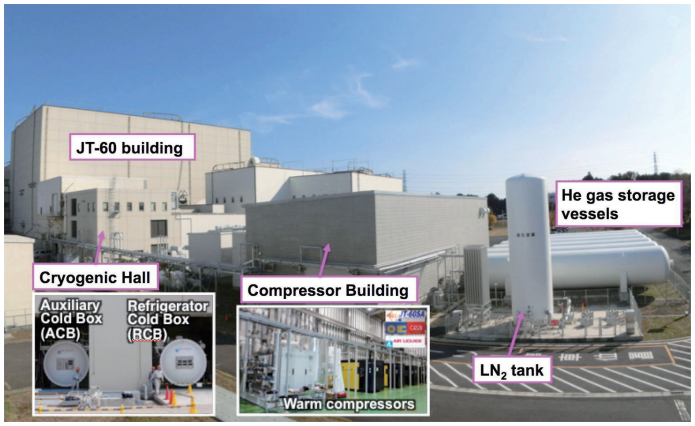

Fig. 4 Cryogenic system in the Naka site.

2.2.5 High-temperature superconductor current lead

High-temperature superconductor current lead (HTS-CL), in which bismuth alloy (Bi-2223/AgAu) is used, is installed between the superconducting coils and the external feeders. Since the HTS-CLs maintain superconducting state at 60 K, cooling power of the cryogenic system can be significantly reduced. Six HTS-CLs for the TF coils and 20 HTS-CLs for the PF coils were fabricated by Karlsruhe Institute of Technology in Germany. All of them are tested at the CuLTKa (Current Lead Test facility Karlsruhe) facility. All HTS-CLs for TF coils have already been delivered to the Naka site, and the other HTS-CLs will be delivered in 2017.

2.2.6 Cryogenic system

A cryogenic system is procured by EU (Fig. 4). The system is composed of 6 helium gas storage vessel, 8 warm compressors, 4 helium compressors, a refrigerator cold box and an auxiliary cold box. All of the system components were delivered and installed in 2015. After that, commissioning work by EU team started in March 2016, and was successfully finished in October 2016.

2.2.7 Power supplies

Many kinds of power supplies are newly installed for JT-60SA although existing power supplies used for JT-60U are reused as much as possible.

The superconducting magnet power supplies are procured by France and Italy. About half of them have been delivered to the Naka site and installed in 2016, and the remaining ones will be delivered by autumn 2017.

The quench protection circuit procured by Italy was delivered to the Naka site in September 2014, and commissioning work was completed in June 2015.

The switching network unit, which is used to produce high voltage during plasma breakdown and current ramp-up, was fabricated in Italy and delivered to Naka in 2015.

The power supplies for the fast plasma position control coils were fabricated in Italy and delivered to the Naka site in June 2016. Other power supplies such as the ones for resistive wall mode suppression coils, error field correction coils, and the electron cyclotron range of frequency (ECRF) system are under fabrication.

2.3 Development of Heating Systems

JT-60SA equips a neutral beam (NB) system and an ECRF system for auxiliary heating (Fig. 5). In both systems, existing facilities for JT-60U is reused as much as possible. To meet the requirement in JT-60SA, operations of these systems are continued.

The NB system is composed of the positive-ion-based NB (P-NB) system with the beam energy of ~85 keV and the negative-ion-based NB (N-NB) system with the beam energy of 500 keV. The total injection power of the P-NB and N-NB systems are 24 MW and 10 MW, respectively. In the P-NB system, beam acceleration at 2 MW (80 keV, 25 A) for 100 s has been demonstrated successfully [2].

The ECRF system is used for localized heating (ECH) and current drive (ECCD). In addition, this system is used for plasma initiation and first-wall cleaning. To enable ECH/ECCD under a wide range of operation conditions, a dual-frequency gyrotron, which can output 110 GHz and 138 GHz electron cyclotron (EC) waves, has been developed. In 2014, 1 MW output for 100 s at both frequencies was successfully demonstrated [3]. In 2016, 1 MW output for 1 s at 82 GHz using this gyrotron was also successful [4]. Although the output duration is limited to 1 s because this gyrotron is not optimized for 82 GHz output, this result is noteworthy because plasma initiation and plasma-facing wall cleaning by fundamental harmonic EC waves is possible. Further operations aiming at output power higher than 1.5 MW are in progress [4].

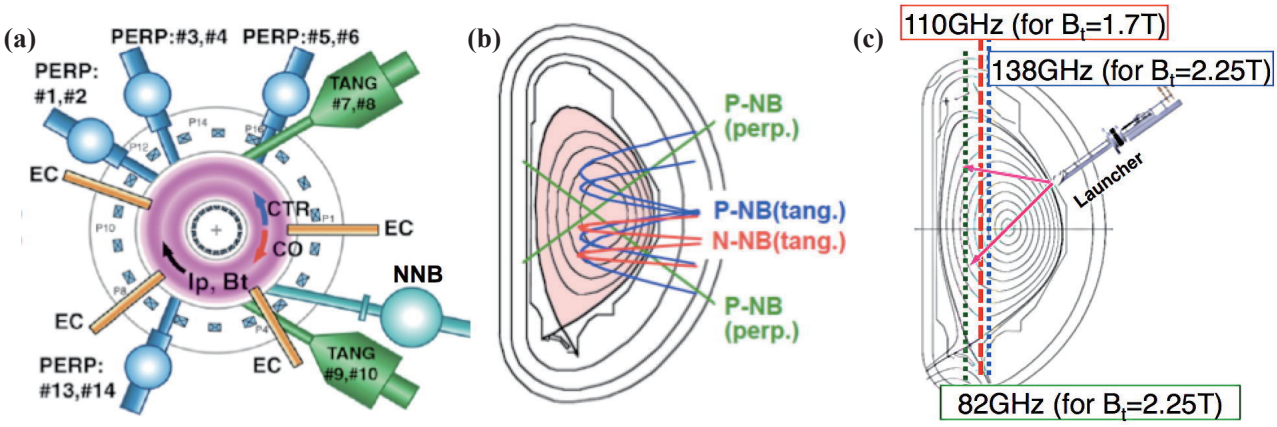

Fig. 5 (a) and (b) Layout of NB system. (c) Layout of ECRF system and resonance locations.

2.4 Progress in Research Activities

To address research issues and resolve them, the Research Coordination Meeting (RCM) is annually held, and the 5th RCM was held at the Naka site in May 2016. At RCMs, update of the JT-60SA Research Plan is also discussed. The latest version of the JT-60SA Research Plan is 3.3, to which 378 researchers contributed both from EU and Japan. The JT-60SA Research Plan summarizes research items in the following research areas: (a) operation regime development, (b) MHD stability and control, (c) transport and confinement, (d) high energy particle behavior, (e) pedestal and edge physics, (f) divertor, scrape-off layer and plasma-wall interaction, (g) fusion engineering, and (h) theoretical models and simulation codes [5].

Experiments in support of JT-60SA are also conducted. In 2016, dedicated experiments on the cleaning of the plasma-facing wall using second harmonic EC waves were conducted in TCV [6]. It was observed that the exhausted gas amount by the EC waves drastically changes by changing gas pressure, toroidal field strength, poloidal field pattern etc., which indicates that optimization of the discharge cleaning condition is important.

3. Summary

The fabrication of components/systems, their delivery to the Naka site, and the commissioning of the systems by EU workers are steadily in progress. In particular, the fabrication of a large cryogenic system was successfully finished in October 2016. Three TF coils have arrived at the Naka site as of the end of November 2016. The other coils are under fabrication/ shipping. The construction of the JT-60SA tokamak is also progressing, and the 340º vacuum vessel was completed. The installation of the TF coils will start in December 2016.

The development of heating systems, namely the NB injection system and the ECRF system, is also in progress, and results satisfying requirements in JT-60SA have been obtained.

Research activities toward JT-60SA experiments are also progressing. The JT-60SA Research Plan version 3.3, to which 378 researchers from EU and Japan contributed, is now open to public. The RCM is held annually, and the results of analysis and the update of the JT-60SA Research Plan are discussed.

Acknowledgements

This work was partly supported by the JSPS-NRF-NSFC A3 Foresight Program in the field of Plasma Physics (NSFC: No. 11261140328, NRF: No. 2012K2A2A6000443).

References

[1] H. Shirai *et al.*, Proc. 26th IAEA Fusion Energy Conf. (Kyoto, Japan, 2016), OV/3-3.

[2] A. Kojima *et al*., Fusion Eng. Des. **102** (2016) 81.

[3] T. Kobayashi *et al*., Nucl. Fusion **55** (2015) 063008.

[4] R. Ikeda *et al*., Proc. 26th IAEA Fusion Energy Conf. (Kyoto, Japan, 2016), FIP/1-6Rb.

[5] www.jt60sa.org/pdfs/JT-60SA_Res_Plan.pdf

[6] D. Douai *et al*., Proc. 26th IAEA Fusion Energy Conf. (Kyoto, Japan, 2016), EX/P8-3.

Characteristics in turbulent transport in flux-driven toroidal plasmas

Y.Kishimoto[1], K.Imadera[1], W. Wang[1,2], Z.Z. Wang[2], J.Q. Li[3,1]

[1]Kyoto University, Uji, Kyoto 611-0011, Japan
[2]Dalian University of Technology, China
[3]Southwestern Institute of Physics, Chengdu, China

Abstract

We have presented an overall picture of flux-driven ITG turbulent transport which reveals *resilience and stiffness in profile* and *self-similarity in relaxation* coupled with *SOC type intermittent bursts*. The transport is found to be regulated by different types of non-diffusive process as (1) *radially localized fast time scale avalanche*, (2) *radially extended global burst*, (3) s*low time scale avalanche* coupled with a shear layer of radial electric field E_r. Among them, the process (2) is the key, which results from instantaneous formation of radially extended ballooning type mode with nearly up-down symmetry in poloidal cross section. The repetitive occurrence of such a global mode is found to be the origin leading to a constraint on the profile causing the resilience and stiffness. The process (3) results from zonal flow and pressure governed by the extended global modes and dynamical evolution causes a new type of long time scale breezing in the transport. The spatio-temporal linkage of such different non-diffusive processes leads to *a new turbulent state dominated by long range correlation in time and space*. The magnetic shear is a key control parameter that regulates the turbulent structure.

1. Introduction

Turbulent transport and confinement in magnetically confined fusion plasmas exhibit a hierarchical nature dominated by spatio-temporally different processes such as force balance and equilibration process, neo-classical process, macroscale MHD and microscale turbulent process, etc. Among them, the global nature of turbulence is then of specifically importance in understanding and evaluating them. This is because the turbulence is dominated not only by local plasma parameters but also by their global extent and spatial variation [1-2]. A fundamental global nature related to turbulent is the mode structure which exhibits mesoscale in a toroidal system represented by $\Delta r \sim \sqrt{\rho_i L/\hat{s}}$, i.e. geometrical mean between microscale unit, i.e. ion gyro-radii ρ_i, and macro-scale unit, i.e. plasma scale length L, e.g. such as temperature and density scale length, L_T and L_n, resulting from toroidal coupling due to finite magnetic shear $\hat{s}$ [2-4]. Such a structure has been shown to exist numerically from global toroidal simulation [2] and theoretically from the first order ballooning theory which considers the effect of global profile variation, e.g. expressed by magnetic drift frequency shear, i.e. $\partial_r \omega_d$ [3-4].

It was found in the simulation that the corresponding transport exhibits multi-scale nature in time and space which provides a constraint on the transport process leading to the *resilience and stiffness in profile formation* and *self-similarity in relaxation* [2]. However, it is noted that the simulations showing above transport included neither the effect of zonal flow nor that of mean radial electric field. Therefore, it is

necessary to confirm whether the above transport dynamic reveals even in global toroidal simulation where such effects are treated properly consistent with experimental condition.

Here, using the GKNET (Gyro-kinetic based Numerical Experiment of Tokamak), which is a 5-dimensioanl full-*f* flux-driven global toroidal gyrokinetic code including neoclassical effect and heat source and sink [6,7], we revisit turbulent transport dominated by ITG turbulence under the condition that the zonal flow and mean radial electric field are introduced. Based on the simulation, we deduce an overall picture of turbulent transport in flux driven toroidal system emphasizing the global nature of turbulence covering whole plasma. Even in the presence of zonal flow and radial mean electric field, we have observed similar mesoscale turbulent structure and associated self-organization leading to profile resilience and stiffness. The turbulent transport is found to exhibit rich dynamics such that qualitatively different non-diffusive processes with different spatio-temporal scales coexist and incorporate with each other.

2. Flux-driven ITG turbulence and transport

Here, we study a circular plasma of $a/R_0 = 0.36$ and $a/\langle \rho_i \rangle = 150$ where $\langle\ \rangle$ denotes the spatial average over minor radius a. The collision effect is introduced for parallel velocity which conserves energy and momentum, where normalized frequency is given by $\nu_* = 0.565$ corresponding to a banana regime with $k = 0.01$ (neoclassical parameter) and is spatially constant [6.7]. A nearly flat density profile with $R_0 / L_n = 2.22$ at $r/a = 0.5$ is used and the parabolic safety factor profile $q(r) \propto r^2$ shown in Fig.1 is employed. The heat source and sink are given near center and edge as shown in Fig.1, which drives heat input given by $P_{in} = 16$MW. The GKNET simulation is performed in an electrostatic modelling with adiabatic electron so that no particle transport takes place [6].

2.1 Spatio-temporal structure of turbulent transport [7]

Figure 1 shows (a) turbulent heat flux $\langle Q_{tub}(t) \rangle$ where heat flux $Q_{tub}(r,t)$ is averaged over $60 \le r \le 80$, (b) $Q_{tub}(r,t)$, and (c) radial electric field $E_r(r,t)$ in $900 \le t \le 1300$ (quasi-steady state phase). Here, time and space are normalized as $t\upsilon_i / R \to t$ and $r/\langle \rho_i \rangle \to r$, respectively. The ion temperature $\langle T_i \rangle^*(r)$, which is averaged over $900 \le t \le 1300$, is shown in Fig.1. It is found that $\langle T_i \rangle^*(r)$ is suffered from a constraint exhibiting an exponential function form, i.e. $T_i(r) \sim \exp(-r/L_T)$, in two regions, i.e. $L_T \sim L_{T1}$ in $0 < r \le 80$ (inside) and $L_T \sim L_{T2}$ in $80 \le r < 150$ (outside), showing a *knee* for scale length at $r \sim 80$. Near the center $0 \le r < 30$, quasi-periodic bursts coupled with the generation of radial electric field E_r take place due to the external heating and supply turbulence to the bulk region via fast time scale avalanches as seen in Fig.1 (b) and (c).

Figure 2 (a) represents $E_r(r)$ at $t = 25$ and $t = 62$, i.e. before and after the linear mode saturation. The former corresponds to the mean $E_r(r)$ mainly determined by the initial temperature profile and the latter exhibits an oscillatory nature due to zonal flows produced by the turbulence. Figure 2 (b) illustrates $E_r(r)$ and $R/L_T(r)$ at $t = 1360$ in a quasi-steady state phase. A quasi-periodic oscillation and/or corrugation of temperature coupled with that of $E_r(r)$ superimposed on the self-organized profile can be seen, which is referred to as $E \times B$ staircase.

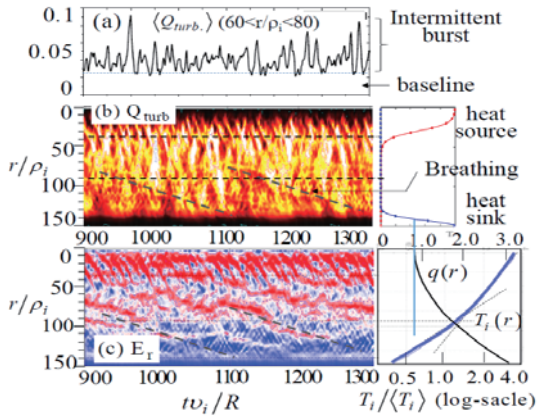

Fig.1. (a) Evolution of averaged heat flux $\langle Q_{\text{turb}}\rangle$ in $60<r/\rho_i<80$, (b) spatio-temporal evolutions of heat flux $Q_{\text{turb.}}(r,t)$ and (c) radial electric field $E_r(r,t)$. Ion temperature profile (log-scale) and $q(r)$ are shown [**from Ref.7**]

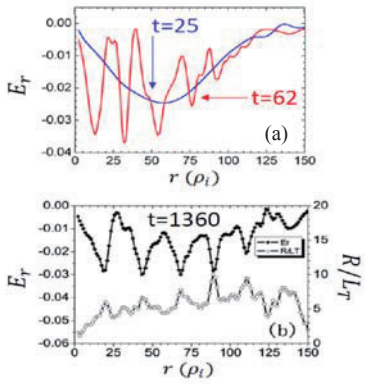

Fig.2. (a) Radial profile of mean radial electric field $E_r(r)$ at t=25 (blue) before saturation of linear mode and t=62 (red) redafter the saturation. (b) Radial profile of $E_r(r)$ and and R/L_T. at quasi-steady state. [**from Ref.7**]

In the source/sink free region $30 \le r \le 130$, various types of non-diffusive transport events with different time and spatial scales are found to appear, which are summarized as follows,

(1) Radially localized avalanches which propagate in the radial direction with fast time scale: The typical radial correlation length and propagation velocity are estimated as $\ell_c = \rho_i \sim (\rho_i L_T)^{1/2}$ and $\upsilon_a = 2-3(\rho_i/R)\upsilon_i$, respectively. Here, υ_i is the ion thermal velocity. Two type of avalanches is known to exist, one is temperature hump in the plasma with $\partial_r E_r < 0$ which propagates toward edge, the other is temperature hole in the plasma with $\partial_r E_r > 0$ which propagates toward centre [8].

(2) Radially extended intermittent bursts: The typical radial correlation length ranges from mesoscale to macroscale, i.e. $\ell_c = (\rho_i L_T)^{1/2} \sim L_T$. As seen in Fig.1 (a) and also Fig.2, the corresponding heat flux Q_{tub} in the bulk region ($30 \le r \le 130$) exhibits quasi-periodic bursts which period is roughly estimated as $\Delta t \sim 20(R/\upsilon_i)$.

(3) Radially localized avalanches which propagate in the radial direction with slow time scale coupled with oscillatory and/or corrugated electric field (E_r): The radial location of localized E_r and/or the shear layer roughly corresponds to the edge of global burst in the process (2). This avalanche is also found to be repeated with time interval estimated by $\Delta t = 100-200\,(R/\upsilon_i)$, leading to long time scales breathing in transport [6,7].

2.2 Instantaneous formation of radially extended global mode

Figure 3 shows the radial heat flux $Q_r(r,\theta)$ at nearly a bottom (a) and a peak (b). In the peak, radially extended ballooning-type structure with long radial correlation length ℓ_c which reaches to $\ell_c \sim 80\rho_i$ can be seen. Here, the structure shows nearly up-down symmetry. This is because the effect of finite diamagnetic shear ($\partial\omega_d/\partial r$), which causes asymmetry to the potential ϕ by a finite Bloch angle θ_0 and reduction in γ (mode growth rate) and ℓ_c, is canceled by that of the E_r shear ($\partial\omega_{E\times B}/\partial r$). As the result, the symmetry is recovered ($\theta_0 \sim 0$), which enhances both γ and ℓ_c. Therefore, once the phases of

potential eddies at different radii are aligned spontaneously in the radial direction, the global mode ϕ and thereby Q_r with long ℓ_c from mesoscale to macroscale can grow. Such structures are disintegrated and damped by self-generated zonal flows while the process is repeated intermittently as seen in Fig.1.

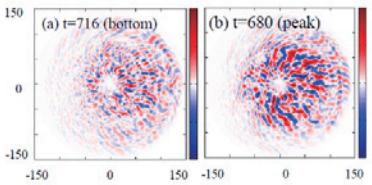

Fig.3: Radial heat flux $Q_r(r,\theta)$ at bottom (a) and peak (b) as in Fig.1 (a)

2.3 Effect of magnetic shear in turbulent transport

Figure 4 (b) shows turbulent heat flux $Q_{tub}(r,t)$ for the week magnetic shear shown in Fig.4 (a), i.e the case of $q \propto r^6$ ($\hat{s}=0.23$). It is found that the radially extended global bursts are suppressed compared with that in Fig.1 where $q \propto r^2$ ($\hat{s}=0.78$) while the transport is dominated by radially localized avalanches as in the process (2) in 2.1. This is because the toroidal coupling leading to ballooning mode is hardly established due to week magnetic shear., suggesting that the magnetic shear can be a control parameter.

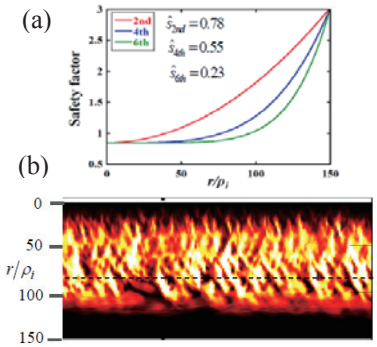

Fig.4: (a) three cases of q-profile. (b) s heat flux $Q_{\text{turb.}}(r,t)$ for week magnetic shear case (s=0.23).

3. Summary

We have presented an overall picture of flux-driven ITG turbulent transport which reveals resilience and stiffness in profile and self-similarity in relaxation coupled with SOC type intermittent bursts. The transport is found to be regulated by qualitatively different processes (1)-(3) as discussed in 2.1. Among them, the process (2) is the key, which results from instantaneous formation of radially extended global structure ranging from mesoscale to even macro-scale. The $E\times B$ staircase originates from zonal flows produced by such global structure while it dynamically evolves causing long time scale breathing in transport. The magnetic shear which can regulate the transport process (1)-(3) can be a control parameter for transport.

Acknowledgements

This work was partly supported by the JSPS-NRF-NSFC A3 Foresight Program in the field of Plasma Physics (NSFC: No.11261140328, NRF: No.2012K2A2A6000443). Primary contents and discussions of this proceeding including figure 1 and 2 are described flowing those in Ref.7.

Reference

[1] Z. Lin, et al. Science, 281, 1835 (1998).

[2] Y. Kishimoto, *et.al.* Phys. Plasmas, **3** (1996) 1289.

[3] J. Y. Kim et. al., Phys. Plasma **3**, 3689 (1996).

[4] Y. Kishimoto, *et al.*, Plasma Phys. Controlled Fusion **41**, A663 (1999).

[6] K. Imadera *et al.*, 25th Fusion Energy Conference, TH/P5-8, Oct. 16 (2014).

[7] Y. Kishimoto et al., 26th Fusion Energy Conference, TH/P3-2, Oct. 19 (2016).

[8] M. Kikuchi and A. Azumi, Rev. Mod. Phys 84, 1807 (2012).

Internal transport barrier (ITB) formation in KSTAR: Initial observations with inboard limited discharges

Jinil Chung, Y. M. Jeon, H. S. Kim, J. Kim, K. D. Lee, J. Ko, H. H. Lee, W. H. Ko, J. H. Lee, J. M. Kwon and S. W. Yoon

National Fusion Research Institute, Daejeon, Korea

Abstract

An ITB formation during L-mode has been observed which shows improved core confinement. Time trace parameters indicating the plasma performance such as temperatures, the stored energy and the β_N are comparable to the H-mode in the discharge. Ion and electron temperature profiles show the barrier clearly in the temperature, and it was sustained for about 7 s in the dedicated experiment. In this work, we introduce the ITB formation observed during the 2016 KSTAR campaign.

1. Introduction

One of important goals of tokamak experiments is the exploration of enhanced confinement regimes, and the access of the internal transport barrier (ITB) formation is dealt with an important physics issue in the most of tokamaks [1-3]. Investigation of the ITB formation condition in the KSTAR is also valuable in that point of view although its heating and current drive systems are not fully equipped to see the ITB with H-mode.

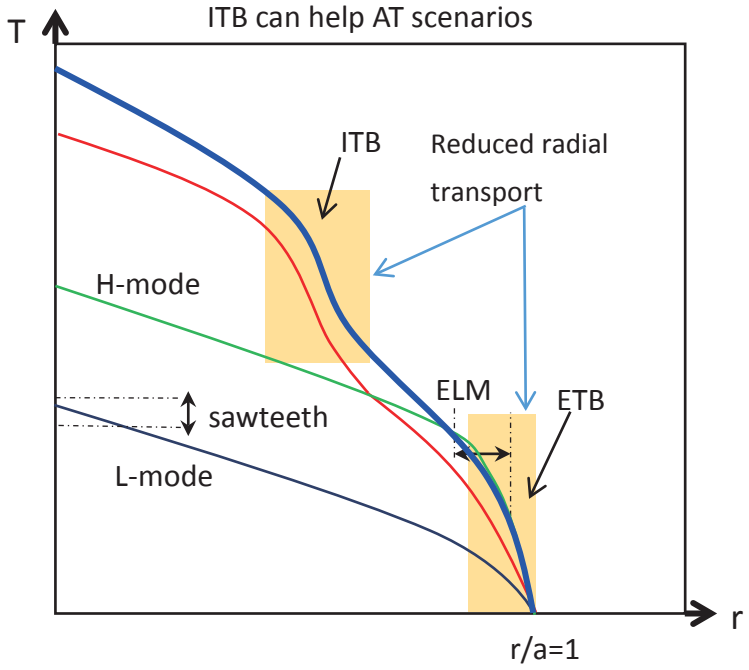

Fig.1 Illustrating temperature profiles during L-mode, H-mode, and ITB plasmas in a tokamak.

When a sufficient power is applied to the L-mode plasma, the edge confinement is improved in a sudden, and this region of the edge pedestal is called edge transport barrier (ETB) in H-mode. The ITB which is not fully understood as the ETB is also observed probably in a similar way of physics. The ITB enhance the discharge performance by a significant factor like the H-mode, and with both ITB and ETB we could improve the confinement even more. We have observed these ITB formations during the last KSTAR campaign (2016). Here the H-mode with ETB is robust and reproducible. It provides good confinement, and no q-control is required. However, we experience large ELMs. Pulse length of the H-mode is still limited, so we need advanced tokamak (AT) scenarios with an alternative approach. The ITB is a strong candidate of the AT scenario which need controls of q- and pressure profiles, but we could avoid serious instabilities and increase fusion power density.

2. ITB discharges in KSTAR

In 2012, we had observed ITB-like phenomena for the first time in KSTAR with a limited NBI-1 power and the maximum available plasma current ramp-up rate of 0.8 MA/s. We observed a sudden rise of core temperature, while the density stays constant with also limited diagnostic channels. The first shot #8046 was designed to inject the neutral beam during the Ip ramp-up phase. We had scanned the beam energy and injected all available external current drive sources for the experiment. However, it was difficult to judge that the ITB was clearly formed due to lack of core profile diagnostics as well as the experiment could not be continued due to a machine safety with the highest current ramp-up rate.

The beam power of the fully equipped NBI-1 heating beam consists of three ion sources is now 5.5 MW. The motional Stark effect (MSE) diagnostic for measuring the q-profile [4-6] and a charge exchange recombination spectroscopy (CES) for measuring the ion temperature profile are sitting next to the heating beam. The electron cyclotron emission (ECE) system for measuring the electron temperature profile was also the key diagnostic of this experiment.

According to a scaling law of the ITB threshold power [2], KSTAR needs at least 4 to 5 MW of heating power to see the ITB, and KSTAR has 5.5 MW of neutral beam injection (NBI) system. This will be doubled in 2018 but it seemed marginal until we have the second NBI system, and since the diverted plasma easily go to the H-mode, we suggested to hold down to the inboard limiter to avoid the H-mode transition.

Figure 2 shows you the first result of ITB during an L-H-L transition. A total of 4.5 MW neutral beam injected during the current ramp-up, and the ITB formed just before the flattop of the plasma current. The ITB sustained until the H-mode transition at around 3 s. Here, time trace parameters indicating the plasma performance such as temperatures, the stored energy, the β_N, and neutron rate are comparable to the H-mode in the discharge. The formed internal barrier is clearly shown in the temperatures, and it is in both ion and electron thermal channels (not shown in this article). Profiles with red dots are during the ITB phase at 2.5 s, and the profiles in blue are during H-mode without ITB. We can clearly see the ITB foot and the ETB pedestal as shown in Fig. 3.

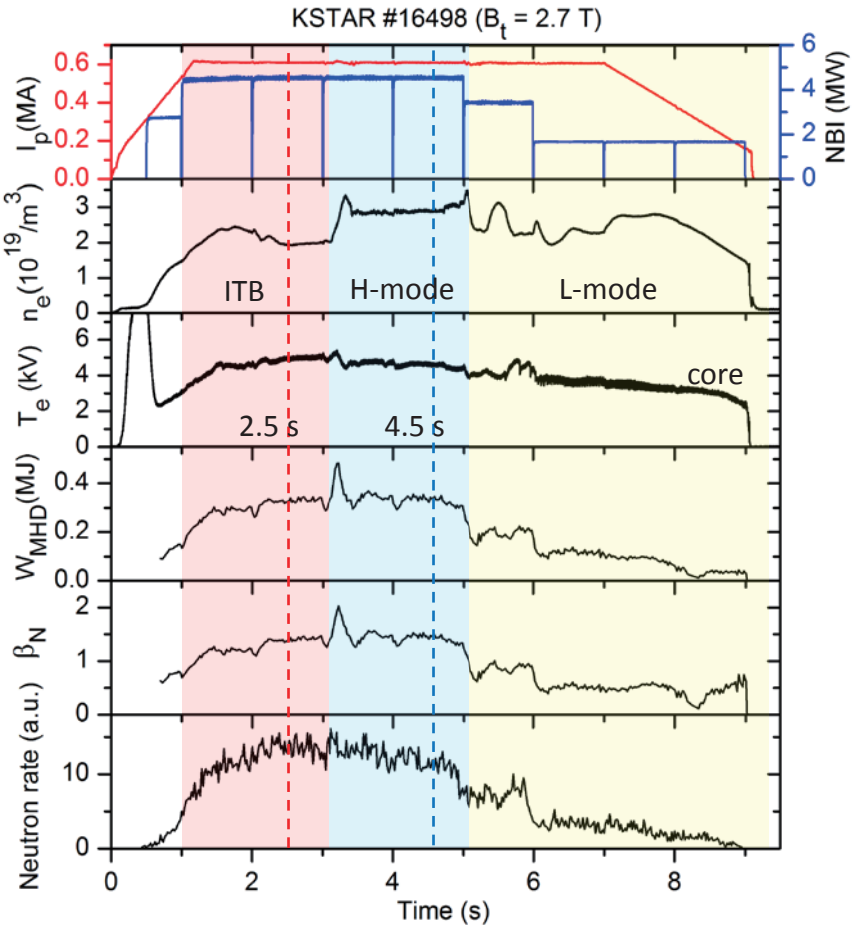

Fig.2 Time trace parameters of the first ITB discharge in KSTAR (#16498).

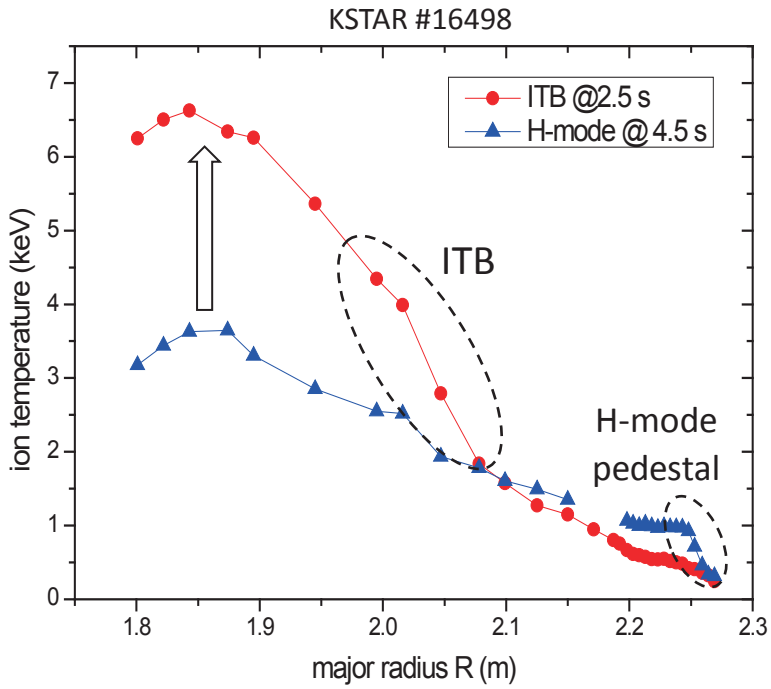

Fig. 3 Ion temperature profiles at 2.5 s and 4.5 s of the shot #16498 show the plasma performance during the ITB.

We have measured the pitch angle profile with the MSE diagnostic, and we have got q-profiles using the MSE-constrained EFIT. The ITB foot is in q = 2 surface, and the profile is flattened in the core region. This profile is the biggest change since we measure the pitch angle within the operation regime in KSTAR. The q_0 starts at 2 with the ITB formation at 1 s goes to below 1, and it show clearly the three different phase, ITB, H-mode, and L-mode in a single shot.

We have observed the ITB during a simple L-mode discharge. A total of 4.5 MW NBI power delivered during the I_p ramp-up. The ITB formed just before the flattop and sustained for about 3.6 s. The ion temperature in the core region is much higher, but the signal level on the CES detector was easily saturated. This is maybe due to an accumulation of the carbon impurity in the core. However, we still clearly see the ITB in the electron temperature profile. To get the position of the ITB foot, we have carefully fitted profile. Maximum of 2nd derivative of the fitted line is the position of the ITB foot, and it is always in 2.0 m to 2.1 m in time. We have also produced stationary ITB discharges in a slightly lower B_t at 2.5 T, and higher power input. We applied 5.5 MW of full NBI power during the ramp-up, and the ITB sustained until the ramp-down of the NBI at 8 s. The ITB foot move outward in time and stay constant after few seconds later. There were no instabilities and all the measured parameters are very stable, so we believe that we could extent the length of this ITB discharge even longer. We have observed a double barrier, both ITB and ETB together for a few hundreds of ms after a H-mode transition. The H-mode ETB providing a further improvement in confinement, but it is unstable and leading to a disruption.

In conclusion, we have observed the ITB formation with a significant improvement in confinement over inboard limited discharges in KSTAR. The ITB formed in both ion and electron thermal channels, and performances are comparable to the H-mode in KSTAR. Big enough NB power (> 4 - 5 MW) under a limited L-mode is the key of the ITB access in KSTAR. We have also produced stationary ITB discharges in slightly different B_t and power conditions. Closer look of the saturated T_i and Gyrokinetic simulations with measured profiles and the characteristic parameters are in progress.

Acknowledgements

This work was partly supported by the JSPS-NRF-NSFC A3 Foresight Program in the field of Plasma Physics (NSFC: No.11261140328, NRF: No.2012K2A2A6000443).

References

[1] R. C. Wolf, Plasma Phys. Control. Fusion 45 R1–R91 (2003)

[2] J.W. Connor, et. al. Nucl. Fusion, 44 R1–R49 (2004)

[3] X Litaudon, Plasma Phys. Control. Fusion 48 A1–A34 (2006)

[4] J. Chung, et. al. Rev. Sci. Instrum. 85, 11D827 (2014)

[5] J. Ko, et. al. Fus. Eng. and Design 109–111 (2016)

[6] J. Chung, et. al. Rev. Sci. Instrum. 87, 11E503 (2016)

Recent study of internal kink mode instability on EAST Tokamak

Liqun Hu[1], Yi Yuan[1,2], Liqing Xu[1], Kaiyun Chen[1], Ling Zhang[1], Yanmin Duan[1], and EAST team.

[1] Institute of Plasma Physics, Chinese Academy of Sciences
[2] University of Science and Technology of China

Abstract

As the diagnostics and the auxiliary heating systems improve and develop on EAST tokamak, series of interesting magnetohydrodynamic phenomena have been identified and studied. Among the observed MHD instabilities, internal kink mode related modes such as fishbones, snakes and sawteeth are of particular interests. Repetitive fishbones near the trapped ion procession frequency were observed for the first time in the neutral beam injection high confinement plasmas on EAST. Using a high spatial-temporal-resolution multi-array Soft-X ray diagnostic and compact solid-state neutral particle analyser (ssNPAs), its 1/1 mode structure and energetic particle driven nature are revealed. In plasma discharges with consecutive H-L-H transitions, repetitive snakes are found to damping on core toroidal rotation. The repetitive appearance of snakes revealed a impurity threshold. Due to its localized heating effects, electron cyclotron resonant heating (ECRH) is used to sawtooth control experiments. With respect to the q =1 surface, the effects of ECRH deposition position on sawtooth periods demonstrate different outcomes. Inside the q=1 surface, sawtooth is destabilized (reduced periods). Outside the q=1 surface, sawtooth is stabliziezd.

1. Introduction

Internal kink mode related phenomena such as snake oscillation, sawtooth and fishbone in global mode structure are among the most frequently encountered MHD activities in tokamak plasma discharges. Sawteeth and snake oscillations can directly lead to a redistribution of plasma parameters such as electron temperature and density. Large sawtooth and snakes can supply a seed island for 2/1 NTM destabilization, which is another undesirable effect. Conventional fishbones (FBs, in precession frequency) correspond to the so-called energetic-ions particle driven instabilities. FBs have the similar detrimental effects by interacting with thermal plasma strongly which affect equilibrium, stability and confinement, and inducing significant fast ion loss.

Understanding these instabilities is very important for future ITER operations where the q=1 surface can reach up to half of minor radius and large population of energetic particles are generated from fusion-born alpha particles as well as auxiliary heating

2. Fishbone activity in Neutral Beam Injection plasma

Repetitive fishbones near the trapped ion procession frequency were observed for the first time in the neutral beam injection high confinement plasmas in Experimental Advanced Superconducting. This 1/1 typical internal mode propagates in the ion-diamagnetism direction, With typical frequency chirping, and

rotation higher than the bulk plasma rotation (T-CXRS) (see Fig1, 2).

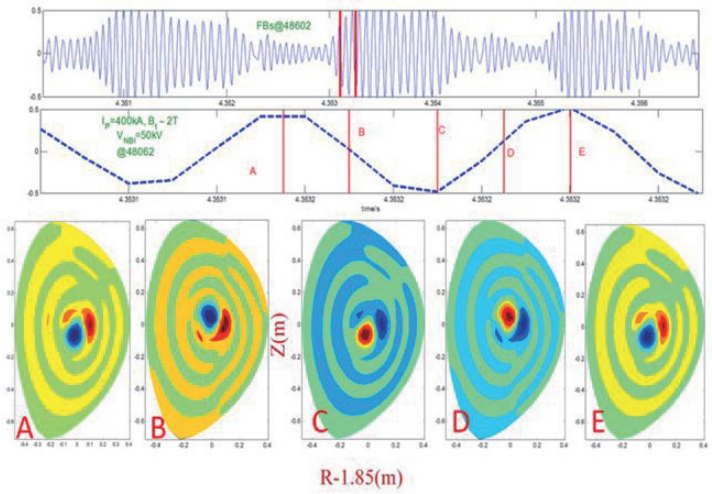

Fig.1 Poloidal structure and poloidal rotation direction analysis of fishbone in Shot #48605. upper-Fishbone shown in the core SX signal; mid and bottom-contour plots of the reconstructed perturbation of the local emission intensities from the perturbation signals extracted by the SVD method. The numbers on the left of the reconstructed frames correspond to those in the upper frame. The propagation of the fishbone-induced hot core in the poloidal section is along the ion-diamagnetism direction (counter-clockwise poloidal direction)

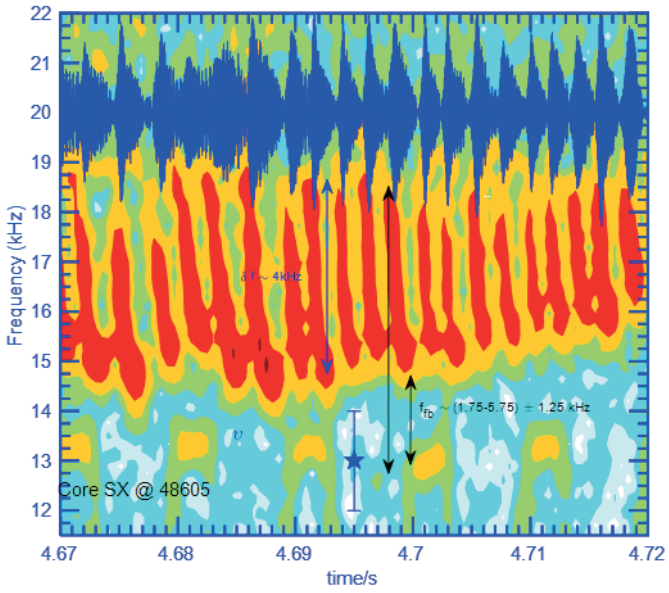

Fig. 2 Typical frequency whistling-down spectrograms of fishbone as observed from a central SX channel together with the central bulk plasma rotation speed (blue star) measured by X-ray crystal spectrometer. The overlaid blue signals correspond to raw core SX signals. The difference in frequency between the onset and quenching of the fishbone is up to df ≈ 4 kHz. The frequency of fishbone is in the range f_{fb} =(1.75 -5.75)±1.25 kHz.

An individual ssNPA vertical detector filtered with W-dominated foil of thickness 100/200nm was used to measure the NBI beam ions energy. The100/200nm W foil provides a low detection threshold for deuterium

of around 22.0keV and 45.6keV. A detailed comparison between the ssNPA signal and the fishbone is given in Fig. 3.

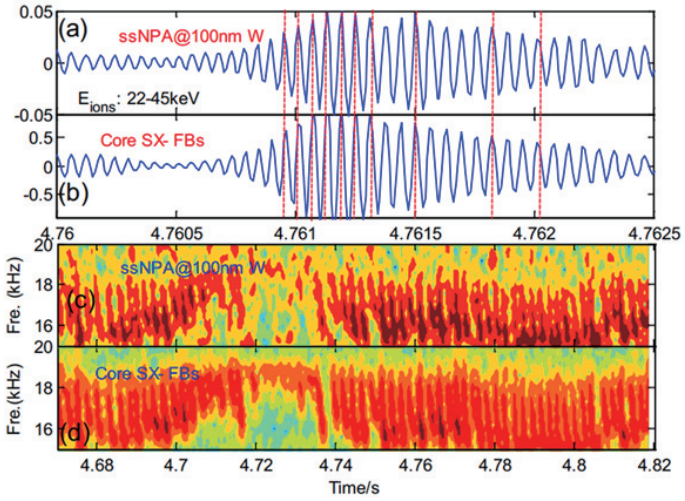

Fig. 3 Corresponding to the energetic particle-driven feature, Good correlation was found between FBs and ssNPA signal with 100 nm W filter (35keV).

3. Repetitive impurity snakes and their dumping effect on core toroidal rotation in plasma charges with multiple H–L–H transitions.

Examination of the data in Fig. 4 demonstrates that the 1/1 snake mode only occurs when dw/dt > 0 during the confinement improvement stage following the H–L phase of an H–L–H transition as the plasma starts to recover the H-mode. By examining all EAST shots which exhibited repetitive H–L–H transitions, it was observed that repetitive bursting of snake modes correlated with repetitive H-mode phases, with the first snake mode starting after the first H–L transition. Further, snake modes were observed to start within 20 ms of the associated L–H return transition. The vertical dashed line in Fig. 4 marks the termination of a typical snake mode and the beginning of a ‘slow ramp-up’ phase toward maximal stored energy, before the beginning of another H–L–H transition and the formation of another snake mode.

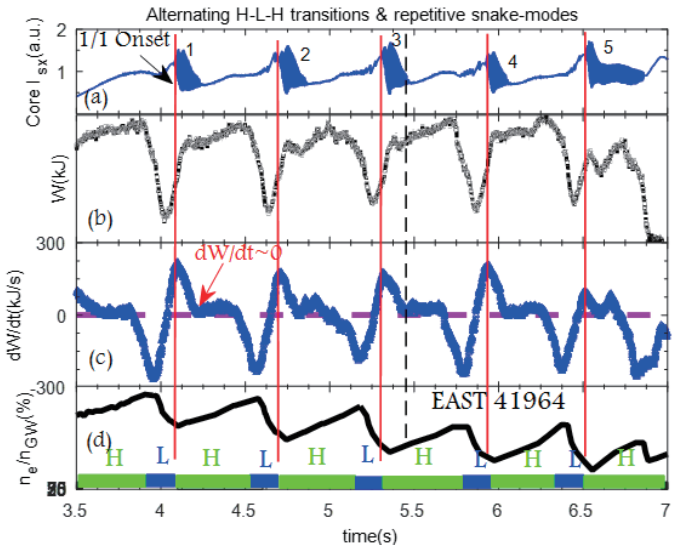

Fig.4 Repetitive snakes in an EAST discharge with multiple H–L–H transitions: (a) the core soft x-ray signal Isx; (b) the plasma stored energy W; (c) the plasma stored energy growth rate dw/dt ; (d) n/nGW, where nGW(10^{20} m^{-3}) = Ip (MA)/ π a $(m)^2$ is the 'Greenwald limit' density. The vertical dashed line designates the end of a snake mode and the beginning of a slow 'ramp-up' to maximal stored energy. L and H letters in the bottom indicate the low-confnement and high confinement, respectively.

The increase in plasma confnement during L–H transitions and the erosion of the plasma facing components caused by both the higher edge temperature and increased heat load from large edge localized modes (ELMs) account for the Mo impurity influx during H-mode plasmas.

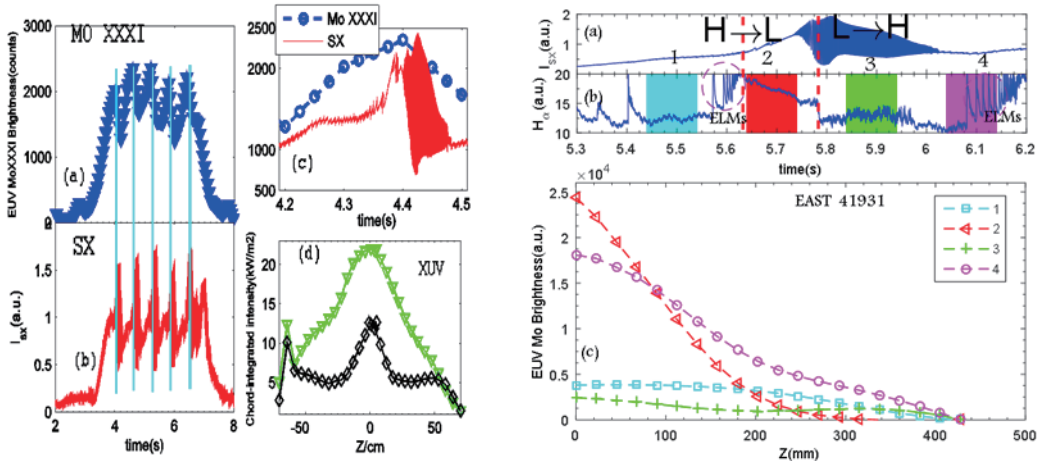

Fig.5 Central peaking impurity profile before snake onset was measured by EUV spectrometer as well as XUV detectors. The quasi-periodical burst of SX signals show good correlation with Mo emission measured by EVU system. The formation and stability of snake here is rely on the plasma conditions which are directly connected with large ELMs crash.

The strong toroidal rotation damping due to the 1/1 snake mode has been observed, as shown in Fig. 6

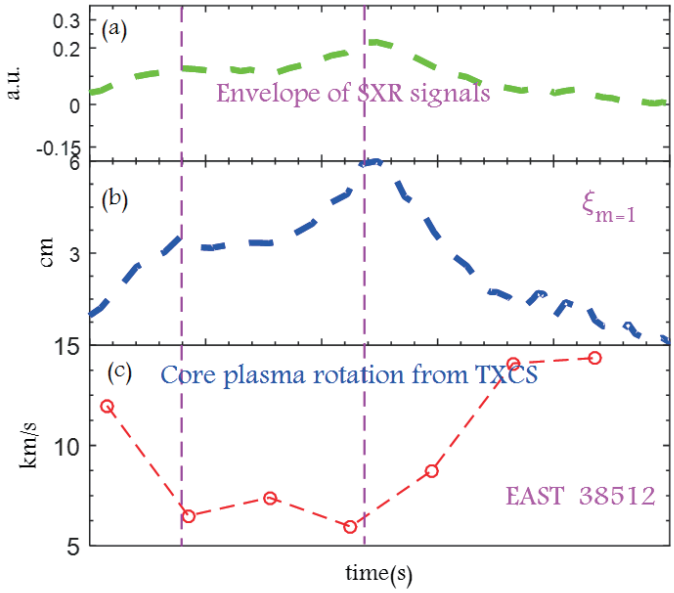

Fig.6 An example of core plasma toroidal rotation dampening by a snake mode. (a) The envelope of the core SXR sinusoidal signal. (b) The displacement $\xi_{m=1}$. (c) The core plasma toroidal rotation Δv_{ϕ}. Envelope of SXR signal in (a) means the mean of peaks and valleys of the core SXR sinusoidal signal. The core plasma rotation(r/a ~0.2) shown in (c) is measured by the TXCS system in EAST.

4. Sawtooth control experiments using ECRH

Due to the localized heating effects (see Fig.7), ECRH is used to modify the magnetic shear at q=1 surface. According to Porcelli Model, the magnetic shear at q=1 surface (see Fig. 8) determines sawtooth crash.

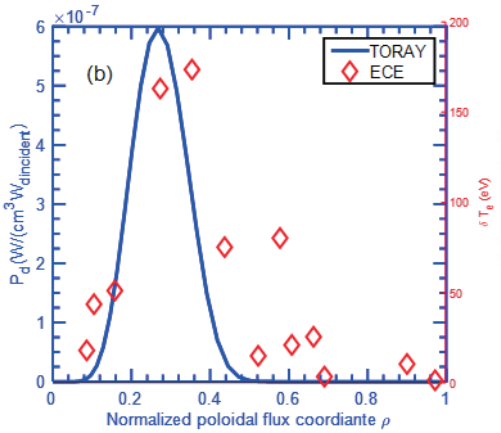

Fig. 7

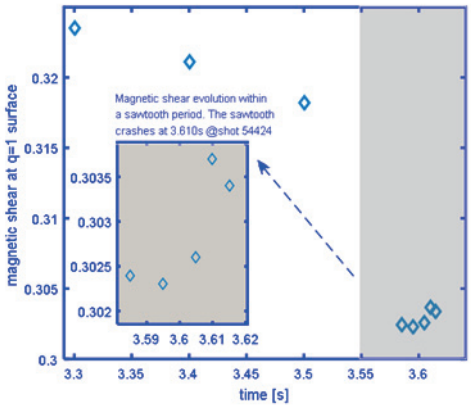

Fig. 8

Fig.7 Electron temperature variation after 15ms of ECRH injection. The temperature variation profile (in red diamond) correspond well with ECRH heating deposition (in blue line) calculated by TORAY-ray tracing code,

Fig.8 Magnetic shear evolution in one sawtooth period suggests the existence of a threshold for sawtooth crash.

By changing EC wave injection angle between different shots, the relation between sawtooth period and ECRH deposition position is investigated.

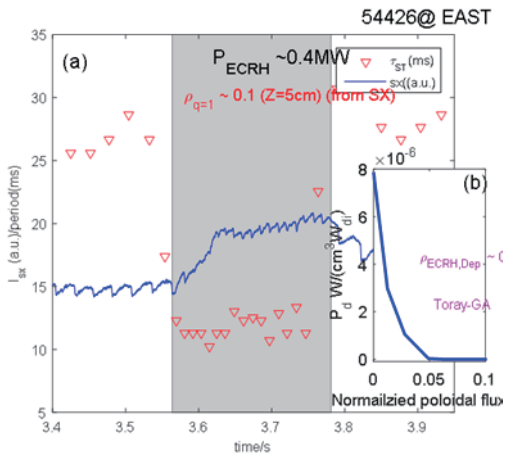

Fig. 9

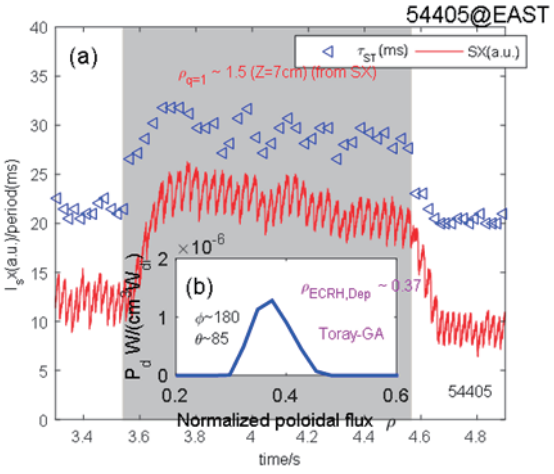

Fig.10

Fig.9 (a) Temporal evolvement of sawtooth period of shot 54426; the time domain when ECRH was injected was illustrated with shading; triangular represents the sawtooth period; and sawtooth was destabilized (characterized by reduced period) due to ECRH. (b) ECRH deposition position calculated by TORAY-GA ray-tracing code.

Fig.10 (a) Temporal evolvement of sawtooth period of shot 54405; the time domain, when ECRH was injected, is illustrated with shading; triangular represents the sawtooth period; and sawtooth is stabilized (characterized by prolonged period) due to ECRH. (b) ECRH deposition position calculated by TORAY-GA ray-tracing code.

Acknowledgements

This work was partly supported by the JSPS-NRF-NSFC A3 Foresight Program in the field of Plasma Physics (NSFC: No.11261140328). The National Magnetic Confinement Fusion Science Program of China under Contract No. 2013GB106003B, the National Magnetic Confinement Fusion Science Program of China (Grant No. 2014GB124006), and the National Magnetic Confinement Fusion Science Program of China under Contract No. 2012GB103000

References

[1] Fishbone activity in experimental advanced superconducting tokamak neutral beam injection plasma. PHYSICS OF PLASMAS 22, 122510 (2016).

[2] Repetitive ‘Snakes’ and Their Damping Effect on Core Toroidal Rotation in EAST Plasmas with Multiple H–L–H Transitions. CHIN.PHYS.LETT. Vol.31, No. 10 (2014)105201

[3] Control of sawtooth via ECRH on EAST tokamak PHYSICS OF PLASMAS 23, 062503 (2016).

Explicit high-order non-canonical symplectic particle-in-cell schemes for Vlasov-Maxwell systems

Jianyuan Xiao[1,2], Hong Qin[1,3], Jian Liu[1,2], Yang He[1,2], Ruili Zhang[1,2], and Yajuan Sun[4]

[1]School of Nuclear Science and Technology and Department of Modern Physics, University of Science and Technology of China, Hefei, Anhui 230026, China

[2]Key Laboratory of Geospace Environment, CAS, Hefei, Anhui 230026, China

[3]Plasma Physics Laboratory, Princeton University, Princeton, NJ 08543, U.S.

[4] LSEC, Academy of Mathematics and Systems Science, Chinese Academy of Sciences, P.O. Box 2719, Beijing 100190, China.

Abstract

Explicit high-order non-canonical symplectic particle-in-cell algorithms for classical particle-field systems governed by the Vlasov-Maxwell equations are developed. The algorithm conserves a discrete non-canonical symplectic structure derived from the Lagrangian of the particle-field system. The electromagnetic field is spatially-discretized using the method of discrete exterior calculus with high-order interpolating differential forms for a cubic grid. The resulting time-domain Lagrangian assumes a non-canonical symplectic structure. It is also gauge invariant and conserves charge. The system is then solved by using a high-order explicit structure-preserving splitting method. The explicit, high-order, and conservative nature of the algorithms is especially suitable for long-term simulations of particle-field systems with extremely large number of degrees of freedom on massively parallel supercomputers.

1. Introduction

The importance of numerical solutions for Vlasov-Maxwell (VM) systems cannot be overemphasized. In most cases, important and interesting characteristics of the VM system are the long-term behaviors and multi-scale structures, which demand long-term accuracy and fidelity of numerical calculations. Conventional algorithms for the VM systems used in general do not preserve the geometric structures of the physical systems, which will lead to not reliable results when calculating long-term multi-scale problems. To overcome this difficult, a series of geometric algorithms, which preserve the geometric structures of the VM system have been developed recently [1-9]. However, none of these methods is high-order local explicit, electromagnetic and charge-conserved. So in this paper, we have developed an explicit, high order, non-canonical symplectic PIC algorithm for the Vlasov-Maxwell system. The algorithm conserves a discrete non-canonical symplectic structure derived from the Lagrangian of the particle-field system [10, 11]. With the usage of discrete exterior calculus (DEC) [12] and high-order interpolating forms inspired from the Whitney forms [13], this discretization preserves the gauge invariance

of the original Vlasov-Maxwell system, which means the charge conservation nature is also preserved. The spatially-discretized system is solved by using a Hamiltonian splitting method discovered by He et al. [14, 15], which is high-order explicit. The explicit and high-order nature of the symplectic algorithms developed in the present study made it especially suitable for long-term simulations of particle-field systems with extremely large number of degrees of freedom on massively parallel supercomputers.

2. NON-CANONICAL SYMPLECTIC PARTICLE-IN-CELL ALGORITHMS

The starting point is the Lagrangian of a collection of charged particles and electromagnetic field [10, 11].

$$L = \iiint \mathrm{d}\mathbf{x} \left(\frac{\epsilon_0}{2} \left(-\dot{\mathbf{A}}\left(\mathbf{x}\right) - \nabla\phi\left(\mathbf{x}\right) \right)^2 - \frac{1}{2\mu_0} \left(\nabla \times \mathbf{A}\left(\mathbf{x}\right) \right)^2 + \sum_s \delta\left(\mathbf{x} - \mathbf{x}_s\right) \left(\frac{1}{2} m_s \dot{\mathbf{x}}_s^2 + q_s \mathbf{A}\left(\mathbf{x}\right) \cdot \dot{\mathbf{x}}_s - q_s \phi\left(\mathbf{x}\right) \right) \right) , \tag{1}$$

where $\mathbf{A}(\mathbf{x})$ and $\phi(\mathbf{x})$ are the vector and scalar potentials of the electromagnetic field, $\mathbf{x}_s$, m_s and q_s denote the location, mass and charge of the s-th particle, and permittivity and permeability in vacuum. We let $\varepsilon_0 = \mu_0 = 1$ to simplify the notation. This Lagrangian is naturally discrete in particles, and we choose to discretize the electromagnetic field in a cubic mesh. To preserve the symplectic structure of the system, the method of Discrete Exterior Calculus [12] is used. The DEC theory in cubic meshes can be found in Ref. [16]. For field-particle interaction, the interpolation function is used to obtain continuous fields from discrete fields. The spatially-discretized Lagrangian L_{sd} can be written as follows

$$L_{sd} = \frac{1}{2} \left(\sum_J \left(-\dot{\mathbf{A}}_J - \sum_I \nabla_{\mathrm{d}JI} \phi_I \right)^2 - \sum_K \left(\sum_J \mathrm{curl}_{\mathrm{d}KJ} \mathbf{A}_J \right)^2 \right) \Delta V + \sum_s \left(\frac{1}{2} m_s \dot{\mathbf{x}}_s^2 + q_s \left(\dot{\mathbf{x}}_s \cdot \sum_J W_{\sigma_{1J}}\left(\mathbf{x}_s\right) \mathbf{A}_J - \sum_I W_{\sigma_{0I}}\left(\mathbf{x}_s\right) \phi_I \right) \right) , \tag{2}$$

where integers I, J and K are indices of grid points, ∇_d and curl_d are the discrete gradient and curl operators, which are linear operators on the discrete fields A_J and φ_I. Functions $W_{\sigma 0_J}$ and $W_{\sigma 1_I}$ are interpolation functions for 0-forms (e.g. scalar potential) and 1-forms (e.g. vector potential), respectively. The interpolating forms used here is quite different from the original Whitney form described in Ref. [13]. The original Whitney form is developed for simplex meshes (e.g. the triangle or tetrahedron mesh) while our interpolating form is designed for rectangle or cubic meshes, and the original Whitney interpolating function is only non-zero within one layer of grid cell while our new interpolating form can effect multiple layer of grids.

The action integral reads

$$S = \int \mathrm{d}t L_{sd} , \tag{3}$$

and the dynamic equations are obtained from Hamilton's principle,

$$\frac{\delta S}{\delta \mathbf{A}_J} = 0 \ , \tag{4}$$

$$\frac{\delta S}{\delta \phi_I} = 0 \ , \tag{5}$$

$$\frac{\delta S}{\delta \mathbf{x}_s} = 0 \ . \tag{6}$$

Equations (4) and (5) are Maxwell's equations, and Eq. (6) is Newton's equation with the Lorentz force for the s-th particle. For the dynamics to be gauge independent [16], it requires that the discrete differential operators and interpolation functions satisfy the following relations,

$$\nabla \sum_I W_{\sigma_{0I}}(\mathbf{x})\,\phi_I = \sum_{I,J} W_{\sigma_{1J}}(\mathbf{x})\,\nabla_{\mathrm{d}JI}\phi_I \ , \tag{7}$$

$$\nabla \times \sum_J W_{\sigma_{1J}}(\mathbf{x})\,\mathbf{A}_J = \sum_{J,K} W_{\sigma_{2K}}(\mathbf{x})\,\mathrm{curl}_{\mathrm{d}KJ}\mathbf{A}_J \ . \tag{8}$$

The gauge independence of this spatially-discretized system implies that the dynamics conserves charge automatically. In this paper, as a practical example, two-cell interpolating functions and the corresponding discrete exterior derivative operators are defined in the following way.

$$\sum_{i,j,k} W_{\sigma_{0,i,j,k}}(\mathbf{x})\,\phi_{i,j,k} \equiv \sum_{i,j,k} \phi_{i,j,k} W_1(x)\,W_1(y)\,W_1(z)\,, \tag{9}$$

$$\sum_{i,j,k} W_{\sigma_{1,i,j,k}}(\mathbf{x})\,\mathbf{A}_{i,j,k} \equiv \sum_{i,j,k} \begin{bmatrix} A_{xi,j,k} W_1^{(2)}(x-i) W_1(y-j) W_1(z-k) \\ A_{yi,j,k} W_1(x-i) W_1^{(2)}(y-j) W_1(z-k) \\ A_{zi,j,k} W_1(x-i) W_1(y-j) W_1^{(2)}(z-k) \end{bmatrix}^T , \tag{10}$$

$$\sum_{i,j,k} W_{\sigma_{2,i,j,k}}(\mathbf{x})\,\mathbf{B}_{i,j,k} \equiv \sum_{i,j,k} \begin{bmatrix} B_{xi,j,k} W_1(x-i) W_1^{(2)}(y-j) W_1^{(2)}(z-k) \\ B_{yi,j,k} W_1^{(2)}(x-i) W_1(y-j) W_1^{(2)}(z-k) \\ B_{zi,j,k} W_1^{(2)}(x-i) W_1^{(2)}(y-j) W_1(z-k) \end{bmatrix}^T , \tag{11}$$

$$\sum_{i,j,k} W_{\sigma_{3,i,j,k}}(\mathbf{x})\,\rho_{i,j,k} \equiv \sum_{i,j,k} \rho_{i,j,k} W_1^{(2)}(x-i) W_1^{(2)}(y-j) W_1^{(2)}(z-k), \tag{12}$$

$$W_1^{(2)}(x) = -\begin{cases} W_1'(x) + W_1'(x+1) + W_1'(x+2) \ , & -1 \le x < 2 \ , \\ 0 \ , & \text{otherwise} \ . \end{cases} \tag{13}$$

$$(\nabla_{\mathrm{d}}\phi)_{i,j,k} = [\phi_{i+1,j,k} - \phi_{i,j,k}, \phi_{i,j+1,k} - \phi_{i,j,k}, \phi_{i,j,k+1} - \phi_{i,j,k}] \ . \tag{14}$$

$$(\mathrm{curl}_{\mathrm{d}}\mathbf{A})_{i,j,k} = \begin{bmatrix} \left(A_{zi,j+1,k} - A_{zi,j,k}\right) - \left(A_{yi,j,k+1} - A_{yi,j,k}\right) \\ \left(A_{xi,j,k+1} - A_{xi,j,k}\right) - \left(A_{zi+1,j,k} - A_{zi,j,k}\right) \\ \left(A_{yi+1,j,k} - A_{yi,j,k}\right) - \left(A_{xi,j+1,k} - A_{xi,j,k}\right) \end{bmatrix}^T , \tag{15}$$

$$
\begin{aligned}
(\mathrm{div_d}\mathbf{B})_{i,j,k} &= \left(B_{xi+1,j,k} - B_{xi,j,k}\right) + \left(B_{y_{i,j+1,k}} - B_{y_{i,j,k}}\right) \\
&\quad + \left(B_{zi,j,k+1} - B_{zi,j,k}\right) \ ,
\end{aligned} \tag{16}
$$

where the one-dimensional interpolation function W_1 is chosen in this paper to be

$$
W_1(x) = \begin{cases}
0, & x \le -2, \\
-\frac{x^6}{48} - \frac{x^5}{8} - \frac{5x^4}{16} - \frac{5x^3}{12} + x + 1, & -2 < x \le -1, \\
\frac{x^6}{48} - \frac{x^5}{8} - \frac{5x^4}{16} - \frac{5x^3}{12} - \frac{5x^2}{8} + \frac{7}{12}, & -1 < x \le 0, \\
\frac{x^6}{48} + \frac{x^5}{8} - \frac{5x^4}{16} + \frac{5x^3}{12} - \frac{5x^2}{8} + \frac{7}{12}, & 0 < x \le 1, \\
-\frac{x^6}{48} + \frac{x^5}{8} - \frac{5x^4}{16} + \frac{5x^3}{12} - x + 1, & 1 < x \le 2, \\
0, & 2 < x \ .
\end{cases} \tag{17}
$$

Since the dynamics are gauge independent, we can choose any gauge that is convenient.

For simplicity, the temporal gauge, i.e. $\phi_I = 0$, is adopted in the present study. To obtain the Poisson bracket, we let $q = [\mathbf{A}_J \ , \mathbf{x}_s]$, and the Lagrangian 1-form can be written as

$$
\gamma = \frac{\partial L_{sd}}{\partial \dot{q}} \mathbf{d}q - H\mathbf{d}t \ , \tag{18}
$$

where $\mathbf{d}$ denotes the exterior derivative. In Eq. (15),

$$
\frac{\partial L_{sd}}{\partial \dot{q}} = \left[\dot{\mathbf{A}}_J \Delta V, m_s \dot{\mathbf{x}}_s + q_s \sum_J W_{\sigma_{1J}}(\mathbf{x}_s)\, \mathbf{A}_J\right] \ , \tag{19}
$$

and

$$
H = \frac{\partial L_{sd}}{\partial \dot{q}} \dot{q}^T - L_{sd} \tag{20}
$$

$$
= \frac{1}{2}\Delta V \left(\sum_J \dot{\mathbf{A}}_J^2 + \sum_K \left(\sum_J \mathrm{curl}_{\mathrm{d}KJ} \mathbf{A}_J\right)^2\right) + \sum_s \frac{1}{2} m_s \dot{\mathbf{x}}_s^2 \tag{21}
$$

is the Hamiltonian. The dynamical equation of the system can be written as [10, 17]

$$
i_{[\dot{q},\ddot{q},1]} \mathbf{d}\gamma = 0 \ , \tag{22}
$$

where $[\dot{q}, \ddot{q}, 1]$ represent vector field $[\dot{q}\frac{\partial}{\partial q} + \ddot{q}\frac{\partial}{\partial \dot{q}} + \frac{\partial}{\partial t}]$. The non-canonical symplectic structure is

$$
\Omega = \mathbf{d}\left(\frac{\partial L_{sd}}{\partial \dot{q}} \mathbf{d}q\right) \ , \tag{23}
$$

and the dynamical equation (22) is equivalent to

$$\frac{d}{dt}\begin{bmatrix}\mathbf{A}_J\\ \mathbf{x}_s\\ \dot{\mathbf{A}}_J\\ \dot{\mathbf{x}}_s\end{bmatrix}=\Omega^{-1}\begin{bmatrix}\frac{\partial}{\partial \mathbf{A}_J}\\ \frac{\partial}{\partial \mathbf{x}_s}\\ \frac{\partial}{\partial \dot{\mathbf{A}}_J}\\ \frac{\partial}{\partial \dot{\mathbf{x}}_s}\end{bmatrix}H\ . \tag{24}$$

The corresponding non-canonical Poisson bracket is

$$\{F,G\}=\left[\frac{\partial F}{\partial \mathbf{A}_J},\frac{\partial F}{\partial \mathbf{x}_s},\frac{\partial F}{\partial \dot{\mathbf{A}}_J},\frac{\partial F}{\partial \dot{\mathbf{x}}_s}\right]\Omega^{-1}\left[\frac{\partial G}{\partial \mathbf{A}_J},\frac{\partial G}{\partial \mathbf{x}_s},\frac{\partial G}{\partial \dot{\mathbf{A}}_J},\frac{\partial G}{\partial \dot{\mathbf{x}}_s}\right]^T, \tag{25}$$

or more specifically,

$$\begin{aligned}\{F,G\}=&\frac{1}{\Delta V}\sum_J\left(\frac{\partial F}{\partial \mathbf{A}_J}\cdot\frac{\partial G}{\partial \dot{\mathbf{A}}_J}-\frac{\partial F}{\partial \dot{\mathbf{A}}_J}\cdot\frac{\partial G}{\partial \mathbf{A}_J}\right)+\sum_s\frac{1}{m_s}\left(\frac{\partial F}{\partial \mathbf{x}_s}\cdot\frac{\partial G}{\partial \dot{\mathbf{x}}_s}-\frac{\partial F}{\partial \dot{\mathbf{x}}_s}\cdot\frac{\partial G}{\partial \mathbf{x}_s}\right)+\\ &\sum_s\frac{q_s}{m_s\Delta V}\left(\frac{\partial G}{\partial \dot{\mathbf{x}}_s}\cdot\sum_J W_{\sigma_{1J}}(\mathbf{x}_s)\frac{\partial F}{\partial \dot{\mathbf{A}}_J}-\frac{\partial F}{\partial \dot{\mathbf{x}}_s}\cdot\sum_J W_{\sigma_{1J}}(\mathbf{x}_s)\frac{\partial G}{\partial \dot{\mathbf{A}}_J}\right)+\\ &-\sum_s\sum_J\frac{q_s}{m_s^2}\frac{\partial F}{\partial \dot{\mathbf{x}}_s}\cdot\left[\nabla\times W_{\sigma_{1J}}(\mathbf{x}_s)\mathbf{A}_J\right]\times\frac{\partial G}{\partial \dot{\mathbf{x}}_s}\ .\end{aligned} \tag{26}$$

Now, we introduce two new variables $\mathbf{E}_J$ and $\mathbf{B}_K$, which are the discrete electric field and magnetic field,

$$\begin{aligned}\mathbf{E}_J&=-\dot{\mathbf{A}}_J\ ,\\ \mathbf{B}_K&=\sum_J \mathrm{curl}_{dKJ}\mathbf{A}_J\ .\end{aligned} \tag{27}$$

In terms of $\mathbf{E}_J$ and $\mathbf{B}_K$, the Poisson bracket is

$$\begin{aligned}\{F,G\}=&\frac{1}{\Delta V}\sum_J\left(\frac{\partial F}{\partial \mathbf{E}_J}\cdot\sum_K\frac{\partial G}{\partial \mathbf{B}_K}\mathrm{curl}_{dKJ}-\sum_K\frac{\partial F}{\partial \mathbf{B}_K}\mathrm{curl}_{dKJ}\cdot\frac{\partial G}{\partial \mathbf{E}_J}\right)+\\ &\sum_s\frac{1}{m_s}\left(\frac{\partial F}{\partial \mathbf{x}_s}\cdot\frac{\partial G}{\partial \dot{\mathbf{x}}_s}-\frac{\partial F}{\partial \dot{\mathbf{x}}_s}\cdot\frac{\partial G}{\partial \mathbf{x}_s}\right)+\\ &\sum_s\frac{q_s}{m_s\Delta V}\left(\frac{\partial F}{\partial \dot{\mathbf{x}}_s}\cdot\sum_J W_{\sigma_{1J}}(\mathbf{x}_s)\frac{\partial G}{\partial \mathbf{E}_J}-\frac{\partial G}{\partial \dot{\mathbf{x}}_s}\cdot\sum_J W_{\sigma_{1J}}(\mathbf{x}_s)\frac{\partial F}{\partial \mathbf{E}_J}\right)+\\ &-\sum_s\frac{q_s}{m_s^2}\frac{\partial F}{\partial \dot{\mathbf{x}}_s}\cdot\left[\sum_K W_{\sigma_{2K}}(\mathbf{x}_s)\mathbf{B}_K\right]\times\frac{\partial G}{\partial \dot{\mathbf{x}}_s}\ ,\end{aligned} \tag{28}$$

and the Hamiltonian can be written as

$$H=\frac{1}{2}\left(\Delta V\sum_J\mathbf{E}_J^2+\Delta V\sum_K\mathbf{B}_K^2+\sum_s m_s\dot{\mathbf{x}}_s^2\right)\ . \tag{29}$$

The evolution equations is

$$\dot{F}=\{F,H\}\ , \tag{30}$$

where

$$F=[\mathbf{E}_J,\mathbf{B}_K,\mathbf{x}_s,\dot{\mathbf{x}}_s]\ . \tag{31}$$

This is a Hamiltonian system with a non-canonical symplectic structure or Poisson bracket. In general, symplectic integrators for non-canonical systems are difficult to construct. However, using the splitting method discovered by He et al. [14, 15], we have found explicit high-order symplectic algorithms for this Hamiltonian system that preserve its noncanonical symplectic structure. We split the Hamiltonian in Eq. (29) into five parts,

$$
\begin{aligned}
H &= H_E + H_B + H_x + H_y + H_z \ , \\
H_E &= \frac{1}{2}\Delta V \sum_J \mathbf{E}_J^2 \ , \\
H_B &= \frac{1}{2}\Delta V \sum_K \mathbf{B}_K^2 \ , \\
H_r &= \frac{1}{2}\sum_s m_s \dot{r}_s^2, \quad \text{for } r \text{ in } x,\ y,\ z \ .
\end{aligned}
\tag{32}
$$

It turns out that the sub-system generated by each part can be solved exactly, and high-order symplectic algorithms follow by combination. The evolution equation for H_E is $\dot{F} = \{F, H_E\}$, which can be written as

$$
\begin{aligned}
\dot{\mathbf{E}}_J &= 0 \ , \\
\dot{\mathbf{B}}_K &= -\sum_J \mathrm{curl}_{\mathrm{d}KJ}\mathbf{E}_J \ , \\
\dot{\mathbf{x}}_s &= 0 \ , \\
\ddot{\mathbf{x}}_s &= \frac{q_s}{m_s}\sum_J W_{\sigma_1 J}\left(\mathbf{x}_s\right)\mathbf{E}_J \ .
\end{aligned}
\tag{33}
$$

The exact solution $\Theta_E\ (\Delta t)$ for any time step Δt is

$$
\begin{aligned}
\mathbf{E}_J\left(t+\Delta t\right) &= \mathbf{E}_J\left(t\right) \ , \\
\mathbf{B}_K\left(t+\Delta t\right) &= \mathbf{B}_K\left(t\right) - \Delta t\sum_J \mathrm{curl}_{\mathrm{d}KJ}\mathbf{E}_J(t) \ , \\
\mathbf{x}_s\left(t+\Delta t\right) &= \mathbf{x}_s\left(t\right) \ , \\
\dot{\mathbf{x}}_s\left(t+\Delta t\right) &= \dot{\mathbf{x}}_s\left(t\right) + \frac{q_s}{m_s}\Delta t\sum_J W_{\sigma_1 J}\left(\mathbf{x}_s(t)\right)\mathbf{E}_J(t) \ .
\end{aligned}
\tag{34}
$$

The evolution equation for H_B is $\dot{F} = \{F, H_B\}$, or

$$
\begin{aligned}
\dot{\mathbf{E}}_J &= \sum_K \mathrm{curl}_{\mathrm{d}KJ}\mathbf{B}_K \ , \\
\dot{\mathbf{B}}_K &= 0 \ , \\
\dot{\mathbf{x}}_s &= 0 \ , \\
\ddot{\mathbf{x}}_s &= 0 \ ,
\end{aligned}
\tag{35}
$$

whose exact solution $\Theta_B\ (\Delta t)$ is

$$
\begin{aligned}
\mathbf{E}_J\left(t+\Delta t\right) &= \mathbf{E}_J\left(t\right) + \Delta t\sum_K \mathrm{curl}_{\mathrm{d}KJ}\mathbf{B}_K(t) \ , \\
\mathbf{B}_K\left(t+\Delta t\right) &= \mathbf{B}_K\left(t\right) \ , \\
\mathbf{x}_s\left(t+\Delta t\right) &= \mathbf{x}_s\left(t\right) \ , \\
\dot{\mathbf{x}}_s\left(t+\Delta t\right) &= \dot{\mathbf{x}}_s\left(t\right) \ .
\end{aligned}
\tag{36}
$$

The evolution equation for H_x is $\dot{F} = \{F, H_x\}$, or

$$
\begin{aligned}
\dot{\mathbf{E}}_J &= -\sum_s \frac{q_s}{\Delta V} \dot{x}_s \mathbf{e}_x W_{\sigma_{1J}}(\mathbf{x}_s) \ , \\
\dot{\mathbf{B}}_K &= 0 \ , \\
\dot{\mathbf{x}}_s &= \dot{x}_s \mathbf{e}_x \ , \\
\ddot{\mathbf{x}}_s &= \frac{q_s}{m_s} \dot{x}_s \mathbf{e}_x \times \sum_K W_{\sigma_{2K}}(\mathbf{x}_s) \mathbf{B}_K \ .
\end{aligned}
\tag{37}
$$

The exact solution $\Theta_x\ (\Delta t)$ of this sub-system can also be computed as

$$
\begin{aligned}
\mathbf{E}_J(t+\Delta t) &= \mathbf{E}_J(t) - \int_0^{\Delta t} dt' \sum_s \frac{q_s}{\Delta V} \dot{x}_s(t) \mathbf{e}_x W_{\sigma_{1J}}(\mathbf{x}_s(t) + \dot{x}_s(t) t' \mathbf{e}_x) \ , \\
\mathbf{B}_K(t+\Delta t) &= \mathbf{B}_K(t) \ , \\
\mathbf{x}_s(t+\Delta t) &= \mathbf{x}_s(t) + \Delta t \dot{x}_s(t) \mathbf{e}_x \ , \\
\dot{\mathbf{x}}_s(t+\Delta t) &= \dot{\mathbf{x}}_s(t) + \frac{q_s}{m_s} \dot{x}_s(t) \mathbf{e}_x \times \int_0^{\Delta t} dt' \sum_K W_{\sigma_{2K}}(\mathbf{x}_s(t) + \dot{x}_s(t) t' \mathbf{e}_x) \mathbf{B}_K(t) \ .
\end{aligned}
\tag{38}
$$

Exact solutions $\Theta_y\ (\Delta t)$ and $\Theta_z\ (\Delta t)$ for sub-systems corresponding to H_y and H_z are obtained in a similar manner. These exact solutions for sub-systems are then combined to construct symplectic integrators for the original non-canonical Hamiltonian system specified by Eqs. (28) and (29). For example, a first order scheme can be constructed as

$$
\Theta_1(\Delta t) = \Theta_E(\Delta t) \Theta_B(\Delta t) \Theta_x(\Delta t) \Theta_y(\Delta t) \Theta_z(\Delta t) \ ,
\tag{39}
$$

and a second order symmetric scheme is

$$
\begin{aligned}
\Theta_2(\Delta t) = \Theta_x(\Delta t/2) \Theta_y(\Delta t/2) \Theta_z(\Delta t/2) \Theta_B(\Delta t/2) \Theta_E(\Delta t) \\
\Theta_B(\Delta t/2) \Theta_z(\Delta t/2) \Theta_y(\Delta t/2) \Theta_x(\Delta t/2) \ .
\end{aligned}
\tag{40}
$$

An algorithm with order $2(l\ +\ 1)$ can be constructed in the following way,

$$
\begin{aligned}
\Theta_{2(l+1)}(\Delta t) &= \Theta_{2l}(\alpha_l \Delta t) \Theta_{2l}(\beta_l \Delta t) \Theta_{2l}(\alpha_l \Delta t) \ , \\
\alpha_l &= 1/(2 - 2^{1/(2l+1)}) \ , \\
\beta_l &= 1 - 2\alpha_l \ .
\end{aligned}
\tag{41}
$$

3. NUMERICAL EXAMPLES

We have implemented the second-order non-canonical symplectic PIC algorithm described above. To test the algorithm, two physics problems are simulated. The first problem is the nonlinear Landau damping of an electrostatic wave in a hot plasma. Simulation parameters are set as follows. The density of electron ne is $1.2\ \times\ 10^{16}\ \mathrm{m}^{-3}$, and the electron velocity is Maxwellian distributed with thermal speed $v_T\ =$ 0.1c, where c is the speed of light in vacuum. The computation is carried out in a 672 × 1 × 1 cubic mesh, and the size of each grid cell is $\Delta l\ =\ 2.4\ \times\ 10^{-4}$ m. There is no external electromagnetic field, and there are 40000 sample particles in each cell when unperturbed. The initial electric field is $\mathbf{E}_1 = E_1\ \cos\ (kx)\mathbf{e}_x$, where $k = 2\pi/224\Delta l$ is the wave number, and the amplitude is $E_1 = 36$kV/m. The simulation is carried out for 15000 time-steps, and the electric field is recorded during the simulation. We plot the evolution of electric field to observe the Landau damping phenomenon (Figs. 1 and 2).

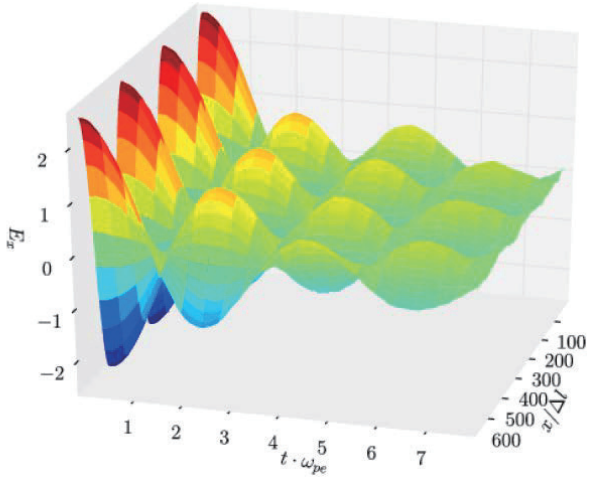

Figure 1: The time evolution of an electrostatic wave in a hot plasma.

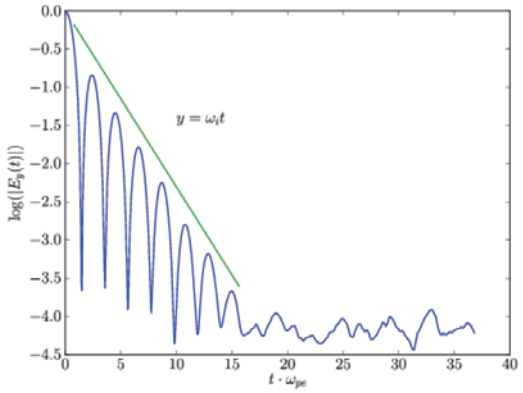

Figure 2: Logarithmic plot of the time evolution of absolute value of the electric field. The slope of the solid green line is the theoretical damping rate.

Another test problem is the dispersion relation of electron Bernstein waves [18]. In this problem, an electromagnetic wave propagates perpendicularly to an uniform external magnetic field $B_0 = B_0 e_z$ with $B_0 = 5.1T$. Other system parameters are

$$\begin{aligned} n_e &= 2.4 \times 10^{20}\mathrm{m}^{-3} , \\ v_T &= 0.07c , \\ \Delta l &= 2.5 \times 10^{-5}m , \\ \Delta t &= \frac{\Delta l}{2c} . \end{aligned} \tag{42}$$

The computation domain is a 768 × 1 × 1 cubic mesh, and the average number of sample points per grid is 4000. An initial electromagnetic perturbation is imposed, and after simulating 6000 time steps the space-time spectrum of E_x is plotted in Fig. 3, which shows that the dispersion relation simulated matches the theoretical curve perfectly.

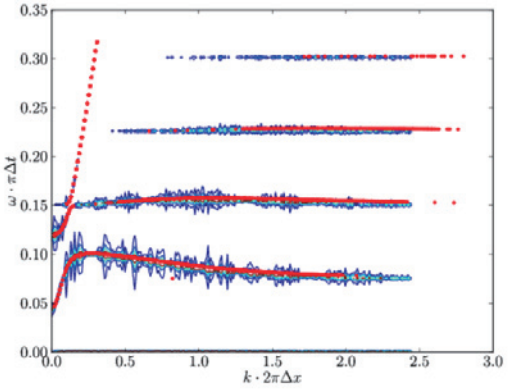

Figure 3: Logarithmic plot of the time evolution of absolute value of the electric field. The slope of the solid green line is the theoretical damping rate.

4. SUMMARY AND DISCUSSION

We have developed and tested a non-canonical symplectic PIC algorithm for the VM system. The non-canonical symplectic structure is obtained by discretizing the electromagnetic field of the particle-field Lagrangian using the method of discrete exterior calculus. A high-order interpolating method for differential forms is developed to render smooth interpolations of the electromagnetic field. The effectiveness and conservative nature of the algorithm has been verified by the physics problems of nonlinear Landau damping and electron Bernstein wave.

References

[1] J. Squire, H. Qin, and W. M. Tang, Geometric Integration of the Vlasov-Maxwell System with a Variational Particle-in-cell Scheme, Tech. Rep. PPPL-4748 (Princeton Plasma Physics Laboratory, 2012).

[2] J. Squire, H. Qin, and W. M. Tang, Physics of Plasmas (1994-present) 19, 052501 (2012).

[3] J. Xiao, J. Liu, H. Qin, and Z. Yu, Phys. Plasmas 20, 102517 (2013).

[4] J. Xiao, J. Liu, H. Qin, Z. Yu, and N. Xiang, Physics of Plasmas (1994-present) 22, 092305 (2015).

[5] E. Evstatiev and B. Shadwick, Journal of Computational Physics 245, 376 (2013).

[6] E. Evstatiev, Computer Physics Communications 185, 2851 (2014).

[7] B. A. Shadwick, A. B. Stamm, and E. G. Evstatiev, Physics of Plasmas 21, 055708 (2014).

[8] N. Crouseilles, L. Einkemmer, and E. Faou, Journal of Computational Physics 283, 224 (2015).

[9] H. Qin, Y. He, R. Zhang, J. Liu, J. Xiao, and Y. Wang, Journal of Computational Physics 297, 721 (2015).

[10] H. Qin, R. Cohen, W. Nevins, and X. Xu, Physics of Plasmas (1994-present) 14, 056110 (2007).

[11] H. Qin, J. W. Burby, and R. C. Davidson, Physical Review E 90, 043102 (2014).

[12] A. N. Hirani, Discrete Exterior Calculus, Ph.D. thesis, California Institute of Technology (2003).

[13] H. Whitney, Geometric Integration Theory (Princeton University Press, 1957).

[14] Y. He, H. Qin, Y. Sun, J. Xiao, R. Zhang, and J. Liu, arXiv preprint arXiv:1505.06076 (2015).

[15] Y. He, Y. Sun, Z. Zhou, J. Liu, and H. Qin, arXiv preprint arXiv:1509.07794 (2015).

[16] A. Stern, Y. Tong, M. Desbrun, and J. E. Marsden, in Geometry, Mechanics, and Dynamics

(Springer, 2015) pp. 437–475.
[17] H. Qin, Fields Institute Communications 46, 171 (2005).
[18] T. H. Stix, Waves in Plasmas (Springer, 1992) pp. 276–277.

The Effect of Non-axisymmetric Magnetic Fields on the LH transition and Rotation in KSTAR

Won-Ha Ko[1*], Y. In[1], H.S. Kim[1], J.H. Lee[1], H.H. Lee[1], J. Seol[1], H.S. Hahn[1], J.W. Juhn[1], K. Ida[2], Y.M. Jeon[1], J. Kim[1], S.W. Yoon[1], Y.K. Oh[1], and H. Park[3]

[1]National Fusion Research Institute, Daejeon, Korea
[2]National Institute for Fusion Science, Toki, 509-5292, Gifu, Japan
[3]Ulsan National Institute of Science and Technology, Ulsan, Korea
*Email : whko@nfri.re.kr

Abstract

Non-axisymmetric magnetic fields reduce both height and width of pedestal in the KSTAR H-mode plasma. Significantly low H-mode power threshold (P_{TH}) has been observed in KSTAR in comparison with other conventional devices. Lower P_{TH} has been measured without external non-axisymmetric magnetic fields than other devices. It is attributable to an order of magnitude lower intrinsic error field ($<\delta B/B_0>_{m/n=2/1} \sim 1x10^{-5}$ [1]) and toroidal field ripple (δ_{TF}=0.05% [2]) and systematically scanned at low non-axisymmetric magnetic fields in KSTAR [3]. Non-axisymmetric magnetic fields influence on L-H power threshold is consistent with other studies, suggesting the importance of low order intrinsic error field in future machine. Benefits of low non-axisymmetric magnetic fields on P_{TH} are confirmed in KSTAR. Multiple error fields should be considered to determine low H-mode power threshold which has been systematically scanned, showing non-flat dependence for n=1 and n=2 on low non-axisymmetric magnetic fields. Minimized error fields are desirable to access low H-mode power threshold in ITER and future reactors.

1. Introduction

Non-axisymmetric magnetic field is actively employed in ELM control experiments. Generally, non-axisymmetric magnetic field can change pedestal transport and regulate pedestal profiles to stay below the thresholds for the peeling-ballooning instabilities [3, 4]. Non-axisymmetric magnetic field is important role on the pedestal transport and confinement in KSTAR which has low error field [1] and low toroidal field ripple [2], as compared with other similar sized machine. It is the most important to estimate H-mode threshold power in future machine, ITER which should make low error field machine for saving LH transition power. Pedestal rotation profiles are of great importance for ITER, in the multiple contexts of confinement enhancement, the source of intrinsic torque in H-mode, and their response to ELMs and to ELM suppression techniques. The toroidal rotation and ion temperature behaviors were shown from the effect of resonant magnetic perturbations (RMPs) in KSTAR associated with the helical magnetics related to the non-axisymmetric magnetic fields. The non-axisymmetric magnetic fields make not only ELM suppression but also torodial rotation decrease in KSTAR H-mode plasma. What interaction of

non-axisymmetric magnetic field with H-mode threshold power is important in ITER from the toroidal rotation behavior by non-axisymmetric magnetic field. What further advancement in non-axisymmetric magnetic field experiments is in pedestal and further studies are still needed to resolve the mechanism of it. The effects of non-axisymmetric field on pedestal transport and confinement are important subject to study for better understanding of the underlying physical mechanisms of ELM suppression by non-axisymmetric field. The more detail scan of H-mode threshold power is required for all range of non-axisymmetric field in KSTAR. It is the most important to estimate H-mode threshold power in ITER which should be made of low error field machine.

In Section2, a description of pedestal behavior in KSTAR H-mode plasma with low error field and non-axisymmetric magnetic fields showed. In Section 3, the effect of non-axisymmetric magnetic fields with n=1 and n=2 on H-mode threshold power are discussed. A summary is given in Section 4.

2. Pedestal reduced by the non-axisymmetric magnetic fields

Both pedestals of toroidal rotation and ion temperature dropped by the non-axis symmetric magnetic field as shown in Fig. 1. Non-axisymmetric magnetic field reduced the both pedestal of toroidal rotation and ion temperature. The whole toroidal rotation decreased during ELM suppression with n=1 RMP in H-mode KSTAR plasma heated by NBI. There is a damping of the toroidal rotation in L-mode with RMPs, due to the magnetic braking. Traditional changes of pedestal profiles of KSTAR during applied RMPs are shown in Fig. 1. The disparity between the width of the toroidal rotation pedestal and that of the ion temperature pedestal is shown in Fig. 1 while conventionally the ion temperature pedestal should be broader, as the residual turbulence in H-mode is expected to drive quite modest levels of turbulent χ_ϕ. Thus, we expect the neoclassical ion thermal diffusivity in the pedestal to exceed the turbulent viscosity [3].

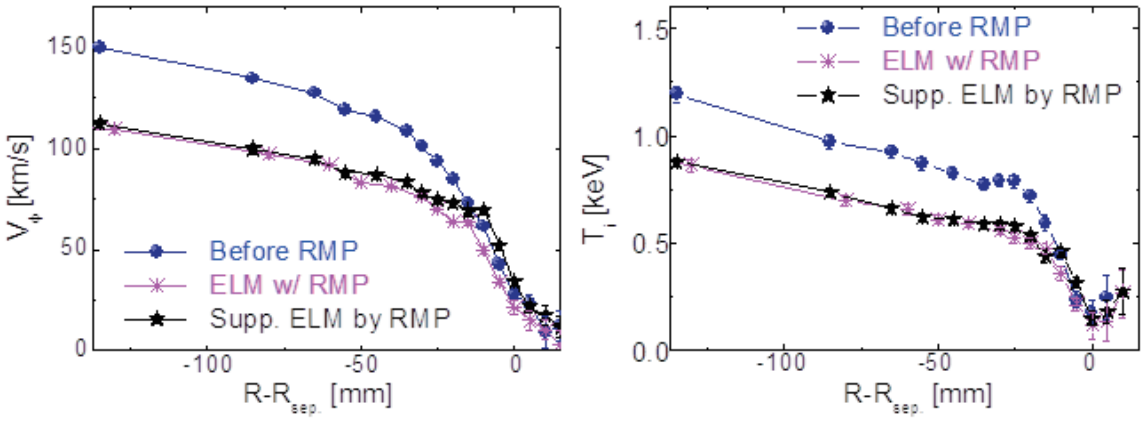

Figure 1. Pedestal Reduced by the non-axisymmetric Fields. Regardless of full suppression of ELM-crash, n=1 non-axisymmetric magnetic field affects pedestal of toroidal rotation and ion temperature.

3. H-mode threshold power in KSTAR plasma with low error field and non-axisymmetric magnetic fields

The H-mode threshold power was scan in low error filed and non-axisymmetric magnetic field with n=1, 90 phasing component in Fig. 2. Figure 2 shows unambiguously that H-mode threshold power increase when non-axisymmetric field increases in KSTAR. We have low threshold power as compared with other conventional devices with nominal error field. We showed that KSTAR has lower H-mode power threshold than other conventional devices [5] with similar densities due to the low error field in Fig. 2. The threshold powers of KSTAR for $\delta B/B_0$ shows a similar trend to DIII-D under the condition of the same error field.

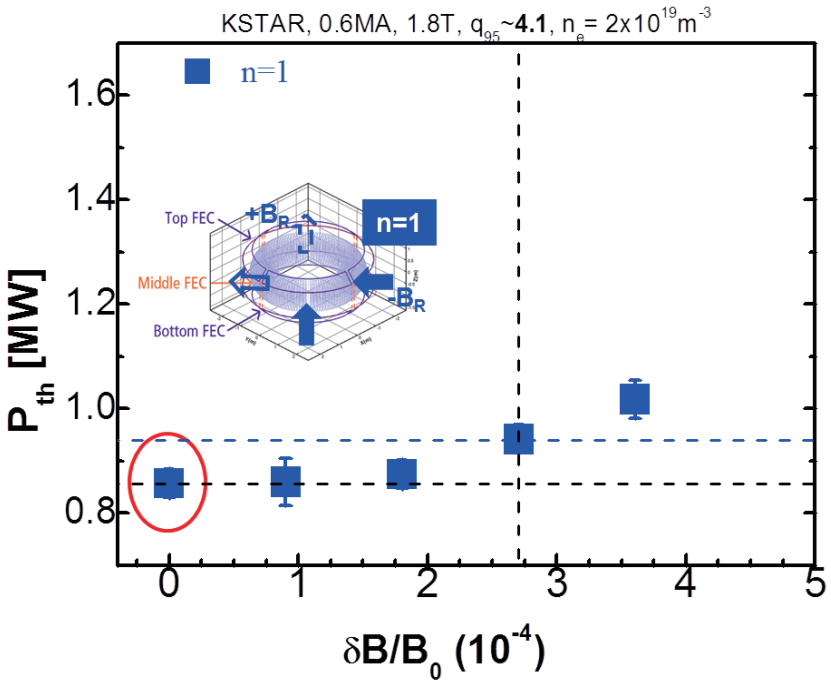

Figure 2. KSTAR with low intrinsic error filed has low H-mode power threshold as compared with other conventional devices with nominal error field and similar size for n=1 RMP

The target discharges we analyzed in this work are following in KSTAR: the toroidal magnetic field is Bt = 1.8 T, the plasma current is Ip = 600 kA, the line integrated density ne = 2 $\times 10^{19}$ m^{-3} in L-mode, and the NBI heating power was changed depending on current of non-axisymmetric magnetic field. The L to H-mode transition was determined from Da signal and pedestal of ion temperature and rotation profiles. The net power threshold was determined from the sum of the input power of NBI and ohmic heating and subtraction of the beam shine-through and ion orbit losses and the time derivative of the diagmagnetic energy, dW/dt in KSTAR. The net threshold power was not considered the bulk radiated power from the KSTAR plasma while that of other conventional devices was determined from the sum of the input power (NBI, ECH, and ohmic) minus the beam shine-through and ion orbit losses, the bulk radiated power from the plasma and the time derivative of the diagmagnetic energy, dW/dt in DIII-D [5]. If the net threshold power considers the bulk radiated power, we can achieve less H-mode power threshold as compared now.

The H-mode threshold power was scan in low error filed and non-axisymmetric magnetic field with n=2 component in Fig. 3. It is important that the n=2 error field is higher than n=1error field to affect the H-mode threshold power for the same $\delta B/B_0$. Multiple error fields should be considered to determine

H-mode threshold power. KSTAR has lower P_{TH} during L to H-mode transition with n=1 and n=2 non-axisymmetric field than other conventional devices with nominal error field. Figure 2 and 3 show the experimental results of the H-mode power threshold in KSTAR, where P_{TH} linearly increases with low and high $\delta B/B_0$ for the n=1 and n=2 while the dashed line from other conventional devices with nominal error field.

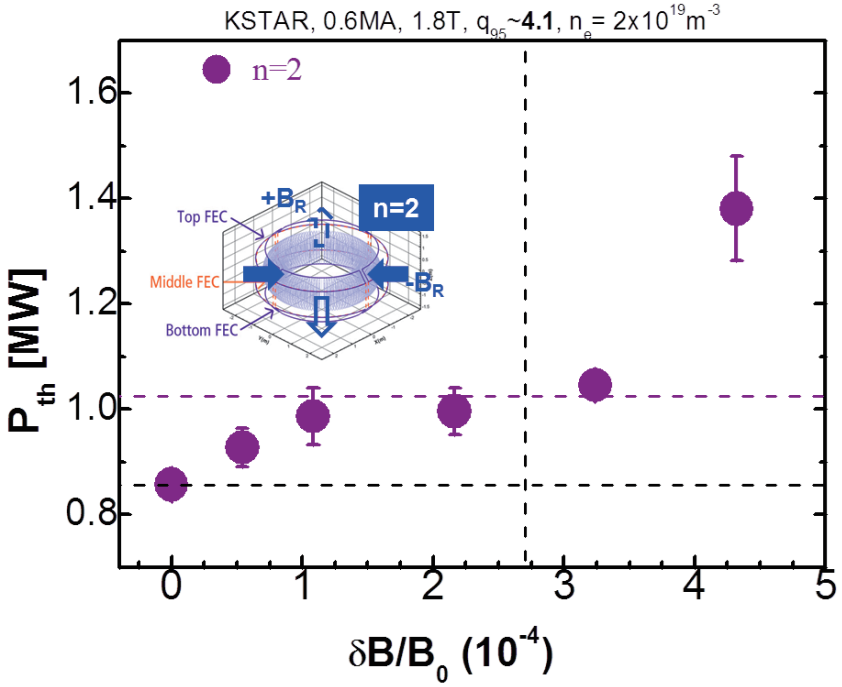

Figure 3. The H-mode threshold power for $\delta B/B_0$ (n=2) in KSTAR is lower than other conventional devices with nominal error field

4. Summary and future work

Non-axisymmetric magnetic field with n=1 component globally and strongly reduced rotation and ion temperature pedestal in KSTAR. Non-axisymmetric field reduced the toroidal pedestal rotation and ion pedestal temperature as shown in between profiles.

Lower H-mode threshold power in KSTAR has been measured without external non-axisymmetric magnetic field than other conventional devices with nominal error field ($\delta B/B_0 \sim 2.7 \times 10^{-4}$) and similar size. The H-mode power threshold increased with $\delta B/B_0$ while the normalized rotation pedestal decreased. The P_{TH} on low non-axisymmetric magnetic field has been systematically scanned, showing non-flat dependence for n=1 and n=2 in KSTAR with low intrinsic error field. Multiple error fields should be considered to determine H-mode threshold power. It is important that the n=2 error field is comparable to or higher than n=1error field to affect the H-mode threshold power. Minimized error fields are desirable to access low P_{TH} in ITER and future reactors. Ongoing work is concerned primarily with H-mode threshold power to low error field and pedestal transport by non-axis symmetric magnetic field.

Acknowledgements

This work was partly supported by the JSPS-NRF-NSFC A3 Foresight Program in the field of Plasma Physics (NSFC: No.11261140328, NRF: No.2012K2A2A6000443).

References

[1] Y. In et al, Nucl. Fusion 55 043004 (2015)

[2] S.W. Yoon et al, IAEA-FEC (2014)

[3] Won-Ha Ko et al., Nucl. Fusion, 55, 083013 (2015).

[4] Jeon, Y.M. et al., Phys. Rev. Lett. 109, 035004 (2012)

[5] P. Gohil, et. al., Nucl. Fusion 51 103020 (2011)

Design of Ultra-fast Charge eXchange Recombination Spectroscopy diagnostic in EAST tokamak

Yi Yu[1], Minyou Ye[1,*], Yinyin Li[2], Yuejiang Shi[1], Bo Lyu[2], Baonian Wan[2]

[1]School of Nuclear Science and Technology, University of Science and Technology of China, Jinzhai Road 96#, 230026, Hefei, China

[2]Institute of Plasma Physics, Chinese Academy of Sciences, Hefei 230031, China

Abstract

In this article, we present the design of four-channel Ultra-Fast Charge eXchange Recombination Spectroscopy (UF-CXRS) diagnostic on EAST (Experimental Advanced Superconducting Tokamak) device. This diagnostic is based on the active charge exchange to diagnose ion temperature with a time resolution at the order of 10 us and a spatial resolution of 1 cm. It has a view range from core to edge plasma with a minimum ion temperature of 0.38kev. The design of the main components are carefully discussed, including the dichroic mirror light path, the fiber, the spectrometer, and the customered lens. All of this parameter will make it be a keen tool for ion temperature diagnosing.

1. Introduction

Turbulence is believed to be the key to understand the underlying physics of transport in tokamak plasma. Pedestal physics, especially the shape of pedestal, is related to the L-H mode transition[1,2] , which still remains open and needs more investigations. This insufficient understanding of pedestal physics comes partly from the lack of diagnostic data. Pedestal, which means a sharp pressure gradient in edge plasma, is the most important sign of L-H transition. Unfortunately, Langmuir probe[3], the only diagnostic which can measure the density and temperature fluctuations simultaneously, can not intrude into the pedestal area. In recent years, many spectroscopy and microwave diagnostics are developed on EAST and similar tokamaks, such as Beam Emission Spectroscopy[4,5] and Doppler Reflectometer[6]. So the key matter to get the pressure data is to develop ion temperature diagnostics. In the last three year, EAST device has finished developing many sets of Charge eXchange Recombination Spectroscopy diagnostics and caught the radial ion temperature distribution[7]. But the time resolution is limited in the order of several mini-seconds and is not sufficient for pedestal diagnostic. On DIII-D tokamak, a new kind of diagnostic which is named Ultra-Fast Charge eXchange Recombination Spectroscopy (UF-CXRS) diagnostic is successfully developed in recent years[8-10], and the ion temperature signal is caught in a time resolution of micro-seconds. In this article, we present the design of this kind of diagnostic on EAST tokamak.

2. Experimental setup

EAST device is a fully superconducting tokamak with a large radii of 1.85 m, a minor radii of 0.45 m and elongation of 1.6-2. It has a typical toroidal field of 3.5 T and a plasma current of 1.0 MA. 4MW Neutron Beam Injection is used to sustain the plasma discharge , which supplies the base for CXRS diagnostic (Figure 1).

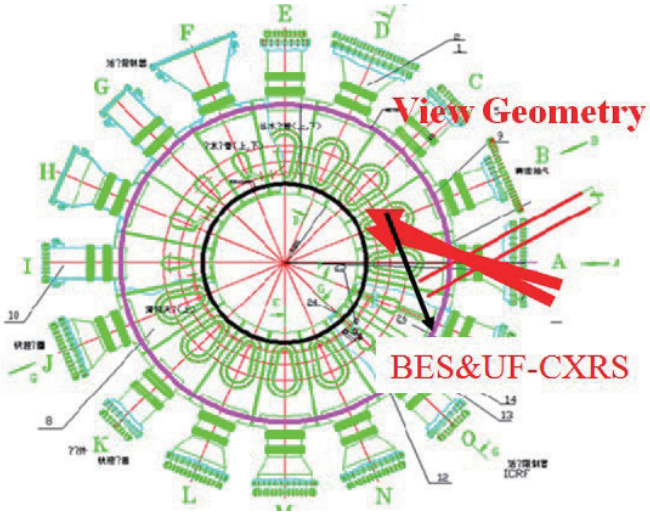

Figure 1, the NBI and the view angle of UF-CXRS diagnostic.

3. Main idea of UF-CXRS

The injected NBI particles will collide with the C6+ impurity particles and exchange charge. The electrons will moved to excited state of the impurity particles and irradiate light when the particles de-excite to lower state. By means of collecting the irradiated light to the diagnostic system, we can deduce the ion temperature of plasma.

The UF-CXRS diagnostic is planned to locate on the left part of port P, which will be integrated to BES diagnostic and will share the optical path with it. Four trial UF-CXRS channels arranged as a rectangle will be firstly developed in the center area of BES view plane, which has an excellent spatial resolution of about 1 centimeter. By means of adding a dichroic mirror into the BES optical path to induce parts of light into the UF-CXRS system, we can integrate this two diagnostic together. The designed optical path is shown in figure 2. The F number is designed 2.5 and NA number is 0.22. Changing the angle of the scanning mirror in the optical path, we can effectively change the view plane in the cross section. As shown in figure 2, the red, blue and green optical paths exhibit the three status of object plane, which mean three different view plane in the core, in the middle and in the edge.

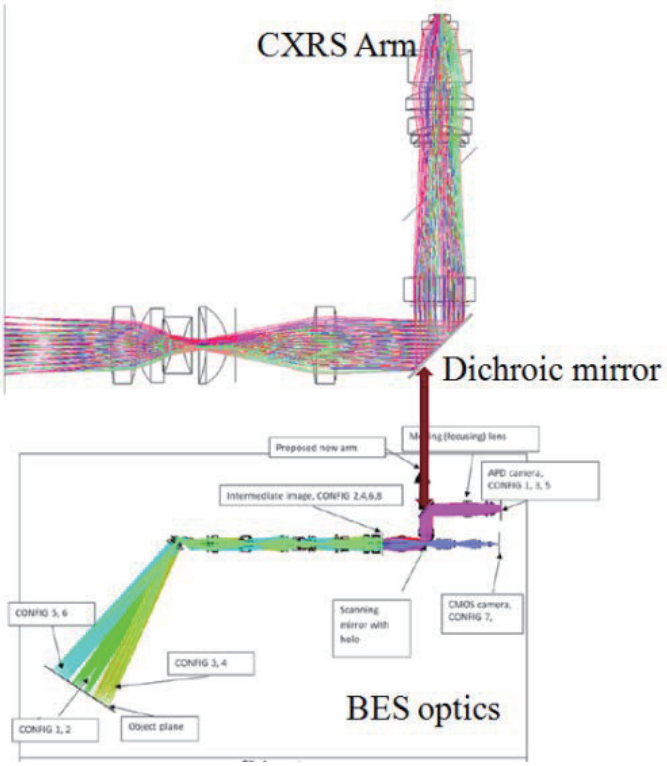

Figure 2, optical path of UF-CXRS.

Fibers are one of the key components of this diagnostic. Fused silica fiber with a core diameter of 0.2mm is chosen as the transmitting component. 39 fibers are compactly arranged as one channel and the occupy rate reaches 0.63. AR coating is coated in the surface to ensure a transmission of higher than 99% in the wavelength of 529nm.

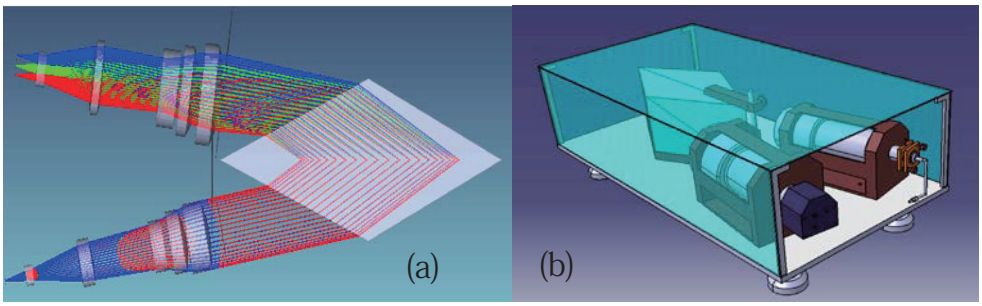

Figure 3, the optical (A) and mechanical (B) design of spectrometer

Figure 3 shows the optical (A) and mechanical (B) design of spectrometer. The key component of grism grating is composed of three parts, i.e., one VPH volume grating and two grisms. One of this grism is used to make the incident light satisfy Bragg diffraction condition, and the other is used to limit the angle of outgoing light. This spectrometer is design to have a wavelenght range of 529±3nm. The grating efficiency for the working spectral ranges is higher than 90%. The F number is 2.74. The spectral resolution is about 0.23nm which determines the minimum of the diagnosed ion temperature of 0.38kev. The magnification of this machine is designed of 1.12 at horizontal direction and 1 at vertical direction and the

image plane size is 18.4×13mm.

Table 1, the main parameters of lens.

Specification	Value
Grating size	100*192mm
Slit size	0.66(H)*13mm(V)
wavelength range	529±3nm
f number and NA	2.74/0.18
Focal Length	200mm
Effective Aperture	73mm(Collimated)； 100mm(Focused)
Angle of view	6°
Resolution	>150lp/mm
Number of elements	5/6
Transmission	~0.90
total length of lens	~260mm

The transmission of the commercial lens which are easily got from Canon or Nikon are about 0.5 because of the many lens. Our diagnostic is only used to transmit the light at a certain wavelength, so we design and fabricate collimated and focused lens for UF-CXRS. The main parameters of these lens are shown if table 1. The MTF comparison of customered and commercial lens are shown in figure 4 (a-c), and one can clearly see that the designed lens under fixed wavelength band is superior to commercial lens.

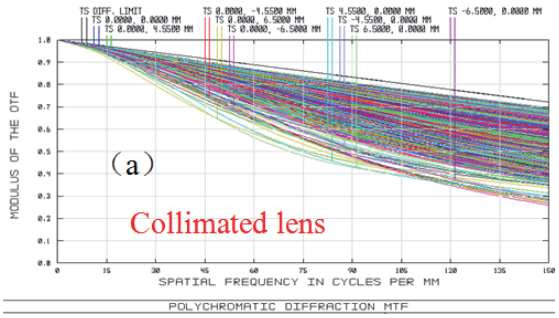

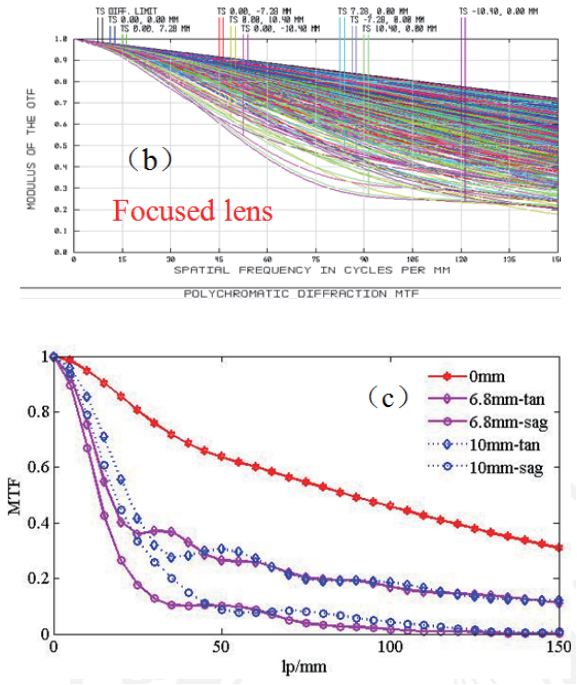

Figure 4, MTF of collimated lens (a) , focused lens (b), and commercial lens (c), respectively.

4. Conclusion

The design of UF-CXRS diagnostic is finished. Four-channel UF-CXRS diagnostic is integrated into the BES system to get the distribution of plasma pressure. It will have a time resolution of higher than 100k and a spatial resolution of 1 centimeter. By means of changing the angle of lens, this diagnostic can cover a view range of from R=1850mm to 2350mm with a minimum ion temperature of 0.38kev.

Acknowledgements

This work was supported by the National Natural Science Foundation of China (Grant No. 11535013), the National Magnetic Confinement Fusion Energy Research Project (Grant No.2012GB101001, 2015GB120002), and the Natural Science Foundation of Anhui Province (Grant No. 1608085MA08).

References

[1] WAGNER F, BECKER G, BEHRINGER K, et al., Phys. Rev. Lett. 49 (1982) 1408.

[2] F. Wagner, Plasma Phys. Control. Fusion 49 (2007) B1

[3] Chen S.L. and Sekiguch T., J.Appl.Phys. 36 (1965) 2363

[4] McKee GR, Fenzi C, Fonck RJ, et al., Rev Sci Instrum 74 (2003) 2014

[5] Pace D.C, Cooper C.M, Taussig D, et al., Rev Sci Instrum (2016) 87

[6] Hirsch M, Holzhauer E, Baldzuhn J, Plasma Phys. Contr. Fusion et al., 43 (2001) 1641

[7] Ye MY, Li YY, Yu Y, et al., Fusion Eng. Des. 96 (2015) 1017

[8] McKee G.R., Schlossberg D.J. and Shafer M.W., Rev. Sci. Instrum. 79 (2008) 10F528

[9] Uzun-Kaymak I.U., Fonck R.J., McKee G.R., et al., Rev. Sci. Instrum. 81 (2010) 10D714

[10] Uzun-Kaymak I.U., Fonck R.J., McKee G.R., et al., Rev. Sci. Instrum. 83 (2012) 10D526

Analysis of LH frequency effect on LHCD characteristics in EAST

Bojiang Ding for LHCD group and colloborators
Institute of Plasma Physics, Chinese Academy of Sciences, Hefei 230031, China

Abstract

The effect of LH (lower hybrid) wave frequency (2.45GHz and 4.6GHz) on lower hybrid current drive (LHCD) characteristics has been studied on EAST for the first time ever with two different source frequencies applied in the same discharge, showing that higher frequency improves penetration of the coupled RF power into the plasma core, leading to a better effect on plasma characteristics. The improvement in LHCD is mainly ascribed to a reduction in parametric instability (PI) and to a lesser extent collisional absorption (CA) in the edge region with the 4.6GHz wave, demonstrating the role and mitigation of parasitic effects of the plasma edge in LHCD in a density range that is lower than the regime where a ubiquitous density limit is typically observed.These results are encouraging considering that the LHCD tool is essential for control of the off-axis current profile in reactor grade plasmas.

1. Introduction

In order for the tokamak to be a commercially viable energy source, it will be necessary to operate these devices in 'advanced' modes characterized by high energy confinement and high fractions of the non-inductive bootstrap current [1]. A critical aspect of these modes of operation is the creation of a non-monotonic profile of the current density profile with an internal transport barrier that is maintained at large minor radius via control of the minimum in the current density profile via the application of off-axis non-inductive current drive. Lower hybrid current drive (LHCD) [2-4], produced by coupling high levels of microwave power at several gigahertz to plasma could in principle satisfy this current profile control need, but the coupled radiofrequency (RF) power faces the challenge of effectively penetrating into the main plasma without excessive power dissipation in the relatively high density plasma of the plasma radial periphery (n_e ~$0.8\times10^{20}m^{-3}$ at about two thirds of the minor plasma radius), possibly due to parametric instability (PI) behavior [5,6], collision absorption (CA)[7] and scattering by density fluctuation (SDF) [8,9] in the edge region. Failure of LHCD was indeed generally observed when approaching high plasma density conditions in machines operating at frequencies $\leqslant$8GHz [10-12]. On FTU, LHCD effects were still observed at densities even higher than those envisaged for ITER, by operating with an appropriate method for producing higher temperatures at the plasma edge [13]. The latter proved to be useful for diminishing the parasitic effect of PI, as previously theoretically predicted [6]. Here, we describe experiments and analysis that demonstrate the beneficial effects of increasing LH source frequency in a density range that is significantly lower than the density regime where a ubiquitous decline in LHCD is typically observed and found to be mitigated by increasing source frequency.

2. Experimental results

Specifically new results of recent experiments performed on EAST (major and minor radii of 1.85 and 0.45 m, respectively) have been interpreted using dedicated modeling analysis in order

to determine the effect of operating frequency on the PI, CA and SDF mechanisms which can produce parasitic damping of the coupled RF power at the plasma periphery. The combined experiments and analysis have helped to asses this important issue and suggest a means for mitigating these parasitic effects. Indeed, two LHCD systems have been implemented on EAST at the frequencies, respectively, of 2.45 GHz [15] and 4.60 GHz [16] (the latter is close to that envisaged for ITER).

The experiments (plasma current~ 500kA) were carried out by injecting the two different frequency waves (f_0 = 2.45GHz and 4.6GHz) with the same coupled power (P_{LH} ~ 1MW) in one discharge with an almost constant density (n_e = 2.0 × $10^{19}m^{-3}$) in a lower single null (LSN) configuration. In the experiments, the peak value of the antenna power spectrum, estimated by the ALOHA coupling code model [17] with the measured edge density, has a refractive index along the direction of the toroidal magnetic field of $N_{//0} \approx 2$, which satisfies the wave accessibility condition for the operating values of central plasma density (2.6 × $10^{19}m^{-3}$) and toroidal magnetic field (2.3T)[18].

The typical discharge (#54439) waveforms are shown in Fig. 1. It is seen that for a similar injected LH power (~1MW), the residual voltage (V_{loop}) (Fig.1 (b)) at 2.45 GHz(0.27V) is larger than with 4.60 GHz (0.15V). This implies that higher CD efficiency occurs when operating with a higher LH source frequency. Consistently, higher hard X-ray emission (HXR) from fast electrons is observed (Fig. 1 (c)). Better plasma heating effect also occurs for 4.6GHz as indicated by time evolution of plasma stored energy (W_{MHD} ~ 68.3kJ and 74.8kJ, respectively for 2.45GHz and 4.60GHz) (Fig. 1(e)),central electron temperature (T_{e0}~ 1.85 keV and 2.1keV, respectively for 2.45 GHz and 4.60 GHz) and central ion temperature (T_{i0}~ 1.0keV) (Fig. 1(f)) as measured by a X-ray Crystal Spectrometer (XCS) [19]. Also, the internal inductance (l_i) (Fig. 1(g)) is higher with 4.6GHz operation, indicating the production of a more peaked current profile. A larger change (~2.2 km/s and ~4.8km/s, respectively for 2.45 GHz and 4.60 GHz) of plasma rotation occurs in the core with 4.6 GHz as measured by XCS during LHCD phase, possibly due to the different LH power deposition and the absorbed LH wave momentum [20].

Frequency spectra detected by an RF probe located outside the machine, which documents the occurrence of wave-plasma interactions shows (see Fig. 2) that for #54439 a clear spectral broadening of the LH pump wave (Δf_p) occurs and is larger for 2.45GHz (1.6MHz) than for 4.6GHz case (0.74MHz) [21], which is the width at 20 dB below the peak (for the line frequency, $\Delta f_p \lesssim 0.1$ MHz). As discussed in the analysis this broadening can be associated with nonlinear decay of the pump wave into an ion sound wave quasi-mode which could be partially responsible for LH pump wave depletion at 2.45 GHz.

Thus these results show that a stronger LHCD effect occurs by operating at 4.6 GHz than at 2.45 GHz in terms of driven current, plasma heating, modification of current profile, plasma rotation, production of fast electrons and RF probe spectrum signals. Furthermore the improvement in LHCD performance occurs in a density regime that is lower than the range where increased source frequency is typically expected to recover current drive performance as shown in Fig. 3. Note that the LH power-produced fast electron population decreases much more strongly than the expected ($1/n_e$) trend for the 2.45 GHz case, as documented by HXR count rate than for the 4.6 GHz case (Fig. 3 (top)). In addition, a larger broadening with 2.45 GHz wave also occurs, and a clear downshifted sideband appears in the 2.45 GHz case which is associated with the excitation of an ion cyclotron quasi-mode that is not seen in the 4.6 GHz case (Fig. 3 (bottom)).

3. Analysis

Effects of PI and SDF in modifying the initial wave spectrum, as well CA, may play an important role in determining properties of wave propagation and damping in the plasma, hence possibly affecting power deposition and current drive. With the experimental parameters in Fig. 1, using a ray-tracing/Fokker-Planck code (C3PO/LUKE)[22], power deposition and driven current profiles were calculated using the initial nominal antenna spectrum [21].The simulations also neglected the residual DC electric field present in these discharges as well as any spectral modifications due to PI or SDF. Though the calculated driven current with 2.45GHz wave is somewhat smaller (about 10kA) than with 4.6 GHz wave, it cannot completely account for the experimental discrepancy (~100kA) estimated by the loop voltage, which is little affected by the change of electron temperature. Consequently, the slight change of accessibility condition at the two different operating frequencies and minor differences in the launched antenna spectrum could not explain the markedly different LHCD effects that are observed, as well as the difference in spectral broadening. Therefore the contributions of PI and SDF effects should be considered.

Concerning the standard LH wave scattering model due to density fluctuation, the frequency effect is certainly very small since the LH source frequency is much larger than the frequency of the drift wave fluctuations. Also the parallel wavenumber of the incident LH wave will be much larger than the parallel wavenumber of the drift wave fluctuations since they are long wavelength. Thus it is only possible for the $k_{\perp}$(wavevector component perpendicular to the toroidal magnetic field) to be rotated during a scattering event [8]. Using the same edge plasma parameters for 2.45 GHz and 4.6GHz LHCD plasmas, the effect of the LH scattering from plasma fluctuations on the power spectrum *vs.* the parallel refractive index has been evaluated following Ref. 23. We have assumed that the characteristic wavenumbers of the plasma fluctuations at the edge are in the range 0.1-1.0 in units of the inverse Larmor radius of the plasma ions. As a result, the drift-wave scattering has a negligible effect, producing a spectral broadening $\Delta N_{//}$ not larger than about 0.25 for 2.45 GHz source and not larger than about 0.15 for 4.6 GHz source in the region of the LH power absorption (r/a ~ 0.9). Compared to the PI induced spectral broadening $\Delta N_{//}>>1$ in the edge region with relatively low (15 eV) edge electron temperature, such broadening is not dominant. Therefore, the different LHCD effect observed with different source frequencies should be not ascribed to the SDF.

Conversely, signatures of PI can be recognized in the aforementioned RF probe spectra results that clearly indicate non-linear wave plasma interaction attributable to PI mechanism. In particular, with density increase, the downshifted signal occurring more strongly for the case of 2.45GHz operation.

With standard EAST parameters in Fig. 1, the effect of broadening of the launched antenna spectrum that the PI mechanism produces, and its impact in determining the radial profiles of LH-driven current and power deposition, has been considered following the approach in Refs. [6, 24] for the different LHCD behaviors with f_0=2.45 GHz and f_0=4.6 GHz.

Using the LHPI (Lower Hybrid Parametric Instability) code [25], which has the special feature of modeling the PI mechanism retaining convective losses due to plasma inhomogeneity and finite extent of the pump wave region, the calculated frequencies and growth rates of PI driven mode are shown in Fig. 4, in which the RF coupled power of 1MW, and the EAST antenna dimensions have been considered. For the pump frequency of 4.60 GHz, the analysis shows that

the PI mechanism is mostly driven by a low frequency quasi-mode having a maximum homogeneous growth rate ($\gamma / \omega_0 \approx 8 \times 10^{-4}$) that is slightly smaller (by about 20%) than for operating frequency of 2.45 GHz, implying a stronger PI effect in the case of 2.45GHz LH wave, consistent with the RF probe data. Taking into account the available data of kinetic profiles, which show relatively low electron temperatures occurring in a quite large radial interval of the scrape-off and periphery of the plasma column (in the range of 10 eV– 500 eV in a layer extending up to about 15 cm away from the antenna-plasma interface), it has been found that convective losses due to plasma inhomogeneity and finite extent of the pump wave region weakly depress the PI phenomenon. Therefore, PI can be significant in EAST, mostly in the scrape off layer (SOL) since it is there favored by lower plasma temperature [10, 15]. Consequently, strong PI can significantly deplete the launched power spectrum. This power is redistributed over LH spectral components with large $n_{//}$, especially for the 2.45GHz case (up to $n_{//max} \approx 40$, and $n_{//max} \approx 30$ for 4.6 GHz, owing to the smaller growth rate). In both cases, the fraction of the coupled RF power (p_{PI}) redistributed on PI sidebands exceeds the perturbative limit (of 10%) that is at the basis of the pump depletion model. However it is likely that the pump power depletion would be very large ($p_{PI} >> 10\%$) for the operating frequency of 2.45 GHz case, and more moderate ($p_{PI} \gtrsim 10\%$) for 4.6 GHz.

In addition, CA loss in the edge region could be another candidate for the discrepancy since CA damping should decrease as a function of frequency [7]. For the typical scale length of $Ln_e \sim L_{Te} \sim 1.2$ cm in EAST, WKB analysis of the absorption based on a plane-stratified SOL model(see Fig. 5) shows that the CA loss in the SOL for a LH wave passing into and out of the SOL (i.e. the 'round trip') is about 5% at 2.45 GHz and half that at 4.6 GHz, being in agreement with the results with GENRAY code [12,26]. Although this 'round-trip' damping through the SOL is low, the cumulative damping after several passes is by no means negligible since the core electron temperature is not high enough for the waves to be absorbed in a single pass into the plasma and the LH rays actually undergo many radial reflections in the SOL as indicated by the ray tracing /Fokker Planck simulations.

4. Summary

Available data of experiments performed on EAST show that operation at higher frequency (4.6 GHz), close to that of the LHCD system proposed for ITER (5GHz), improves penetration of the coupled RF power into the plasma core with respect to operation with 2.45GHz source. Furthermore the density range in which the improvement in LHCD performance is found is significantly lower than the density regime where a ubiquitous decline in LHCD is typically observed and found to be mitigated by increasing source frequency. Modeling results show that this beneficial behavior is a consequence of the diminished parasitic effects of the plasma edge expected to occur through PI and CA mechanisms. In addition, the parasitic effects of these phenomena would be further diminished under reactor conditions where a markedly warmer edge and core plasma would exist as compared to present experiments. These results bode well for the use of the LHCD actuator as an essential tool for current profile control in a thermonuclear fusion reactor.

Acknowledgements:

This work is supported by the National Magnetic Confinement Fusion Science Program of China (Grant No. 2015GB102003, 2013GB106001B, 2013GB112003), the National Natural

Science Foundation of China under Grant No. 11175206, 11305211 and 11275233, Hefei Science Center CAS (2015HSC-UE005,2016HSC-IU008), and the JSPS-NRF-NSFC A3 Foresight Program in the field of Plasma Physics (NSFC No. 11261140328). It is partly supported by the China-Italy, the China-France and the China-US Collaboration (DE-SC-0010492) programs. In addition, one of the authors, B J Ding would like to thank Drs. F M Poli, S. Shiraiwa, and S G Baek for the useful discussions.

References:

[1] S. C. Jardin *et al*, Fusion Engineering and Design **38** (1997) 27.
[2] N.J. Fisch. Phys. Rev. Lett.**41**(1978)873.
[3] S. Bernabei *et al.,*Phys. Rev. Lett.**49**(1982)1255.
[4] N. J. Fisch, Rev. Mod. Phys.**59**(1987)175.
[5] C. S. Liuand V. K. TRIPATHI, Phys. Rep.**130**(1986)143.
[6] R. Cesario*et al.,* Phys. Rev. Letters, **92** (2004)175002
[7] P. T. Bonoli and R. C. Englade, Phys. Fluids**29**(1986)2937.
[8] Y. Peysson *et al*., Plasma Phys. Contr. Fusion**53** (2011) 124028.
[9] N. Bertelli et al, Plasma Phys. Control. Fusion 55 074003 (2013).
[10] B. J. Ding *et al*., Nucl. Fusion **53**(2013) 113027.
[11] V. Pericoli-Ridolfini V. *et al*Nucl. Fusion**34** 469 (1994).
[12] G. M. Wallace *et al.,* Phys. Plasmas**17**(2010)082508.
[13] R. Cesario*et al.*, Nature Communications, 1 (5) 55 (2010).
[15]B. J. Ding *et al*., Nucl. Fusion **55** 093030 (2015).
[16]F. K. Liu *et al*., Nucl. Fusion **55**(2015)123022.
[17] J. Hillairet J et al.,Nucl. Fusion**50** 125010 (2010).
[18] Y. Takase *et al.,* Phys. Fluids**28**(1985)983.
[19] B. Lyu*et al*., Rev. Sci. Instrum. **85**(2014) 11E406.
[20] B Chouli et al, Plasma Phys. Control. Fusion **56**(2014)095018.
[21] M. H. Li*et al*., Physics of Plasmas **23**(2016) 102512.
[22]Y. Peysson*et al*., Plasma Phys. Control. Fusion **54**(2012)
045003. [23] P. L. Andrews and F. W. Perkins Phys. Fluids
26(1983)2537. [24] R. Cesario *et al*., Nucl. Fusion **46**(2006)462.
[25] R. Cesario*et al*., Nucl. Fusion **54** (2014) 043002.
[26] C. Yang *et al.*, Plasma Phys. Control. Fusion**56**(2014) 125003.

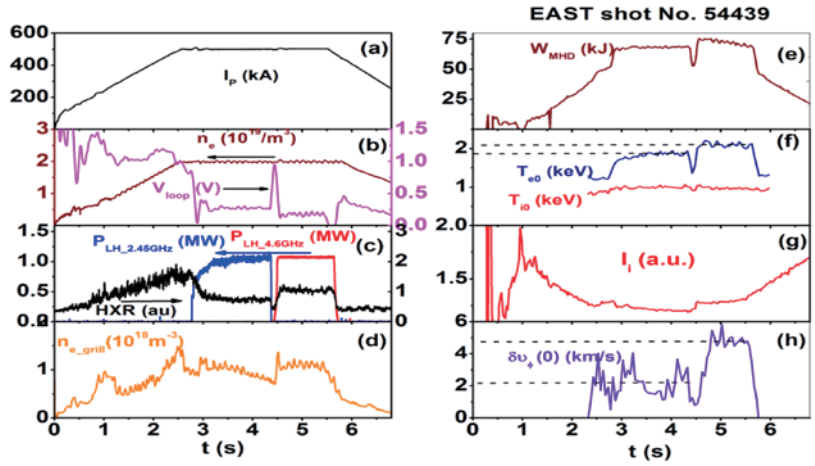

Fig. 1 Typical waveforms of LH frequency effect on plasma characteristics (a) plasma current (Ip), (b) line averaged density (n_e) and loop voltage (V_{loop}), (c) LH power, and hard X-ray emission (HXR), (d) grill density (n_{e_grill}) measured by Langmuir probe, (e) stored energy (W_{mhd}) calculated with magnetic measurement, (f) central electron and ion temperature by CXS, (g) internal inductance (li), and (h) central toroidal rotation by CXS.

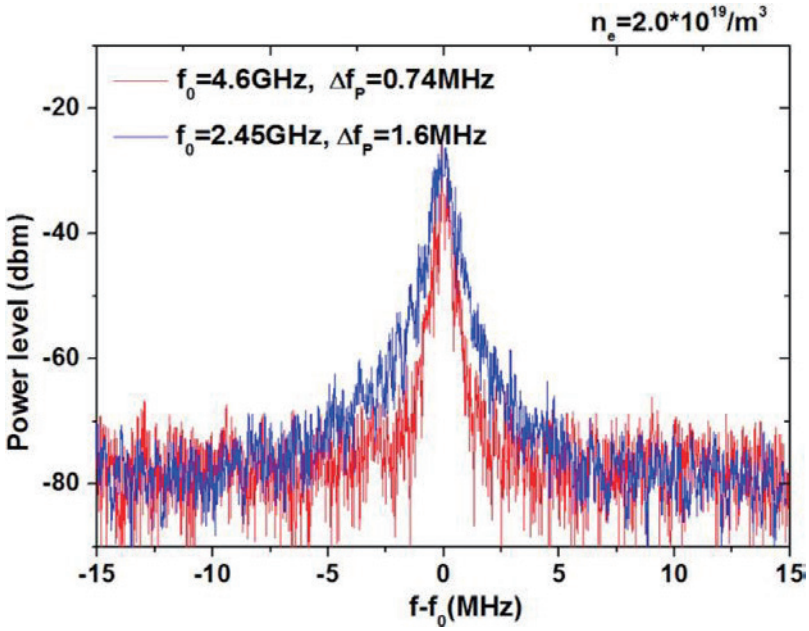

Fig. 2. Comparison of the frequency spectra between 2.45 GHz (blue) and4.6 GHz (red) with n_e = 2×10^{19} m^{-3} (#54439).

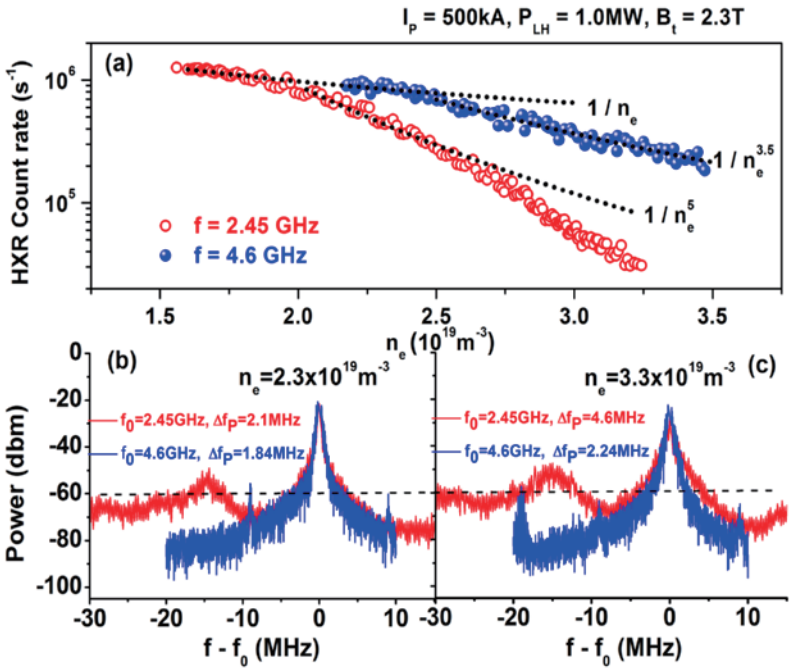

Fig. 3. Top: (a) HXR count rates vs density, Bottom: RF probe spectra measured at two different plasma densities for the two operating LH frequencies with (b) $n_e = 2.3 \times 10^{19}\text{m}^{-3}$ and (c) $n_e = 3.3 \times 10^{19}\text{m}^{-3}$.

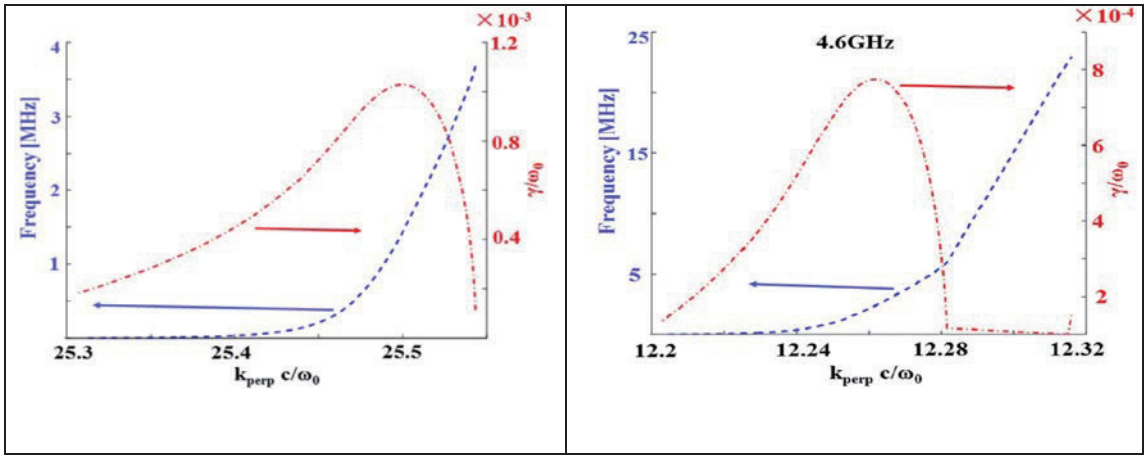

Fig. 4 (left) Calculated frequencies and growth rates for the 2.45 GHz pump wave, assuming local values of $n_e = 4 \times 10^{17}$ m^{-3}, $T_e = 30$ eV.

(right) Frequencies and growth rates calculated as in (left), but considering a pump frequency of 4.6 GHz .

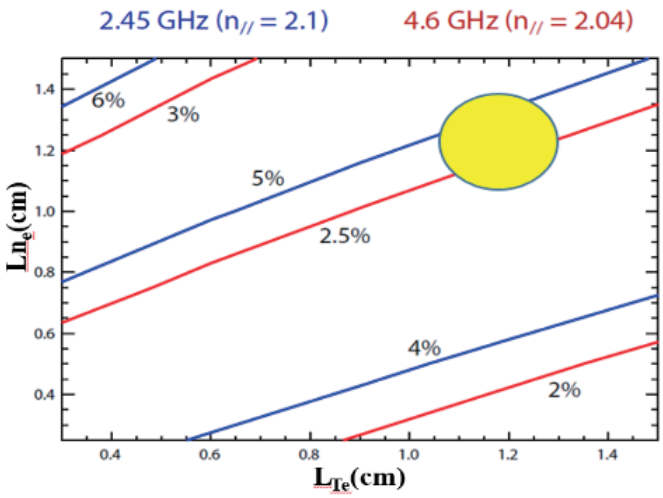

Fig. 5Round trip loss contours *vs* scale lengths in SOL

Current status and plan of KSTAR NBI system

S. W. Jung[1], S. J. Wang[1], J. H. Jeong[1], W. Cho[1], B. Na[1], Y. S. Bae[1], J. G. Kwak[1], Y. K. Oh[1], and Y. S. Kim[1], T. S. Kim[2], S. H. Jeong[2]

[1]National Fusion Research Institute, Daejeon, Korea

[2]Korea Atomic Energy Research Institute, Daejeon, Korea

Abstract

NBI system is the most effective heating device in KSTAR. Now, KSTAR NBI-1 can inject neutral beam up to 5.8MW. During this year's campaign, neutral beam energy fraction was measured by using MSE. NBI-1 source A's full energy was 60% and source B and C were 45%. NBI-1 injected the beams for 78.1seconds. KSTAR NBI-1 has upgrade plans for stable steady state operation. To enhance heating power and to drive off-axis current, a new NBI system, which called NBI-2, will be built. The NBI-2 system can inject 2MW for on-axis heating and 4MW for off-axis current driving.

1. Introduction

Main mission of KSTAR is to achieve "Advanced Tokamak (AT)" operation mode in long pulse capable superconducting tokamak device. To achieve high beta N and steady state plasma [1], tokamak should increase heating power and drive the off axis current. In this year campaign, KSTAR did around 70 s steady state operation and around high beta N operation. NBI-1 was contributed long pulse operation and high beta N operation. Also KSTAR have a plan to increase heating powers to succeed Advanced Tokamak. As a part of them, a new NBI system, which calls NBI-2, will be added. The system consists of 2MW on axis heating source and 4MW off axis current drive sources.

NBI-1 is the main heating device of KSTAR. Since NBI-1 A was installed in 2010, NBI-1 B and C were installed in stages. As each ion source was added, the available injecting power was increased up to 5.8MW. In addition, as the operational stability was secured, the duration for beams to be injected into the tokamak has increased. The ion sources can inject 100keV deuterium beams. For long pulse operation, multi aperture grid was made with CuCrZr.

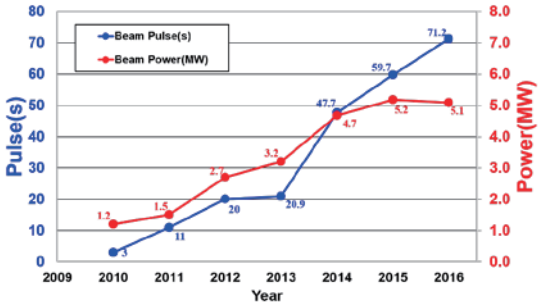

Fig. 1 Enhancement of KSTAR NBI injection power

2. Experimental results in 2016

Before 2016 campaign, the NBI-1 conditioning was performed. It was confirmed that a total of 5.8MW neutral beam can be injection through conditioning. Each beam power is 1.71MW, 2.04MW, and 2.05MW. The energy fractions of NBI were measured using MSE without toroidal magnetic field. We obtained 60% full energy fraction of NBI-1 A and 45% for B and C, respectively. Based on these results, we will conduct research to improve the energy fraction of NBI. In the 2015 campaign, a steady state operation of 59 seconds was performed. In the 2016 campaign, more than 10 seconds were added. Three neutral beams of 3.7MW was injected for 71.2 seconds.

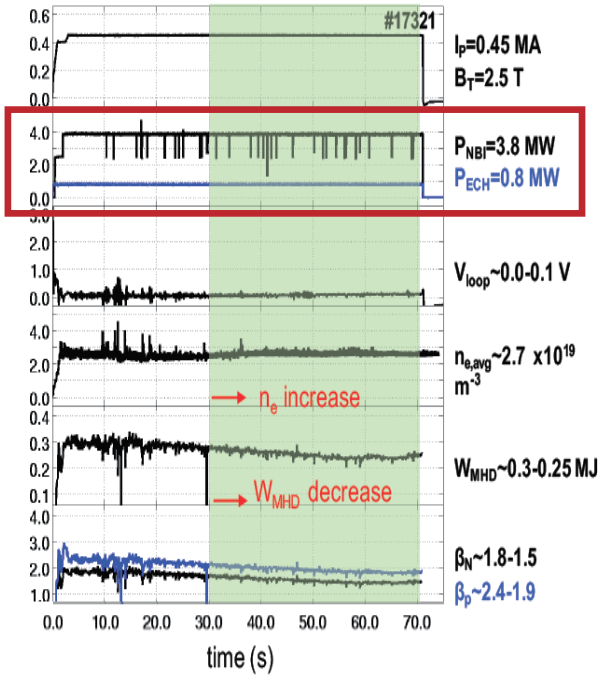

Fig. 2 Longest pulse of 71.2 seconds with 3.8MW of injecting power achieved in the H-mode KSTAR operation

Currently, KSTAR's NBI-1 has been successfully performing On-axis heating using three ion sources. Efficient bulk heating is the mission of KSTAR NBI. Up to now, On-axis heating has been driven, but off-axis current driving has not been considered. In the future, KSTAR plans NBI-2 with off axis current driving and on axis heating in addition to 6MW on axis heating NBI-1 system. NBI-2 consists of one on axis heating source and two off axis sources. On-axis heating will be 2MW, and off-axis current drive will be 4MW.

The advantages of off axis current driving are as follows: maximizing driving current, maximizing/optimizing off-axis CD capability, peak minor radius, width of profile, compromise with installation constraints, minimizing additional R&D requirements. NBI-2 was also designed to have three ion sources like NBI-1. But, in the case of NBI-2, ion sources are arranged in the vertical axis differently from NBI-1. By this arrangement, we try implement on axis heating through the center ion source and off axis current drive using the upper and lower ion sources.

The specifications of the beam for NBI-2 are as follows. We will implement 6 MW and 100keV of

neutral beam into tokamak to realize heating and current driving. The injection power of each ion source is 2MW. The vertical slant angle of the ion source is 5.5degree, and the beam target is 1.6 m from the center of the tokamak. The size of the ion source is 450mm×130mm. It will be implemented with 280 beamlets in total, and it will be implemented to be focused at 10m from the ion source in order to increase the beam transmission efficiency. To predict beam transport and beam loading on beamline component, beam trajectory calculation was treated with BTR code [3]. Beamline components such as neutralizer, ion dump, calorimeter, and scrapers so on were placed and simulated. It is the results of simulating 8:1:1 fraction of full, half and 1/3 energy. The transmitted beam power is 2.14 MW of full energy, 0.134MW of half energy and 0.095MW of 1/3 energy, and a total of 2.284MW is considered to be injected. Total transmission efficiency was estimated to be 84.1%. The maximum beam loading of neutralizers and scrapers is less than 4 MW/m^2. It was confirmed that this satisfies the cooling capacity of $10MW/m^2$ of hypervapotron [4]. The following is the calculation results for the components with the largest beam loading. They are the beam loading distributions for Full energy, half energy, and 1/3 energy, respectively, Of course, the most power is loaded onto a full energy dump. At this time, the peak beam loading power density is 6.7 MW/m^2. It is expected that sufficient cooling will be possible when cooling using hypervapotron. The maximum energy deposition positions do not overlap. Therefore, it is considered that the system will operate normally even if three beams are incident simultaneously. The result is the power density to be loaded into the calorimeter during calorimeter operation. The maximum power density is 6.49 MW, which satisfies the cooling capacity for hypervapotron.

The first grid power supply has 200 power modules connected in series. Each module is capable of outputting up to 500V and has an integrated IGBT switch and freewheeling element. The power supply can apply 100kV of voltage and 60A of current, with a ripple frequency of 1MHz. The ripple voltage is designed to be less than 1kV. To prevent damage to the grid due to breakdown, the following devices will be installed. The arc energy was designed to be less than 10J. Redundancy modules will be inserted in order to prepare for failure of individual modules during the operation. In NBI-1, the voltage divider using high voltage resistor was used to supply the voltage to G2. In NBI-2, a direct tab will be installed in the PSM module to supply G2 voltage directly from the 1st grid power supply.

3. Summary

NBI-1 system in KSTAR is the most important heating device. It contributed a steady state operation in 2016 campaign. NBI-1 system injected the neutral beam for 71.2 seconds. There were three accidents in campaign 2016: Two were at ion source B, the other was at the residual ion dump. The ion dump water leak was the most dangerous accident of 2016 campaign. To prevent the accident, we have two plan which are real time monitoring of ion dump surface's temperature with IR cameras and a depressed ion dump. A new NBI system will be operational from 2018. The system can inject neutral beams which are 4MW of off-axis beams and 2MW of on-axis beam.

Acknowledgements

This work was partly supported by the JSPS-NRF-NSFC A3 Foresight Program in the field of Plasma Physics (NSFC: No.11261140328, NRF: No.2012K2A2A6000443).

References

[1] G.S. Lee, et al., Nuclear Fusion, 1515, Vol. 41, No. 10 (2001)

[3] B. H. Oh and E. D. Dlougach, 20th IEEE/NPSS Symposium onFusion Engineering, **474-477** (2003)

[4] H.D. Falter, E. Thompson, Fusion Sci. and Technol. Vol.29, **584** (1996)

Improvement on vertical stabilization control of KSTAR

Sang-hee Hahn[1], D. A. Humphreys[2], D. Mueller[3], J.G. Bak[1], N. W. Eidietis[2], Y. M. Jeon[1], **A.** Hyatt[2], M. J. Lanctot[2], M. L. Walker[2]

[1]National Fusion Research Institute, Daejeon 34133, Korea
[2]General Atomics, San Diego, CA, USA
[3]Princeton Plasma Physics Laboratory, Princeton, NJ, USA

Abstract

By dedicated experimental measurements on the VS controllability done in 2012-2015, it was found that the maximum controllable vertical displacement ΔZ_{MAX} is 2.47 ± 0.94 cm for the plasmas with elongation=1.75, γ_Z ~ 110 rad/s. In order to improve VS controllability for the extended axisymmetric magnetic controls, in 2013-2014 campaigns introduction of a dedicated speed estimator enabled to reduce the PD gains with same controllability. After that, a new approach using decoupling in the frequency domain was introduced in 2015, in order to aim more effective reduction of fast/slow control competitions. The application of the decoupling, combined with a relay-feedback tuning technique, demonstrated extension of the available vertical position up to -10 cm without manual compensations of the Z target and the shape target.

1. Measurement of stability metric

In principle, According to the known literature [1,2], two important metrics are found to be useful for assessing the level of performances for the vertical position stabilization controls: one is the stability margin, which is approximately the ratio of the unstable growth time to the wall penetration time, $m_s \equiv \gamma_z/\gamma_w$. The other is known as the maximum controllable vertical displacement, ΔZ_{MAX}, which can be measured experimentally and can in addition quantify the nonlinear constraints imposed by the actuator (in this case, the IVC power supply [3]). The ΔZ_{MAX} strongly depends on the open-loop vertical growth rate(γ_z) of the vertical displacement event, and the actuator limits, such as maximum allowable PS current/voltages (ΔI_{max}, V_{sat}), the self-inductance of the coils (L_c), and the effective delay time of the power supply and signal conditioning circuits (TPS). The dependence of I_p is indirectly included to ΔZ_{MAX} as a term of vertical field at the center(B_{z0}).

As the first step, a series of dedicated "release-and-catch" experiments are performed at KSTAR to measure these two principal metrics for vertical stability in 2012-2015 campaigns. The typical experimental setup is to program a few occasions of the current freeze algorithm during the discharge with different durations of the control-off time. A dedicated control setup, called as "VDE current freeze", was installed to the KSTAR plasma control system so that we invoke the algorithm whenever we want during the discharge. When the algorithm is triggered, it tries to maintain present level of control coil current, disregarding all the preprogrammed shape/VS controls. After that, the PCS gets the feedback gains back and tries to catch the plasma from the VDE.

The principal diagnostics for the measurement of the open-loop vertical growth rate is the magnetic reconstruction (EFIT) [4,5], both offline and online [6]. Not every VDE can be reconstructed, but it gives a reasonable estimate when the thermal quench was not the main cause of the disruption, i.e. in the case of a VDE by control loss. The vertical movement speed by the magnetic reconstruction result was verified and validated by comparing with the intensity profile of the horizontal soft X-ray measurements. Details are available in the reference [7].

By this measurement, as shown in Figure 1, both the m_s and the ΔZ_{MAX} are experimentally measured by disabling coil feedback for an amount of time (10~20 ms) in a stable KSTAR plasma discharge. The current freeze algorithm turned the coil controls off by 8/16/20ms. The discharge survived when the control of vertical stability by the IVC was off until 16 ms, but 20ms off blew the discharge off. The estimate of ΔZ_{MAX} from the initial position can be obtained by measuring maximum vertical displacement that the control system was not able to catch the plasma again. In this case the measured ΔZ_{MAX} was 2.47 ± 0.94 cm. The experiment used discharges with elongation=1.7~1.9, depending on the discharges available in each campaign, and a range of (βp, li) which can be obtained by adding/removing the neutral beam power. It was found that the change of the gain at the VS controller PID loop did not change the growth rate (γ_z).

2. Extending vertical controllability

In order to extend the operational range of the available shape, especially for the available elongation κ, there have been many attempts to improve the vertical stability controls. The present control scheme for the VS is based on a ~20kHz SISO feedback using a position estimator which consists of 2 inboard normal field probes, with are located ~6 cm away from each other, behind the inboard limiter. The actuator, the in-vessel control coil (IVC) with max 1000V, 6000A*6 turns switching power supply, is anti-series connected to a Cu load. Since the vertical stabilization is the fastest feedback loop, the 4 kHz isoflux control loop responsible for the shape feedback does not directly control the current center, hence does not include the IVC as actuator.

Since the estimate of the vertical position at could be different from the other, the two controllers tend to fight one another, since the isoflux/DNULL algorithm basically does not care about the Z location by definition. This became more serious when the 1-turn gap resistor value increased in years 2013-2014. Typical signature of fighting algorithms was seen as very-low frequency oscillations on Z [around several Hz at the Z position]. Even the optimal setup was found, but changes in the isoflux setup design may cause the problem again, which may result in limitations on the controllable vertical ranges. For example, for 2012-2014 runs, the maximum "drSep" (defined as the distance between the flux of the upper separatrix and the lower one at the double null shape) practically allowed was +- 2 cm unless we adjusted the Z location target at the VS algorithm target. For +4 cm of drSep, we had to adjust the Zp target as +2 cm also. The problem here is that no one (even the operator who made it work) knows why we need to set it as +2 cm, not 4 cm. This discrepancy between the VS algorithm and the isoflux seems to be the cause of high DC offset at the IVC coil current, which reduces the IVC coil current margin available and hence the ΔZ_{MAX}.

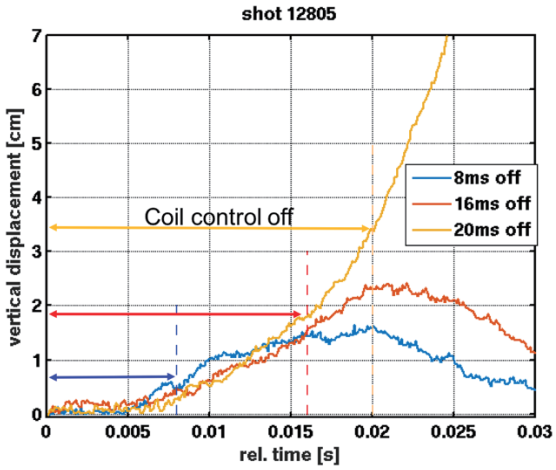

Figure 1. ΔZ_{MAX} measurement in the shot 12805. When the shape feedbacks were off by up to 16ms, the system was able to catch the plasma again, but 20ms-off lost the plasma.

There are also issues of the coils aligned at the same line of influence in geometry: If we draw a line between the plasma center and the PF6U/L circuits, the IVC coil is on the way, hence the magnetic field by the IVC is constantly interfered by a large load PF6. Moreover, the IVC coil circuit is too fast

compared to the speed of the PF6U/L circuits. During the applications of the dZ/dt signals into the VS algorithm done in 2014, it was pointed out that we need to let the isoflux control the slowest part of vertical position in order to reduce the DC current at IVC, but the responsible coils (PF6 for example) are too slow to get along with the Z offset signals produced in the present Zp feedback. The interference of the PF & IVC produced unpredictable DC offset on the IVC coil current, resulted in the higher value of the proportional gain that is to be required.

In order to find solutions to reduce dependency on the absolute value of the Zp estimator, two ways are suggested historically: One is to use another estimator signal that measures the speed of Z (=dZ/dt), not the absolute position of Z. The method has been demonstrated to be feasible in 2013-2014, as described in [8]. The other way is at first suggested in 2014, which makes separation of related feedback loops in the frequency domain, moving the slow part (< 2 Hz) to the isoflux and let the IVC care only the fast movement.

The separation of control in the frequency domain has been demonstrated in 2015 for the first time as a prerequisite of the ITER similar shape (ISS) development research. The idea is to create a "fast Z" signal by extracting high-frequency responses from the original Zp estimator (or any other proxies we can represent the disturbance of the current center). A realtime software highpass filter was introduced for the calculation of the signals. The corner frequency of the highpass is determined by analyzing the frequency responses of each main actuator circuit, shown in Figure 2(a). Since the PF6 shows a very slow response (1.5 Hz corner), the corner frequency of the HP filter was selected as 2Hz. In the scheme feedback of the slow part, i.e. the center movement less than 1Hz, is essential. Since the isoflux does not calculate the center of the current profile in the realtime manner, a "slow Z proxy" was defined as a difference of two up/down segment errors to represent the corresponding movement of the center. Figure 2(b) shows an example of the definition of the slow Z proxy for a lower single null (LSN) discharge. In the reality, the proxy was determined by a few trial and error and was tested by a simulation that gets the equilibrium information of an old shot for the construction of the response model [9].

Figure 3 shows a dedicated demonstration of the algorithm for a set of highly elongated shots: #12481 is a reference using the present Z feedback and the isoflux scheme that was very common through the 2015 campaign. Increasing the bottom Zx target, hence increasing the elongation, the discharge becomes oscillatory when it reaches to -92 cm, corresponding to the elongation=1.8. Without frequency decoupling, oscillations get bigger and bigger to disrupt finally in the shot 12481. The shot #12493 uses a decoupled Z estimator (recorded as LMSZFAST) by applying a software highpass filter with corners 2 Hz in the VS algorithm, and switched the feedback measurement from the old-school (LMSZ) to the decoupled Z (LMSZFAST) at 3.0-3.2s.

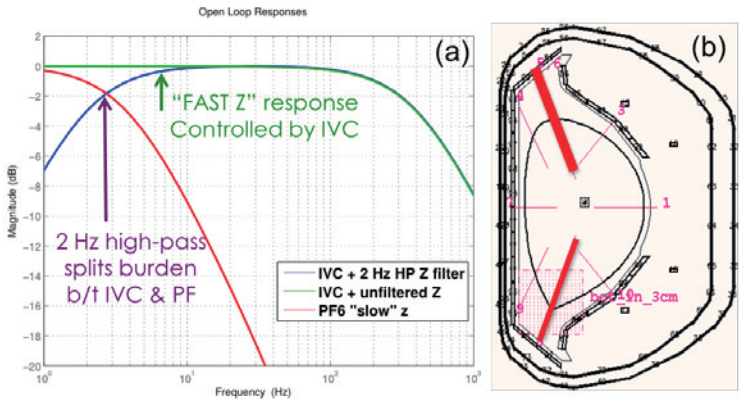

Figure 2. (a) Frequency responses of the vertical position controllers. The unfiltered response for the IVC+fast Z (green) is altered by 2Hz highpass Z filters (blue) so that the "slow Z" proxy control by the PF6U&L can only respond to the slow movement relevant to the shape control. (b) The location of the control segments, denoted by thick red bars, for calculating the slow Z proxy.

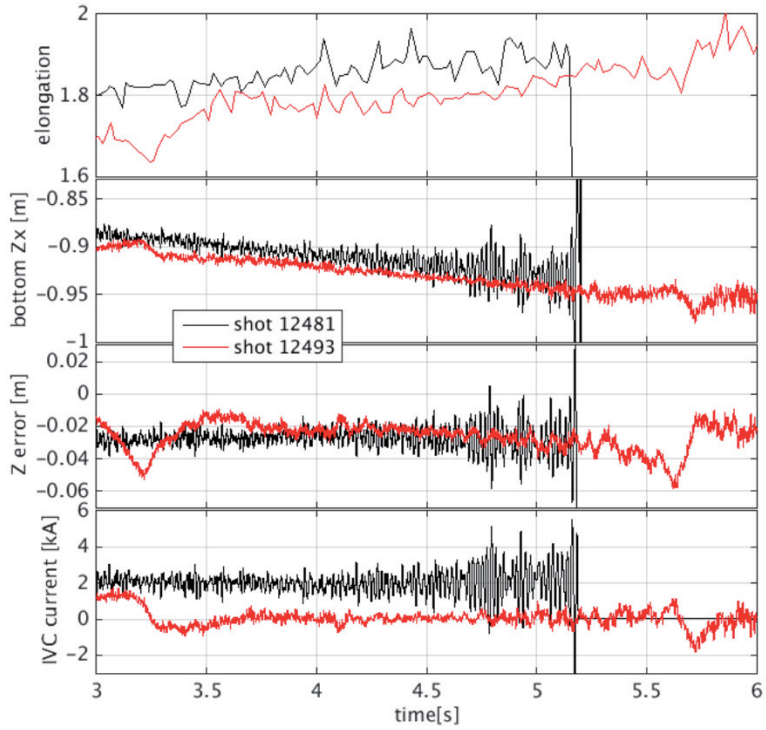

Figure 3. Experimental demonstration of feasibility on the control separation in the frequency domain: Without any frequency decoupling, the bottom Zx starts oscillating as it reaches to -92 cm (#12481, black). In the shot #12493 (red), after applying the frequency separation using high-pass filtered Z estimator (Zfast) at t=3.0-3.2s, the IVC DC current offset disappears and the bottom Zx went to -96 cm (kappa~1.88) earlier, without any significant oscillations.

The slower motion, a sub-Hz Z position drift, was defined at the Isoflux algorithm in a form of subtraction from SEG05 to SEG11, that is by definition a difference between the upper/lower reference flux errors. The application of frequency separation immediately removed the IVC current offset by ~2kA/turn, and the Zx oscillation is not triggered even at a high-elongation target Zx = -96cm, which made the discharge last until the Ip rampdown occurred at 5.7s. During the ISS control development, the decoupling algorithm was tested to be able to create a discharge that the current center positioned up to -10 cm from the machine geometry center.

Acknowledgement

This research was supported by Ministry of Science, ICT, and Future Planning under KSTAR project and was partly supported by the JSPS-NRF-NSFC A3 Foresight Program in the field of Plasma Physics (NRF No. 2012K2A2A6000443).

References

[1] D.A. Humphreys et al., “Experimental Vertical Stability Studies for ITER Performance and Design Guidance”, Nucl. Fusion 49 (2009) 115003.

[2] M. Ferrara et al., “Plasma inductance and stability metrics on Alcator C-Mod”, Nuclear Fusion, 48(6), 065002–8 (2008).

[3] Jong-Kook Jin et al., IEEE Transactions on Plasma Science, 41(7), 1799–1804 (2013).

[4] L.L. Lao, H.S. John, R.D. Stambaugh, A.G. Kellman, W. Pfeiffer, Nucl. Fusion. 25 (1985) 1611–1622.

[5] O. Katsuro-Hopkins, et al., Nuclear Fusion, 50(2), p.025019 (2010).

[6] J.R. Ferron, M.L. Walker, L.L. Lao, H. John, Nucl. Fusion. 38 (1998) 1055–1066.

[7] S. Hahn et al., “Measuring and extending the vertical stabilization controllability of KSTAR”, the 26th IAEA Fusion Energy Conference, Kyoto, Japan, EX/P4-12 (2016).

[8] D. Mueller et al., "Improvements in the fast vertical control systems in KSTAR, EAST, NSTX and NSTX-U", the 25th IAEA Fusion Energy Conference, St. Petersburg, Russia, PPC/P8-17 (2015).

[9] S.-H. Hahn, A.S. Welander, S.W. Yoon, et al., Fusion Engineering and Design. 89 (2014) 542–547.

Preliminary result of cross-field impurity transport study in stochastic magnetic field layer of LHD

S.Morita[1,2], H.M.Zhang[3], S.Y.Dai[4], T.Oishi[1,2], M.Goto[1,2], X.L.Huang[1] and Y.Liu[2]

[1] National Institute for Fusion Science, Toki 509-5292, Gifu, Japan

[2] Graduate University for Advanced Studies (SOKENDAI), Toki 509-5292, Gifu, Japan

[3]Institute of Plasma Physics CAS, Hefei 230026, Anhui, China

[4]Dalian University of Technology, Dalian 116024, China

Abstract

In Large Helical Device (LHD), two-dimensional (2-D) distributions of edge carbon emissions of CIII to CVI have been measured at extreme ultraviolet (EUV) wavelength range for studying the transport coefficient of edge carbon ions. The measured carbon distribution is analyzed with three-dimensional edge plasma transport simulation code, EMC3-EIRENE. It is found that the narrow strip-shaped impurity trace emitted along the edge X-point and its width are sensitive to the cross-field impurity diffusion coefficient, $D_{Z\perp}$. As a preliminary result, the value of $D_{Z\perp}$ is evaluated for C^{3+} ions to be 20 times larger than that of the bulk ions in the R_{ax} = 3.90 m configuration.

1. Introduction

It is important experimentally to study the impurity transport in the edge stochastic magnetic field layer of LHD plasmas as the feedback information to the theoretical consideration in addition to the physical understanding on the role of edge stochastic magnetic field layer necessary for further confinement improvement. The magnetic field lines with short connection length ($L_c \leq 10$m) are directly linked to vacuum vessel near helical coils, whereas ones with long connection length ($10 \leq L_c \leq 2000$m) are connected to divertor plates passing nearby X-points. Therefore, the cross-field transport perpendicular to the magnetic field lines becomes important in LHD in addition to the parallel transport along the field line, when the impurity transport in the stochastic magnetic field layer is studied. If the magnetic field connection length is short like tokamak scrape-off layer, the parallel transport is more important than the cross-field transport. In order to study the cross-field transport in the stochastic magnetic field layer, 2-dimensional (2-D) distribution of line emissions from edge impurity ions has been measured in LHD. The cross-field transport coefficient of carbon ions in the stochastic magnetic field layer has been recently obtained from the analysis of the 2-D distribution of carbon emissions with help of 3-D edge plasma transport simulation code, EMC3-EIRENE [1], as a preliminary result [2].

2. 2-D distribution of CIII-CV at R_{ax}=3.90m

The 2-D distribution of CIII–V is measured at a flattop phase of LHD discharges in R_{ax} = 3.90 m plasma axis position. The result is shown in Fig. 1. Footprints of inboard and outboard separatrix X-points are indicated with dashed-dotted and long-dashed lines, respectively. The CIII and CIV shown

in Figs. 1 are dominantly emitted in the top and bottom edges and the vicinity of outboard separatrix X-point denoted with long-dashed line. The CIII and CIV are only enhanced along a trace parallel to the outboard X-point at the upper half region, while those in inward-shifted configurations like Rax=3.60 and 3.75m are entirely different. The CV and CVI emissions are considerably uniform (CVI distribution is not shown in Fig. 1).

3. Analysis of cross-field transport coefficient

In order to understand these 2-D distributions the simulation is done with EMC3-EIRENE, as shown in Fig. 2. Two enhanced strip-shaped emission traces parallel to the outboard X-point appear in the simulation for CIII and CIV emissions shown in Figs. 2(a) and (d), respectively. The upper emission trace in the simulation can be also seen in the measured CIII and CIV 2-D distributions (see Figs. 1(a) and (b)), whereas the lower emission trace almost disappears in the measured 2-D distribution. Although the reason for the asymmetric emission trace observed in the experiment is now unclear, it strongly suggests the necessity of additional concern regarding the physical mechanism in the simulation, e.g. particle drift.

The simulation is also carried out for three different impurity diffusion coefficients of $D_{Z\perp}$ = 0.2, 1.0 and 4.0 m^2/s, as shown in Fig.2. In order to determine the diffusion coefficient the CIV profile perpendicular to the X-point footprint is compared between the measurement and simulation. Here, the coordinate x perpendicular to the outboard X-point footprint is defined as the reference point of (Y, Z) = (−100 mm, 100 mm), which is denoted by arrow in Fig. 2(d). The measured perpendicular profile is plotted with simulated profiles in Fig. 3 as a function of x. The measured profile seems to be wide and the simulated profile is gradually wider as $D_{Z\perp}$ increases. Then, the experiment shows a good agreement with the simulated profile assumed $D_{Z\perp}$ = 4.0 m^2/s. The impurity diffusion coefficient in the stochastic magnetic field layer obtained in the present analysis is 20 times bigger than the bulk ion diffusion coefficient which is also obtained from radial density profile in the plasma edge.

In addition, it is clear in Fig. 2 that the length of the two outboard strip-shaped emission traces appeared in the 2-D distribution of CIII and CIV is also sensitive to the diffusion coefficient. In order to explain why the length of two outboard traces changes against the diffusion coefficient, the poloidal distributions of magnetic field connection length, L_c, and simulated CIV emissivity at different toroidal angle, ϕ, are plotted in Figs. 4 and 5, respectively. As the toroidal angle moves from the horizontally elongated plasma position at ϕ = 18° to the vertically elongated plasma cross section at ϕ = 0° or 36°, the magnetic field structure near outboard edge X-point becomes gradually asymmetric. The reason is explained in detail in Ref. [3]. One of the two divertor legs at the outboard X-point tends to have longer L_c, i.e. upper divertor leg at ϕ = 9° in Fig. 4(a) and lower divertor leg at ϕ = 27° in Fig. 4(e).

The effect of impurity diffusion on the 2-D distribution of CIV is shown for two different $D_{Z\perp}$ values of 0.2 and 4.0 m^2/s in Figs. 5 (a)–(c) and (d)–(f), respectively. The two arrows denote the vertical observation range. It is clearly shown that the CIV emissivity at outboard side is much stronger than at inboard side in the R_{ax} = 3.90 m configuration and the CIV distributes in radially wider region when the $D_{Z\perp}$ is large. If the $D_{Z\perp}$ is larger at the shorter L_c region in the vicinity of the outboard X-point, the radially diffused carbon ions immediately move toward the divertor plates and the emission intensity is

resultantly weaker. The difference in the CIV emissivity between upper and lower sides of the outboard X-point is expressed in Figs. 5(d) and (f) which correspond to the horizontal position of Y=−140 and 140 mm in the 2-D plot, respectively. In addition, the chord integration length in CIV emissions above (below) the outboard X-point is longer than that below (above) the outboard X-point at $\phi = 16°$ ($\phi = 20°$). Therefore, the carbon intensity near outboard X-point becomes different between upper and lower sides as explained above. As a result, the CIII and CIV emissions are weaker in upper strip-shaped emission trace at Y = 140 mm and lower strip-shaped emission trace at Y = −140 mm as shown in Fig. 2, when the $D_{Z\perp}$ is large. We thus understand that the length of the emission trace seen in Fig. 2 is a function of diffusion coefficient. When we compare the CIII distribution in Figs. 2(a) −(c) with Fig. 1(a) and the CIV distribution in Figs. 2(d)−(f) with Fig. 1(b), the simulation with $D_{Z\perp} = 4.0$ m^2/s also seems to have a good agreement with the experiment.

Although the reason why the cross-field impurity transport in the fully stochastic magnetic field layer is so large is unclear at present, the Larmor radius of partially ionized carbon ions is at least larger than that of protons as the bulk ion, i.e. $\rho(C^{2+})/\rho(p) = 1.7$ and $\rho(C^{3+})/\rho(p) = 1.15$. An anomalous transport may be also important. The blob can create a perpendicular convective flux near the X-point with velocities of 0.1−1 km/s in LHD which are clearly smaller than those of the blob in tokamaks, e.g. 2.5 km/s. In addition, the direction of E×B force is frequently changeable in the stochastic magnetic field layer of LHD because the gradients of magnetic field strength and magnetic field curvature are considerably different due to the presence of helical ripple. Since the perpendicular CIV profile is symmetric as seen in Fig. 3, the particle drift does not seem to sufficiently contribute to the large impurity diffusion coefficient.

4. Summary

Two strip-shaped emission traces are appeared at upper and lower sides of X-points along the outboard edge X-point footprint in the simulation, while in the experiment only a single emission trace is observed at upper side. It is found that both the width and the length of the strip-shaped emission trace are sensitive to the impurity cross-field transport coefficient. The cross-field carbon diffusion coefficient is then analyzed from the observed width and length of the emission trace by comparing with the simulation. As a result, the cross-field diffusion coefficient of C^{3+} ions at R_{ax}=3.90m is successfully determined to be $D_{Z\perp} = 4.0$ m^2/s, while that of the bulk plasma ion is much smaller ($D_{\perp} = 0.2$ m^2/s).

Acknowledgements

This work was partly supported by Grant-in-Aid for Scientific Research (B) 16H04088 and the JSPS-NRF-NSFC A3 Foresight Program in the field of Plasma Physics (NSFC: No.11261140328, NRF: No.2012K2A2A6000443).

References

[1] S.Y.Dai, M.Kobayashi, G.Kawamura, S.Morita, et. al., Nucl. Fusion **56** (2016) 066005.

[2] H.M.Zhang, S.Morita, S.Y.Dai, T.Oishi, et al., submitted to Phys. Plasmas.

[3] S. Morita, E. H. Wang, M.Kobayashi, et al., Plasma Phys. Control. Fusion **56** (2014) 094007.

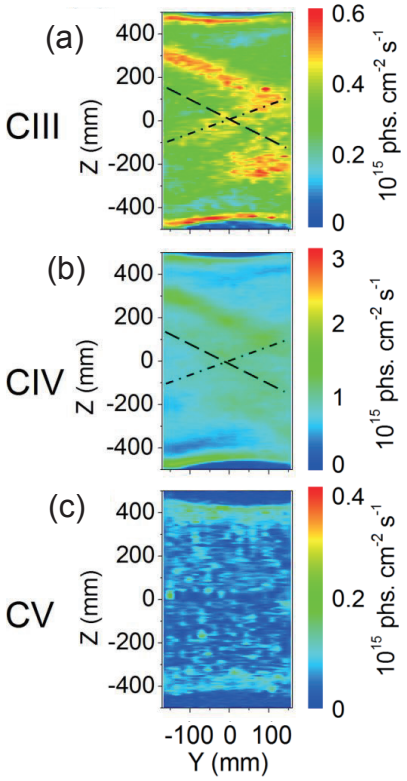

Fig.1 Measured 2-D distribution of CIII-CV.

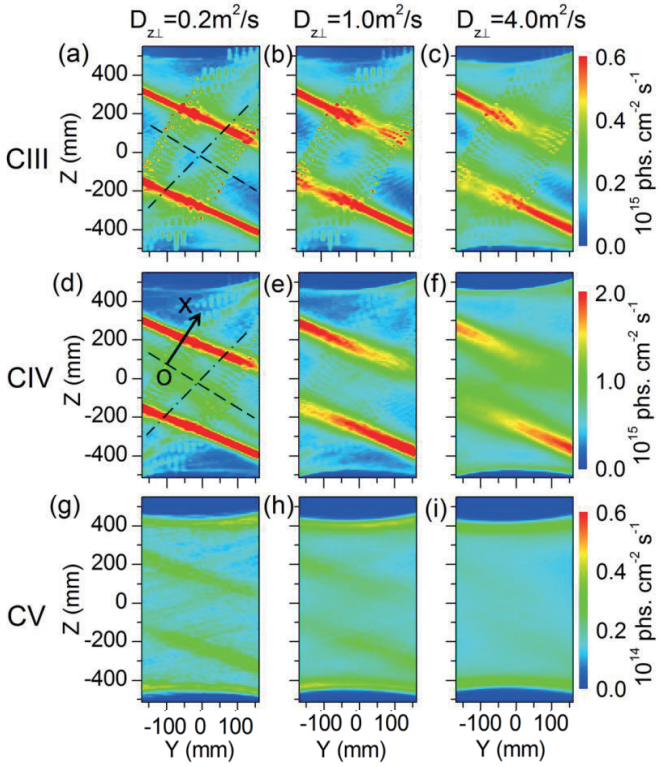

Fig.2 Simulated 2-D distribution of CIII-CV.

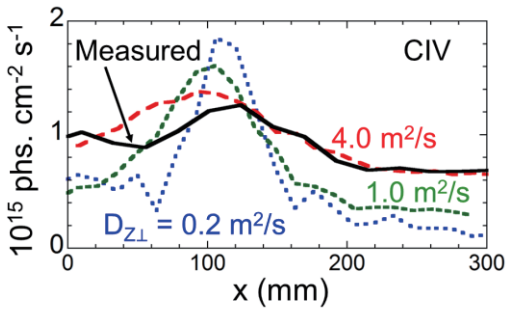

Fig.3 Measured (solid line) and simulated CIV profiles as functions of x which is denoted in Fig. 21(d).

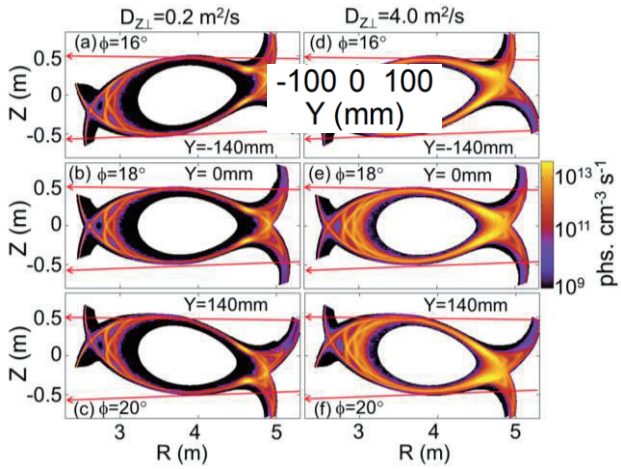

Fig.5 CIV simulation at different toroidal angles. Typical observation chords are indicated with arrows.

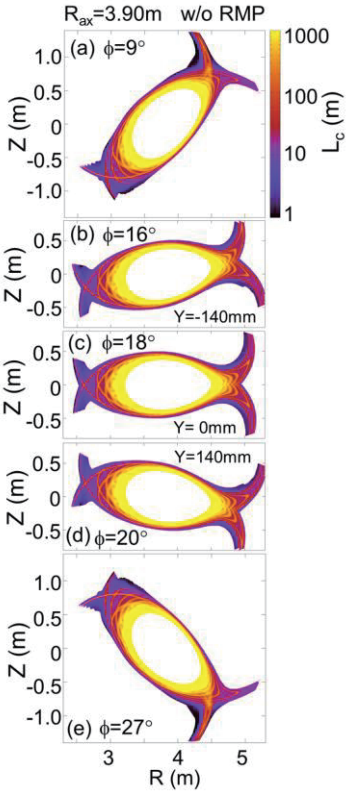

Fig.4 Connection length, L_c, in the ergodic layer at R_{ax} = 3.90 m at (a) ϕ = 9°, (b) ϕ = 16°, (c) ϕ = 18°, (d) ϕ = 20° and (e) ϕ = 27°. The positions of ϕ = 16°, 18° and 20° correspond to Y = –140 mm, 0 and 140 mm in the 2-D plot, respectively.

Impact of impurity flow on the impurity transport in the edge stochastic magnetic field layer of LHD

T. Oishi[1,2], S. Morita[1,2], S. Y. Dai[3], M. Kobayashi[1,2], G. Kawamura[1], X. L. Huang[1], Y. Liu[2], M. Goto[1,2], and the LHD Experiment Group[1]

[1]National Institute for Fusion Science, Toki 509-5292, Gifu, Japan (10.5pt)

[2]Department of Fusion Science, Graduate University for Advanced Studies, Toki 509-5292, Gifu, Japan

[3]School of Physics and Optoelectronic Technology, Dalian University of Technology, Dalian 116024, PR China

Abstract

The parallel flow of carbon impurity in a thick stochastic magnetic field layer called "ergodic layer" located at the edge plasma of Large Helical Device (LHD) is studied by space-resolved vacuum ultraviolet (VUV) spectroscopy. The result shows that (1) the carbon flow at the top and bottom edges in the ergodic layer has the same direction toward outboard side along the major radius direction and (2) the observed flow quantitatively agrees with simulation result calculated with a three-dimensional simulation code, EMC3-EIRENE. It experimentally verifies the validity of edge parallel flow driving the impurity screening.

1. Introduction

Stochastization of edge magnetic fields is extensively studied not only for the ELM mitigation but also for the plasma detachment and the impurity transport. A thick stochastic magnetic field layer called "ergodic layer" of the large helical device (LHD) consists of stochastic magnetic fields with three-dimensional structure intrinsically formed by helical coils, while well-defined magnetic surfaces exist inside the last closed flux surface [1]. It is therefore extremely important to study the impurity behaviour and transport in the ergodic layer and to compare with those in the scrape-off layer of tokamaks. In LHD, it is found that carbon impurities are screened by the presence of the ergodic layer [2]. The effect of "impurity screening" has been also compared between the scrape-off layer of a tokamak and the ergodic layer of a helical device [3]. In this study, measurement of carbon impurity flow is attempted by using a space-resolved VUV spectroscopy and relation between the flow and the impurity screening effect is discussed.

2. Impurity screening evaluated by carbon line emissions

Impurity spectroscopy was attempted in an experiment with a magnetic configuration with R_{ax} = 3.6 m and B_t = 2.75 T. Figure 1 shows a typical waveform of a

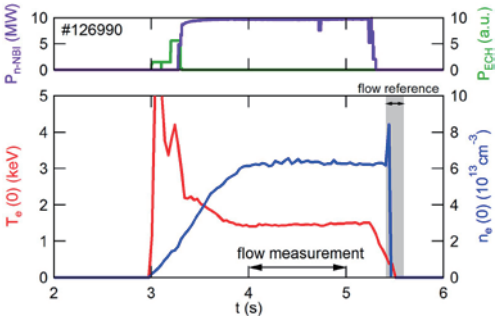

Fig. 1 Typical waveform of a discharge in which the impurity spectroscopy is attempted.

discharge. ECH and n-NBI power, central electron temperature and central electron density are shown together. The averaged electron density n_e was scanned from 1.5 to 6.5 × 10^{13} cm^{-3}. Intensities of carbon line emissions are monitored as an indicator of the impurity screening. Figure 2 shows carbon impurity lines used for evaluation of the impurity screening effect. VUV spectrum including CIII (977.03 Å, $2s^2$-2s2p) and CIV (1548.02 Å, 2s-2p) is measured using a 20 cm normal incidence VUV spectrometer [4] while EUV spectrum including CV (40.27 Å, $1s^2$-1s2p) and CVI (33.73 Å, 1s-2p) is measured using a grazing incidence EUV spectrometer [5]. The ionization potential, E_i, for C^{2+}, C^{3+}, C^{4+}, and C^{5+} is 48 eV, 65 eV, 392 eV, and 490 eV, respectively. Therefore, CIII and CIV are released from carbon ions with low E_i located at the outer region of the ergodic layer, while CV and CVI are released from carbon ions with high E_i located at inner region of the ergodic layer.

Figures 3 (a-d) show electron density dependence of line intensity of (a) CIII, (b) CIV, (c) CV, and (d) CVI normalized by the electron density, respectively. Carbon lines emitted from outer region of the ergodic layer (CIII, CIV) increase while those from inner region (CV, CVI) decrease in higher ne discharges. It indicates enhancement of the impurity screening in high density regime. A line ratio of CVI / CIV can be used as an indicator of the impurity screening effect. Figure 3(e) shows the line ratio for inward-shifted magnetic configuration with R_{ax} = 3.6 m and outward-shifted magnetic configurations with R_{ax} = 3.9 m. The impurity screening effect is more obvious in the outward-shifted configuration because of the thick ergodic layer.

3. Measurements of flow velocity of the carbon impurity

A space-resolved VUV spectroscopy was also attempted by using a 3m normal incidence VUV spectrometer [6]. Figure 4(a) shows a full vertical profile of C^{3+} impurity flow evaluated from Doppler shift of the second order of CIV line emission (2 × 1548.20 Å) at a horizontally-elongated plasma position of LHD. The poloidal flow is supposed to be derived from the observed CIV Doppler shift. At present, a spectral peak of the CIV spectrum in a recombination phase at the plasma termination is regarded as the reference of the Doppler shift because the plasma temperature is extremely low and any

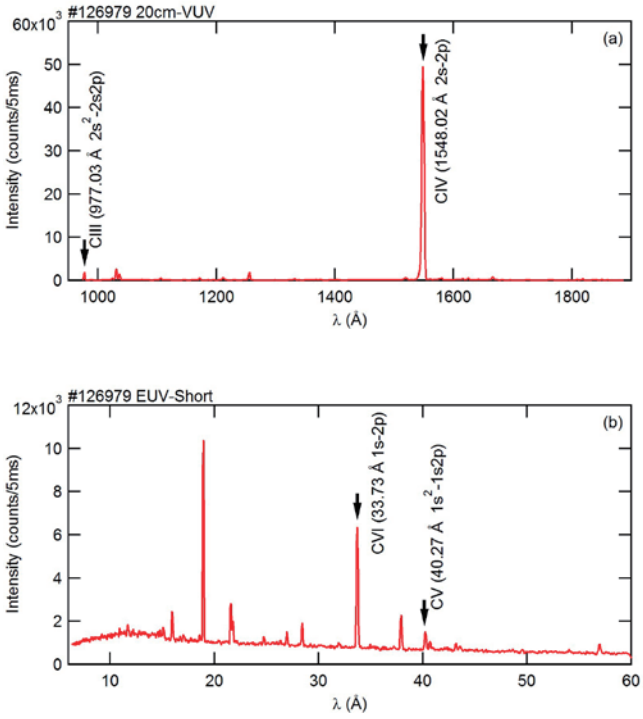

Fig. 2 Carbon impurity lines used for evaluation of the impurity screening effect. (a) VUV spectrum including CIII (977.03 Å, $2s^2$-2s2p) and CIV (1548.02 Å, 2s-2p) measured using a 20 cm normal incidence VUV spectrometer. (b) EUV spectrum including CV (40.27 Å, $1s^2$-1s2p) and CVI (33.73 Å, 1s-2p) measured using a grazing incidence EUV spectrometer.

plasma flow seems to have already disappeared. The observation range of the VUV spectroscopy is also illustrated in Fig. 4(b). Two arrows in Fig.4 (a) correspond to the observation chords located with two solid arrows in Fig.4 (b). The measured flow velocity in Fig. 4(a) is projection of the flow along the observation chord which can be approximately considered to be the direction of the plasma major radius. From the figure it is found that the flow direction is the same, i.e. the outboard direction, for both the top (Z = 480 mm) and bottom (Z = -480 mm) edges of the ergodic layer. Figure 4(c) shows the flow at the top and bottom edges of the ergodic layer as a function of density. It indicates that the flow velocity increases with the density.

The carbon flow measured with spectroscopic method for the first time is compared with the impurity transport simulation based on a three-dimensional simulation code, EMC3-EIRENE [7]. A synthetic profile of the simulated flow is also shown in Fig. 4(a) with solid line, which is obtained by integrating the Doppler-shifted CIV intensities along the observation chord. The excellent agreement between experiment and simulation in the present study concludes that the parallel flow in the ergodic layer can be well explained by the presently used theoretical modelling on the edge impurity transport. Therefore, the impurity parallel flow can be mainly determined by the momentum balance along the magnetic field line. In particular, the friction force between impurity and bulk ions and the ion thermal force driven by the ion temperature gradient are dominant terms in the momentum balance. The calculated friction force has the maximum

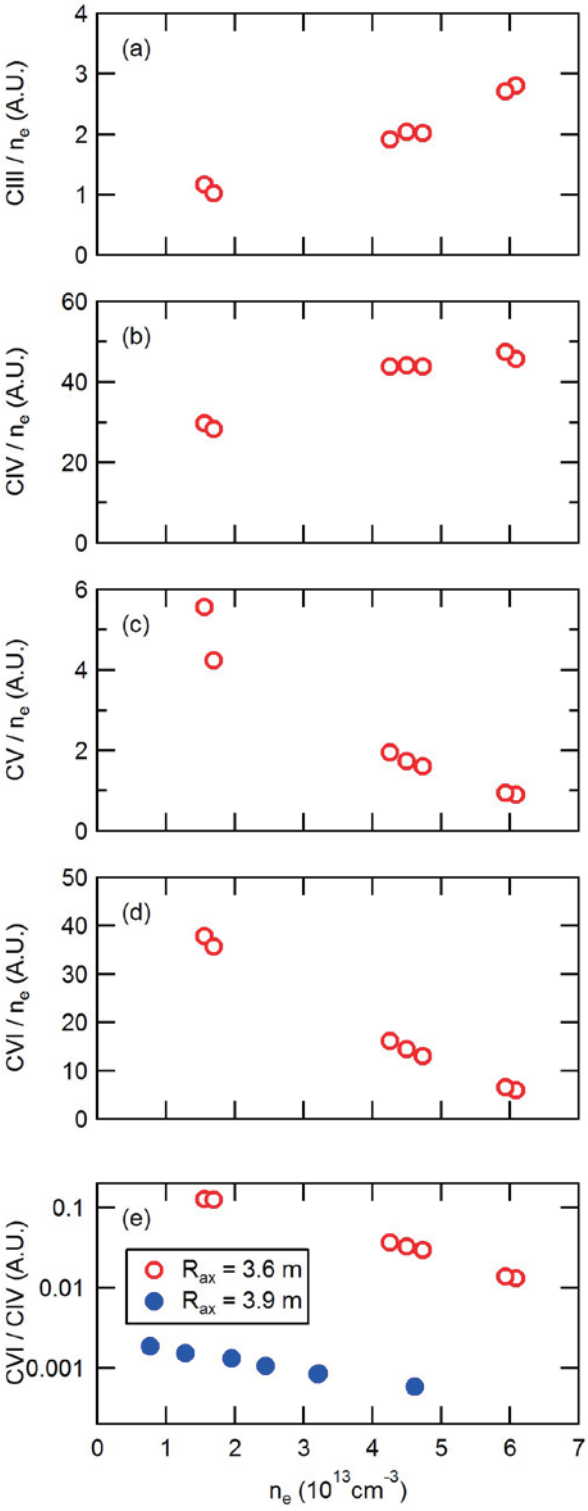

Fig. 3 Electron density dependence of line intensity of (a) CIII, (b) CIV, (c) CV, (d) CVI normalized by the electron density and (e) line ratio CVI / CIV for inward-shifted magnetic configuration with R_{ax} = 3.6 m and outward-shifted magnetic configuration with R_{ax} = 3.9 m.

value at both the top and bottom edges of the ergodic layer where the impurity parallel flow also takes the maximum value. The impurity screening driven by the friction force can be more effective at higher electron density range. The density dependence of the flow in the modelling can be also clarified by the experimental result shown in Fig. 4(c).

4. Summary

The parallel flow of carbon impurity in a thick stochastic magnetic field layer called "ergodic layer" located at the edge plasma of Large Helical Device (LHD) is studied by space-resolved vacuum ultraviolet (VUV) spectroscopy. The observed carbon flow at the top and bottom edges in the ergodic layer quantitatively agrees with simulation result calculated with a three-dimensional simulation code, EMC3-EIRENE. It experimentally verifies the validity of edge parallel flow driving the impurity screening.

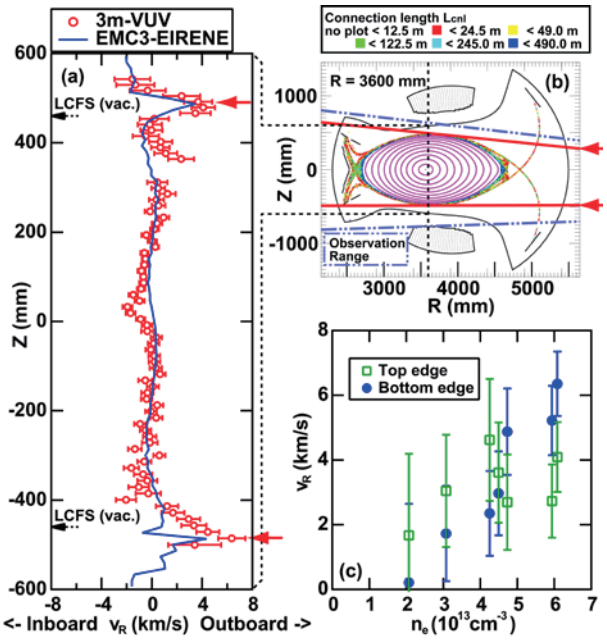

Fig. 4 (a) Vertical profile of C^{3+} impurity flow evaluated from Dopplar shift of the second order of CIV line emission (2 × 1548.20 Å) measured by VUV spectroscopy. A synthetic profile of the C^{3+} flow simulated with EMC3-EIRENE code is also plotted with solid line. (b) The observation range of the VUV spectroscopy. Two solid arrows in (a) correspond to the observation chords located with two solid arrows in (b). (c) Observed C^{3+} flow at the top and bottom edges of the ergodic layer as a function of density.

Acknowledgements

The authors thank all the members of the LHD team for their cooperation with the LHD operation. This work is partially supported by the JSPS-NRF-NSFC A3 Foresight Program in the Field of Plasma Physics (NSFC: No.11261140328, NRF: No.2012K2A2A6000443), the LHD project financial support (NIFS14ULPP010), and Grant-in-Aid for Young Scientists (B) 26800282.

References

[1] T. Morisaki, K. Narihara, S. Masuzaki *et al.*, J. Nucl. Mater. **313-316** (2003) 548.

[2] M. B. Chowdhuri, S. Morita, M. Kobayashi *et al.*, Phys. Plasmas **16** (2009) 062502.

[3] S. Morita, C. F. Dong, M. Kobayashi *et al.*, Nucl. Fusion **53** (2013) 093017.

[4] T. Oishi, S. Morita, X. L. Huang *et al.*, Plasma Fus. Res. **10** (2015) 3402031.

[5] M. B. Chowdhuri, S. Morita and M. Goto, Appl. Opt. **47** (2008) 135.

[6] T. Oishi, S. Morita, C. F. Dong *et al.*, "Appl. Opt. **53** (2014) 6900.

[7] S. Y. Dai, M. Kobayashi, G. Kawamura *et al.*, Nucl. Fusion **56** (2016) 066005.

Simulation analysis of the dust shielding effect by the ergodic layer in long pulse discharges in LHD

M. Shoji[1], G. Kawamura[1], R. Smirnov[2], A. Pigarov[2], Y. Tanaka[3], S. Masuzaki[1], Y. Uesugi[3], and the LHD Experiment Group[1]

[1]National Institute for Fusion Science, Toki 509-5292, Gifu, Japan
[2]University of California at San Diego, La Jolla 92093, CA, USA
[3]Kanazawa University, Kakuma 920-1192, Kanazawa, Japan

Abstract

The dust shielding effect by ergodic layers in the Large Helical Device is investigated by simulation analysis using an EMC3-EIRENE code coupled with a DUSTT code in three magnetic field configuration with narrow, medium, and wide ergodic layers. Simulations for iron dust emission from the surface of a helical coil can in the inboard side of the torus show that the wide ergodic layer configuration is effective to reduce the impurity (iron) ion content in the peripheral plasma in high plasma heating power conditions for higher plasma densities.

1. Introduction

Most of recent long pulse discharges in the Large Helical Device (LHD) have been interrupted by the emission of carbon or iron dusts from divertor regions or the surface on the vacuum vessel. In a long pulse discharge, a plasma termination process induced by iron dust emission was observed with a stereoscopic fast framing camera installed in an outer port. The investigation of the effect of the iron dust emission on the sustainment of the long pulse discharge is an essential issue for extending the duration time of the long pulse discharges. In order to investigate the effect of the dust emission, impurity transport simulation in the LHD peripheral plasma has been performed using a three-dimensional peripheral plasma transport code (EMC3-EIRENE) coupled with a dust transport simulation code (DUSTT).

Non-axisymmetric magnetic components produced by helical coils intrinsically form an ergodic magnetic field line structure (an ergodic layer) around the main plasma confinement region which is inside of the Last Closed Flux Surface (LCFS). This ergodic layer can be effective to protect the main plasma from the dust emission. Thus, the dust shielding effect by the ergodic layers is investigated by the simulation in three different magnetic configurations which have narrow, medium, and wide ergodic layers in the iron dust emission case.

2. Set-up for the impurity transport simulation for the iron dust emission

The EMC3-EIRENE code has been applied to investigation of the impurity transport in the peripheral plasma induced by the iron dust emission. The simulation code provides the plasma parameter profiles by solving fluid equations of 3-D flux tubes in the peripheral plasma including the transport of impurity (iron) ions along magnetic field lines with cross field diffusion, ionization and recombination terms. Figure 1

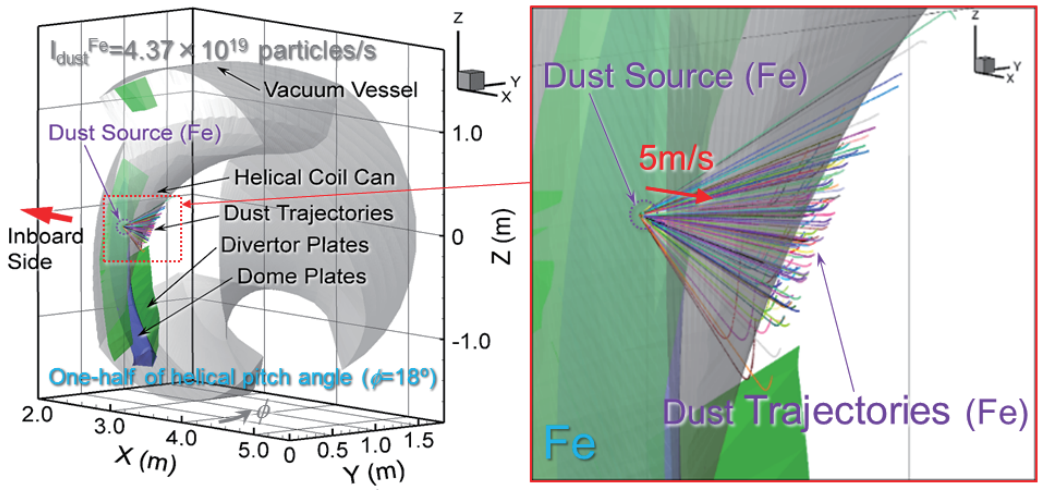

Fig.1 Three-dimensional model for impurity transport simulation for iron dust emission.

shows a three-dimensional model for the impurity transport simulation for one-half of a helical pitch angle (toroidal angle ϕ=18˚), in which some representative trajectories of iron dusts released from the surface on a helical coil can in the inboard side are indicated as thin colored lines. In this simulation, the direction of the dust emission is chosen from the cosine distribution with a velocity of 5 m/s which is the typical initial dust velocity estimated from the observations with the stereoscopic fast framing camera. The dust radius is randomly picked from a Junge distribution in the range from 1 μm to 0.1 mm, which was found by the

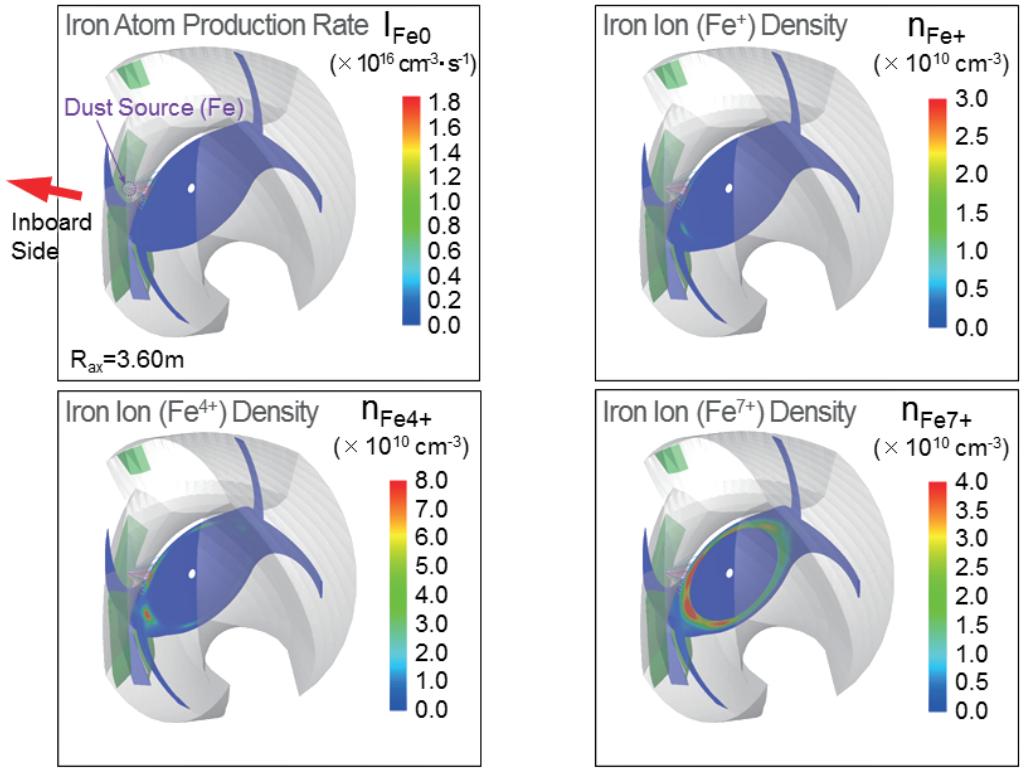

Fig.2 Calculations of poloidal cross sections of iron atom production rate and iron ion density profiles.

statistical analysis of dust sizes collected in the vacuum vessel after previous experimental campaigns.

The simulation can calculate the three-dimensional profile of the neutral iron atom production rate and the iron ion density induced by the dust emission. Figure 2 indicates poloidal cross-sections of the density

profiles of the iron atom production rate produced by evaporation of the iron dusts, and that of iron ions with three ionization stages (Fe^{+}, Fe^{4+}, and Fe^{7+}) at the toroidal position where the dust source locates. The density profile of the production rate is localized near the dust source, and that of iron ions becomes spatially distributed in accordance with the ionization stages. By these simulations, we can obtain the total impurity (iron) ion content in the peripheral plasma.

3. Investigation of the dust shielding effect by the ergodic layer

In LHD, the width of the ergodic layer can be controlled by changing the radial position of the magnetic axis R_{ax}. The total iron ion content is calculated by the simulation in the three magnetic configurations which have narrow (R_{ax} =3.60 m), medium (R_{ax} =3.75 m), and wide ergodic layers (R_{ax} =3.90 m) as shown in Figure 3 (a). Figure 3 (b) shows the dependence of the calculated impurity ion content on the plasma heating power for a low plasma density at the LCFS of 1×10^{19} m^{-3}, indicating that for the narrow ergodic layer configuration, the impurity ion content decreases with the heating power. On the other hand, for the wide ergodic layer, it significantly rises with the heating power. For the low plasma density, the wide ergodic layer is not effective to protect the main plasma from the dust emission for high heating power conditions, which is not compatible with the high performance plasma discharge operation.

The simulation can explain the decrease of the impurity ion content with the heating power for the narrow ergodic layer, which reveals that in this magnetic configuration, a thermal force dominant area is formed around the LCFS, and a friction force dominant area are formed at the outermost surface in the ergodic layer. The thermal force driven by the plasma temperature gradient causes the impurity accumulation in the main plasma, and the friction force driven by the plasma flow from the main plasma to the divertor regions induces impurity ion exhaust. In the low plasma heating power case, the position of the impurity source produced by evaporation of the iron dusts is in the middle of the ergodic layer, causing the high impurity ion content in the peripheral plasma. On the contrary, for the high plasma heating power, the impurity source locates in the friction force dominant area at the outermost surface of the ergodic layer, which contributes to the low impurity ion content in the peripheral plasma.

For the wide ergodic layer configuration, the simulation shows that the thermal and friction force dominant areas are mixed alternately in the ergodic layer. It also proves that the position of the impurity source locates in this region in both low and high plasma heating power cases. The thermal force around the LCFS is not large in the lower plasma heating power case. It contributes to the relatively low impurity ion content. On the other hand, in the high plasma heating power case, the thermal force around the LCFS is quite large, which enhances the impurity accumulation in the ergodic layer. This is a reason for the large impurity ion content in this case.

Figure 3 (c) gives the calculated impurity ion content for a medium plasma density at the LCFS of 4×10^{19} m^{-3}. The dependence on the plasma heating power is different from that in the low plasma density case, which shows that the wide ergodic layer is quite effective for reducing the impurity ion content for high plasma heating power. The simulation can explain it by the fact that the thermal force around the LCFS is small because of the low temperature gradient and the large friction force due to the increased plasma density. In addition, in the high plasma heating power case, the position of the impurity source is far

from the LCFS compared to that in the low heating power case because the radial position of the electron temperature which is enough for evaporating the iron dusts is in outer regions in the high heating power case. It is effective for reducing the impurity ion content in the ergodic layer. The simulation reveals that the wide ergodic layer configuration is effective for shielding the main plasma from the dust emission in the higher plasma density.

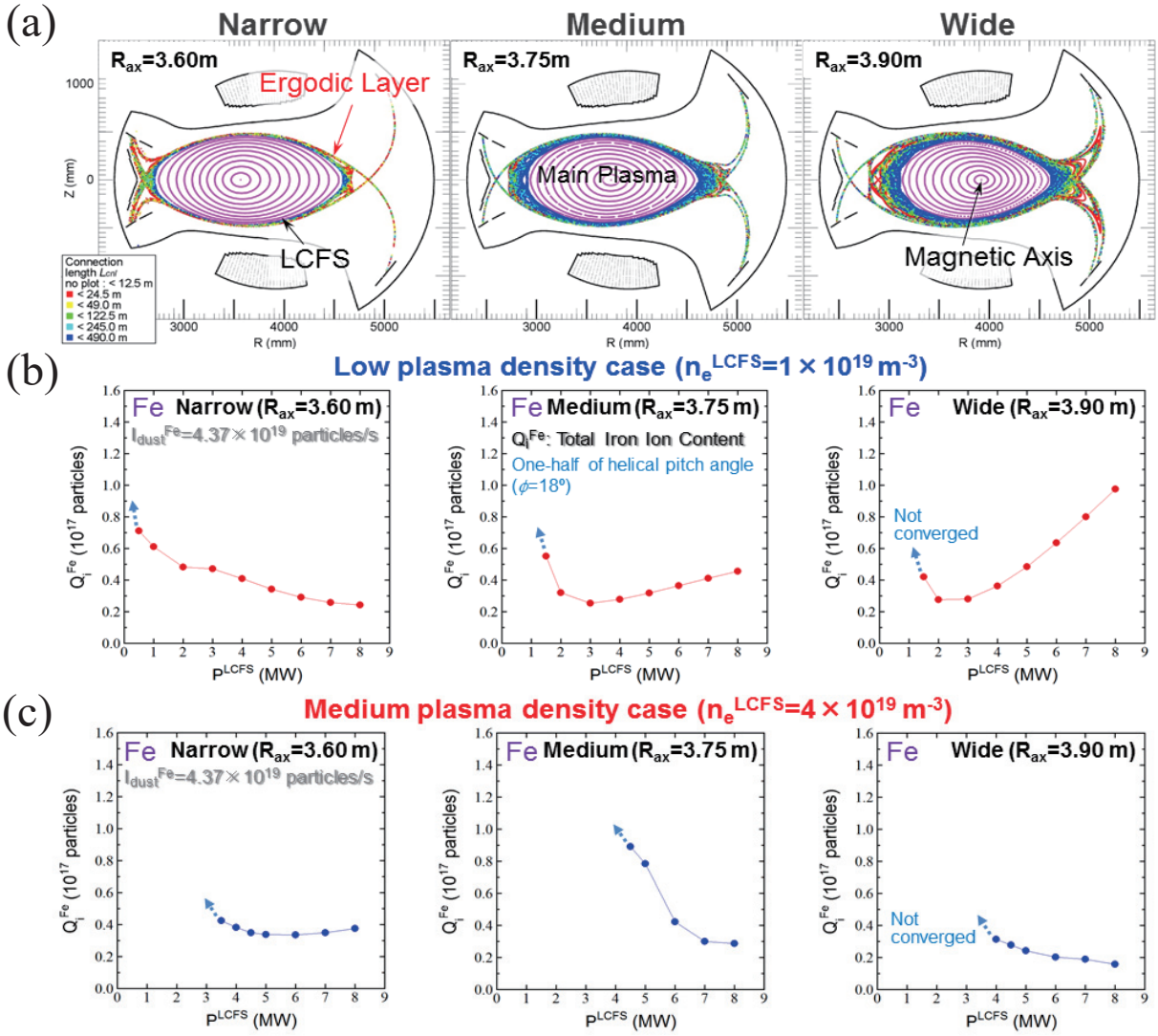

Fig.3 Poloidal cross sections of the magnetic field lines in three magnetic configurations with narrow, medium, and wide ergodic layers (a). The dependence of the total iron ion content in the peripheral plasma on the plasma heating power in the three magnetic configurations for n_e^{LCFS}=1×10^{19} m^{-3} (b) and 4×10^{19} m^{-3} (c).

Acknowledgements

This work is financially supported by a NIFS budget (NIFSULPP015) and is performed with the support and under the auspices of the NIFS Collaboration Research program (NIFS12KNXN236) and NIFS/NINS under the project of Formation of International Scientific Base and Network (KEIN1111). This work is partly supported by the JSPS-NRF-NSFC A3 Foresight Program in the field of Plasma Physics (NSFC No.11261140328) for studies on critical physics issues specific to steady state sustainment of high-performance plasmas. One of the authors (M.S.) is grateful for the computational resources of the LHD numerical analysis server and the plasma simulator in NIFS.

Predictive modeling for performance assessment of ITER-like divertor in China Fusion Engineering Testing Reactor

F.Q. Wang[1], Y.P. Chen[2], L.Q. Hu[2], Z. P. Luo[2], G.Q. Li[2], H.Y. Guo[2, 3, 4], M.Y. Ye[4]

[1] Department of Applied Physics, Donghua University, Shanghai 201620, China
[2] Institute of plasma physics, Chinese academy of sciences, Hefei 230031, China
[3] General Atomics, P.O. Box 85608, San Diego, California 92186, USA
[4] School of Nuclear Science and Technology, University of Science and Technology of China, Hefei 230027, China

Abstract

To facilitate the design of the China Fusion Engineering Testing Reactor (CFETR), predictive modeling for the assessment and optimization of the divertor performances is an indispensable approach. This paper presents the modeling of the edge plasma behaviors as well as the W erosion and transport properties in CFETR with ITER-like divertor by using the B2-Eirene/SOLPS 5.0 code package together with the Monte Carlo impurity transport code DIVIMP. As expected, SOLPS modeling of divertor-SOL plasmas finds that the peak heat flux onto the divertor targets greatly exceeds 10MW/m^2, an engineering limit posed to the steady-state and/or long-pulse operation of the next-step fusion devices, for a wide range of plasma conditions, and thus modeling of Ar puffing by scanning the puffing rate for radiative divertor is performed. As the increase of the Ar puffing rate, the peak target heat fluxes and plasma temperature decreases exponentially, reflecting that Ar puffing is highly effective at power exhausting. Based on the ion fluxes from SOLPS, the W erosion is calculated by taking into consideration the bombardment of both D and Ar ions, and then the W plasma concentrations are calculated based on the W erosion fluxes using DIVIMP. The calculations show that if the Ar puffing only being used to reduce the divertor heat load, the W plasma contamination in the core plasma is a little bit high, which demonstrates that some further upgrading of the divertor geometry is still needed.

1. Introduction

Currently, the China Fusion Engineering Testing Reactor (CFETR), which has a sketch shown in figure 1, is under design. This device is expected to bridge the gap between ITER and DEMO. As a fusion test reactor providing technical support for DEMO, CFETR is designed for steady-state or long-pulse operation with the duty-cycle time $\geq 30\% \sim 50\%$, demonstrating deuterium (D) and tritium (T) fusion energy production with a typical fusion power of 50-200 MW. Although this device is designed with goals different from ITER, ITER can be a good basis for it both on burning plasma physics and some technologies in the steady-state operation [1].

As a key component in the tokamak device, the divertor should be carefully designed and built to get the access to regimes with low power load onto the divertor target and acceptable divertor erosion and to achieve sufficient particle removal capability [2], especially for the next-step fusion devices, such as ITER and CFETR. For this reason, several divertor concepts for CFETR are currently under investigation, including the standard vertical target configuration, as adopted by ITER, and the advanced divertors such as snowflake [3] and super-X [4] configurations. ITER-like divertor with low single null (LSN) configuration appears to be the possible option for CFETR from viewpoints of the engineering accessibility as well as the particle

[a)]Email:wangfq@ipp.ac.cn

and heat flux controllability. Moreover, investigating ITER-like divertor for CFETR can give the opportunity to make the most of ITER physics and engineering basis for the divertor and steady-state operation.

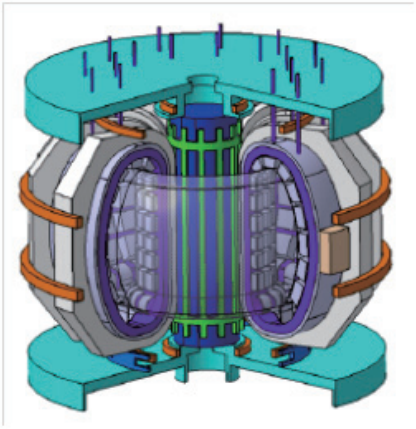

Fig. 1 The sketch of CFETR

Predictive modeling of divertor-SOL plasma and impurity behaviors is considered as an effective and indispensable approach to the determination of the divertor operation scenario and optimization of the divertor design for the next-step fusion devices, such as ITER and DEMO [5-11]. To understand the overall divertor-SOL behaviors in tokamaks, three main components, i.e. the background plasmas,, the neutrals, including both the hydrogen and impurity neutrals, as well as the impurity ions, should be simultaneously taken into consideration. Meanwhile, due to the quite different behaviors of these three components in the tokamak edge, generally, different transport models have to be chosen for them in the divertor-SOL modeling processes. SOLPS [12-14] code, which couples the plasma multi-fluid code B2 [13-15] to the Monte Carlo neutral transport code Eirene [16. 17], is able to treat the complex atomic physics processes as well as complicated geometries involved and has been validated against an extensive set of experimental measurements [13]. Thus, this code is widely used in the predictive modeling for the assessment and optimization of the divertor performances in the next-step fusion devices [7-11]. The DIVIMP impurity transport code [18, 19] has been developed with accessibility to modeling the impurity behaviors in SOLPS-generated plasma conditions by launching a large amount of test particles, typically 10000, into the SOLPS given plasma and then tracing the states and orbits of these particles. Therefore, the erosion of the target material, which is expected to be Tungsten (W) for CFETR, and the transport properties of the W impurities sputtered from the divertor targets can be modeled based on the plasma conditions constructed by the SOLPS code.

This paper presents the SOLPS modeling of the divertor-SOL plasma behaviors with and without impurity seeding and the DIVIMP modeling of W impurity transport properties in CFETR. Section 2 illustrates the basic divertor-SOL plasma behaviors in CFETR with ITER-like divertor. Section 3 presents the detailed effects of Ar puffing at the reduction of the peak heat load on the divertor targets. Section 4 gives some prediction of the target erosion and the W impurity transport properties. Finally, the summary and conclusions are given in section 5.

2. Edge plasma density scan for the survey of different divertor operation regimes

2.1 Simulation details

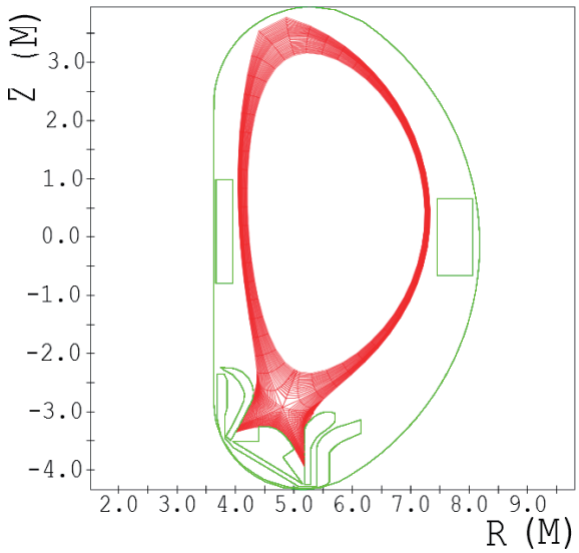

Fig. 2 Grid used for the simulation

Table I. Main design parameters for CFETR

Parameters	Expected values
Major radius R (m)	5.7
Minor radius a (m)	1.6
Toroidal field B_t (T)	5.0
Plasma current I_p (MA)	8-10
Elongation κ	1.9-2.0
Triangularity δ	0.4-0.8
Fusion power P_{fus} (MW)	200
Heating and driving power P_{aux} (MW)	60
Duty cycle	30%~50%
Tritium breeding ratio (TBR)	>1

CFETR is designed with the main parameters shown in table 1 [1], from which the expected maximum fusion power, P_f, is 200MW and the auxiliary heating power, P_{aux}, is 60MW. Thus, the power flow into the scrape-off layer (SOL) is estimated to be ~80MW, assuming that 20% of the total heating power ($P_\alpha + P_{aux}$) is radiated as bremsstrahlung and cyclotron radiation in the core. Where P_α is the heating power given by the helium particles, ~20% of the fusion power. Predictive modeling for finding a divertor most effective at handling such a large power has been carried out. Since P_{SOL}/R~ 14 MW/m, a measure of required power handling capability, is similar to that of ITER, the modeling of edge plasma and impurity behaviors has been deliberately carried out for CFETR with an ITER-like low single null (LSN) divertor configuration. Figure 2 shows the grid used for the simulation. From figure 2, the calculation region extends from the SOL, which is generally defined as the region of open magnetic field lines outside the separatrix established by a diverting magnetic field [20], to a small portion of the core. That is, the calculation region includes the whole private flux zone (PFZ), the SOL and the outer core.

First, basic behaviors of the divertor-SOL plasmas have been predicted by SOLPS modeling. The particle species considered in the simulation are electrons (e^-), D^0 atoms and D^+ ions

(representing both D and T). In SOLPS modeling, the 2-D fluid models in B2 are used for the electrons and ions, and the Monte Carlo code, Eirene, is for neutral transport, in consideration of all the detailed atomic processes, such as ionization, recombination and charge-exchange. The hydrogenic species related atomic reactions considered in the simulations are listed in table 2, from which some additional models are also considered in this work apart from the default ones in EIRENE. The additional reactions are considered to be key processes responsible for the divertor detachment, without which detachment cannot be achieved even at a very high plasma density in the modeling [21].

Table 2. Hydrogen species related atomic reactions considered in this work

Default reactions	Additional reactions
1) $D^0 + e \rightarrow 2e + D^+$	
2) $D^+ + D^0 \rightarrow D^0 + D^+$	
3) $D_2 + e \rightarrow 3e + 2D^+$	1) $D_2 + e \rightarrow 2e + D_2^+$
4) $D_2 + e \rightarrow e + 2D^0$	
5) $D_2 + e \rightarrow 2e + D^+ + D^0$	2) $D^+ + e \rightarrow D^0$
6) $D_2 + D^0 \rightarrow D^0 + D_2$	
7) $D^+ + 2e \rightarrow e + D^0$	

In the calculations, boundary conditions at the core-edge interface, the wall, the inner boundary of the Private flux zone (PFZ), and the divertor targets need to be specified [23, 24]. At the core-edge interface, the power flux is fixed at 80MW, including both the ion and electron channels, assuming that T_e=T_i at the core-edge interface. To achieve different regimes of the divertor operation, the core-edge interface D^+ density n_u, which is usually has a linear relation with the line-averaged plasma density $\overline{n}_e$ [25], is selected as a key control parameter and varied from 1×10^{19} to 5×10^{20} m^{-3}. Because of the relatively high temperature and strong ionization at the core-edge interface, density of D^0 is estimated to be very low, and thus particle flux of D^0 at the interface is assumed to be 0. When the plasma ions strike at the wall or target surfaces, the recycling coefficient of the ions to neutrals is set to 1.0. At the divertor target, the plasma flow velocity V_T is assumed to be ion-sound speed. The total heat flux onto the divertor target *fht* is given by:

$$fht = fhpe + fhpi + fhme + fhe + fhmi + fhi + fhj \quad (1)$$

from which, the total target heat flux consists of the target flux of the potential energy released from the electrons (*fhpe*) and ions (*fhpi*), the kinetic energy of the electrons (*fhme*) and (*fhmi*), the electric heat energy fhj, as well as the heat flux of electrons (*fhe*) and ions (*fhi*). More detailed description of these components of the target heat flux can be seen in reference [24].

Transport parallel to **t**he magnetic field line is assumed to be classical but flux limited. The cross-field particle and heat fluxes are given by:

$$\Gamma_\perp = D_\perp \frac{dn}{dr} + nV_{pinch} \quad (2)$$

$$q_\perp = -n\chi_\perp \frac{dkT}{dr} + \frac{5}{2}\Gamma T \quad (3)$$

nV_{pinch} and $\frac{5}{2}\Gamma T$ are convective particle and heat fluxes, respectively. Although convective transport is important in the edge plasma, due to no reliable theory for magnitude of the 'inward pinch velocity', V_{pinch} is set to 0 for the predictive modeling presented in this paper. Meanwhile, the cross-field drifts are not included in the simulation. $D_\perp \frac{dn}{dr}$ and $-n\chi_\perp \frac{dkT}{dr}$ are conductive particle and heat fluxes respectively. Due to the lack of the reliable physical models, the cross-field heat and particle diffusivities are usually assumed to be constant, which is considered to be the simplest and appropriate approximation introducing the least variables [8]. It is remarkable that, generally, the constant transport coefficients correspond to the L-mode, while the next-generation tokamak device are supposed to operate in the H-mode regime in which the transport coefficients may drop at some region, e.g at the edge transport barrier, typically located several centimeter inside the separatrix [26]. The modeling of H-mode operation regimes, which is not the concentration of this paper, will be performed and reported on latter. Typically, similar to that for ITER [13], assumes that the anomalous particle diffusivity, $D_\perp$=0.5 m^2/s, and the thermal heat diffusivities, $\chi_{\perp i} = \chi_{\perp e} = \chi_\perp$=1.0 m^2/s.

2.2 Main properties of the divertor-SOL plasmas

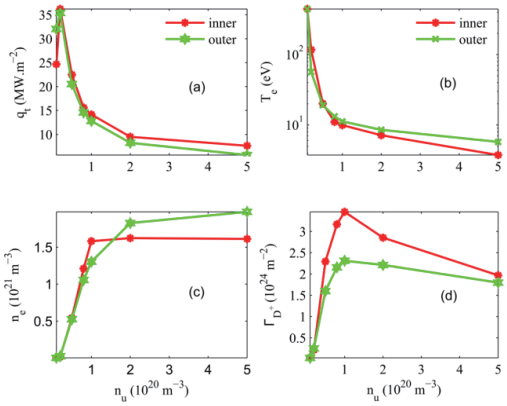

Fig. 3 Peak values of the plasma parameters at the divertor targets versus the plasma density

Basically, the divertor exhibits three different regimes, i.e., sheath-limited (low recycling), conduction-limited (high recycling), and detached divertor regimes, which are largely determined by the classical transport along the magnetic field [20]. To fully investigate the divertor-SOL plasma behaviors in all the three divertor regimes, SOLPS modeling with assumptions presented in the previous part has been carried out for CFETR. at the core-edge interface

Figure 3 shows the peak values of the target plasma conditions, including the electron density, n_e, and temperature T_e as well as the particle and heat flux density, Γ_{D^+} and q_t, verse n_u. This figure encompasses all the three divertor regimes:

(a) Sheath-limited regime: As is demonstrated in subplot (c) and (d) of figure 3, the divertor plasma is in the sheath-limited regime with low core-edge plasma density, i.e. $n_u<2\times10^{19}m^{-3}$. From these two subplots, both the peak target plasma density and D^+ target flux density increase linearly with the upstream density, which is a characteristic of the sheath-limited regime also presented in reference [20]. Additionally, as is shown in subplot (a) of figure 3,

peak values of the target heat flux q_t tends to increase as the increase of the upstream density due to the increase of the ion flux density.

(b) Conduction-limited regime: As the upstream density increases, the divertor plasma gradually enters the conduction limited regime. From figure 3, the target plasma density and the D^+ ion flux density increase more rapidly than that in the sheath-limited regime and the peak heat flux tends to decrease. However, even when the upstream plasma density is as high as $1\times10^{20}m^{-3}$, the peak heat flux onto the divertor target is still much higher than $10MW/m^2$, which is a limit posed by engineering to the fusion devices. Moreover, the divertor plasma, still, doesn't enter detachment when the upstream plasma density is as high as $1\times10^{20}m^{-3}$, as is evidently manifested by the increasing tendency of the D^+ flux density shown in the subplot (d) of figure 3.

(c) Detachment: When the upstream density is, further, increased to be comparable to or higher than $2\times10^{20}m^{-3}$, the divertor plasma enters partially detachment, where plasma density at the target and D^+ target flux density saturates and starts to fall, near the strike points at both the inner and outer divertors. To illustrate, figure 4 shows the profiles of the pressure, p, target electron temperature T_e, D^+ flux density Γ_{D^+}as well as the heat flux onto the divertor targets q_t for $n_u=2\times10^{20}m^{-3}$ and $n_u=5\times10^{20}m^{-3}$ respectively. As can be seen from figure 4, the peak heat flux onto the divertor target decreases to below $10mw/m^2$ when the n_u is increased to be higher than $2\times10^{20}m^{-3}$. The degree of the detachment (DOD) increases as the increase of n_u and the divertor plasma region in detachment regime extends from the strike point region outwards, but it is still impossible to enter full detachment when the upstream density is as high as $5\times10^{20}m^{-3}$.

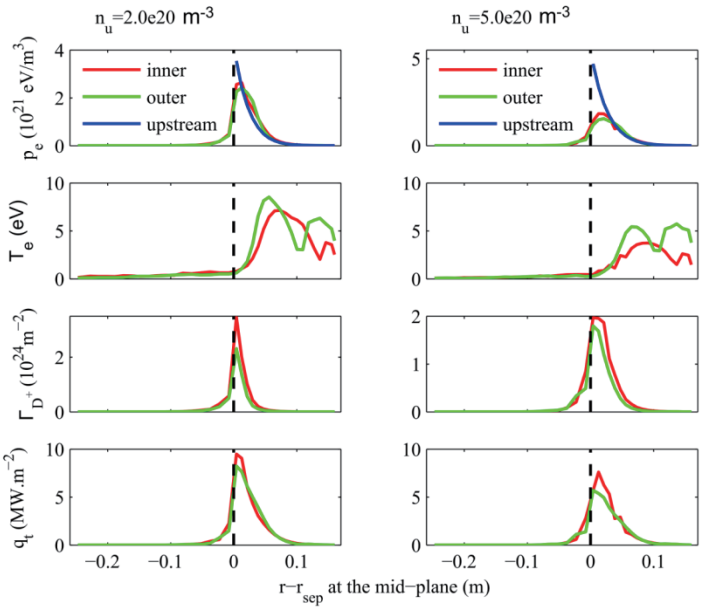

Fig. 4 Electron pressure, p_e, for the upstream and target plasmas, as well as the electron temperature, T_e, and the heat flux at the divertor target plate, q_t, versus the distance from the separatrix, mapped to the mid-plane, for the edge density $n_u = 2\times10^{20}$ m^{-3}

Actually, the upstream density n_u has to satisfy the density-limit criteria related to stability and the Greenwald density limit is the maximum line-average density to reach [27]. For CFETR with design parameters shown in table 1, the estimated tolerable maximum line-average density is

given by

$$\bar{n}_e^{max}[10^{20}\ m^{-3}] = \frac{I_p}{\pi a^2} = \frac{10}{3.14\times 1.6^2} \approx 1.24. \quad (4).$$

Generally, the line-average density $\bar{n}_e$ has a linear relationship with the core-edge plasma density n_u for a given magnetic configuration [24], e.g. as given by [25]

$$n_u = 0.0023\bar{n}_e^{1.08}\kappa^{1.1}B_\phi^{0.78} \quad (5)$$

Where κ is the plasma elongation and B_ϕ is the toroidal magnetic field in Tesla. Both n_u and $\bar{n}_e$ are expressed in m^{-3}. Thus, it is estimated that for CFETR in the steady-state operation, n_u has to be kept below ~$9\times10^{19}m^{-3}$ to prohibit instability. In that case, the peak heat flux onto the divertor target, which is a critical issue for the steady-state operation of the next-step fusion devices, will become much higher than 10 MW/m^2. Moreover, in the operation regimes with smaller transport coefficients than those used in simulations presented in this paper, the resulting density and temperature profiles along the divertor target plates should be much narrower and the heat load density at the target plates would be even larger [28]. That is, to achieve steady-state operation, some measures, such as impurity seeding and upgrading of the divertor geometry, should be taken to reduce peak heat load on the divertor targets.

3. Argon (Ar) puffing for radiative divertor operation

3.1 Simulation details

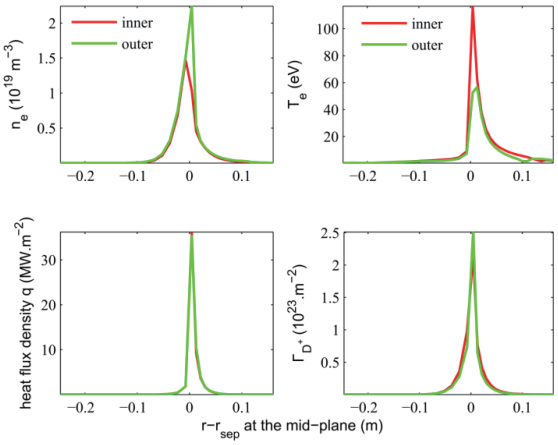

Fig. 5 SOLPS calculated Target conditions for the case with the density at the core-edge interface $n_u = 2.0\times10^{19}$ m^{-3}

Impurity seeding has been adopted as a common technique for stationary heat flux control in present tokamak experiments, and is foreseen for ITER [29, 30]. The widely used Monte Carlo impurity transport code, DIVIMP, has previously been developed to investigate the fine details of impurity transport in given plasma conditions [18, 19]. That is, generally, detailed effects of impurities on the background plasma can't be considered in DIVIMP. To survey the effects of gas puffing on the plasma performances of CFETR with ITER-like divertor, SOLPS code is also chosen for the modeling of divertor-SOL plasma behaviors with argon (Ar) puffing and then the erosion of target material, which is expected to be tungsten (W), as well as the transport properties of W impurity are predicted by DIVIMP code based on the SOLPS-generated plasma conditions. This section only focuses on the former part, i.e. the SOLPS modeling of Ar puffing to increase

divertor radiation and promote plasma detachment to achieve realistic divertor heat loads. The W erosion and transport behaviors will be concentrated on in the next section.

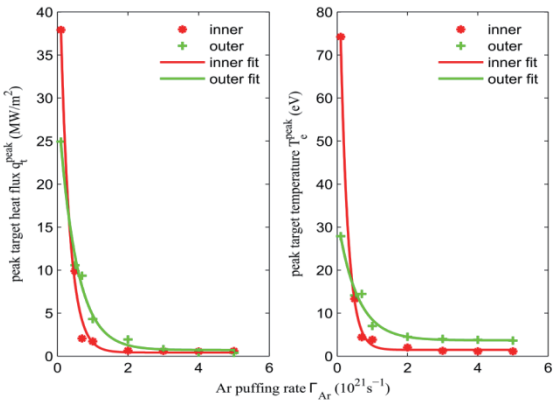

Fig. 6 Peak divertor heat flux and temperature as functions of the Ar puffing rate

In the modeling, Ar puffing is introduced from the top. Since low edge densities are desirable for efficient current drive and good confinement, the modeling is focused on a case with relatively low edge density, *i.e.*, $n_u = 2\times10^{19}$ m^{-3}, which should also keep the plasma away from the density limit discussed in the last section. Figure 5 illustrates the target plasma conditions, including the plasma density n_e, temperature T_e, as well as the density of heat and D^+ flux, q_t and Γ_{D^+}, for $n_u = 2\times10^{19}$ m^{-3} without Ar puffing introduced, from which the plasma temperature at the divertor target and the target heat flux are both too high to be tolerable for the divertor operation. The puff rate Γ_{Ar} is varied from 1.0×10^{20}/s to 5.0×10^{21}/s to cover the detailed processes of plasma detachment promoted by Ar puffing. In addition, the amount of Γ_{Ar} is initially specified by comparing with the integrated steady-state target D^+ ion fluxes 5.7×10^{23}/s, and thus is considered to be appropriate for avoiding impurity contamination. Behaviors of the neutral such as D^0 and Ar^0 are handled by the 3-D Monte Carlo neutral transport code EIRENE, and the transport properties of the electrons and ions from both D and Ar are modeled by the multi-fluid code B2.

3.2 Results and discussions

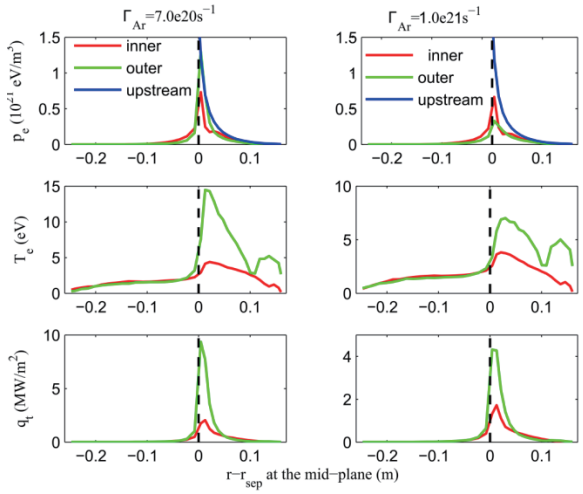

Fig. 7 The pressure profiles at the targets and upstream, the target T_e and ne profiles for $\Gamma_{Ar} = 7.0\times10^{20}/s$ and $\Gamma_{Ar} = 1.0\times10^{21}/s$, respectively.

Ar puffing at the top of the device is found to be an effective approach to reduce the power load onto the divertor target. As is shown in figure 6, the peak heat flux density and target temperature decay exponentially with the increase of Γ_{Ar}. From figure 6, heat flux onto the inner target tends to decay more rapidly than that onto the outer target, and, also, the plasma temperature T_e at the inner target tends to decrease more rapidly than plasma temperature at the outer target. To reduce peak value of the target heat flux density to below 10MW/m^2, the minimum puffing rate needed is 5.0×10^{20}/s. Plasma at the inner target exhibits partial detachment when Γ_{Ar} is increased to 7.0×10^{20}/s, which is manifested by the significant drop of the pressure at this position, while plasma at the outer target exhibits partial detachment when the Γ_{Ar} is increased to 1.0×10^{21}/s. Figure 7 displays the pressure, p. profiles at the targets and upstream, the T_e and q_t target profiles for $\Gamma_{Ar} = 7.0\times10^{20}/s$ and $\Gamma_{Ar} = 1.0\times10^{21}/s$, respectively. When the Ar puffing rate is further increased to 5.0×10^{21}/s, both the inner and the outer targets enter full detachment and T_e at the both targets decease to ~1 eV. The Ar concentration at the core-edge interface (inner most of the computational grid) is less than 5% even when the puffing rate is increased to 5.0×10^{21}/s, indicating strong divertor screening for Ar.

Although Ar puffing can effectively reduce the target power load and temperature, which is assumed to reduce the sputtering yield, this process introduces Ar^{X+} ions into the plasma, which dominant the erosion of the target material due to the relatively heavy mass and high Z of Ar^{X+} ions. To estimate the detailed effect of Ar puffing on the erosion of W as well as the W impurity transport properties in CFETR with ITER-like divertor, DIVIMP modeling has been carried out and is presented in the next section.

4. W erosion and plasma density

4.1 Simulation details

To realize steady-state or long-pulse operation, the following requirements for acceptable divertor operation have to be satisfied:

Peak heat load on targets $q_t^{peak} < 10MW/\mathrm{m}^2$

Average density of core plasma $\bar{n}_e \lesssim 1.24\times10^{20}m^{-3}$

In additional, for the tungsten (W) plasma facing components (PFCs), W erosion should be kept in a tolerable level so that the W plasma concentration in the core plasma could be comparable to or below ~10^{-5} m^{-3}, which is the maximum allowable core W concentration to avoid excessive radiation in the core. To fully explore the possibility of Ar puff in CFETR, besides the SOLPS modeling of divertor-SOL plasmas with/without Ar puffing, DIVIMP modeling for predicting the W erosion and plasma density has been carried out, taking into account the impact of both the D^+ and Ar^{X+} ions on the divertor targets simultaneously.

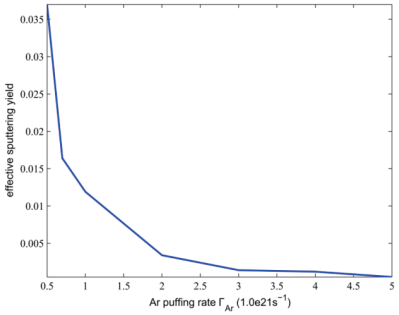

Fig. 8 The effective sputtering yield caused by Ar^{X+} verses the Ar puffing rate

CFETR is expected to be manufactured with W plasma facing components, PFCs, including the divertor and main wall. DIVIMP was initially designed to simulate the erosion and transport of C in divertor and SOL regions of tokamaks. Meanwhile, it can only treat erosion at the divertor targets and is limited to one incident eroding and one target/impurity. Therefore, W erosion at the main wall, which is not part of DIVIMP's calculation grid, is not handled in this paper. Another important thing to be noted, the erosion of W by Ar^{X+} ions [31] cannot be directly handled by DIVIMP, and thus it has to be calculated in a separated step, while that is not the same case for W erosion by D^+ ions, which can be .directly calculated by DIVIMP. Besides, the W self-sputtering is taken into consideration and is handled automatically by DIVIMP.

Most of the erosion occurs through highly charged Ar ions and D only contributes through its charge exchanging species due to the low temperature at the divertor. Based on the SOLPS-calculated Ar^{X+} and D^+ fluxes onto the divertor targets, the W erosion flux was calculated using the energy dependence of sputtering yield given by Eckstein and Preuss [32] which gives generally a better description of the available yield values [33] The impact energy of an incident ion with charge state q was given by equation (6) [20].

$$E_{iMP} = 3qT_e + 2T_i \qquad (6)$$

The target temperature was also directly taken from SOLPS calculation. The launch probabilities of W impurity along the divertor targets were calculated based on the calculated W erosion flux along the divertor targets and were input into DIVIMP, and then W atoms are launched as neutrals with a spatial distribution according to these input probabilities.

The W atoms are launched from the divertor targets with the initial velocity, *v*, and angle to the target normal, θ, given by[34]

$$\mathrm{v} = \sqrt{\frac{2E_{bind}}{m_t}}\frac{1}{(1/\sqrt{\varepsilon})}\sqrt{\{\cos(\beta)^2 + [\sin(\beta)^2 cos(\varphi)^2]\}} \qquad (7)$$

$$\theta = tan^{-1}(tan(\beta)\cos(\varphi)) \qquad (8)$$

where $\beta = sin^{-1}(\sqrt{\alpha})$, $\varphi = \pi\eta$, E_{bind} is the binding energy of the target material, and m_i is the atomic mass of the target material. The parameters α, $\eta \in [0,1]$ and $\varepsilon \in [0, max]$ are random numbers, where *max* corresponds to the maximum energy of the sputtered particles. Once the launched impurity neutrals are ionized, the along-field and cross-field motion are considered separately. The along-field forces include the impurity pressure gradient force, which is modelled as parallel-to-B diffusion, background friction force, electrostatic force and temperature forces from electrons and ions. The cross-field motion is assumed to be anomalous with diffusion coefficient $D_\perp = 1.0m^2/s$. Physical processes such as ionization, recombination, and charge exchange of W impurities are taken into consideration simultaneously in the modeling, and the relevant atomic data is taken from ADAS [22].

4.2 Results and discussions

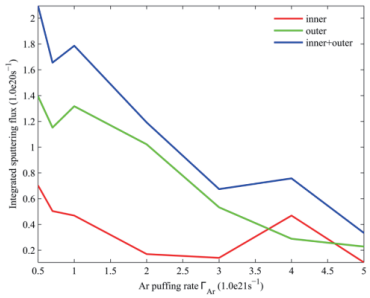

Fig. 9 The W erosion flux (s^{-1}) at the inner target and outer target as well as the total of that at both the targets for different Ar puffing rates.

Figure 8 shows the effective sputtering yield, which is defined as the mean number of W atoms removed from the surface of the W target per incident ion , caused by Ar^{X+} for different Ar puffing rates. From figure 8 the sputtering yield decreases from several percent to ~10^{-4} when Γ_{Ar} is increased from $5.0\times10^{20}s^{-1}$ to $5.0\times10^{21}s^{-1}$. The introduction of Ar^{X+} ions could result in an increase of W erosion due to their higher mass and potentially higher impact energy compared with D. However, this increase in erosion could be compensated by the reduction in plasma temperature due to radiation cooling by Ar^{X+} ions. The W erosion flux is the total result of these two effects. Figure 9 shows the evolution of total W sputtering flux (s^{-1}), which is integrated along the divertor target, as a function of Γ_{Ar}. When the puffing rate is low, e.g. $\Gamma_{Ar} = 5.0\times10^{20}/s$, due to the relatively high temperature and thus the relatively high sputtering yield, the total W erosion flux at both the inner and outer targets is as high as $\sim2.1\times10^{20}s^{-1}$, while when the Ar puffing rate is increased to $5.0\times10^{21}/s$, the W erosion flux decreases to $\sim3.0\times10^{19}/s$.

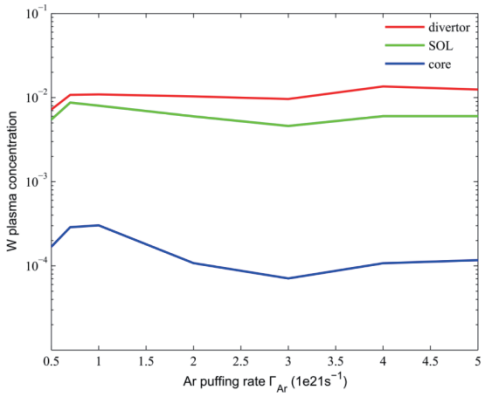

Fig. 10 DIVIMP calculated W plasma concentrations in the core plasma, the main SOL and the divertor respectively

Figure 10 shows the estimated W plasma concentration from DIVIMP calculation for different puffing rates Γ_{Ar} in the regions of divertor, main SOL and core respectively. From figure 10, the W plasma concentrations corresponding to these puffing rates are of the order of ~10^{-5}-10^{-4} for the core plasma (inner most of the calculation grid to the separatrix) and are of the order of 10^{-3} in the main SOL (separatrix to the outer boundary of the calculation region). In the divertor region the concentration is in the order of 10^{-2}. From figure 10, the resultant W concentrations corresponding to all the Ar puffing rates are estimated to be a little bit high to be

acceptable for the CFETR operation, which means that using the approach of Ar puffing to reduce the peak heat load onto the divertor target may causes intolerable W erosion and plasma contamination. Therefore, from the W erosion and plasma contamination points of view, besides Ar puffing, some upgrading of this divertor geometry, e.g. setting of 'V-shape corner' [5], should be also performed to get further reduction of the peak heat load onto the divertor target in future.

It is remarkable that DIVIMP modeling of impurity transport is only in consideration of the influence of background ions (e.g. D) on the transport of impurities, and the interaction of different impurity species cannot be simultaneously considered. That is, for the DIVIMP modeling of W impurity transport in plasmas with Ar puffing, the effects of Ar^{X+} on the W impurity transport, which is estimated to be important in the divertor region due to the large Ar density (comparable to the background plasma density), are not taken into account. Thus, the W plasma concentration may be overestimated by DIVIMP due to the missing of Ar effects on the transport of W impurities, which is expected to providing friction forces to drag the W impurities towards the divertor.

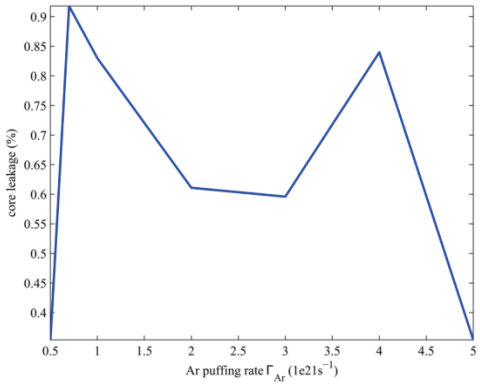

Fig. 11 DIVIMP estimated divertor leakage of W impurity for different Ar puffing rates.

Divertor leakage, defined as the percentage of gross-eroded particles reaching the core plasma, is an important criterion for the assessment of the divertor performance [20]. Figure 11 describes the W divertor leakage for cases with different Ar puffing rates estimated by DIVIMP calculation. From figure 11, the divertor leakage is in the order of 10^{-3}. It may be because of no consideration of the Ar on the transport of W impurities, which is mentioned above, no evident relationship between the divertor leakage and the Ar puffing rate is found in the modeling.

5. Summary and conclusions

Handling of the huge exhaust power in the SOL/divertor region is one of the key issues in validating the design parameters of CFETR. ITER-like divertor with lower single null divertor configuration has been adopted in the design of CFETR, as it has a similar size and P_{SOL}/R to ITER. To facilitate the design of CFETR, predictive modeling for the assessment and optimization of the divertor performances has been carried out. First, SOLPS/B2-Eirene code has been used to simulate the basic divertor plasma behaviors. The calculations show that the divertor peak heat load greatly exceeds $10MW/m^2$, the maximum engineering limit for steady-state operation, for a wide range of plasma conditions. As the edge plasma density increases, the divertor plasma moves from the low-recycling regime to the high-recycling regime and then gradually enters partial detachment. The divertor peak heat load also decreases, but to reduce the divertor peak heat flux

to below 10MW/m^2, the edge plasma density has to be very high so that instabilities related to density limit may be brought about..

Therefore, SOLPS modeling has been performed to assess the effects of Ar puffing, as an approach to reduce the divertor heat load, on the divertor-SOL plasmas. The results show that the divertor peak heat flux and temperature decrease exponentially as the increase of the Ar puffing rate, demonstrating that Ar puffing at the top of the device is highly effective at reducing the divertor heat load. To reduce the peak heat flux onto the divertor to below 10 MW/m^2, the minimum Ar puffing rate needed is 5.0×10^{20}/s. When the Ar puffing rate is increased to 7.0×10^{20}/s, plasma at the inner target enters partial detachment, and the plasma at the outer target partially detaches when the puffing rate is increased to 1.0×10^{21}/s. As the Ar puffing rate further increases, the degree of detachment increases and the divertor plasma enters full detachment in which the target temperature decreases to ~1eV when the puffing rate is 5.0×10^{21}/s.

Although Ar puffing can effectively reduce the target power load and temperature, which is assumed to reduce the sputtering yield, the externally introduced Ar^{X+} ions may cause a considerable amount of erosion due to the relatively heavy mass and high Z. To estimate the detailed effect of Ar puffing on the erosion of W as well as the W plasma density in CFETR with ITER-like divertor, DIVIMP modeling has been carried out, which reflects that the W plasma contamination may be a bit high, so that, besides Ar puffing, some other measures, such as upgrading of the divertor geometry, should also be taken to handle the relatively large exhaust power in CFETR. However, the W plasma contamination may be overestimated by DIVIMP because of on consideration of the Ar effects on the W impurity transport. Moreover, the divertor leakage of W impurity has been estimated by DIVIMP and is in the order of 10^{-3}.

Acknowledgements

This work was sponsored by the National Natural Science Foundation of China (Nos. 11261140328, 10975158) and partially supported by the National Magnetic Confinement Fusion Science Program (No. 2013GB105002). The authors would like to acknowledge the support from the rest of the National CFETR design team.

References

[1] Yuanxi Wan, consideration of the missions of CFETR, CFETR meeting, Yichang, China, 2013

[2] Alberto Loarte, Plasma Phys. Control. Fusion 43, **R183** (2001)

[3] D. D. Ryutov, R. H. Bulmer, R. H. Cohen, D. N. Hill, L. Lao, J. E. Menard, T. W. Petrie, L. D. Pearlstein, T. D. Rognlien, P. B. Snyder, V. Soukhanovskii, M. V. Umansky. 22nd International Fusion Energy Conference, 2008, Geneva, Switzerland.

[4] P. M. Valanju, M. Kotschenreuther, S. M. Mahajan, J. Canik. Phys. Plasmas **16**, 056110 (2009).

[5] H. Kawashima, K. Shimizu, T. Takizuka, K. Tobita, S.Nishion, S. Skurai and H. Takenaga, Nuclear Fusion, **49** (2009) 065007

[6] Nobuyuki Asakura, Katsuhiro Shimizu, Kazuo Hoshino, Kenji Tobita, Shinsuke Tokunaga, and Tomonori Takizuka, Nuclear Fusion **53** (2013) 123013

[7] A.S. Kukushkin, H.D. Pacher, A. Loarte, V. Komarov, V. Kotov, M. Merola, G. W. Pacher

and D. Reiter, Nuclear Fusion **49** (2009) 075008
[8] A S Kukushkin and H D Pacher, Plasma Phys. Control. Fusion **44** 9(2002) 31-943
[9] A.S. Kukushkin, H.D. Pacher, G. Janeschitz, A. Loarte, D.P. Coster, G. Matthews, D. Reiter, R. Schneider, V. Zhogolev, Nucl. Fusion **42** 187-191 (2002)
[10] A.S. Kukushkin, H.D. Pacher, V. Kotov, G. W. Pacher, D. Reiter, Fusion Engineering and Design **86** (2011) 2865
[11] M. Ishida, K.Maeki, R. Hiwatati, X. Bonnin, S. Zhu, A. Hatayama, R. Schneider, and D. Coster, Contrib. Plasma phys. **50** (2010) 362
[12] V. Rozhansky, E. Kaveeva, P. Molchanov, I. Veselova, S. Voskoboynikov, D. Coster, G. Counsell, A .Kirk, S. Lisgo, ASDEX-Upgrade Team, and MAST Team, Nucl. Fusion **49**, 025007 (2009)
[13] R. Schneider, X. Bonnin, K. Borrass, D. P. Coster, H. Kastelewicz, D. Reiter, V. A. Rozhansky, and B. J. Braams, Contrib. Plasma Phys. **46**(1-2), 3-191(2006).
[14] D. P. Coster, X. Bonnin, G. Corrigan, G. S. Kirnev, G. Matthews, J. Spence, and Contributor to the EFDA-JET Work Programme, J. Nucl. Mater. **337-339,** 366-370 (2005)
[15] B. J. Braams, Contrib. Plasma Phys. **36**, 276 (1996)
[16] D. Reiter, J. Nucl. Mater. **196-198** 80 (1992)
[17] D. Reiter, C. May, D. Coster, and R. Schneider, J. Nucl. Mater. **220-222**, 987 (1995)
[18] P.C. Stangeby et al., Nuclear Fusion **28**(1988) 1945
[19] P.C. Stangeby, J.D. Elder, J. Nucl. Mater. **196–198** (1992) 258.
[20] Stangeby P.C. 2000 The Plasma Boundary of Magnetic Fusion Devices (Bristol: Institute of Physics Publishing)
[21] C. Guillemaut, R.A. Pitts, J. Bucalossi, G. Corrigan, A. S. Kukushkin, D. Harting, A. Huber, M. Wischmeier, G. Arnoux, S. Brezinsek, S. Devaux, J. Flanagan, M. Groth, S. Jachmich, U. Kruezi, S. Marsen, J. Strachan, S. Wiesen, JET EFDA contributors. J. Nucl. Mater. 438, S638-642 (2013).
[22] H.P. Summers, M.G. O'Mullane, Springer Series in Chemical Physics, 399 (2005)78
[23] YiPing Chen, D.S. Wang, H. Y. Guo, Nuclear Fusion, **51** (2011) 3042.
[24] Y. Chen. Phys. Plasma 18, 062506 (2011).
[25] Porter G D, Davies S, LaBombard B, Loarte A, McCormick K, Monk R, Shimaka M, Sugihara M. J. Nucl. Mater. 266-269, 917 (1999).
[26] V. Rozhansky at al., Nuclear Fusion **49** (2009)025007
[27] M. Tendler. Journal of Nuclear Materials 128 100 (1984).
[28] Stangeby P.C. Canik J.M. and Whyte D.G. 2010 Nucl. Fusion 50 125003
[29] A. Loarte, B. Lipschultz, A. S. Kukushkin, G. F. Matthews, P. C. Stangeby, N. Asakura, G. F. Counsell, G. Federici, A. Kallenbach, K. Krieger, A. Mahdavi, V. Philipps, D. Reiter, J. Roth, J. Strachan, D. Whyte, R. Doerner, T. Eich, W. Fundamenski, A. Herrmann, M. Fenstermacher, P. Ghendrih, M. Groth, A. Kirschner, S. Konoshima, B. LaBombard, P. Lang, A. W. Leonard, P. Monier-Garbet, R. Neu, H. Pacher, B. Pegourie, R. A. Pitts, S. Takamura, J. Terry, E. Tsitrone and the ITPA Scrape-off Layer and Divertor Physics Topical Group. Nucl. Fusion 47 S203-S263 (2007).
[30] A. Kallenbach, M. Balden, R. Dux, T. Eich, C. Giroud, A. Huber, G. P. Maddison, M. Mayer, K. McCormick, R. Neu, T. W. Petrie, T. Puetterich, J. Rapp, M. L. Reinke, K. Schmid, J. Schweinzer, S. Wolfe. J. Nucl. Mater. **415**, S19 (2011).

[31] K. Schmid, K. Krieger, A. Kukushkin, A. Loarte, J. Nucl. Mater., **363-365**, 674 (2007)
[32] W. Eckstein, R. Preuss: J. Nucl. Mater. **320**, 209 (2003)
[33] Rainer Behrisch, Wolfgang Eckstein, Topics in Applied Physics, **110** (2007)
[34] A Järvinen, C Giroud, M Groth, K Krieger, D Moulton, SWiesen, S Brezinsek and JET-EFDA contributors, Phys. Scr. **T145** (2011) 014013

Analysis of MHD phenomena just after hydrogen pellet injections in LHD

T. Bando[A], S. Ohdachi[AB], Y. Suzuki[AB], Y. Narushima[AB], Y. Takemura[AB], K. Y. Watanabe[B], S. Sakakibara[AB], and X. D. Du[C], LHD Experiment Group[B]

[1]National Institute for Fusion Science, 322-6 Oroshi-cho, Toki 509-5292, Japan
[2]SOKENDAI (Graduate University for Advanced Studies), 322-6 Oroshi-cho, Toki 509-5292, Japan
[3]University of California, Irvine, Irvine, California, USA

Abstract

Three types of new MHD phenomena just after pellet injections are observed. These three types are (i) damping oscillation observed on soft X-ray (SX) diagnostic without correlated magnetic fluctuations, (ii) oscillation on SX diagnostic and magnetic diagnostic with n/m = 1/1 structure and (iii) oscillation on SX diagnostic and magnetic diagnostic with n/m = 1/2 structure. In the article, spatial structures of oscillation observed on SX diagnostic and CO2 laser imaging interferometer are introduced. Especially, phenomena with n/m = 1/1 and 1/2 modes show different spatial structures respectively. Also, the plasma parameters with n/m = 1/1 or 1/2 modes are examined.

1. Introduction

High-central-beta plasmas are one of promising scenarios for helical reactors. In LHD, multi-fueling pellet injections can induce the high-central-beta plasmas. MHD instabilities are observed when large Shafranov shifts or steep pressure gradients are realized with such high-central-beta plasmas in LHD [1-2]. In this article, three types of new MHD phenomena just after pellet injections are reported. These three types are (i) damping oscillation observed on soft X-ray (SX) diagnostic without correlated magnetic fluctuations, (ii) oscillation on SX diagnostic and magnetic diagnostic with n/m = 1/1 structure and (iii) oscillation on SX diagnostic and magnetic diagnostic with n/m = 1/2 structure. Each duration time is up to about 0.03 s, 0.04 s, and 0.2 s respectively. In the following sections, spatial structures of oscillation observed on SX diagnostic and CO2 laser imaging interferometer are introduced. Especially, phenomena with n/m = 1/1 and 1/2 modes show different spatial structures respectively. Also, the plasma parameters with n/m = 1/1 or 1/2 modes are examined and indicate the kind of phenomena.

2. Experimental setup

LHD is a heliotron type devise which has a set of continuous superconducting helical coils with a poloidal/toroidal winding number, 2/10. The positions of magnetic axes of plasmas with phenomena reported in this articles are 3.6, 3.75 and 3.8 m. Typical averaged minor radius is 0.5 m. The rotational transform, ι, profile is monotonically increasing with low β plasmas including $\iota = 0.5$ and 1 surfaces. With high β plasmas, the reversed shear can be realized and the $\iota = 1$ surface can disappear.

Figure 1 shows the geometrical information of diagnostic used in this article. Hydrogen pellets are injected from outboard side of plasmas. The Hα detector is located near the pellet injector. SX diagnostic

[3] has 17 channels, which covers whole vertical poloidal cross section. In the opposite side of the SX diagnostic, CO2 laser imaging interferometer is located and has 77 channels [4], which does not cover whole poloidal cross section. Magnetic probes and saddle loops are set toroidally and poloidally to determine toroidal and poloidal mode numbers.

3. Typical Observation of three types of phenomena

In this section, typical observations of three types of phenomena are introduced. At first, types of (i) and (ii) are explained when the magnetic axis is 3.6 m. Figure 2 shows time evolution of (a) SX signals, (b) the line integrated electron density induced by CO2 imaging laser interferometer, (c) magnetic fluctuations and (d) Hα signals. A hydrogen pellet is injected at 3.74 s and ablated for 386 μs. Figure 3 shows (a) horizontally elongated poloidal cross section and (b) a ι profile assuming a pressure profile when the pellet is injected. In Fig. 3 (b), the blue line means the radial profile of ablated amounts of the pellet estimated by the speed of the injected pellet and Hα signals. The almost pellet seems to ablate around the ι = 1 surface. After the pellet ablated, damping oscillation appeared on SX signals viewing around the ι = 1 surface. This oscillation seems to have m = 1 mode structure. It is noted that there is no obvious correlated fluctuations on magnetic diagnostic during this damping phase.

After damping phase, m/n = 1/1 mode structure appeared on magnetic diagnostic. The rotation directions of the structure, induced by magnetic diagnostic, are the magnetic field direction toroidally and electron diamagnetic direction poloidally. At the same time, SX signals and the line integrated electron density show m = 1 structure. Figure 4 shows spatial structures of amplitudes and phases from (a) SX signals and (b) the line integrated electron density. Around inner and outer positions of the ι = 1 surface, the peaks of amplitudes are observed, and phases are different by π. Because CO2 laser imaging interferometer is not viewing the inner side of the plasma, the peak of the amplitude in the inner region in fig. 4 (b) is not observed.

When the magnetic axis is 3.8 m, the different mode n/m = 1/2 appears. When the mode appears, the β value is high due to some pellet injections. Then the reversed shear seemed to be realized and the ι = 1 surface seemed to disappear. Though damping oscillation on SX signals are observed when the pellet is injected, the structure is not clear. Figure 5 shows spatial structures of amplitudes and phases from (a) SX signals and (b) the line integrated electron density when the n/m = 1/2 mode is observed. Around the ι = 0.5 surface, there are peaks of amplitudes. According to the radial profile of amplitudes of SX signals, the mode width seems to be fairly large. By comparing of phases of channels viewing inner and outer positions of the ι = 0.5 surface, this mode has the odd mode number. However, phases of neighboring sight lines are inverted as well. This structure indicates existence of a magnetic island.

4. Plasma parameters when n/m = 1/1 or 1/2 modes appear

To determine the kind of observed n/m = (ii) 1/1 or (iii) 1/2 modes, the relationship between the magnetic Reynolds number, S, and the volume averaged β, $<\beta>_{dia,}$ are investigated. Figure 6 (a) shows relationship about n/m = 1/1 mode when the magnetic axis is 3.6 m. Red and blue circles mean data with and without n/m = 1/1 mode respectively. As shown in fig. 6 (a), the mode seems to appear in collisional

plasmas. In LHD, the saturation level of the mode amplitude for resistive modes is proportional to S to -1/3 [5]. Therefore the observed n/m = 1/1 mode might be also resistive modes.

Figure 6 (b) shows the case of n/m = 1/2 mode when the magnetic axis is 3.8 m. This mode seems to occur relatively low $<\beta>_{dia}$ region and disappear with high $<\beta>_{dia}$. The $\iota = 0.5$ surface can disappear with high β value with the reversed shear profile. This can explain the disappearance of the mode.

5. Summary and future plan

In this article, three types of phenomena observed just after pellet injections are reported. The phenomenon (i) is damping oscillation observed on SX diagnostic without correlated magnetic fluctuations. The physical mechanism is not clear. The phenomena (ii) and (iii) which show n/m = 1/1 and 1/2 mode respectively with correlated magnetic fluctuations might be resistive MHD instabilities according to S and $<\beta>_{dia}$ dependence. The n/m = 1/2 mode shows phase inversion between neighboring sight lines though the n/m = 1/1 mode does not show this kind of structure.

The n/m = 1/2 mode seems to disappear at the threshold of $<\beta>_{dia}$. The disappearance of the n/m = 1/2 mode occurs by disappearance of the $\iota = 0.5$ surface. The VMEC [6] calculation will be done to calculate the iota profile when the mode disappears.

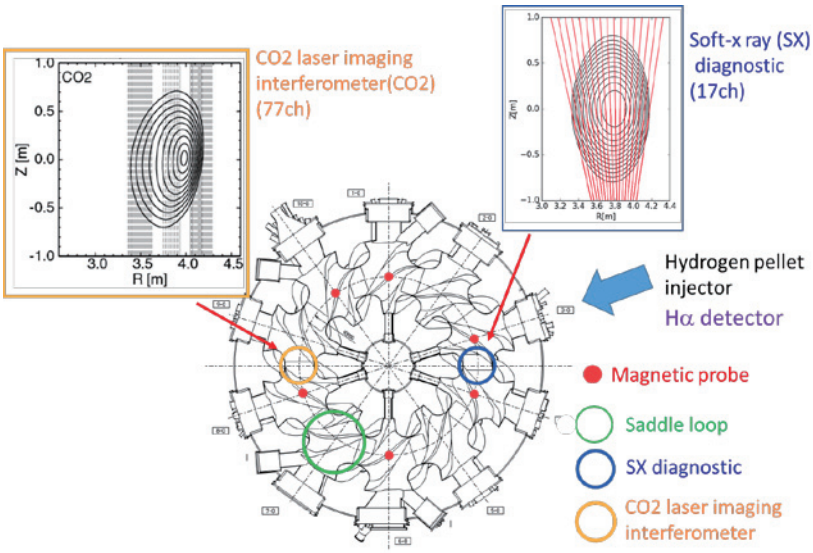

Fig. 1 The geometrical information of diagnostic used in the article.

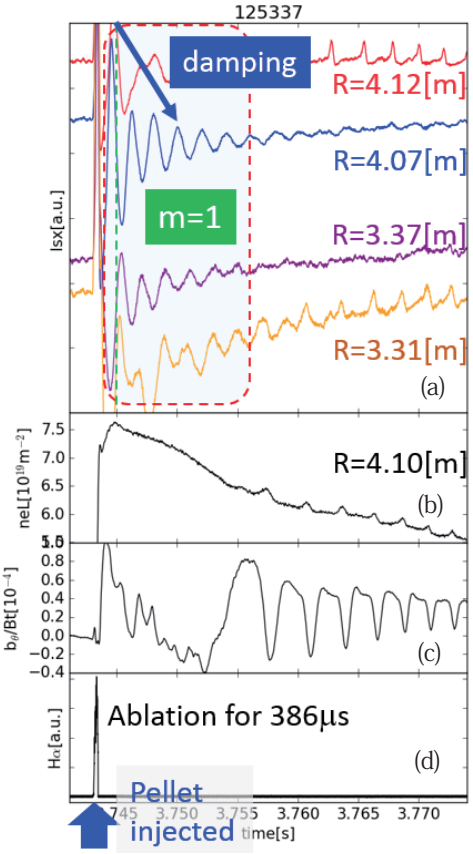

Fig. 2 Time evolution of (a) SX signals, (b) the line integrated electron density induced by CO2 imaging laser interferometer, (c) magnetic fluctuations and (d) Hα signals.

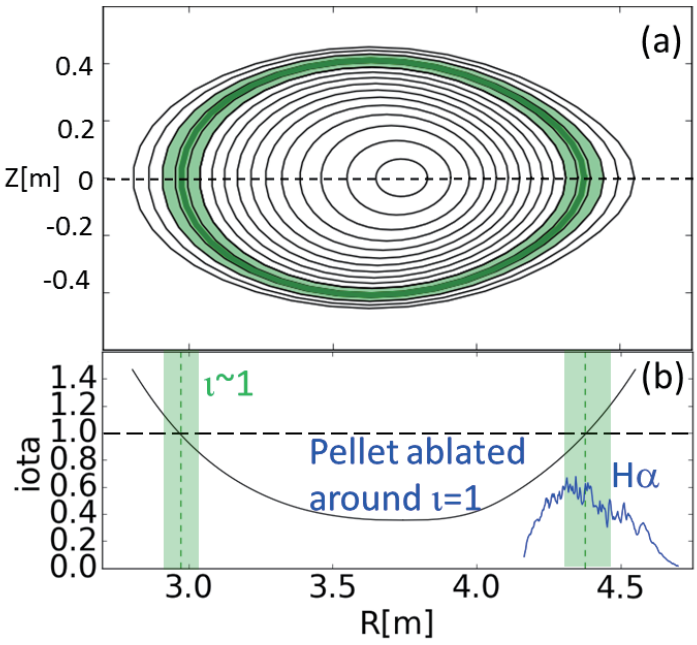

Fig. 3 (a) Horizontally elongated poloidal cross section and (b) a ι profile assuming a pressure profile when the pellet is injected. In (b), the blue line means radial profile of ablated amounts of the pellet estimated by the speed of the injected pellet and Hα signals.

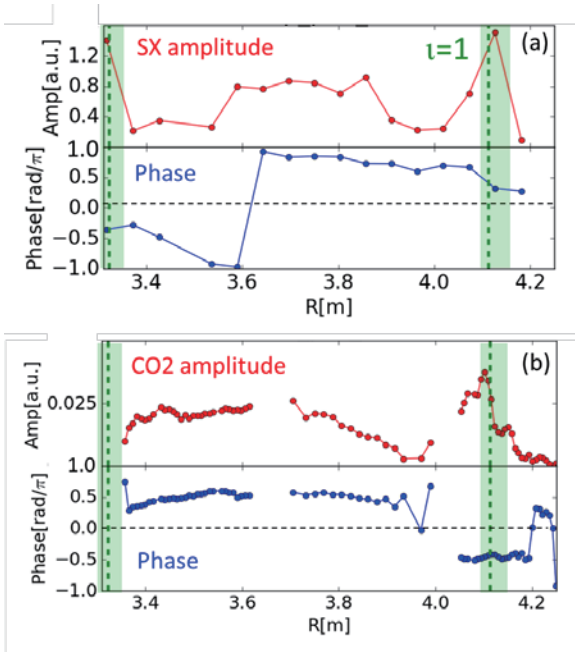

Fig. 4 Spatial structures of amplitudes and phases from (a) SX signals and (b) the line integrated electron density when n/m = 1/1 mode is observed.

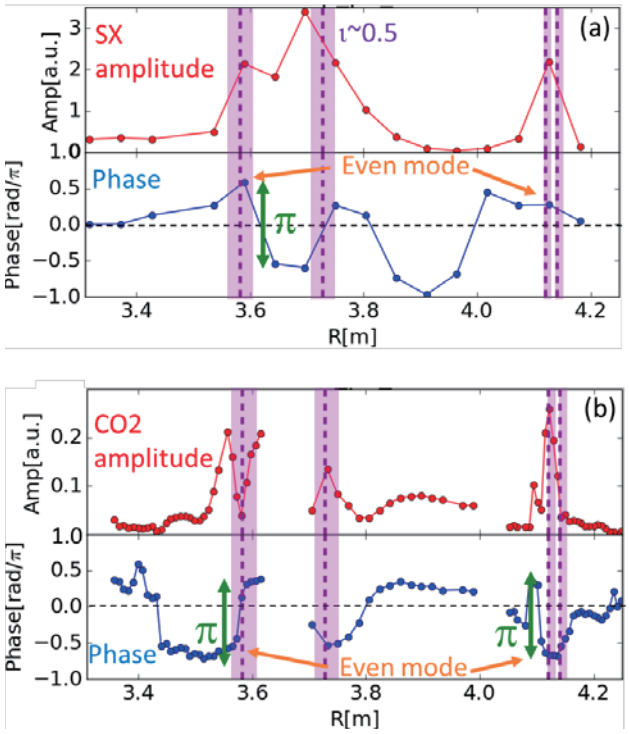

Fig. 5 Spatial structures of amplitudes and phases from (a) SX signals and (b) the line integrated electron density when the n/m = 1/2 mode is observed.

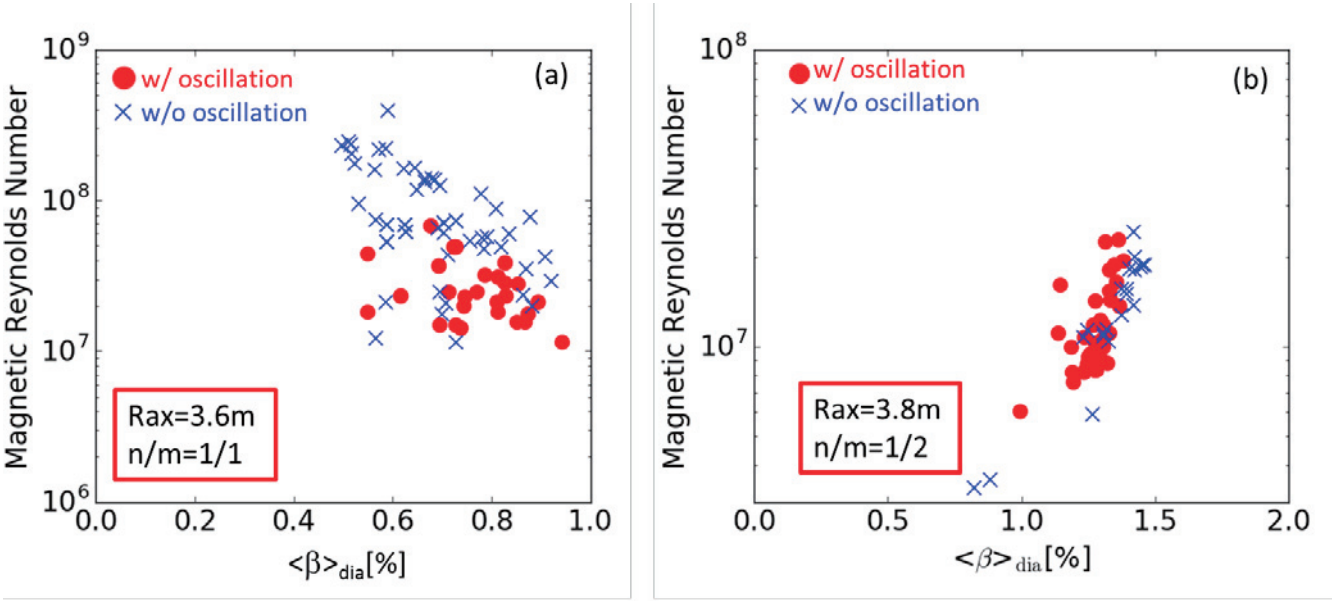

Fig. 6 Relationship between the magnetic Reynolds number and the volume averaged β about (a) n/m = 1/1 or (b) 1/2 modes.

Acknowledgements

This work was partly supported by the JSPS-NRF-NSFC A3 Foresight Program in the field of Plasma Physics (NSFC: No.11261140328, NRF: No.2012K2A2A6000443).

References

[1] S. Ohdachi et al., Contrib. Plasma. Phys., **50**, 552 (2010).

[2] S. Ohdachi et al., "Two–Dimensional Structure of MHD Instabilities and their Non–Linear Evolution in the Large Helical Device." Proc. 21th IAEA Fusion Energy conference, Chegdu, China. (2006).

[3] X. D. Du et al., Plasma and Fusion Research, **7**, 2401088 (2012).

[4] K. Tanaka, Plasma and Fusin Research, **2**, S1033 (2007).

[5] S. Sakakibara et al., Plasma Phys. Control. Fusion, **50**, 124014 (2008).

[6] S. P. Hirshman and J. C. Whitson, Phys. Fluids, **26**, 3553 (1983).

Analysis of deposition inside of the gap of castellated tungsten blocks of different shapes

Eunnam Bang[1], Suk-ho Hong[1,2,3], Kyungmin. Kim, Hongtack Kim[1]

[1]KSTAR research center, National Fusion Research Institute, Daejeon, Korea
[2]Department of accelerator and nuclear fusion physical engineering, Korea University of Science and Technology, Daejeon, Korea
[3]Department of electrical engineering, Hanyang University, Seoul, Korea.

Abstract

In this paper, we report the results from a series of experiment using special tungsten block tiles performed in KSTAR on fuel retention inside the gap of castellated blocks of different shapes. Results are presented a comprehensive understanding on deposition procedure inside the gap and would give valuable information on the Be deposition inside the gap of castellated tungsten tiles in ITER. For the experiment, we have manufactured tiles consisting of four different shapes of tungsten blocks. These tungsten block tiles are exposed to L- and H-mode discharges during 2014-2015 campaign, then removed from the vacuum vessel after the campaign for further analysis. The surface carbon density of gaps is in a range from 1.0×10^{15} C atom/cm^2 up to 7.0×10^{15} C atom/cm^2. Comparing the surface carbon density of toroidal and poloidal gaps of different shapes, contribution of each species can be separated, since the contribution of neutrals is independent of the shape and depth of the gap (or height of the leading edge). At the gap entrance, neutral contribution is about 4.0×10^{15} C atom/cm^2, decreases down to 2.8×10^{15} C atom/cm^2 at a depth of 0.5 mm, and remain constant at 1.0×10^{15} C atom/cm^2 afterwards down to the depth of 5 mm. The contribution of ions is concentrated on very narrow position within 0.6 mm from the entrance.

1. Introduction

Plasma facing components (PFCs) of next generation of fusion machines like ITER or DEMO will be castellated to improve their thermos-mechanical strength and to increase heat load handling capability. Fuel retention inside co-deposited layers along the gap of castellation influences the in vessel fuel inventory which is limited by nuclear safety authority, e.g., 700g in ITER [1,2]. In this paper, we report the results from a series of experiment using special tungsten block tiles performed in KSTAR on fuel retention inside the gap of castellated tungsten blocks of different shapes used in various tokamaks. Results presented a comprehensive understanding on deposition procedure inside the gap and would give valuable information on the Be deposition inside the gap of castellated tungsten tiles in ITER.

2. Experimental Setup, Diagnostics and Analyses

2.1 Tungsten castellated blocks in 2014 campaign

In order to study deposition amount and pattern on the gap of tungsten divertor, castellated tiles based on tungsten (W), copper (Cu), and copper-chrome-zirconium (CuCrZr) alloy are fabricated. Base design of

the block is similar to the ITER divertor monoblock. The base block has rectangular structure with a dimension of 30 mm × 20 mm × 12 mm. The blocks in the first four rows of KM00-2014 are aimed to measure the deposition amount and pattern depending on different shapes and edge. Figure 2 shows the detail of the four shaping: conventional "basic" rectangular shape, chamfered leading edge (1 mm for leading edge experiment), double-chamfered and rounded edge. The gap distance between 1st and 2nd column is 0.5 mm as in ITER case, while that between 2nd and 3rd is 1 mm. The blocks are then installed at central divertor of KSTAR with a graphite cover to protect the side of the blocks and leading edges (Fig. 1). During the plasma shot, the position of the outer strike point of typical KSTAR L- and H-mode discharges lay on central and the outer divertor, tungsten blocks installed at the central divertor, are exposed to the plasmas for as long as possible

Fig. 1. The tungsten maker tile after 2014 campaign.

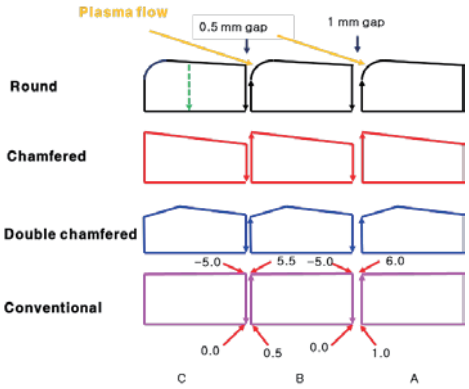

Fig. 2. The four types shape of castellated tungsten tiles (KM00-2014).

2.2 Tungsten castellated blocks in 2015 campaign

A dedicated experiment was designed to understand 1) ELM/inter ELM heat load on leading edge (including melting) and on misaligned blocks. Fig. 3 shows a schematic description of different design of tungsten blocks. Leading edge blocks based on the regular rectangular shape with different "intentional" misalignment of 0.3 mm, 0.6 mm, 1.0 mm, and 2.0 mm with respect to perfectly aligned case were fabricated. In KM02-2015, leading edge blocks for the ELM/inter ELM heat load experiment were positioned. In order to avoid parasitic emission from nearby leading edges, blocks were aligned at zig zag position as shown in Fig. 3. Note that the intrinsic misalignment caused by engineering limits has been carefully considered and minimized down to a level of less than 0.05 mm.

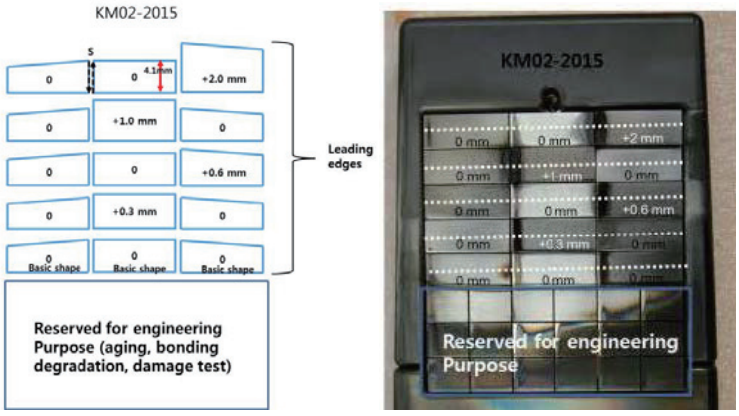

Fig. 3. A schematic description and picture (after campaign) of tungsten blocks (KM02-2015). Label S indicates the direction of S coordinate (set zero at the left corner of the gap).

2.3 EPMA measurements

After each campaign, KM00-2014 and KM02-2015 were taken out from the divertor for various analyses including EPMA (Electron Probe Micro-Analysis, SHIMADZU 1600) measurement. The carbon contents are measured by EPMA with typical setting parameters of 15 keV accelerating Voltage, 20 nA beam current, and 1 um^2 beam size. In order to have complete deposition patterns on the blocks, EPMA measurements were performed along the lines with an interval of 1 mm, not only on the both sides of each gap, but also on the top surface of blocks. Note that the EPMA signals show a minimum level of 1×10^{15} C atoms/cm^2, and this level of carbon contents has been reached at around 4-5 mm down from the gap entrance (S=0).

3. Results and Discussion

3.1 Surface carbon density on the gap of KM00-2014

Tungsten blocks at the central divertor has been exposed to various plasmas. Although we have observed the blocks assuming that the same amount of heat flux has applied to the tungsten blocks due to the toroidal symmetry. After campaign, the tungsten blocks were measured surface carbon density on poloidal toroidal gap by EDS.

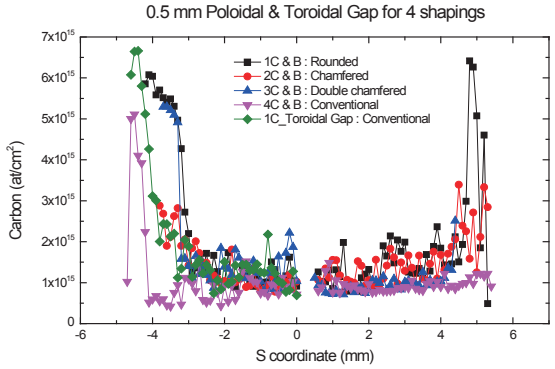

Fig 4. Carbon density on 0.5 mm gap of four shapes of poloidal and toroidal gap

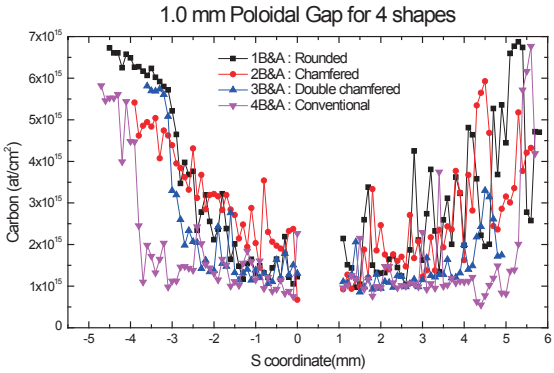

Fig 5. Carbon density on 1 mm gap of four shapes

The surface density on toroidal gap was measured at only round shape tungsten tile. The toroidal gap shape and width are same at whole tiles. The surface density of both gaps are about 1.0×10^{15} atom/cm^2 - 7.0×10^{15} atom/cm^2. In general, the surface density of toroidal gap is higher than that of poloidal gap due to the contribution of both ions and charge exchange neutrals. In the figure 5, the pink trigonometric line is surface density on the conventional shape (rectangular) with 0.5mm poloidal gap and the green diamond line is surface density on rectangular shape with 0.5mm toroidal gap. In this castellated tungsten blocks, the surface density of toroidal gap is higher than that of poloidal gap about 13%. Compare the surface density of toroidal and poloidal gaps, contribution of ions and charge exchange neutrals can be separated by deposition pattern. At the gap entrance, neutral contribution is about 5.0×10^{15} atom/cm^2, decreases down to 2.0×10^{15} atom/cm^2 at a depth of 0.5 mm, and remain constant at 1.0×10^{15} atom/cm^2 afterwards down to the depth of 5 mm. The contribution of ions is concentrated on very narrow position within 0.6 mm from the entrance. In the poloidal gap, the difference depending on the geometry is much more clearly visible. The surface density profiles of double chamfered and conventional blocks were almost identical down to 0.7 mm, meaning the contribution of ions was identical in both shape. There is a small difference from the depth between 0.7 mm and 1.5 mm caused by the different contribution of neutrals, but it would not be a meaningful difference. Blocks of rounded edge shows much broader deposition pattern than others and particles reach a deeper region down to about 1.5 mm, simply due to larger opening. Note that the total quantity of deposited carbon atoms depends on the thickness of the layer, not the surface density. Deposition in 1.0 mm gaps show much larger deposition patterns and particles have reached much deeper inside the gap (Fig 5).

3.2. Deposition profiles contributed by CX neutrals and C ions from KM02-2015

Due to the different contribution of C ions and charge exchange (CX) neutrals, deposition patterns inside gaps of various shapes of castellation are different [4, 5]. Since CX neutrals are not affected by electric and magnetic fields, they can go freely anywhere inside the tokamak vacuum vessel unless they are ionized by collision with electrons. In our previous experiment by using stainless steel coupons with cavity structure in them, we could not distinguish the contribution of ions and CX neutrals. By using leading edges, we could separate the contribution of ions and CX neutrals: The gaps behind leading edges are

hidden from the ions due to the higher height of the edge than aligned ones, which act like “barriers” to the ions entering the gaps. On the other hand, both ions and CX neutrals contribute the deposition inside the gaps between two perfectly aligned blocks. Thus, we define here, from the view point of ions, the side wall of the gaps as “shadowed side” from -5.0 mm to 0.0 mm in S coordinate, while “open side” 0.5 mm to 5 mm. Measured deposition profiles inside gaps along S coordinate are depicted in Fig. 6. Fig. 6a) shows the locations of EPMA measurements inside the gaps between leading edges and perfectly aligned block which are shadowed by leading edges, and corresponding deposition profiles in Fig. 6b). Since ions cannot enter the gap freely, one can expect that the deposition would be dominated by CX neutrals. The carbon contents at the entrance of the gap (at -4.1 mm) of shadowed side were about 4×10^{15} cm^{-2}, and then decreased gradually down to 1×10^{15} cm^{-2} at the bottom (at 0.0 mm). The carbon contents and the deposition pattern on the opposite side of the gap of open side are almost the same and symmetric meaning that the deposition process occurred on both sides of the gap was identical and didn’t depend on the direction of incoming particles. Note that the grey line at the open side in Fig. 6b) is just a mirror-reflected curve of that at the shadowed side. This reveals that the CX neutrals are responsible for the deposition. On the other hand, Fig. 6c) and 6d) show the locations of EPMA measurements inside the gaps inside gaps between two perfectly aligned blocks along S coordinate and corresponding deposition profiles. The deposition patterns inside the gaps between two perfectly aligned blocks at four different locations. First of all, the deposition patterns from different locations are almost identical indicating that the physical process responsible for the deposition inside the gaps was well reproduced at each block. Second, the deposition pattern is different from that caused by CX neutrals shown in Fig. 6a) and not symmetric indicating that there was additional

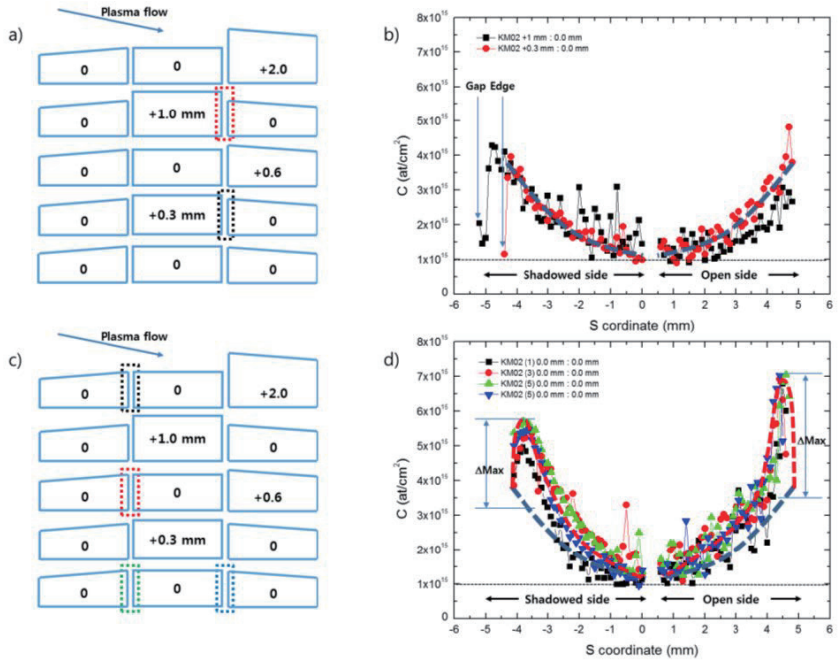

Fig. 6. a) Locations of EPMA measurements inside the gaps shadowed by leading edges along S coordinate, b) deposition profiles of a), c) locations of EPMA measurements inside the gaps inside gaps between two perfectly aligned blocks along S coordinate, d) deposition profiles of c). Dashed grey and red lines are guide to the eye to separate the contribution from CX neutrals (grey) and ions (red).

contribution of ions. By plotting the contribution of CX neutrals (grey lines) found from Fig. 6b) into Fig. 6d), one can separate qualitatively the contribution of ions on the deposition as indicated by red lines. Maximum contribution of ions (Δ Max) at the shadowed side is ~2.5×10^{15} cm^{-2}, while that at the open side is ~3.5×10^{15} cm^{-2}.

3.3. Deposition profiles inside the gaps in front of leading edges

When a leading edge is present, contribution of ions will be significantly changed resulting in different deposition profiles inside the gap in front of the leading edge. Fig. 7 shows the locations of EPMA measurements between perfectly aligned blocks and leading edge blocks along S coordinate and corresponding deposition profiles. In both cases of shadowed and open (leading edge) sides, the amount of deposition increases as the leading edge height increases (label 1 and 2). Especially, the amount of deposition at the bottom inside the gap at the shadowed side rapidly increases from 1×10^{15} cm^{-2} (0.0 mm) up to 5×10^{15} cm^{-2}. This indicates that 5 times more amount of carbon particles could reach the depth down to ~4.1 mm with higher leading edges. In the case of the open (leading edge) side, the amount of carbon increases gradually with a saturation at a level of 7×10^{15} cm^{-2}, which is the side wall of the leading edge directly exposed to plasmas. Note that the deposition patterns at both sides are very different and asymmetric, and the effect is visible if the leading edge is higher than 0.6 mm: CX neutrals cannot be the main player since they will be deposited rather symmetrically as shown in Fig. 7b). Two possible interpretations could be made: 1) Ions are bounced back from the side wall and deposited on the shadowed side wall, 2) deposited layers on the open side were bombarded by ions and eroded carbon atoms/molecules were deposited on the shadowed side wall.

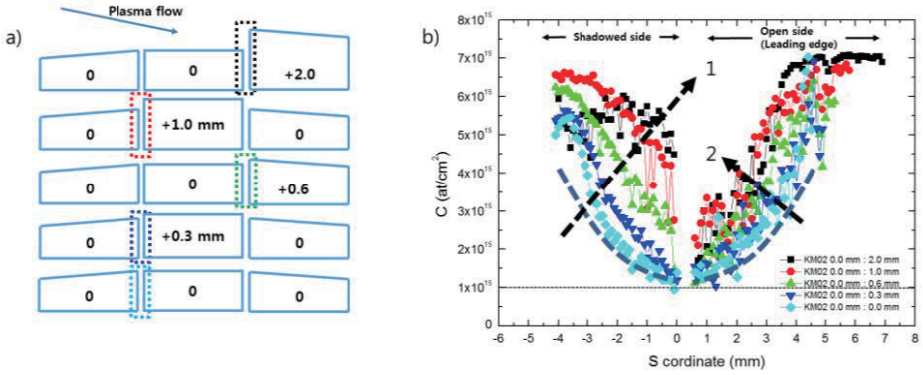

Fig. 7. a) Locations of EPMA measurements between perfectly aligned blocks and leading edge blocks along S coordinate. b) deposition profiles of a), A perfectly aligned case (cyan, diamond) and grey lines indicating CX neutral contribution from Fig. 6b) are added as references.

4. Summary

A series of experiment using special tungsten block tiles were performed in KSTAR on fuel retention inside the gap of castellated blocks of different shapes. We have varied the shapes and gap distance to find the minimum deposition tungsten shape. After long term exposure of tungsten block, we have analyzed the deposition inside the gaps of castellation. The carbon density on toroidal gap is higher than that of poloidal

gap. And found that the deposition is reduced at least by a factor of two by using optimized castellation structure as figure 4. The carbon density on chamfered shape is the lowest in to the four shapes. The carbon density on the rounded shape is the highest, because of this block are more opened than other shapes. The carbon density on all kinds of shapes with 1 mm gap are higher than that of 0.5 mm gap. But the effect of reduced deposition according to the shapes are decreased at 1mm of gap distance as shown figure 5. Of course, there are still difference of carbon density with the four kinds of shapes, but the difference at 1mm gap are lower than 0.5 mm gap. And by comparing the surface density of toroidal and poloidal gaps of different shapes of KM02-2015, contribution of each species (ions, CX neutrals) can be separated. The contribution of ions is concentrated on very narrow position within 0.6 mm from the entrance.

Acknowledgements

This research was partly supported by Ministry of Science, ICT, and Future Planning under KSTAR project and by National Research Council of Science and Technology (NST) under the international collaboration & research in Asian countries (No. PG1314), and partly supported by the JSPS-NRF-NSFC A3 Foresight Program in the field of Plasma Physics (NSFC: No.11261140328, NRF: No.2012K2A2A6000443).

References

[1] A. Litnovsky, et al., J. Nucl. Mater. 386-388 (2009) 809-812.

[2] Suk-Ho Hong, et al., Fus. Sci. Technol. 68 (2015) 36.

[4] K. Ohya, et al., Fus. Eng. Des. 81 (2006) 205

[5] P. C. Stangeby, “The Plasma Boundary of Magnetic Fusion Devices” (Taylor & Francis London, 2000), p. 281

Preliminary Study of the Effect of Magnetic Expansion in Snowflake Divertor on Impurity Screening

S.F. Mao[1], Y.F. Zhou[1], H.S. Wu[1], B. Chen[1], Z.P. Luo[2], X.B. Peng[2], Y. Guo[2] and M.Y. Ye[1,2,]

[1]School of Nuclear Science and Technology, University of Science and Technology of China, Hefei, Anhui 230026, PR China

[2]Institute of Plasma Physics, Chinese Academy of Sciences, Hefei, Anhui 230031, PR China

Abstract

Snowflake Divertor (SFD) is thought to be a possible solution for future fusion reactor, where the heat exhaust would be a critical problem. In a snowflake divertor configuration, the flux expansion is significantly increased in comparison with traditional divertor. As a result, the geometrical connectivity would be increased between main scrape-off layer (SOL) and SFD, which may lead an increase in the impurity flow to the main SOL. In this study, a SOLPS simulation is performed for the SFD and ITER-like (IL) divertor of China Fusion Engineering Test Reactor (CFETR). Carbon target is assumed to provide the non-recycling impurity. Simulated results in conduction-limit regime show that the carbon concentration for SFD is higher than that for IL divertor under similar upstream condition. However, considering a lower electron temperature near the divertor target in SFD due to the increased connection length, the increase of carbon concentration should be a result of deeper impurity penetration.

1. Introduction

For future fusion reactor, heat exhaust is a critical issue. Considering a fusion power 1 -2 GW, and taking into account of the auxiliary heating power and core radiation, about 200 MW will enter into SOL [1]. However, an engineering limit of heat flux is 10 MW/m^2 for the divertor target [2]. To explore an effective way to reduce the heat flux onto divertor target, advanced divertor configurations, such as SFD [3,4], X-divertor [5], Super-X divertor [6] and X-point target divertor [7] are proposed with modified magnetic equilibrium, where an extra X point is introduced in addition to the single null in traditional divertor configuration [8].

Among the advanced divertors, SFD has the advantages that the sets of PF coils and divertor geometry are more compatible with the traditional divertor. Therefore, SFD has already been achieved in TCV [9], NSTX [10], DIII-D [11] and EAST [12], while extensive researches are summarized in Ref. 13. In exact SFD, a second order null is proposed, to provide great flux expansion near null point, and the heat flux would be decreased due to the increase of flux expansion. Because a second null configuration is topologically unstable, a stable form of SFD is SF-plus or SF-minus, where an extra first order null, in addition to the main null, appears in the private flux region or SOL, respectively. Significant decrease in

heat flux onto divertor target is identified in experiment. However, a possible disadvantage, which is noted by Ryutov et al. [4], is the increased geometrical connectivity between divertor and main SOL, due the flux expansion above the main X point. The increased geometrical connectivity may lead to increased impurity flow to the upstream, which means degradation of impurity screening.

In this work, a SOLPS [14] simulations are performed on the SFD and ITER-like (IL) divertor in CFETR [15-17] to study the difference of impurity distribution. Settings of the simulation are given in section 2. In section 3, the simulation results are shown, and a discussion about the impurity distribution is also given. Section 4 contains the conclusion.

2. Simulation Settings

For superconducting CFETR, the key parameters are as follow: P_{fus} = 200 MW, I_p = 10 MA, B_T = 5.0 T, R = 5.7 m, a = 1.6 m, $\kappa \sim 2.0$, $q_{95} \geq 3$, $\beta_N \sim 2$ and P_{aux} = 100 ~150 MW. Assuming P_{rad} in core region is about 40 MW, P_{SOL} = 0.2 P_{fus} + P_{aux} - P_{rad} = 100 MW is used in the simulation. SFD and IL divertor configuration in CFETR are used to study the difference in impurity distribution. A comparison between the SFD and IL divertor configuration is shown in Fig. 1. Poloidal flux surfaces of different distance to the separatrix at outer mid-plane (OMP) r^{mid}, are drawn for both SFD and IL divertor. Due to the limit of PF coil current, the extra X point is still far from the main null [18]. As a result, the increase of flux expansion in present SFD is modest, a factor of ~ 1.6.

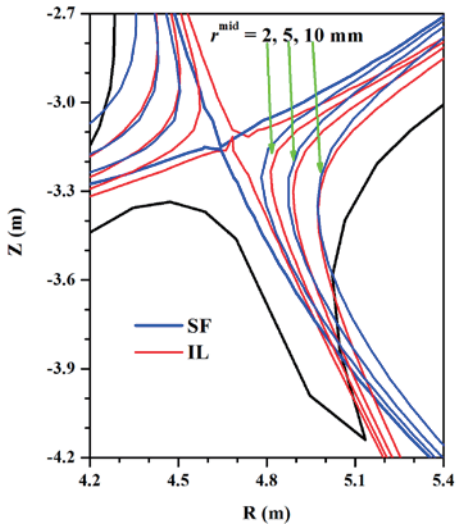

Fig. 1 Comparison of the poloidal flux surfaces for the SFD and IL divertor. r^{mid} is the distance between the relevant flux surface and separatrix at OMP.

The same divertor geometry is used in the simulation for SFD and IL divertor, shown as the thick black line in Fig. 1. Furthermore, in this study, for introducing the non-recycling impurity, carbon target is assumed. The density is adjusted by a D_2 gas puffing from the top of the main chamber. Other simulation settings are the same to our previous work [18]: P_{SOL} is equally divided by ions and electrons, P_{ion} = P_e = 50 MW, $D_\perp$ = 0.3 m2/s, $\chi_e = \chi_i$ = 1.0 m^2/s.

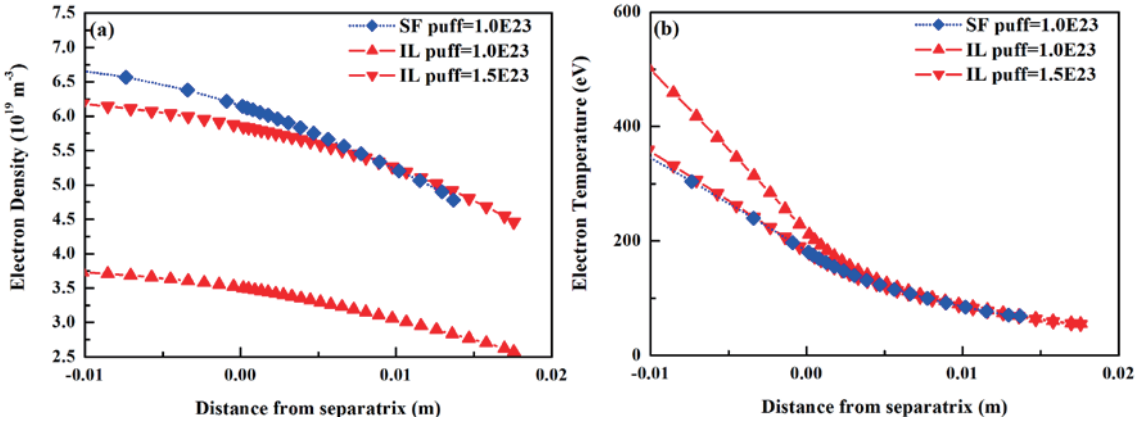

Fig. 2. (a) electron density and (b) electron temperature profile at OMP of SFD configuration and IL divertor configuration (for different gas puffing rate).

3. Results and Discussion

In this preliminary study, we focus on the outer divertor in conduction-limited regime. A similar upstream condition is prepared by adjusting gas puffing rate in SFD and IL divertor configuration. As shown in Fig. 2, for SFD, a gas puffing rate sets to 1.0×10^{23} s^{-1}, while for IL divertor, the gas puffing rate has to be increased to 1.5×10^{23} s^{-1}.

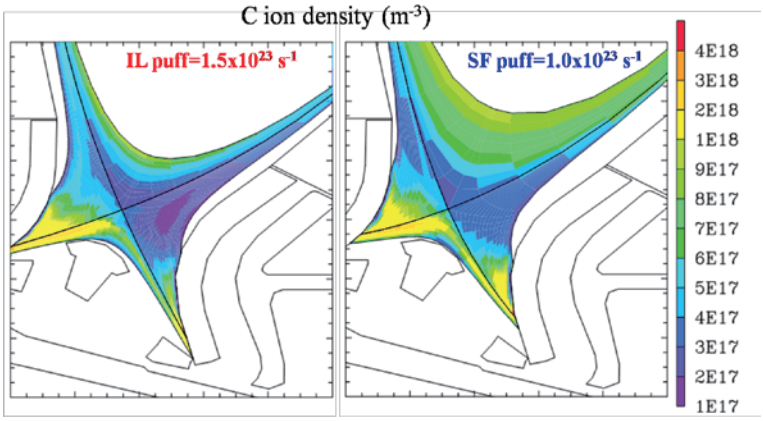

Fig. 3 Comparison of the distribution of carbon impurity density between SFD and IL divertor.

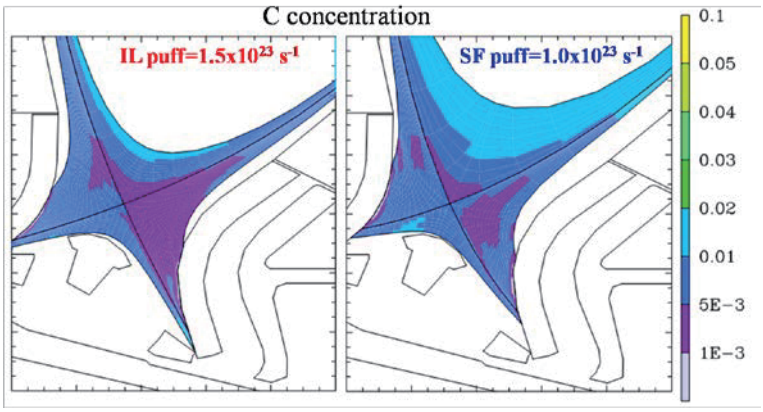

Fig. 4 Comparison of the distribution of carbon impurity concentration between SFD and IL divertor.

Simulated distributions of carbon impurity density and concentration (measured as n_C/n_e) are shown in Fig. 3 and Fig. 4, respectively. It can be seen that, in the outer divertor, impurity density is increased for SFD, especially for the region near the target and far from separatrix. However, as shown in Fig. 4, the impurity concentrations are well below 2% for both SFD and IL divertor. An implication from the comparison is that the impurity is not well baffled, as shown in Fig. 3 that the strike point for SFD is higher than that for IL divertor. Therefore, further optimization of the divertor geometry for SFD is demanded.

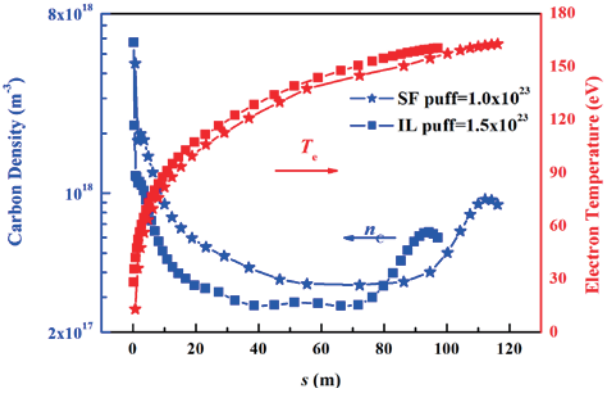

Fig. 5 Carbon density and electron temperature along the selected flux tube (r^{mid} = 1.3 mm).

Further analysis is performed in the flux tube of r^{mid} = 1.3 mm, which is chosen near the parallel heat flux peak. Though the poloidal distance along the flux tube is decreased modestly due to the upper shift of the intersection point between the flux tube and outer target, the connection length is increased due to the increased flux expansion in SFD. The connection lengths are ~ 116 m and ~ 97 m for SFD and IL divertor, respectively. As shown in Fig. 5, divertor electron temperature for SFD (~ 13 eV) is lower than that for IL divertor (~ 28 eV), while the upstream electron temperature (~ 160 eV) is similar. The distributions of electron temperature for both SFD and IL divertor are in consistent with the picture of conduction-limited SOL. The distributions of carbon density along the flux tube are also in well agreement with the picture of non-recycling impurity transport along flux tube [19]. The ratio of lowest impurity density for SFD to IL divertor is ~ 1.28, while the ratio at OMP is ~ 1.47. It is hard to give a conclusion about the effect of increased geometrical connectivity in SFD, due to the ratios are too close to each other. Further study is needed on a SFD with larger flux expansion that could make the greater effect of geometrical connectivity.

From Fig. 5, the distribution of impurity density near outer target is more broaden for SFD than that for IL divertor, which implies that the impurities are penetrated deeper distance for SFD. It is also in consistent with the lower electron temperature at divertor target. Therefore, the increase of impurity density in SFD could be explained as an indirect result of increased flux expansion (therefore connection length), through decreased electron temperature at divertor target and subsequent increasing in distance of impurity penetration.

4. Conclusion

The effect of flux expansion in SFD of CFETR on impurity screening is preliminary studied. Under

the same divertor geometry and with assumed carbon target which is used to provide non-recycling impurity, SOLPS simulation is performed for both SFD and IL divertor. In this study, both divertors are in the conduction-limited regime. Similar upstream condition for SFD and IL divertor is achieved under different gas puffing rates, which are 1.0×10^{23} s^{-1} and 1.5×10^{23} s^{-1}, respectively.

Simulated impurity density and concentration for SFD are higher than those for IL divertor. The ratio of lowest impurity density for SFD to IL divertor and the ratio of the impurity density at OMP are compared. The two ratios are too close to each other, so we could not get a conclusion about the effect of increased geometrical connectivity on impurity screening for SFD. Further study is needed for SFD configuration with larger flux expansion. The increase of the impurity density in SFD is considered as an indirect result of increased flux expansion, where increased connection length leads to a lower electron temperature at divertor target and therefore deeper impurity penetration.

Acknowledgements

This work is supported by the National Magnetic Confinement Fusion Science Program of China (Grant No. 2014GB110000), National Natural Science Foundation of China (Grant No. 11375191, 11305216), Fundamental Research Funds for the Central Universities (Grant No. WK2140000006) and Anhui Provincial Natural Science Foundation (Grant No. 1308085QA21). Numerical computations were performed on the ShenMa High Performance Computing Cluster in Institute of Plasma Physics, Chinese Academy of Sciences and supercomputing system in the Supercomputing Center of University of Science and Technology of China. This work was partly supported by the JSPS-NRF-NSFC A3 Foresight Program in the field of Plasma Physics (NSFC: No.11261140328, NRF: No.2012K2A2A6000443).

References

[1] F. Najmabadi and the ARIES Team, Fusion Eng. Des. **38** (1997) 3.

[2] Y. Shimomura, M. Keilhacker, K. Lackner, et al., Nucl. Fusion **23** (1983) 869.

[3] D.D. Ryutov, Phys. Plasmas **14** (2007) 064502.

[4] D.D. Ryutov, R.H. Cohen, T.D. Rognlien, et al., Phys. Plasmas **15** (2008) 092501.

[5] M. Kotschenreuther, P. Valanju, S. Mahajan, et al., Phys. Plasmas **14** (2007) 072502.

[6] P. Valanju, M. Kotschenreuther, S. Mahajan et al., Phys. Plasmas **16** (2009) 056110.

[7] B. LaBombard, E. Marmar, J. Irby, et al., Nucl. Fusion **55** (2015) 053020.

[8] F. Wagner, G. Becker, K. Behringer, et al., Phys. Rev. Lett. **49** (1982) 1408.

[9] F. Piras, S. Coda, B.P. Duval, et al., Phys. Rev. Lett. 105 (2010) 155003.

[10] V.A. Soukhanovskii, J.W. Ahn, R.E. Bell, et al., Nucl. Fusion 51 (2011) 012001.

[11] V.A. Soukhanovskii, S.L. Allen, M.E. Fenstermacher, et al., J. Nucl. Mater. 463 (2015) 1191.

[12] B.N. Wan, J.G. Li, H.Y. Guo, et al., Nucl. Fusion **55** (2015) 104015.

[13] D.D. Ryutov, V.A. Soukhanovskii, Phys. Plasma **22** (2015) 110901.

[14] D. Coster et al., Further developments of the edge transport simulation package SOLPS, in: Proc. of

the 19th IAEA Conference, Fusion Energy, TH/P2-13, October, 2002.
[15] B.N. Wan, S.Y. Ding, J.P. Qian, et al., IEEE Trans. Plasma Sci. **42** (2014) 495.
[16] Y.T. Song, S.T. Wu, J.G. Li, et al., IEEE Trans. Plasma Sci. **42** (2014) 503.
[17] Z.P. Luo, B.J. Xiao, Y. Guo, M.Y. Ye, IEEE Trans. Plasma Sci. **42** (2014) 1021.
[18] S.F. Mao, Y. Guo, X.B. Peng, et al., J. Nucl. Mater. **463** (2015) 1233.
[19] P. Stangeby, *The Plasma Boundary of Magnetic Fusion Devices* (Taylor & Francis, 2000).

Relation between magnetic structure and emission of hydrogen and carbon in divertor region of LHD

T.Kobayashi[1], M.Kobayashi[1,2], H.Tanaka[3], M.Goto[1,2], G.Kawamura[1,2], LHD experiment group[2]

[1]SOKENDAI (The Graduate University for Advanced Studies), Toki 509-5292, Gifu, Japan
[2]National Institute for Fusion Science, Toki 509-5292, Gifu, Japan
[3]Graduate School of Engineering, Nagoya University, Nagoya 464-8603, Aichi, Japan

Abstract

Two-dimensional emission distribution has been measured to investigate plasma transport in the edge region of LHD with multi-channel spectrometer. Relation between the emission distribution and the magnetic field structure has been investigated with a field line tracing code. It is suggested that emissions from carbon and hydrogen have correlation in space with divertor legs or magnetic field lines with short connection lengths. It is also found that each region of emission corresponds to different connection length.

1. Introduction

To achieve steady confinement of plasma with divertor configuration, it is important to understand physical mechanism of particle transport in edge region with open field lines. However, effects of the magnetic field structure on divertor plasma are not yet fully understood. Spectroscopic measurement in edge region of LHD has been conducted[1] to investigate edge plasma transport properties. In the present analyses, measured emission distributions have been compared with connection length distribution calculated by magnetic field line tracing.

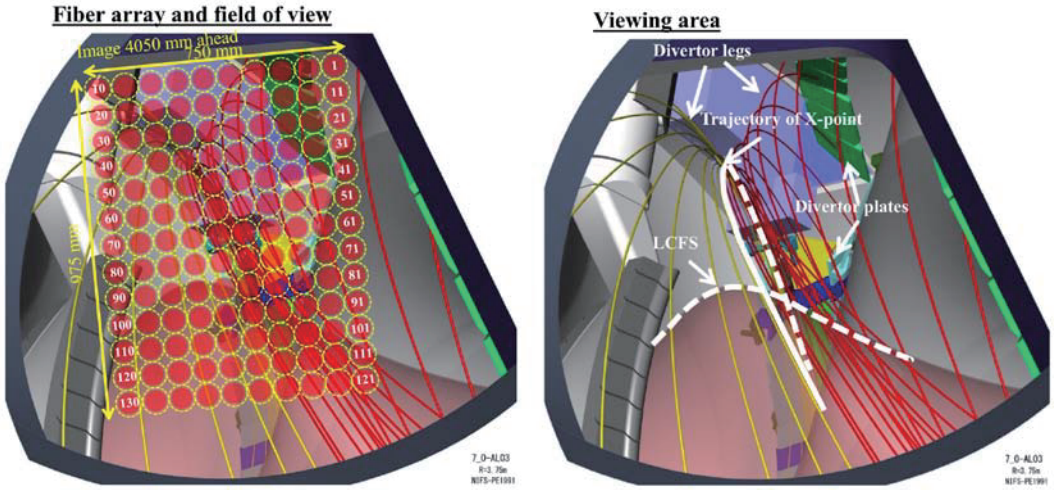

Fig.1 Viewing area

2. Measurement system and its measurement result

The spectrometer used for present experiment equips 130 fibers and uses a CCD camera as a detector.

Two-dimensional emission distribution for visible light can be measured. The viewing area covers LCFS, divertor leg, X-point and divertor plate as shown in fig.1, so the spectrometer can measure emission from impurity and plasma particle in the region from the divertor to the core plasma.

Emission distributions covering transition from attached to detached states with RMP fields have been obtained. In fig.2, emission distributions from carbon and hydrogen of volume recombination are shown. In all the cases, emission distributions change between attached and detached states, and each case has specific shape. It is considered that these global structures are in correlation with the magnetic field geometry, and thus a comparison with magnetic field structure has been conducted.

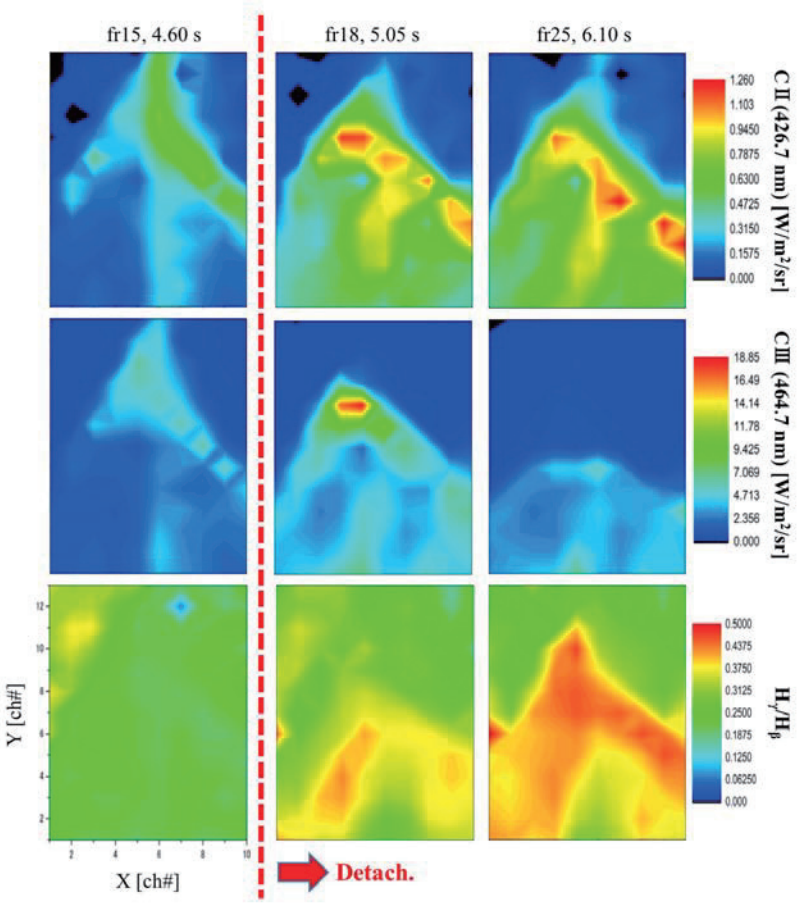

Fig.2 Measurement result

3. Comparison with magnetic field structure

3.1 Comparison with connection length distribution

Emission distributions are compared with the magnetic field structure with KMAG code that can calculate vacuum field of external field coils by Bio-Savart law and can carry out magnetic field line tracing. For comparison with the measurement result, connection lengths are calculated at cross section perpendicular to the line of sight. Fig.3 is the connection length distribution at cross section in the viewing area.

It is confirmed that a part of emissions are outside of LCFS in comparison with emission distribution as shown fig.5. Considering this fact, carbon and hydrogen emissions seem to have relation to divertor leg or magnetic field lines with short connection lengths.

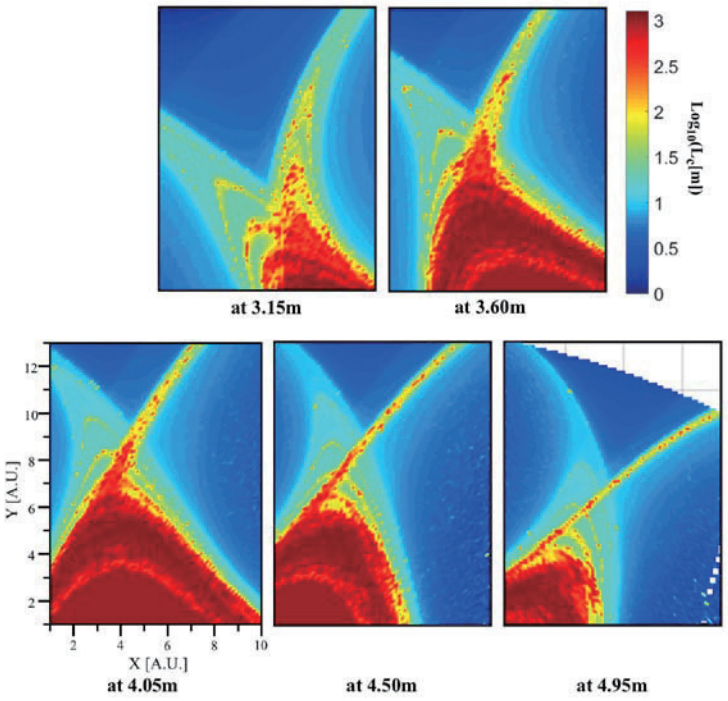

Fig.3 Connection length distribution

3.2 Synthetic diagnostic of emission distribution

By referring to result of section 3.1, the calculation has been conducted by follow procedure to investigate relation between connection length and emission distribution. In this analysis, uniform emission on a selected range of connection length (L_c) is assumed, and two-dimensional emission distribution is reconstructed by line integration along line of sight with connection length distribution at cross section perpendicular to the line of sight calculated every 1cm from the fiber. These results are normalized to unity and are plotted in fig.4. According to the synthetic emission distribution, as the connection length is longer, emission distributions move radially inward. Specifically, synthetic emission distributions move largely between $L_c < 10$ m and 10 m $< L_c < 20$ m.

In the fig.5, boundary lines that are characteristic lines of synthetic emission distribution about $L_c < 10$ m are plotted for comparison measurement result. To find connection length corresponding to emission distribution of CII by synthetic emission distribution, emission distribution was separated into several regions. It is considered that emission is occurred on magnetic field line with connection length less than 10 m by referring that emission region which is out of LCFS is downstream than the boundaries. But emission at the upper part of the image of attached state does not correspond, and correspond to a part of synthetic emission distribution about L_c = 40–60 m. When attached state transitions to detached, the separated regions move the magnetic field line having longer connection length. The region corresponding to divertor leg similarly moves by referring the synthetic emission distribution about L_c = 40–60 m and L_c = 60–80 m. And, it is also confirmed that CIII emission is radially inward than CII. In the present analyses, plasma parameters are not considered, so that physical interpretation of plasma transport is difficult to discuss. But these analyses are useful for future analysis and transport simulation. In this analysis, the emission region of hydrogen could not be fully explained. This reason seems to be that when the reconstruction was done,

emission distribution was not separated into the two divertor legs and the private region. Therefore when this analysis method is improved so, difference between carbon and hydrogen may be mentioned.

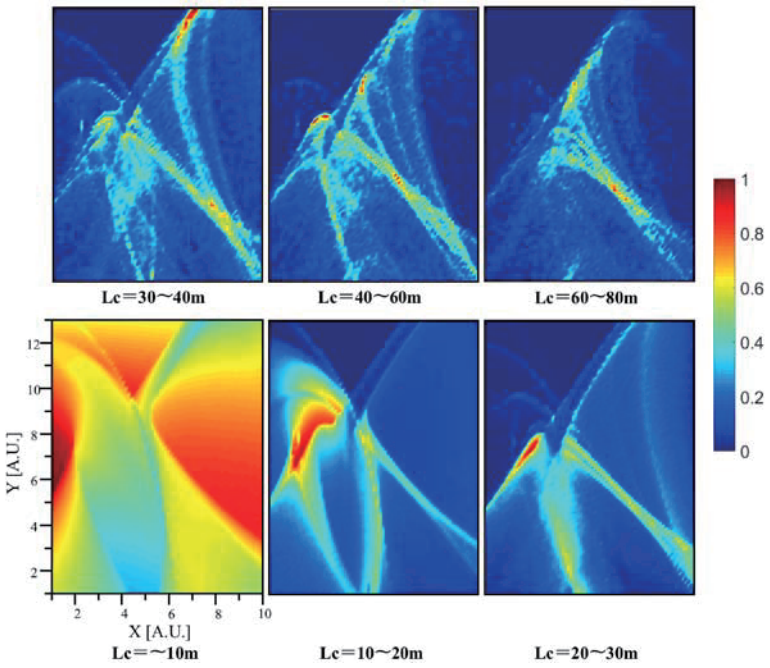

Fig.4 Synthetic emission distribution

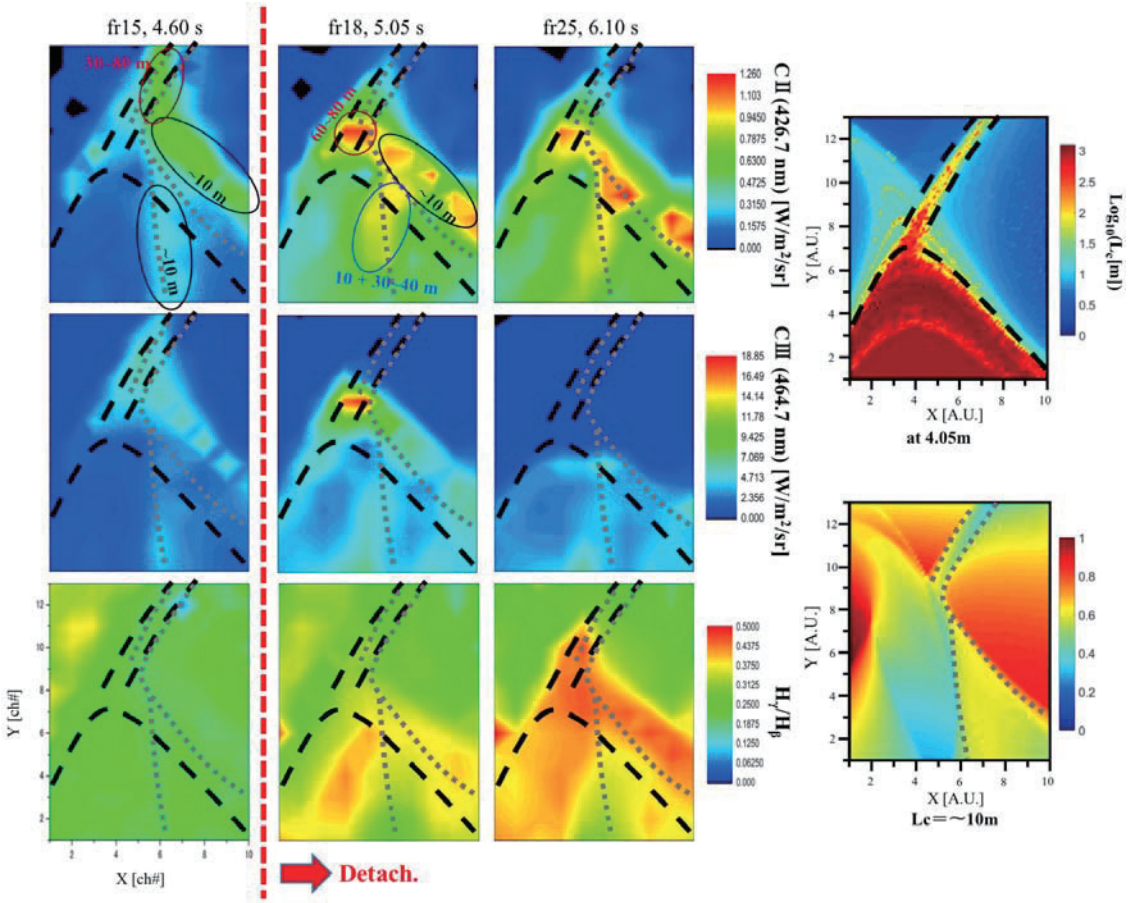

Fig.5 Comparison between emission and magnetic field structure

4. Summary and discussion

In the present analyses, the relation between magnetic field structure and emission distribution obtained by the spectrometer has been investigated in comparison with connection length with emission measurements with spectroscopy in the transition from attached to detached states.

It is understood that global structure of emission distribution has relation with divertor leg and magnetic field lines with short connection lengths based on these analyses. Although the present analyses do not take into account the plasma transport effects, these results are useful information for future analysis with numerical transport simulations. Understanding of the different features of the emission distributions between carbon and hydrogen is also left for future work.

References

[1] M.Kobayashi, et al., 22nd Int'l Conf. on PSI in Controlled Fusion Devices, (2016) Italy

Nonlinear Simulations of Energetic Particle Driven Geodesic Acoustic Mode in 3-Dimensional LHD Equilibrium

H.Wang[1], Y.Todo[1,2], Y.Suzuki[1,2], T.Ido[1]

[1]National Institute for Fusion Science, Toki 509-5292, Gifu, Japan

[2]Graduate University for Advanced Studies, Toki 509-5292, Gifu, Japan

Abstract

Energetic particle driven geodesic acoustic mode (EGAM) in a 3-dimensional Large Helical Device (LHD) equilibrium are investigated using MEGA code. MEGA is a hybrid simulation code for energetic particles interacting with a magnetohydrodynamic (MHD) fluid. The poloidal velocity oscillation is a combination of m/n = 0/0 (strong), 1/0 (medium) and 2/10 (weak) components. This is caused by the LHD configuration, different from the tokamak case. The phenomena of chirping primary mode and the associated half-frequency secondary mode are firstly reproduced with the realistic input parameters and 3-dimensional equilibrium. There are good agreements between simulation and experiment on the frequency chirping of the primary mode, on the excitation of the half-frequency secondary mode, on the mode profile, and on the phase lock. It is found that the bulk pressure perturbation and the energetic particle pressure perturbation cancel out with each other, and thus the frequency of the secondary mode is lower than the primary mode. Also, it is found that the secondary mode is excited by the energetic particles, not by the nonlinear MHD coupling.

1. Introduction

Geodesic acoustic mode (GAM) is an oscillatory zonal flow coupled with density and pressure perturbations in toroidal plasmas. In the last decade, energetic particle driven GAM (EGAM) is observed in Joint European Torus (JET), DIII-D, and Large Helical Device (LHD). In the DIII-D experiment, drops in neutron emission follow the EGAM bursts suggesting beam ion losses. Also, in the LHD experiment, anomalous bulk ion heating during the EGAM activity suggests a GAM channeling. Then, understanding EGAM is important for magnetic confinement fusion where the energetic particles need to be well confined and the bulk plasma need to be efficiently heated. The EGAM has been extensively studied by both the experimentalists and theorists[1-3]. Recently, in LHD, an abrupt excitation of a half-frequency secondary mode was observed when the frequency of a chirping primary EGAM reaches twice of the GAM frequency[4,5].

2. Simulation model and parameters

A hybrid simulation code for energetic particles interacting with a magnetohydrodynamic (MHD) fluid, MEGA, is used for the simulation of EGAMs[6]. In the MEGA code, the bulk plasma is described by the nonlinear MHD equations. The drift kinetic description and the δf particle method are applied to the

energetic particles. A realistic 3-dimensional equilibrium generated by HINT2 code is used for the simulation. This equilibrium data is based on the LHD shot #109031 at time t = 4.94s. At this moment, the EGAM activity is very strong, thus it is good to reproduce the EGAM phenomenon.

In the experiment of LHD, the EGAMs were observed under the bump-on-tail energetic particle distribution. In the present work, a realistic distribution function, which is the same as the experimental observation, is applied. The parameters for the EGAM simulation are based on an LHD experiment, B_0 = 1.5 T, electron density $n_e = 0.1\times10^{19}$ m^{-3}, electron temperature at the magnetic axis T_e = 4 keV, and bulk plasma beta value on the magnetic axis equals to 7.2×10^{-4}. The injected neutral beam energy is E_{NBI} = 170 keV. The safety factor q value is q = 2.82 on the magnetic axis and q = 0.84 on the plasma edge, negative normal shear. The major radius of the magnetic axis is R_0 = 3.7 m. Cylindrical coordinates (R, φ, z) are employed. For LHD equilibrium, there are 10 pitches in the toroidal direction. Since the toroidal mode number of GAM is 0, for simplicity, only 1 pitch is used for the present simulation. The numbers of grid points of this pitch in (R, φ, z) directions are (128, 64, 128), respectively.

3. Simulation Results

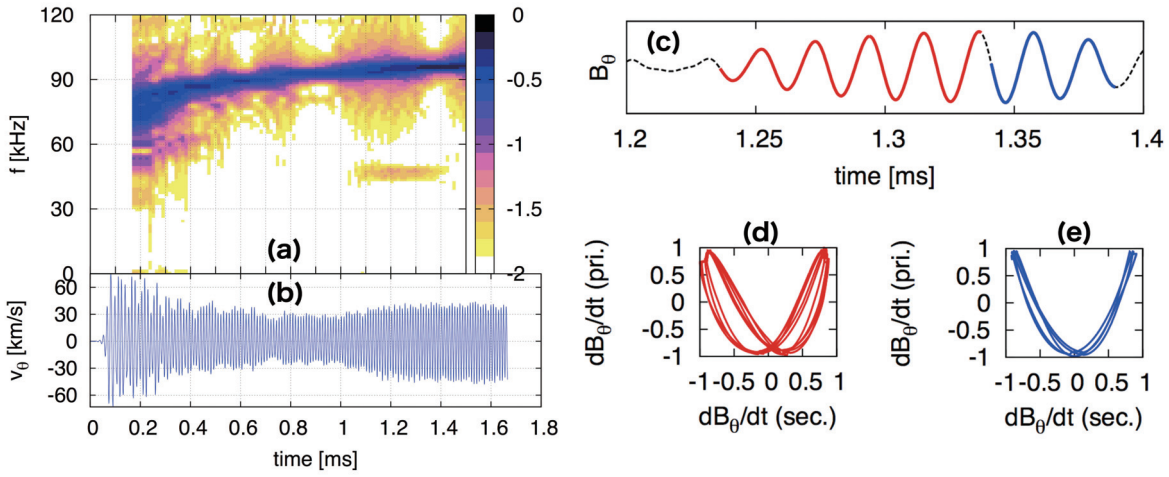

Fig.1 Time evolution of (a) frequency spectrum and (b) poloidal velocity. Panel (c) shows the time evolution of the secondary mode. The Lissajous curves in panel (d) and (e) are plotted in the growth phase and decay phase, respectively.

Both the chirping primary mode and the half-frequency secondary mode are reproduced by the MEGA code, as shown in Fig.1. The primary mode frequency chirps from 70 kHz. The mode is saturated at t = 0.07 ms, and then, steps into the nonlinear phase. At t = 1.1 ms, the frequency of the primary mode reaches to 96 kHz, and a secondary mode with frequency f = 48 kHz is excited. The simulated phenomenon is very similar to the experimental observation, as shown in Fig.2 of Ref.[4]. The Lissajous curves are also shown in order to demonstrate the phase lock between the primary mode and the secondary mode. The frequency relation between these modes is double. The Lissajous curves are similar with the experimental measurements. This is the first time to reproduce both the primary mode and secondary mode with 3-dimensional model and realistic input parameters.

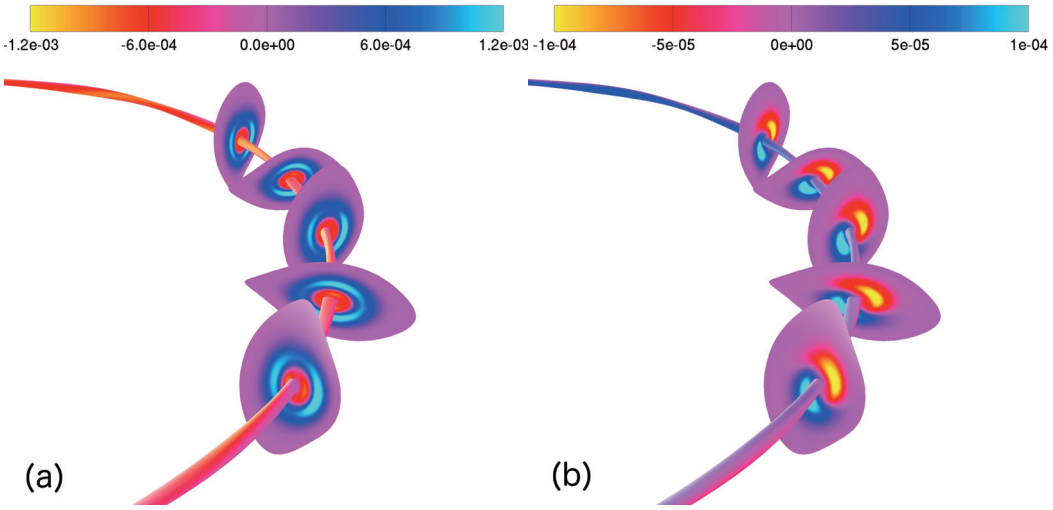

Fig.2 The mode profiles of (a) v_θ and (b) δP_{bulk} in the 3-dimensional form.

The mode profiles of poloidal velocity v_θ and bulk pressure perturbation δP_{bulk} are plotted in 3-dimensional figures, as shown in Fig. 2. The 5 slices in each panel represent 5 poloidal cross-sections, and their toroidal positions are from $\varphi = 0$ to $\varphi = 0.4\pi$ with toroidal interval of 0.1π. Figure 2 shows that the dominant components of v_θ and δP_{bulk} are m/n = 0/0 and 1/0, respectively. Also, further analyses show that both the primary mode and the secondary mode are global. The mode number and the mode structure are consistent with the experiment, as shown in Fig. 4 of Ref.[4]. The poloidal velocity v_θ is a combination of m/n = 0/0 (strong), 1/0 (medium) and 2/10 (weak) components. The m/n = 2/10 components exists due to the LHD configuration. In LHD, there are 10 pitches in the toroidal direction, and there are 2 high field regions and 2 low field regions in the poloidal direction. This is the first simulation of EGAM in the 3-dimensional LHD configuration. The mode number is different from the tokamak case, where the v_θ oscillation is a combination of m/n = 0/0 and 1/0 components.

Both the primary mode and the secondary mode are the EGAMs. The question then arises as to why a same mode has 2 different frequencies. In order to clarify the reason, the bulk plasma pressure perturbation δP_{bulk} and the energetic particle pressure perturbation $\delta P_{h\parallel}$ are analyzed, as shown in Fig. 3. For the primary mode, the phase of δP_{bulk} and $\delta P_{h\parallel}$ are the same. Compared with v_θ, the phase of pressure is 0.5π earlier. The primary mode is driven by both δP_{bulk} and $\delta P_{h\parallel}$. For the secondary mode, the phase difference between δP_{bulk} and $\delta P_{h\parallel}$ is π. They cancel out with each other. Thus, the frequency of the secondary mode is much lower than the primary mode.

In order to clarify the effects of the fluid nonlinearity, another special linear MHD model is applied. In the present work, simulations are run in 2 steps. In the 1st step, the nonlinear code is run, until time t = 0.97 ms when the EGAM is completely saturated but the secondary mode has not been excited yet. Then, in the 2nd step, both the linear and nonlinear MHD codes are run separately from the end of the run of the 1st step. In the 2nd step, the secondary mode appears in both runs. In other words, the secondary mode can be excited even if the MHD equations are linearized. This result is different from that in Ref.[5]. In the present work, the excitation of the secondary mode is only caused by the kinetic nonlinearity, while the fluid nonlinearity hardly works.

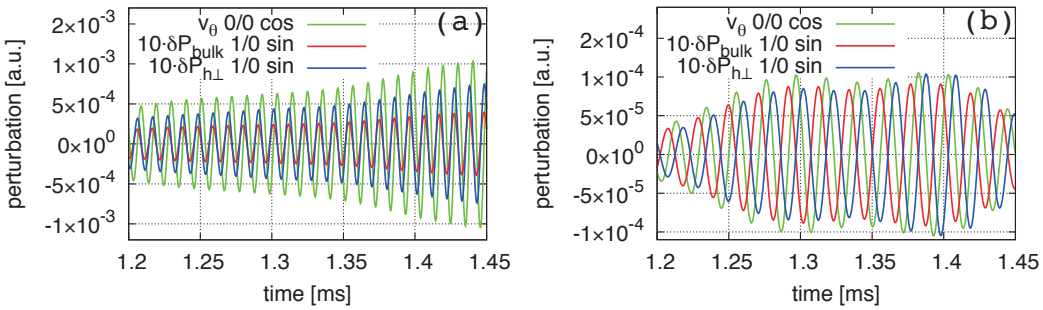

Fig.3 The v_θ, δP_{bulk} and $\delta P_{h\parallel}$ oscillation of (a) primary mode and (b) secondary mode.

4. Summary

In summary, 3 conclusions are obtained in the present work. Firstly, the simulation of EGAM in the realistic 3-dimensional equilibrium is obtained for the first time, and the results are very similar to the experimental observation. It is found that the poloidal velocity oscillation is a combination of m/n = 0/0 (strong), 1/0 (medium) and 2/10 (weak) components. This is different from the tokamak case. Secondly, the chirping EGAM and the associated secondary mode are reproduced with the 3-dimensional model and realistic parameters for the first time. The results are good validations of the simulation. It is found that the phase differences between δP_{bulk} and $\delta P_{h\parallel}$ is π for the secondary mode. The δP_{bulk} and $\delta P_{h\parallel}$ cancel out with each other, and thus, the frequency of the secondary mode is much lower than the primary mode. Thirdly, it is found that the fluid nonlinearity doesn't work for the excitation of the secondary mode.

Acknowledgements

This work was partly supported by the JSPS-NRF-NSFC A3 Foresight Program in the field of Plasma Physics (NSFC: No.11261140328, NRF: No.2012K2A2A6000443).

References

[1] R.Nazikian, G.Fu, M.Austin et al., Phys. Rev. Lett. **101** (2008) 185001.

[2] G.Fu, Phys. Rev. Lett. **101** (2008) 185002.

[3] H.Wang, Y.Todo, C.Kim, Phys. Rev. Lett. **110** (2013) 155006.

[4] T.Ido, K.Itoh, M.Osakabe, et al., Phys. Rev. Lett. **116** (2016) 015002.

[5] M.Lesur, K.Itoh, T.Ido, et al., Phys. Rev. Lett. **116** (2016) 015003.

[6] Y.Todo, T. Sato, Phy. Plasmas, **5** (1998) 1321.

Measurement and characterization of turbulent fluctuations in KSTAR plasmas

W.Lee[1], S.H.Ko[1], M.J.Choi[1], J.Leem[2], G.S.Yun[2], H.K.Park[1,3], W.X.Wang[4], R.V.Budny[4], N.C.Luhmann,Jr.[5], K.W.Kim[6], and the KSTAR team

[1]National Fusion Research Institute, Daejeon 34133, South Korea
[2]Pohang University of Science and Technology, Pohang, Gyeongbuk 37673, South Korea
[3]Ulsan National Institute of Science and Technology, Ulsan 44919, South Korea
[4]Princeton Plasma Physics Laboratory, Princeton, New Jersey 08543, USA
[5]University of California at Davis, Davis, California 95616, USA
[6]Kyungpook National University, Daegu 41566, South Korea

Abstract

In KSTAR L-mode plasmas heated by tangential neutral beam injection (NBI), broadband turbulent fluctuations with peak frequencies at 150−400 kHz were observed in the core region by the multichannel microwave imaging reflectometer (MIR) system. Poloidal wavenumbers of the unstable modes were determined from the peak frequencies and poloidal rotation velocities in the laboratory frame. The experimentally estimated poloidal wavenumbers of 2−3 cm^{-1} were consistent with those predicted by linear and nonlinear gyrokinetic simulations. Spatial and temporal scales of the fluctuations were compared with equilibrium parameters relevant to the ion gyroscale turbulence and they showed linear relations to the parameters, indicating that the measured broadband fluctuations are the ion gyroscale turbulence.

1. Introduction

Short-wavelength and small-amplitude fluctuations in the plasma density and potential driven by micro-instabilities such as ion temperature gradient (ITG) mode, trapped electron mode (TEM), and electron temperature gradient (ETG) mode can be responsible for anomalous transports of energy and particle across the magnetic field. Recent studies about a type of MHD instability, edge localized mode (ELM) crash, have reported that turbulence can interact with ELMs when magnetic perturbations are applied and the nonlinear interactions can result in suppression or mitigation of the ELM crashes [1, 2]. Therefore, understanding and then controlling turbulence driven by the micro-instabilities are critical issues in fusion research. In this regard, measurement and characterization of turbulent fluctuations are important.

In L-mode plasmas heated by tangential neutral beam injection (NBI) in the co-current direction, ion gyroscale density fluctuations were measured by an imaging diagnostic, microwave imaging reflectometer (MIR) system [3, 4, 5] and their characteristics such as the frequencies in the laboratory frame, poloidal wavenumbers, poloidal spatial scales, and temporal scales were investigated.

2. The KSTAR MIR system

Ion gyroscale electron density fluctuations have been measured by the MIR system. The initial MIR system measured density fluctuations with the poloidal wavenumber up to ~4 cm^{-1} through an detector array of vertically aligned 16 detectors and wide-aperture imaging optics [3, 4]. The poloidal spot size was ~1 cm in FWHM (or ~1.6 cm in $1/e^2$ width) and the space between adjacent poloidal channels was ~0.6 cm. Both the poloidal spot size and space slightly changed depending on the radial measurement position so that they were larger in the outer region. The radial space with 4.0 GHz step of the probing frequencies is ~5 cm in L-mode density profiles. The measurement region can be remotely position from the plasma core to the outboard edge by changing the probing frequencies from 78 GHz to 92 GHz and the lens positions in between discharges. The maximum time resolution was 0.5 μs with the sampling rate of up to 2 MHz.

The initial system has been upgraded for the last two years [5]. The number of radial channels increased from 2 to 4 by increasing the number of probing frequencies and this provides 2D (4×16 in the radial and poloidal directions) measurements of fluctuations. With a new detector array and the improved imaging optics, the poloidal spot size is reduced to ~0.7 cm in FWHM or ~1.1 cm in $1/e^2$ width (~30% improvement) so that the detectable poloidal wavenumbers are increased up to ~5 cm^{-1}. The maximum time resolution is reduced to 0.25 μs with the doubled sampling rate of up to 4 MHz.

Note that the experimental data discussed in the following sections were obtained with the initial system.

3. Frequencies of unstable modes in NBI L-mode plasmas

In stationary phases of L-mode discharges (B_{t0} = 3.0−3.3 T and I_p = 600 kA) heated by ~1.4 MW neutral beam injection (NBI) in the co-current direction, broadband fluctuations with peak frequencies at 150−400 kHz were observed in the core region of $r/a \sim 0.4$−0.7 [5, 6]. Figure 1(a) shows the temporal evolution of parameters of an NBI L-mode discharge (#9010). The peak frequencies, which are interpreted as the frequencies of dominant or unstable modes in this manuscript, were determined from frequency spectra or cross correlation spectra (or coherence) when the peak frequencies are not clearly recognized from the frequency spectra. In Figs. 1(b)−1(d), the fluctuation frequency is not clear in the frequency spectrum whereas a broadband (~200−500 kHz) fluctuation with its peak at ~280 kHz can be recognized in the coherence analysis. Note that a low-frequency (< 200 kHz) broadband fluctuation also can be found from the coherence analysis.

The measured frequencies are consistent with predicted ones from a spectral shift model in which the observed fluctuation frequency in the laboratory frame ($f_{\rm Lab} = \omega_{\rm Lab}/2\pi$) is the shifted one from an intrinsic frequency ($\omega_0/2\pi$) due to the equilibrium $E \times B$ flow velocity ($U_{E\times B}$) [7, 8, 9, 10]

$$\omega_{\rm Lab}/2\pi = (k_\perp U_{E\times B} + \omega_0)/2\pi, \tag{1}$$

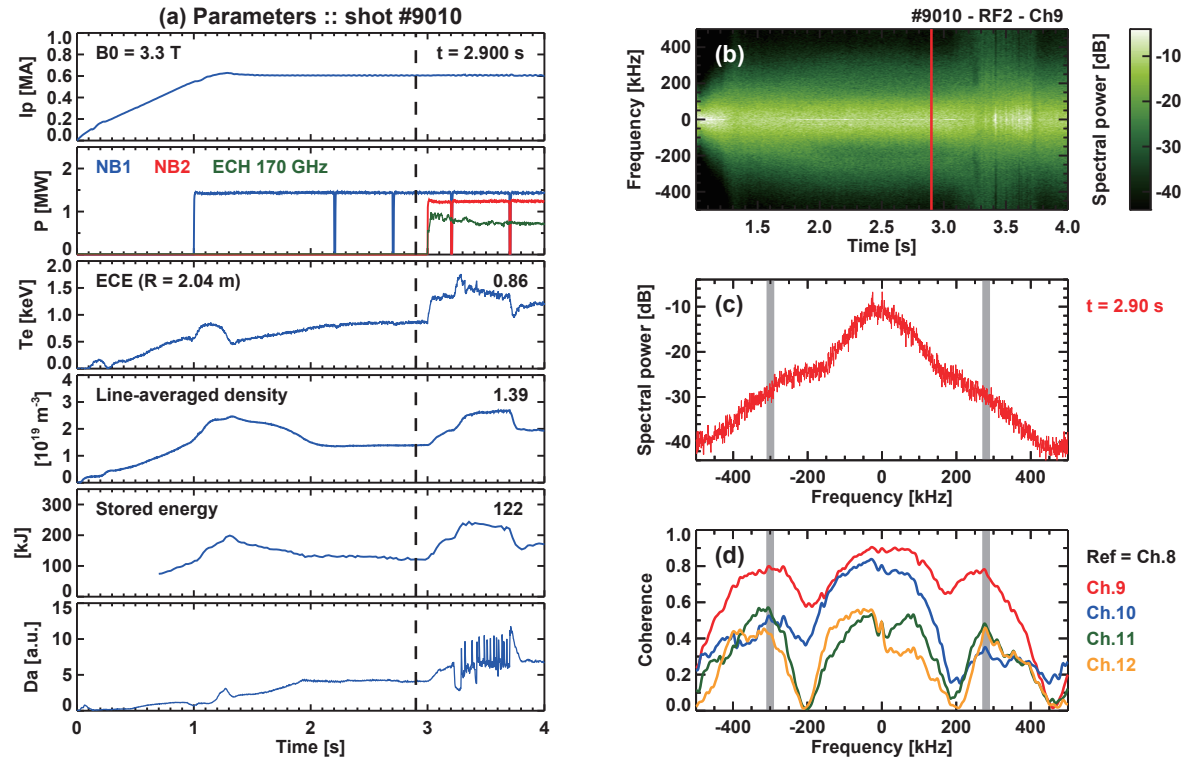

Fig. 1. (a) Time traces of parameters of an NBI L-mode discharge #9010. Frequency analysis results for the fluctuations measured at $R \sim 2.1$ m in the discharge #9010: (b) spectrogram of a center channel 8, (c) frequency spectrum at $t = 2.9$ s, and (d) cross coherences of the channels from 9 to 12 with respect to channel 8 [5].

where $k_\perp$ is the fluctuation wavenumber in the direction perpendicular to the magnetic field line. The intrinsic frequency is the fluctuation frequency in the plasma frame where the equilibrium radial electric field is zero. The intrinsic frequencies were predicted from linear gyrokinetic simulations using the GYRO code [11] and they are less than ∼11 kHz for the analyzed NBI L-mode discharges.

4. Poloidal wavenumbers of unstable modes

In order to estimate the dominant poloidal wavenumbers (k_θ) of the fluctuations, one needs to obtain poloidal rotation velocities of fluctuations (v_θ) as well as the frequencies using a simple relation [5]

$$2\pi f_{\mathrm{Lab}} = k_\theta v_\theta. \tag{2}$$

Mean poloidal rotation velocities of fluctuations can be obtained by applying a time-delayed cross correlation analysis to the signals from 16 poloidal channels of the MIR system. The meaning of the mean poloidal rotation velocity obtained using the cross correlation analysis was well explained in references [10, 12], where the poloidal rotation velocity is called as the apparent poloidal velocity since it is neither the velocity of the plasma poloidal flow nor the intrinsic phase velocity of fluctuations. The apparent poloidal velocities in the core region ($r/a \sim 0.4$–0.7) of the NBI L-mode plasmas were 4–9 km/s in the clockwise (or ion diamagnetic drift) direction.

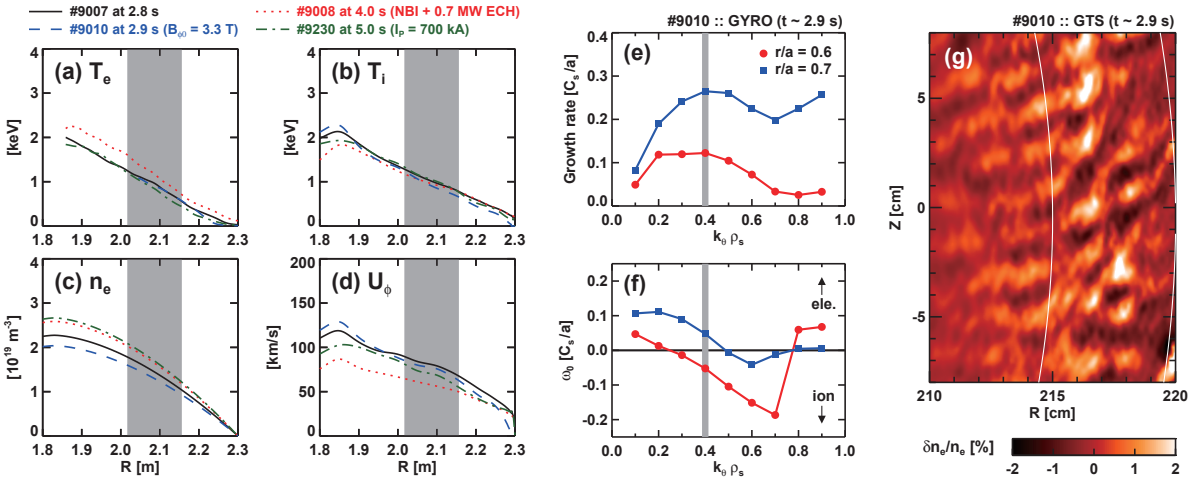

Fig. 2. Radial profiles of parameters of the NBI L-mode discharges: (a) electron temperature, (b) ion temperature, (c) electron density, and (d) safety factor [6, 10]. The measurement region ($r/a \sim 0.4$–0.7) is colored gray. Linear gyrokinetic simulation with the GYRO for the discharge #9010: normalized wavenumber spectra of (e) the linear growth rates and (f) intrinsic angular frequencies of linear modes [5]. (g) Nonlinear gyrokinetic simulation of electron density fluctuations with GTS for the same discharge [10].

Note that the clockwise apparent poloidal rotation in the core region is due to the fast plasma toroidal rotation. The apparent poloidal rotation speed at $R \sim 2.1$ m in the discharge #9010 was ~5.6 km/s. The dominant poloidal wavenumbers of the measured fluctuations deduced from equation (2) are ~3 cm^{-1} for the discharge.

Linear stability analysis using the GYRO was carried out with the plasma parameters as shown in Fig. 2(a-d). Note that the plasma flows and their shears were not included in the linear calculations. The calculation results predicted that turbulence is most unstable at wavenumbers of $k_\theta \sim 2$–3 cm^{-1} or $k_\theta \rho_s \sim 0.4$ as shown in Fig. 2(e), where $\rho_s = \sqrt{m_i T_e}/eB$ is the ion gyroradius at the electron temperature with m_i the ion mass, e the electron charge, and B the total magnetic field strength. The intrinsic frequencies at the unstable wavenumbers are $\omega_0/2\pi = 3$–11 kHz or $|\omega_0| < 0.15\, C_s/a$ for the analyzed NBI L-mode discharges, where $C_s = \sqrt{T_e/m_i}$ is the sound speed and a is the minor radius. The intrinsic frequencies are significantly smaller than the measured peak frequencies of 150–400 kHz. The calculated dispersion relations, real angular frequencies versus normalized poloidal wavenumbers, indicate the propagation directions of the intrinsic phase velocities in the plasma frame. Note that the modes with positive (or negative) ω_0 propagate in the electron (or ion) diamagnetic drift direction. Figure 2(f) shows that the unstable modes in the discharge #9010 can be either ITG modes or TEMs. The turbulence in the discharge #9010 was modeled with a nonlinear gyrokinetic code, GTS [13, 14], with full kinetic electrons and ions including the plasma rotation and shear effects. In the saturated phase of the simulation result, the dominant wavenumber ($k_\theta \sim 2$–3 cm^{-1} or $\lambda \sim 2$–3 cm as shown in Fig. 2(g)) of the turbulent structures are consistent with those from the linear gyrokinetic simulation and measurement.

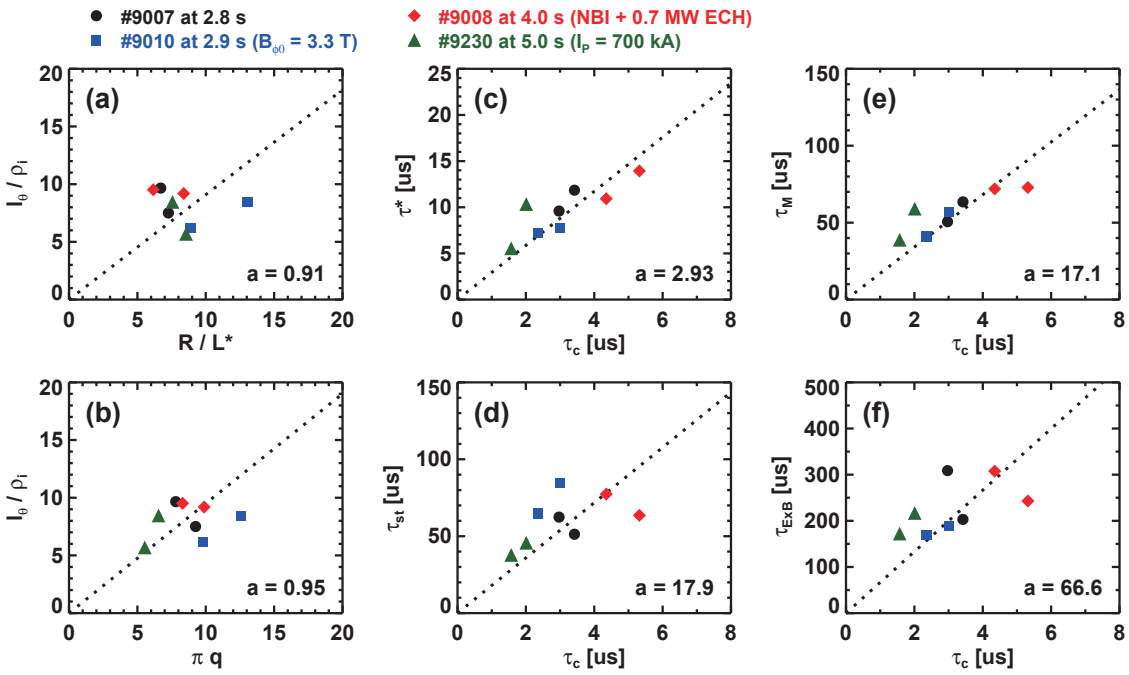

Fig. 3. Normalized poloidal correlation length versus (a) normalized gradient R/L_* and (b) safety factor for the NBI L-mode discharges [10]. The relationship between the correlation time τ_c and four parameters relevant to the ion-scale turbulence: (c) ion drift time, (d) parallel ion streaming time, (e) magnetic drift time, and (f) inverse $E \times B$ shearing rate.

5. Spatial and temporal scales

Spatial and temporal scales, poloidal correlation length (ℓ_θ) and correlation time (τ_c), of the fluctuations measured in the NBI L-mode discharges were analyzed using the cross correlation analysis and compared with local equilibrium parameters [10]. Since the turbulence is known to be driven by radial gradients of equilibrium temperature and density, the poloidal correlation lengths normalized to ion gyroradii (ℓ_θ/ρ_i), where $\rho_i = \sqrt{m_i T_i}/eB$ is the ion gyroradius, were compared with the normalized gradients R/L_*, where $L_* = \min(L_{T_i}, L_{n_e})$. Here, L_{T_i} and L_{n_e} are the scale lengths of ion temperature and density, respectively. In Fig. 3(a), the normalized poloidal correlation lengths are $\ell_\theta/\rho_i \approx 5{-}10$, meaning that the measured fluctuations are at the ion gyroscale. However, they did not show clear linear dependence on the radial gradient in this small data set.

The correlation time of the measured fluctuations ($\tau_c \approx 2{-}6$ μs) was compared with four equilibrium quantities relevant to the ion gyroscale turbulence: the ion drift time τ_* (associated with the temperature and density gradients), parallel ion streaming time $\tau_{\rm st}$ along the magnetic field (associated with the turbulence parallel scale), magnetic drift time τ_M (associated with ∇B and curvature drift), and inverse $E \times B$ shearing rate (It is well known that turbulence is stabilized by the $E \times B$ flow shear) [10, 15]. Figures 3(c)$-$3(f) show linear dependence especially on the drift time and magnetic drift time. In a spherical tokamak, the correlation time was comparable with three quantities as $\tau_c \sim \tau_* \sim \tau_{\rm st} \sim \tau_M$ and the measured turbulence was called

critically balanced [15], while it is about a third of the ion drift time and is much smaller than the parallel streaming time and magnetic drift time as $\tau_{\rm st} \sim \tau_M \sim 17\,\tau_c$ in this experiment. Since $\tau_{\rm st} \sim \tau_M$, it can be found that $\ell_\theta/\rho_i \sim \ell_\parallel/R \sim \pi q$, which is plotted in Fig. 3(b).

6. Summary

In KSTAR L-mode discharges heated by ∼1.4 MW tangential neutral beam injection in the co-current direction, broadband turbulent fluctuations with their peak frequencies at 150−400 kHz were observed in the core region ($r/a \sim 0.4$−0.7) by the multichannel (poloidal 16 and radial 2) MIR system. The poloidal wavenumbers of the unstable modes were determined from peak frequencies and poloidal rotation velocities in the laboratory frame. The peak frequencies were determined from cross correlation spectra (or coherence) and the poloidal rotation velocities were calculated using a time-delayed cross correlation analysis. The measured frequencies (and poloidal rotation velocities) are strongly affected by the $E \times B$ flow velocities and significantly larger than the intrinsic frequencies in the plasma frame, which were predicted from linear gyrokinetic simulations with the GYRO. The experimentally estimated poloidal wavenumbers of 2−3 cm^{-1} were consistent with the wavenumbers of the unstable modes predicted by linear and nonlinear gyrokinetic simulations.

The spatial and temporal scales of the measured fluctuations were estimated by the cross correlation analysis. The poloidal correlation lengths normalized to ion gyroradii indicated that the measured fluctuations are at the ion gyroscale ($\ell_\theta/\rho_i \approx 5$−$10$) but do not seem to be dependent on the radial gradients of ion temperature and density from the small data set. Instead, the normalized poloidal correlation lengths seem to linearly depend on the safety factor. The correlation time ($\tau_c \approx 2$−6 μs) shows clear linear relationship with the local equilibrium parameters relevant to the ion gyroscale turbulence. These results indicate that the measured broadband fluctuations are ion gyroscale turbulence.

Acknowledgements

This work was supported by the KSTAR project contract funded by the Ministry of Science, ICT and Future Planning and the NRF of Korea under contract no. NRF-2014M1A7A1A03029865. And this work was partly supported by the JSPS-NRF-NSFC A3 Foresight Program in the field of Plasma Physics (NSFC: No.11261140328, NRF: No.2012K2A2A6000443).

References

[1] G.R.McKee, Z.Yan, C.Holland, et al., Nucl. Fusion **53** (2013) 113011.
[2] J.Lee, G.S.Yun, M.J.Choi, et al., Phys. Rev. Lett. **117** (2016) 075001.
[3] W.Lee, J.Leem, G.S.Yun, et al., J. Instrum. **8** (2013) C10018.
[4] W.Lee, J.Leem, J.A.Lee, et al., Nucl. Fusion **54** (2014) 023012.
[5] W.Lee, J.Leem, G.S.Yun, et al., Rev. Sci. Instrum. **87** (2016) 11E134.
[6] W.Lee, S.H.Ko, J.Leem, et al., Nucl. Fusion, submitted.

[7] R.A.Koch, et al., Phys. Fluids **21** (1978) 1236.
[8] C.X.Yu, et al., Phys. Fluids B **4** (1992) 381.
[9] K.L.Wong, et al., Phys. Lett. A **236** (1997) 339.
[10] W.Lee, et al., Phys. Plasmas **23** (2016) 052510.
[11] J.Candy and R.E.Waltz, J. comput. Phys. **186** (2003) 545.
[12] Y.-c.Ghim, et al., Plasma Phys. Control. Fusion **54** (2012) 095012.
[13] W.X.Wang, et al., Phys. Plasmas **13** (2006) 092505.
[14] W.X.Wang, et al., Phys. Plasmas **17** (2010) 072511.
[15] Y.-c.Ghim, et al., Phys. Rev. Lett. **110** (2013) 145002.

Cooperative research of spectroscopy diagnostics on HL-2A tokamak

Yi Yu[1], Min Xu[2,*], Yifan Wu[1,2], Rui Ke[2,3], Boda Yuan[1,2], Lin Nie[2], Ting Long[2], Shaobo Gong[1,2], Dong Guo[2], George McKee[4] , Zheng Yan[4] ,Ray Sharples[5], Joe Allcock[5], John Howard[6], Zhongbing Shi[2], Wulv Zhong[2], Shifeng Mao[1], Xuru Duan[1,2], Minyou Ye[1]

[1] School of Nuclear Science and Technology, University of Science and Technology of China, Jinzhai Road 96#, 230026, Hefei, China

[2]Southwestern Institute of Physics, #3, 3rd Section, South of 2nd Ring Road, 610041, Chengdu, China

[3]Tsinghua University, Shuangqing Road #30, 100084 Beijing, China

[4]University of Wisconsin-Madison, 975 University Avenue. 53706, Madison, USA

[5]Durham University, South Road, DH1 3LE, Durham, United Kingdom

[6]Australian National University, ACT 2601, Canberra, Australia

Abstract

In this article we present the cooperative research of spectroscopy diagnostics between SWIP (Southwestern Institute of Physics) and USTC (University of Science and Technology of China). Three spectroscopy diagnostics, i.e., Beam Emission Spectroscopy, Multi-Color Gas Puffing Imaging, and Coherence Imaging Spectroscopy, are developed on HL-2A tokamak in recent years.

1. Introduction

Anomalous transport in tokamak plasma is believed to be induced by turbulence. Diagnostics are the most important for collecting experimental data in investigation of the underlying mechanism of turbulence. After research of a long period, it is found that turbulence in tokamak plasma is a wide-spectrum phenomenon. To investigate some of the important front physics, such as L-H transition, shear flow, inner transport barrier, demands have been put on diagnostics for much higher temporal and spatial resolution. In the last decades, many excellent new idea for plasma diagnosing with a high temporal and spatial resolution at the order of μs is put forward and put into practice, such as microwave diagnostics of Electron Cyclotron Emission Image (ECEI) [1,2] and Doppler Reflectometer [3]. Among all of this diagnostics, spectroscopy diagnostics develop very quickly in recent years, and these diagnostics partly benefit from the great progress of high quality spectrometer and the wide usage of Neutral Beam Injection in large tokamaks.

Focusing on the research on turbulence, the Emission Spectrum Laboratory (ESL) in Southwestern Institute of Physics (SWIP) was established about two years ago, of whom the main work is developing diagnostics with high temporal and spatial resolution. In this article, we present the overview of four sets of diagnostics developed in this laboratory. The rest sections of this article is organized as follows: in section 2~4, we present the developing of Beam Emission Spectroscopy, Multi-Color Gas Puffing Imaging, and Coherence Imaging Spectroscopy on HL-2A tokamak, respectively, and in section 5 a summary.

2. Beam Emission Spectroscopy

BES [4,5] diagnostic is an active diagnostic basing on NBI. The particles from neutral beam will

collide with the ion and electron in the plasma, and de-excite to lower state, radiating light with a certain wavelength. The angle between the view line and the neutral beam will induce Doppler shift and result in a separating peak at a shifted wavelength from the background Dα signal. The fluctuation of electron density is proportional to the intensity of spectrum.

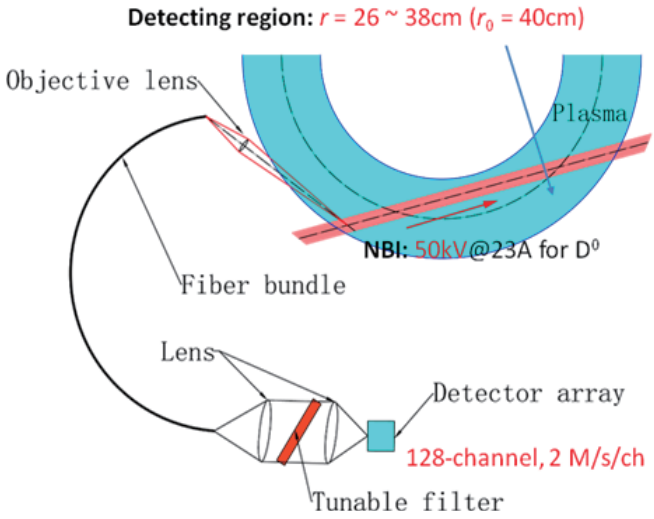

Figure 1, BES diagnostic on HL-2A

Figure 1 shows the sketch of the BES diagnostic on HL-2A tokamak, which includes objective lens, fiber bundle, filter, pre-amplifier, detector array, and data acquasition system. 6 fibers are packed compactly together as one BES transmit channel, as shown if figure 2, and there are totally 128 channels to diagnose a 20cm×10cm rectangular view area in the cross section.

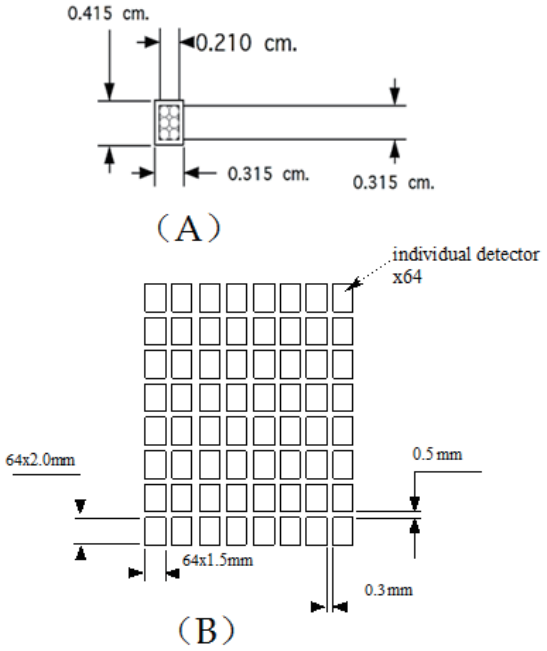

Figure 2, (A) 6 fibers packed together as one channel; (B) half of the 128 BES channels.

This diagnostic has a high quantum efficiency of over 80%. It is used to catch the visible light with a wavelength between 658.5 and 662 nm, and the pronounced peaks of carbon emission near 657.8 and 658.3 are effectively filtered. This system has a temporal resolution of 2 MHz and a spatial resolution of 1-2 cm, according to different view position in the cross section.

3. Multi-Color Gas Puffing Imaging

When we puff neutral particles into the plasma, the particles and the electron in the plasma will collide and radiate light because of de-excitation. Figure 3 shows the ratio between the intensity with two different wavelength (667nm and 728 nm). As one can see, the relationship between the electron density ne and the ratio does not change much at different electron temperature Te. So, it is a good measurement of electron density. Similar relationship can also be seen between the electron temperature and the ratio of light intensity at another two wavelength (728 nm and 706 nm), and it's a good measurement of electron temperature. It is to be noted here that this relationship only applicable in the range of $2\times10^{18}m^{-3}<n_e<2\times10^{19}m^{-3}$ and $10eV<kT_e<250eV$ [6].

As one can see, the most important thing for this diagnostic is to successively filter out the light at three different wavelength of 667 nm, 706 nm and 728 nm. The main sketch of this GPI diagnostic is shown in figure 3.

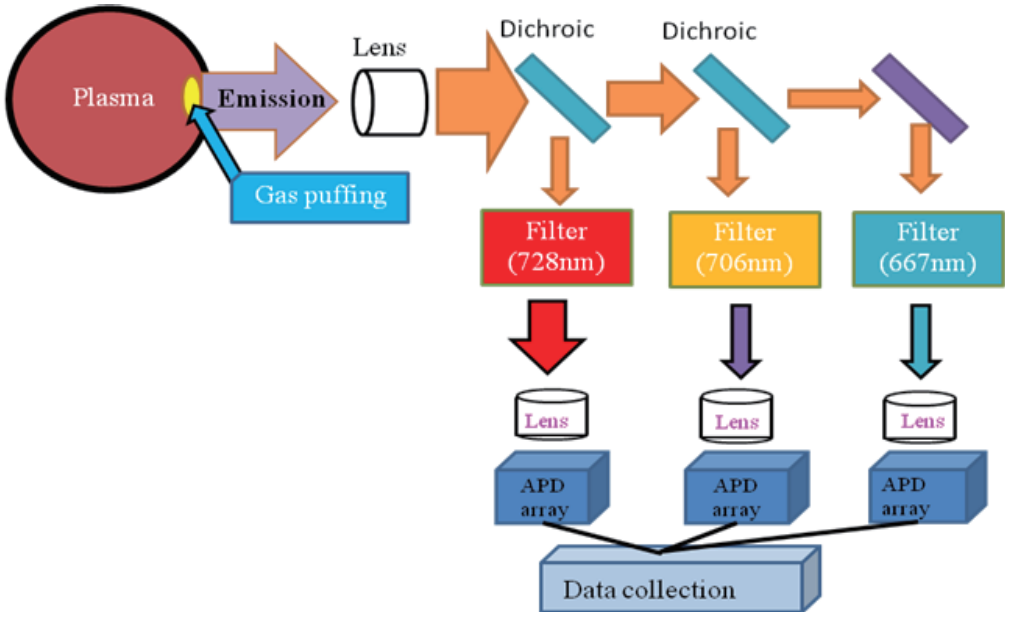

Figure 3, the sketch of Multi-Color Gas Puffing Imaging

A light splitter works as one of the main components in the light path. It can filter out the light at a wavelength of 450nm-610nm, 660nm-670nm, 707nm and 728nm, respectively. A fast camera of Phantom V2010/1 works as the main detection component. It can take photos with a speed of 700k f/s at a resolution of 64×64 pixels.

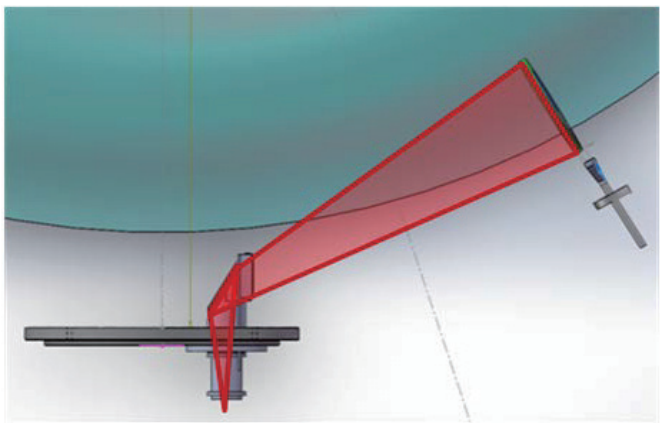

Figure 4, the view area of Multi-Color GPI diagnostic.

The view area of this diagnostic on HL-2A is shown in figure 4. Obviously, it is a kind of edge plasma diagnostic and is not suitable for core plasma. This limitation comes from two inevitable reasons. One is that this kind of diagnostic works only in a small range of plasma parameter as was talked about in the first paragraph of this section. The other reason is that the gas can not puff deeply into the plasma. This diagnostic has a spatial resolution of 5mm×5mm and a temporal resolution of 1-10 μs. The view area in HL-2A plasma is 130mm×130mm in the edge.

4. Coherence Imaging Spectroscopy

The basic principle of CIS is to diagnose the plasma velocity from the wavelength which is calculated from the distance between interference fringes. The changing of phase and the velocity follow:

$$\frac{\Delta\phi}{\kappa\phi_0} \approx \frac{v \cdot l}{c}$$

Figure 5 shows the sketch of the CIS system on HL-2A. The parallel light from the lens firstly passes through a polarizer and transform to linearly polarized light, and then through a delay plate to two 45° polarized lights. A savart plate is used to change the lights to two spatial separated lights, and another polarizer changes the lights to two light with the same polarized direction. The coherent image of these lights will be induced into the detector.

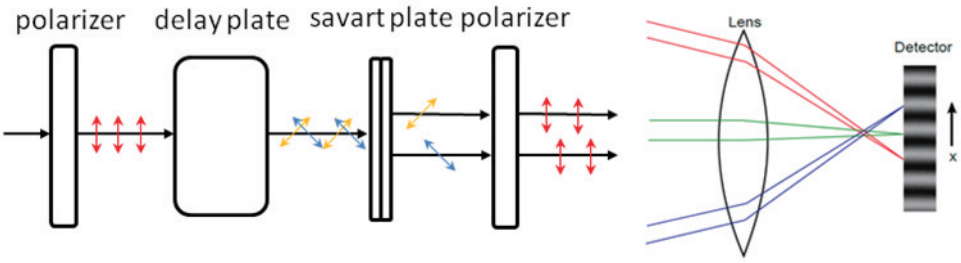

Figure 5, sketch of the CIS system on HL-2A.

The CIS system on HL-2A can catch images with pixels of 64×64 (changeable). It has a spatial

resolution of 1 cm and the temporal resolution is better than 1 ms. It can diagnose the plasma with a view area of 160mm×160mm at edge. Figure 6 shows the first result of CIII intensity image caught by this diagnostic in the last champion in 2016 autumn. More analysis of data is needed and will be discussed carefully elsewhere.

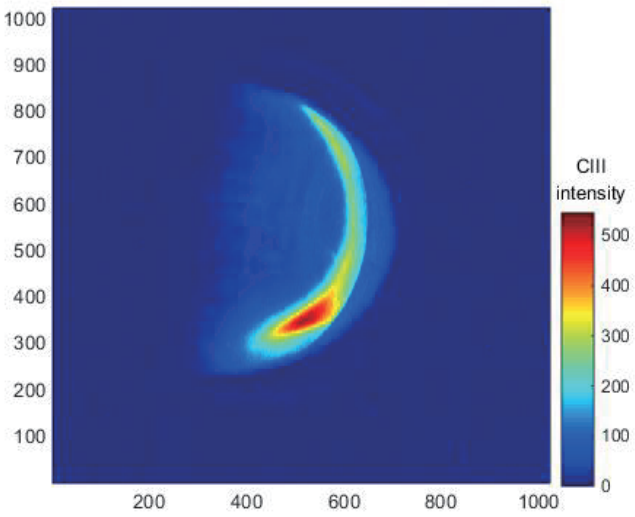

Figure 6, CIII intensity image diagnosed by CIS on HL-2A tokamak.

5. Conclusion

Three sets of spectroscopy diagnostics are recently developed on HL-2A tokamak. High temporal and spatial resolution from core to edge plasma is the goal of these diagnostics for turbulence research.

Acknowledgments

This work was supported by the National Natural Science Foundation of China (Grant No. 11375053), the National Magnetic Confinement Fusion Energy Research Project (Grant No.2013GB107001, 2015GB120002), the Natural Science Foundation of Anhui Province (Grant No. 1608085MA08) and the Program of International S & T Cooperation (Grant No.S2015ZR1057).

References

[1] M.Bomatici, R.Cano, O.De Barbieri and F.Engelmann, Nucl. Fusion 23 (1983) 1153.

[2] H.J.Hartfuss, T.Geist and M.Hirsch, Plasma Phys. Control.Fusion 39 (1997)1693.

[3] Hirsch M, Holzhauer E, Baldzuhn J, Plasma Phys. Contr. Fusion et al., 43 (2001) 1641

[4] FONCK RJ, DUPERREX PA and PAUL SF, Rev. Sci. Instrum. 61 (1990) 3487,

[5] KIM YJ, BREUN RA, BROUCHOUS DA, et al., Rev. Sci. Instrum. 61 (1990) 3046.

[6] H.J.Kunze, Introduction to Plasma Spectroscopy, (2009).

The application of microwave diagnostics on EAST tokamak

C. Zhou[1], A.D. Liu[1], J.L. Xie[1], Y. L. Zhu[1], M.Y. Wang[1], J.Q. Hu[1], J. Zhang[1], Z. L. Zhao[1], D. X. Chen[1], C. M. Qu[1], W. Liao[1], H. Li[1], X.H. Zhang[1], T. Lan[1], W.D. Liu[1], C.X. Yu[1] ,E.J. Doyle[2], G. Wang[2],X. Hu[3], M. Chen[3], X. Ren[3], Alex G. Spear[3], Calvin W. Domier[3], Neville C. Luhmann Jr.[3]

[1]University of Science and Technology of China (USTC), Hefei, China

[2]University of California, Los Angeles, CA, USA

[3]University of California at Davis, CA, USA

Abstract

Four different microwave diagnostics(Profile Reflectometer, eight-channel Doppler Backscattering (DBS8), 384-channel ECE-Imaging, and 96-channel MIR) have been/will been installed on EAST tokamak. The profile reflectometer are used for electron density measurements with the temporal resolution 10/25 μs. The DBS8 are used for turbulence measurements, and the wave number can cover the range 0-12/cm. These two microwave diagnostics system are integrated together at the K-port on EAST. The 384-channel ECE-Imaging can provide evolution of the electron temperature fluctuation with the temporal resolution 1 μs, and the measurements range can be -0.56 to 0.99, which depends on the magnetic field. The 96-channel MIR will be finished in February 2017, and can be used for small wave number turbulence measurements.

1. Introduction

The microwave diagnostics are the advanced diagnostics with the advantages: local measurements with high spatial, temporal, and wave number resolution, nearly no influence on the plasma, and simple quasi-optics system. The profile and fluctuation of electron density and temperature measurements are important for the discharge and physics study in magnetic confined fusion device. And the turbulence study is helpful for the understanding of the confinement and transport. In EAST tokamak, the electron density profile are available for L- and H-mode by the profile measurements, and due to the high temporal resolution, the evolution of the pedestal density can be studied. The turbulence study is probability by the DBS8 with mediate wave number and by the MIR with small wave number. And the imaging of electron temperature fluctuation by the ECE-Imaging is a very powerful instrument for the MHD and sawtooth study. In this article, four different microwave diagnostics will be introduced, include two reflectometer system: the profile reflectometer and the DBS8, and two microwave imaging system: the ECE-Imaging and the MIR system.

2. Application of Microwave reflectometer system on EAST

Two kind of microwave reflectometer system: the profile Reflectometer and eight-channel Doppler Backscattering (DBS8), have been applied in EAST tokamak for electron density profile and fluctuation

measurements. These two system are integrated together at the K port of EAST, and can be used for toroidal coherent measurements with the DBS system at the O port of EAST[1]. The schematic diagram of the two system are show in Fig. 1(a) and (b), respectively. The profile reflectometer as shown in Fig.1(a) launches microwave into plasma with O-mode and X-mode polarization simultaneously by a same horn, and the reflected signal is also received by this horn which is same to the arrangement used for ITER. The

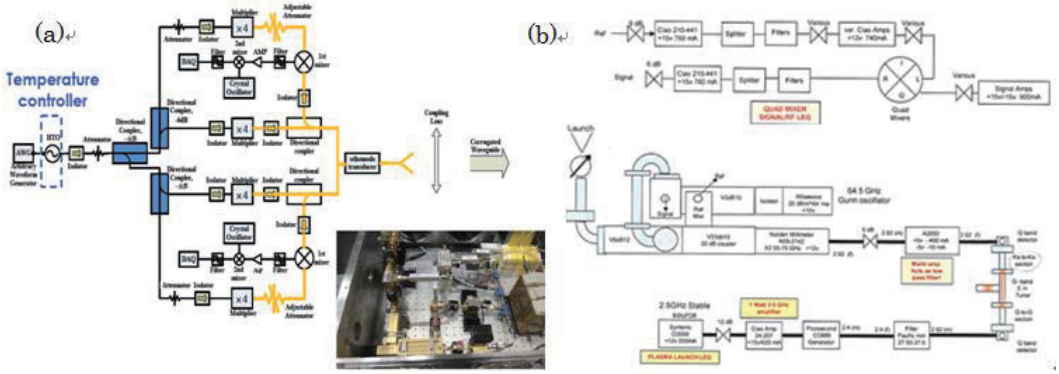

Fig.1 The schematic diagram of the profile Reflectometer (a), and DBS8 (b).

profile reflectometer contains two subsystem: Q-band system and V-band system, and can cover the density range from 0 to 6.5e19/m^3. The DBS8 system shown in Fig. 1(b) can launch eight different microwave into plasma simultaneously in X-mode, and the frequencies are 55, 57.5, 60, 62.5, 67.5, 70, 72.5 and 75GHz. The wave number range can be from 0-12/cm, which is enough for the turbulence measurements on EAST.

The density profile in L- and H-mode is available by the profile Reflectometer, and an example is shown in Fig.2. Fig.2(a) shows the parameter of the shot 48916, and the density profile for L- (blue line) and H-mode(red line) are shown in Fig.2(b). The temporal resolution is 25 μs in this density inversion, and

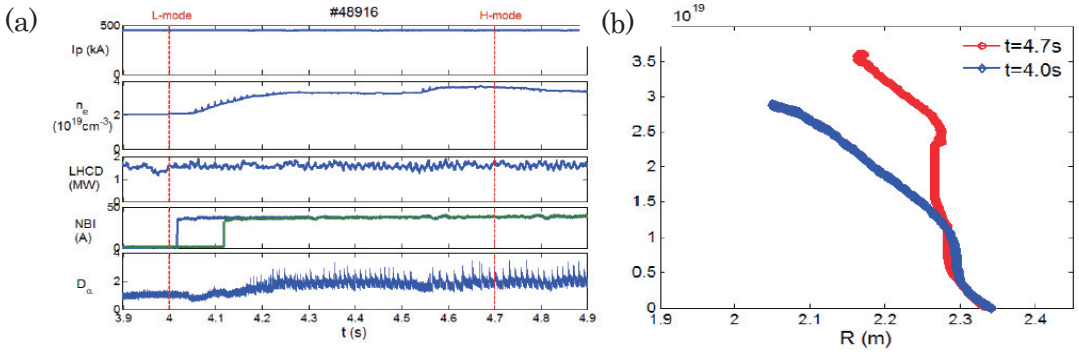

Fig.2 The density profile can be measured by the profile Reflectometer(b), and (a) shows the parameter of the discharge.

the density zero point can be determined by the code automatically. The DBS8 has been used for turbulence measurements on EAST as shown in Fig.3. In Fig. 3(a)(b), the harmonic oscillation was studied by the DBS8, and in Fig. 3(c)(d), the GAM in H mode was measured by the DBS8. The harmonic oscillation appeared in ELM-free H mode when the E×B flow is large enough, and the toroidal number are n=1 to n=7 for the fundamental mode and the different harmonic mode, respectively as shown in Fig. 3(a)(b). We observed the GAM during H mode in EAST, and the spectrum of amplitude(red line) and dφ/dt(blue line)

are shown in Fig.3(c) in L- and H-mode, and we can find that the mode is much more significant in the spectrum of dφ/dt than that of amplitude. We calculated the cross phase between the DBS8signal and the magnetic probe, and we find that the GAM has a magnetic component with a poloidal structure m=2.

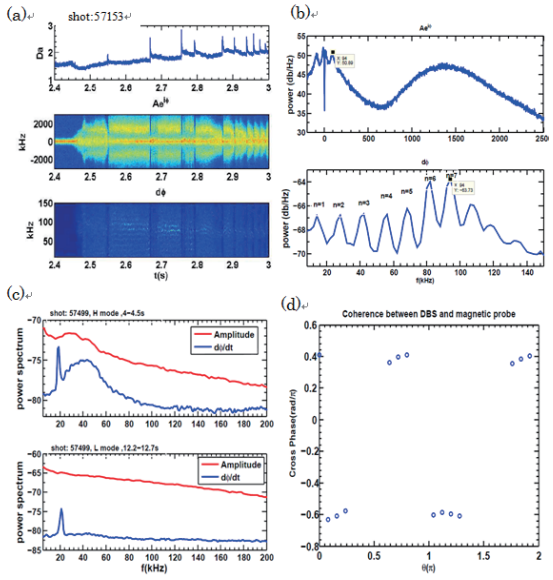

Fig.3 Harmonic oscillation during ELM-free H mode was shown in(a)(b), and in (c)(d) are the GAM during H mode measured by DBS8.

3. Application of Microwave imaging system on EAST

The schematic diagram of the two imaging system are show in Fig. 4(a) and (b), respectively. The 384-channel ECE-Imaging system shown in Fig.4(a) has the widest output frequency range after detector(2-18GHz), and can cover almost the whole q=1 surface. The 96-channel MIR system in Fig.4(b)

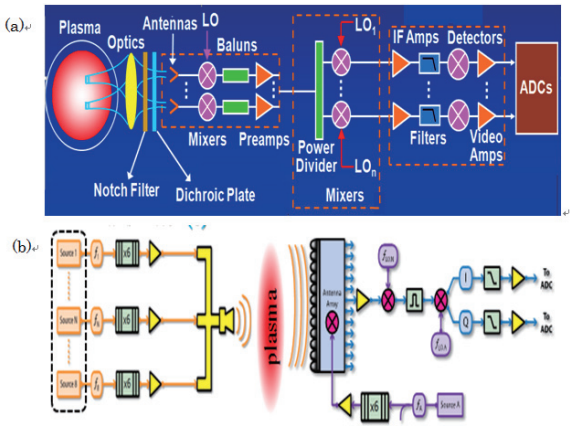

Fig.4 The schematic diagram of the 384-channel ECE-Imaging (a), and 96-channel MIR (b).

uses 8 independent synthesizers to generate the probe beams in W-band, and the microwave are launched into plasma by a same horn. The quasi-optics are integrated together as shown in Fig.5, and four different lens are used to adjust the radial focus, polodial zoom, the field curvature and the incident angle[2].

We can use the ECE-Imaging system to estimate the inversion radius location and the position of the magnetic axis, and to study the sawtooth . In Fig.6(a)(b) are the measurements of the higher harmonic

modes during sawtooth and the compound sawtooth [3][4]. We observed the higher harmonic modes during sawtooth in low βp discharge, and we can find at least three pressure fingers in the frames 2-4 in Fig.6(a) which means a higher harmonic modes. The compound sawtooth was study by ECE-Imaging as

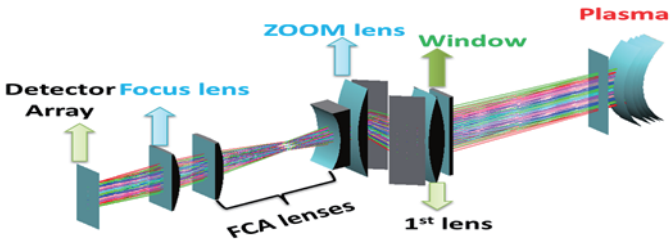

Fig.5 The quasi-optics front-end for the two microwave imaging system.

shown in Fig.6(b). A partial collapse took place in frame 4 and 5, and resulted in a residual hot core which was surrounded by a cold narrow range, and beyond the cold region, there was another relatively hot ring structure. The compound finally collapsed in frame 12. The compound sawtooth occurs mainly at the beginning of an ion cyclotron resonant frequency heating pulse and during the L-H transition phase.

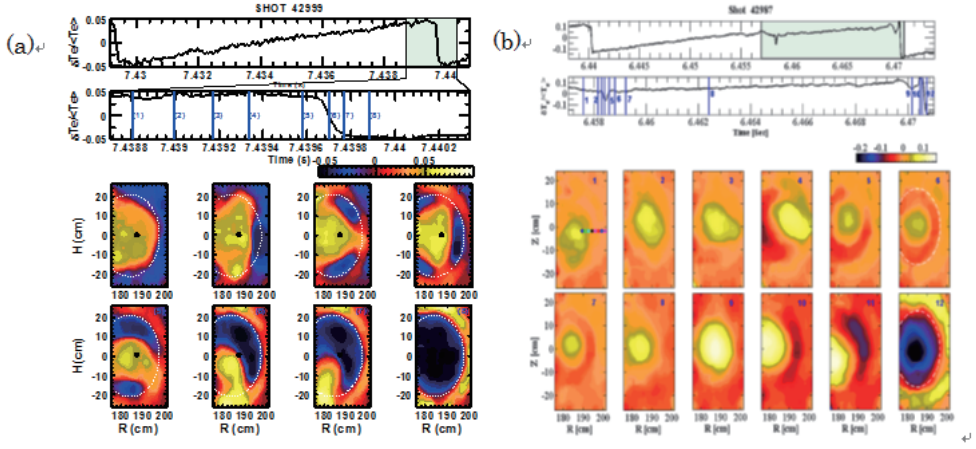

Fig.6 Higher Harmonic modes during sawtooth(a) and the compound sawtooth(b) are studied by ECE-Imaging.

Acknowledgements

This work was partly supported by the JSPS-NRF-NSFC A3 Foresight Program in the field of Plasma Physics (NSFC: No.11261140328, NRF: No.2012K2A2A6000443), Natural Science Foundation of China under Grant No.10990210, 11475173, 11505184, and National Magnetic Confinement Fusion Energy Development Program of China under Grant No. 2013GB106002 and 2014GB109002.

References

[1] C. Zhou, A. D. Liu, et al. REVIEW OF SCIENTIFIC INSTRUMENTS 84, 103511 (2013).

[2]Y. Zhu, et al. Journal of Instrumentation 9.12 (2014): P12014

[3] A. Hussain, B. Gao, et al. Chinese Physics Letters 32.6 (2015): 065201.

[4] A. Hussain, Z. Zhao, J.Xie, et al. Physics of Plasmas 23.4 (2016): 042504

Plasma density profile measurement during ELM suppression by RMP

Seong-Heon Seo[1]

[1]National Fusion Research Institute, Yuseong-Gu, Daejeon 34133, Korea

Abstract

KSTAR plasma density profile is measured by using a frequency sweep reflectometer. The time resolution of KSTAR reflectometer is 25 μs. To obtain more precise density profile, the frequency sweep is perfectly linearized by modeling the VCO input circuit as an RC low pass filter and numerically solving the equation. Since the perfect linear frequency sweep makes the signal shape much simpler, the automatic data analysis becomes more feasible. The frequency linearization method is described in detail and the plasma density profiles measured during ELM suppression and mitigation by RMP are presented.

1. Introduction

Frequency sweep reflectometer is a microwave diagnostics which measures the plasma density profile with fast time resolution. KSTAR reflectometer [1] launches microwave in the frequency range of 33-110 GHz through horn antennas installed in the middle of D-port. Since a single microwave component cannot cover such a broad band, the reflectomter is composed of 3 channels. Each channel covers Q band (33-50 GHz), V band (50-75 GHz), and W band (75-110 GHz), respectively. A channel consists of a launcher and a receiver. Therefore 6 horn antennas are installed in D-port. The whole frequency range is linearly swept in 20 μs with a pause of 5 μs before the next sweep.

The frequency sweep time determines the time resolution. The reflectometer's signal is easily contaminated by the sudden change of plasma density profile or by the microwave scattering due to turbulence. Therefore the frequency should be swept fast enough so that the plasma profile remains fixed during the frequency sweep time. The signal is also distorted by a nonlinear frequency sweep. A perfect linear frequency sweep makes the data analysis much simpler by eliminating this artificial distortion. A commercial voltage controlled oscillator (VCO) is designed to have a linear relation between the output frequency and the tuning voltage. However the linearity is not perfect so that an arbitrary waveform generator (AWG) is normally used to finely adjust the tuning voltage waveform to get a more linear frequency sweep. The output voltage of AWG is determined by inverting the output frequency graph measured as a function of the tuning voltage. However the output frequency measured at a specific voltage by using a spectrum analyzer represents the static characteristics of VCO. There is a time delay before the expected frequency is generated when the tuning voltage is swept fast. In addition, it is not straightforward to measure the frequency itself while the frequency is swept fast. There is a method to measure the time derivative of frequency trace by constructing interferometry [2]. And then it is time integrated to get the

frequency trace. In this paper, a new algorithm which models the VCO input circuit and solves the circuit equation numerically is developed to achieve a perfect linear frequency sweep. The frequency measurement technique is explained in Sec. 2. The frequency linearization method and the result are explained in Sec. 3. In Sec. 4, the plasma density profiles during ELM suppression and mitigation induced by RMP are presented.

2. Frequency measurement based on interferometry

An interferometer shown in Fig. 1 is constructed to measure the VCO output frequency. If two different frequency signals are fed to a mixer, the mixer output frequency is the frequency difference between two signals. Since there is no frequency dispersion in a coaxial cable, it takes a constant time that a signal arrives from the source to the mixer input through coaxial cable. If a frequency chirped signal is divided through a power divider and then these identical two signals are fed to the mixer through coaxial cables of different length, the mixer output frequency is proportional to the time derivative of the signal frequency. The mixer output frequency is integrated to get the frequency.

$$\mathrm{f(t)} = f_0 + \int_0^\tau a \frac{df}{dt} dt \tag{1}$$

, where a is the proportional constant and f_0 is the initial frequency. These two unknown parameters can be obtained by noticing the fact that the initial and final frequency approach the static value measured by spectrum analyzer if a constant voltage is kept long enough before and after frequency sweep. With these integration constants at both ends, the derivative of VCO frequency can be integrated to get the VCO absolute frequency trace.

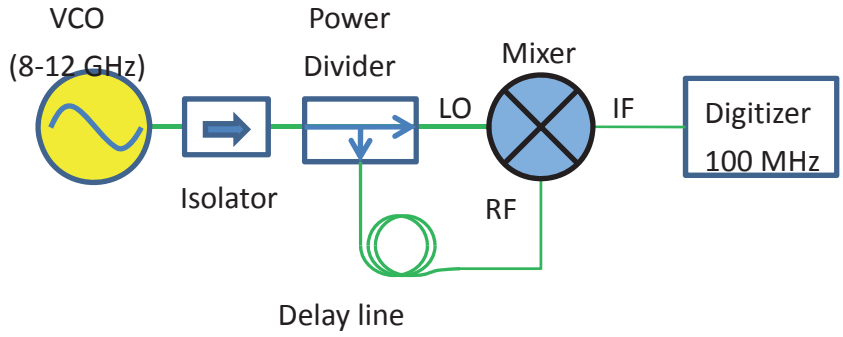

FIG. 1 The inteferometer is assembled to measure the VCO instantaneous frequency

3. Frequency linearization

The block diagram of VCO, Voltage Transducer, and AWG is drawn in Fig. 2. A commercial AWG output voltage range is ±10 V but a commercial VCO tuning voltage range is 1-19 V. So a voltage transducer is needed to drive VCO by AWG. The voltage transducer is homemade based on LF356N operational amplifier. Due to the finite response time of voltage transducer and the RC low pass filter built in inside of the VCO tuning voltage input, the static characteristics of VCO gests deviated as the frequency sweep rate increases. The simplest model of Fig. 2 is to assume that there is a constant time delay of τ_d between the application of a tuning voltage and the appearance of the frequency corresponding to the

statically measured VCO characteristics.

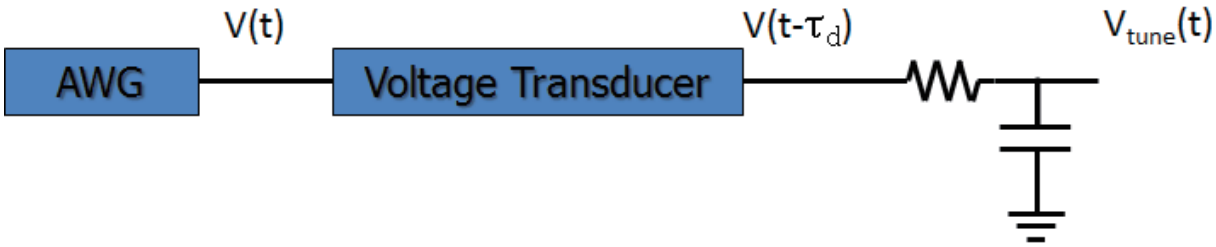

FIG. 2 The circuit diagram of AWG, voltage transducer, and VCO

By inverting the frequency graph with the delay time of τ_d, the tuning voltage waveform is obtained which would linearize the frequency sweep. The resulting frequency graph is shown in Fig. 3 (a). Depending on the delay time, ripples can be reduced but cannot be completely removed. In Fig. 3 (a), the ripples are minimized for τ_d = 0.22 μs (green line).

$$V(t-\tau_d) = RC\frac{dV_{tune}(t)}{dt} + V_{tune}(t) \qquad (2)$$

A more sophisticated model is tried. The RC low filter is modeled as in Eq. (2) and the delay time of voltage transducer is assumed as a constant as before. For a given AWG voltage waveform, the voltage waveform, $v_{tune}(t)$, at VCO internal input is calculated numerically by solving Eq. (2). The VCO characteristics is obtained by measuring the output frequency versus the calculated voltage waveform $v_{tune}(t)$. Then a new AWG voltage trace is obtained by inverting this frequency graph. By first applying this model, the ripple size is much reduced but not completely. However the ripple can be further reduced as shown in Fig. 3 (b) if we apply this procedure repeatedly with an improved tuning voltage waveform and the corresponding measured frequency trace. Although Eq. (2) is not an exact circuit model, it seems that it gives an approximate solution when the nonlinear distortion is small. Therefore the solution converges to a true linear frequency sweep if a more linearized frequency trace is applied to Eq. (2). It is the reason why we could achieve a perfect linearization by repeatedly applying Eq. (2). As a result, the frequency is linearized almost perfectly as shown in Fig. 3 (b). In addition to this perfect frequency linearization, a more accurate plasma density profile can be reconstructed by using a sophisticated phase detection algorithm based on wavelet transform [3].

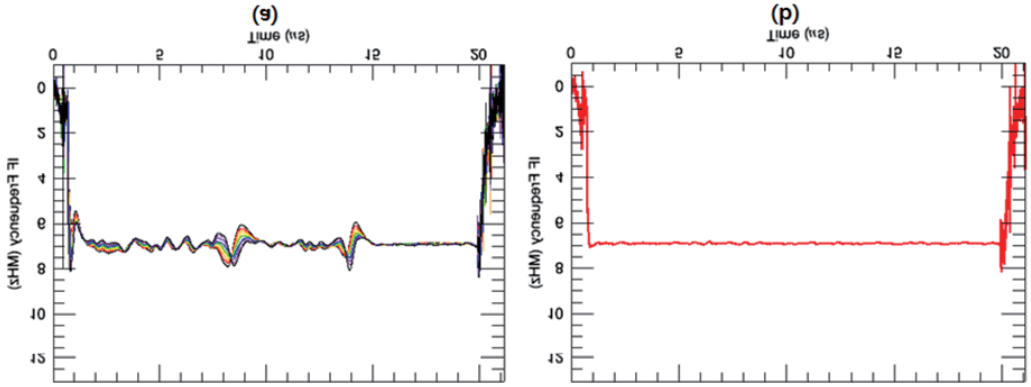

FIG. 3 The IF frequency. (a) a constant delay time model. (b) RC low pass filter circuit model

4. Plasma density profile change due to RMP

RMP makes the ELM suppressed or mitigated, sometimes enhanced depending on the plasma conditions. The RMP coil currents and D_α line is shown in Fig. 5 (a). The line integrated density decreases immediately as the RMP is applied. In Fig. 4 (b) and (c), the density profiles measured by reflectometer are shown. In 2016 campaign, the reflectometer could measure the density profiles only for 160 ms due to memory limit. So the density profiles are investigated through two similar shots. The density profiles before RMP are measured in shot #15716 and the density profiles after RMP are measured in shot #15719. The pedestal height is immediately reduced after applying RMP from $2.3\text{x}10^{19}\text{m}^{-3}$ to $1.4\text{x}10^{19}\text{m}^{-3}$ and this lowered density pedestal height is kept as long as the RMP is applied. Between the ELM suppression and mitigation periods, there is just a little difference in pedestal height but not noticeable change in the density gradient. The ELM occurs when the density pedestal is a little increased from $1.4\text{x}10^{19}\text{m}^{-3}$ to $1.5\text{x}10^{19}\text{m}^{-3}$. This result is consistent with the fact that the line integrated density is a little higher in the same period. This observation indicates that the density pedestal height might be crucial for ELM occurrence.

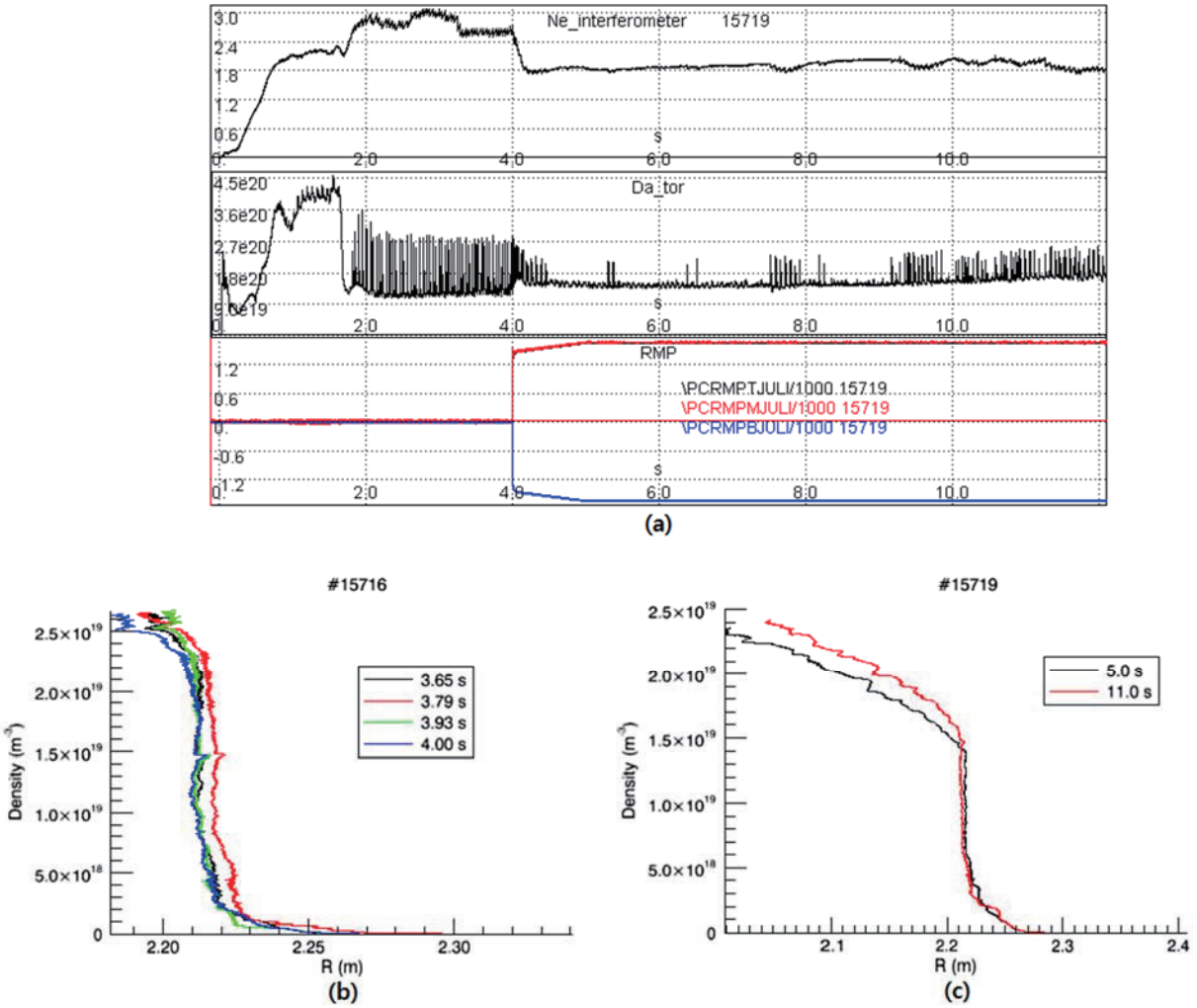

FIG. 4 (a) The integrated density measured by microwave interferometer, Da intensity, and RMP coil current from the top. (b) density profile in shot #15716. (c) density profile in shot #15719

Acknowledgements

This work was partly supported by the JSPS-NRF-NSFC A3 Foresight Program in the field of Plasma Physics (NSFC: No.11261140328, NRF: No.2012K2A2A6000443).

References

[1] Seong-Heon Seo, Jinhyung Park, H. M. Wi, W. R. Lee, H. S. Kim, T. G. Lee, Y. S. Kim, Jin-Seob Kang, M. G. Bog, Y. Yokota, and A. Mase, Rev. Sci. Instrum. **84** ,084702, (2013).

[2] Seong-Heon Seo and Dong Ju Lee, Rev. Sci. Instrum. **77**, 045103 (2006).

[3] Seong-Heon Seo and Dong Keun Oh, Rev. Sci. Instrum. **87**, 11E710 (2016).

Fast ADC system for Thomson scattering diagnostics

I. Yamada[1], H. Funaba[1], R. Yasuhara[1], J. Lee[2], Y. Huang[3], C. Liu[3], and Y. Wang[3]

[1]National Institute for Fusion Science, Toki 509-5292, Gifu, Japan
[2]National Fusion Research Institute, Daejeon 34133, South Korea
[3]Southwestern Institute of Physics, Chengdu 610041, China

Abstract

In the LHD Thomson scattering system, charge integrating analog-to-digital converters (ADCs) have been used to measure Thomson scattering signal intensities. Recently, low cost and compact fast gigasampler ADC modules are commercially available at reasonable price. By applying such fast ADCs to Thomson scattering diagnostics, it is expected to improve data quality. We analyzed the performance of such fast ADC systems when they are applied to Thomson scattering diagnostics.

1. Introduction

The LHD Thomson scattering system has routinely measured electron temperature (T_e) and electron density (n_e) profiles of LHD plasmas at 144 spatial points along the LHD major radius. [1][2] In the LHD Thomson scattering system, charge integrating analog-to-digital converters (ADCs) have been used to measure integrated values of Thomson scattering signal intensities. When the experimental conditions are good, for example, enough signal intensity, high signal-to-noise level, and no accidental noise, the charge integrating ADCs are enough for Thomson scattering diagnostics. However, generally speaking, Thomson scattering signal intensity is weak because the Thomson scattering cross section is very small. Then careful signal acquisition and processing are required. In order to determine the Thomson scattering signal intensity, some Thomson scattering teams have already fast digitizer system. We have a plan to replace the charge integrating ADCs with fast gigasampler ADCs in the LHD Thomson scattering system.

2. Gigasampler analog-to-digital converter

First, figure 1 shows the principal of the Thomson scattering signal measurement using a charge integrating ADC. The ADC measures the integrated value of signal during the ADC gate is open. In the LHD Thomson scattering system case, the gate width is ~100 nsec. First, the Thomson scattering signal + background signal, S1, is measured during the proceeding Gate 1. After 25 microsec, only background signal, S2, is measured. True Thomson scattering is estimated from TS = S1 – S2. If the experimental condition is good, no background level variation and no unexpected noise signal,

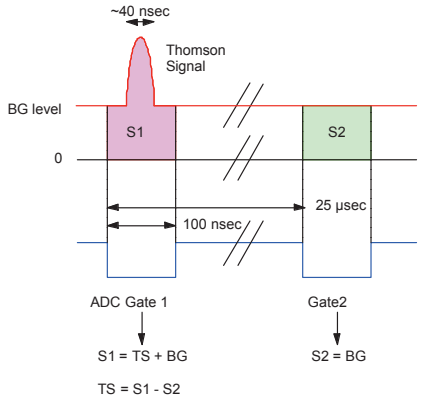

Fig.1. Principal of true scattering signal measurements in charge integrating ADCs.

Thomson scattering signal is accurately obtained. However, the background level may be changed in actual experiments, and undesired noises may come from somewhere. In addition, signal saturation may occur as shown in Fig. 2. It is difficult to directly know such phenomena when charge integrating ADCs are used. In contrast, they are correctly observed and recorded, and accurate estimation of the Thomson scattering signal intensity is possible when fast ADCs are used as in the HL-2A Thomson scattering system. [3]

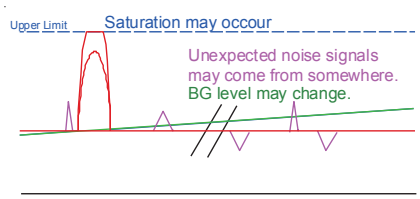

Fig.2. A few unexpected phenomena may occur in actual experiments, resulting in experimental errors.

Until recently, such fast gigasampler digitizers are very expensive. The price per input channel is ten times higher than that of a charge integrating ADC. However low cost and compact fast ADC modules are now commercially available at reasonable price from some electronics instruments companies. Roughly speaking, the price per input channel of the fast ADC is ~500 USD, and that of the traditional charge integrating ADC is ~400 USD. The fast gigasampler ADC systems have been developed based on the Domino Ring Sampler (DRS) chip. The schematic diagram of the DRS chip is shown in Fig.2. The DRS4, in which "4" means the version number, has 1024 small capacitors and fast switching circuit based on invertors inside the chip. The switching trigger signal propagates through the inverters that make temporal delay like domino toppling. The temporal delay between two capacitors can be selected, for example, 0.2 nsec, 1.0 nsec, and so on. When the delay time of 0.2 nsec is selected, the measurement at the sampling frequency of 5GS/s is done and the total observation time length is 204.8 nsec. Since the temporal duration of Thomson scattering signal in YAG Thomson scattering systems are roughly ~50-100 nsec, the observation time of ~200 nsec is enough for YAG Thomson scattering systems.

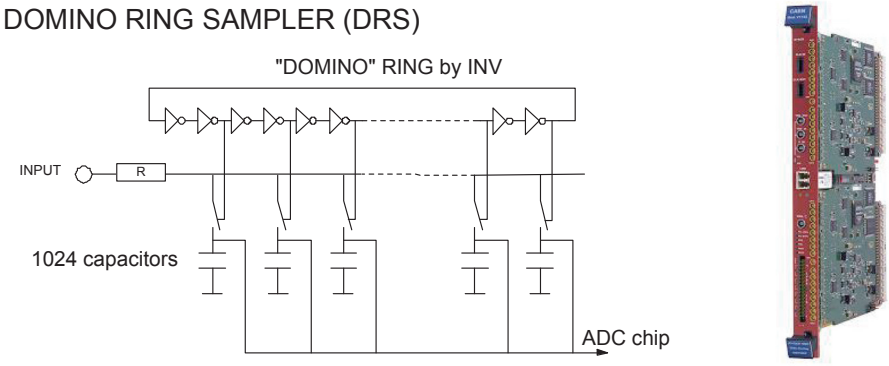

Fig.3. Schematic diagram of the gigasampler ADC based on the DRS4 chip and an example of a VME module based on the DRS4, CAEN V1792. The module has 32 input channels.

3. Simulation analysis

We developed a simulation program to evaluate the benefit of the fast ADC system. The simulation program is divided into two parts. The first part produces Thomson scattering signal waveforms for some experimental condition sets by using a Monte Carlo method. The second part simulates the fast ADC system. The parameters are listed in Tables 1 and 2 for the first and second parts, respectively. The parameters in the Table 1 are typical values in the LHD Thomson scattering diagnostics. In this study, the

simple Gaussian function is used in the Thomson scattering pulse generation in the first step. And the simple Gaussian function is also used as a fit model function in the second step. In real cases, there may be some differences between real Thomson scattering signal shape and Gauss function. So, careful determination of the model function will be needed. For example, a more sophisticated model function has been proposed to describe the experimentally observed Thomson scattering signals in the GAMMA10. [4]

Figures 4 show examples of the simulated Thomson scattering signal waveforms for the pulse heights are 5, 50 and 500 mV, and the background component is 5 mV. Figures 5 show the summary of the values estimated by using the second simulation part that simulates the fast ADC system. The horizontal axis is the ADC resolution (8-14 bit), and the vertical axis is the averaged error. From the results, it is found that the error strongly depends on the signal-to-noise (S/N) ratio. Concerning the ADC resolution, 9-bit resolution will be enough for the LHD Thomson scattering system. In addition, it is found that the estimation error becomes smaller as the ADC sampling rate is increased as expected. For the case of S/N=5, the error is lower than 10 % at the sampling rate of higher than 1 GS/s. For the case of S/N=500, the error is lower than 1 % at the sampling rate of higher than 500 MS/s. It is noted that slow variation of the plasma light component and/or contamination of unexpected noise component were not taken into account in the model calculation. So, no significant difference was found between the results obtained by the simulations for the fast ADC and charge integrating ADC. We are now developing a more sophisticated simulation program to generate more realistic Thomson scattering signal waveform by taking the plasma light variation and abrupt noise components into account.

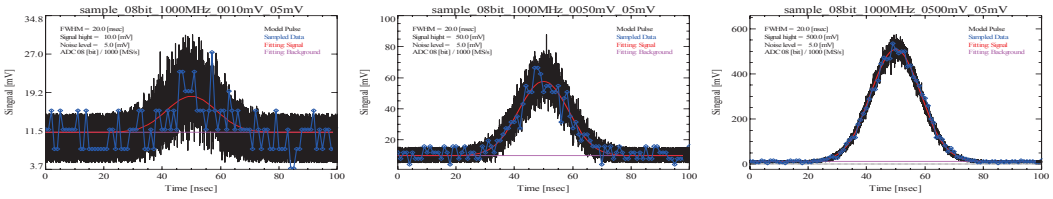

Figs.4. Some examples of the Thomson scattering pulses generated by the simulation program for the pulse height: 5, 50 and 500 mV, the background component: 5 mV, and the DC offset level: 10 mV.

Table 1. Simulation parameters for generating Thomson scattering signal waveform

Thomson scattering signal:	Pure Gaussian + Shot noise
TS pulse height and width:	Height = 2.0 - 1000.0 [mV] and FWHM = 20 [nsec]
Plasma light component:	Flat + Shot noise
Random noise component:	0.01 - 10.0 [mV]
Amplifier offset:	Flat 5 [mV]
Temporal resolution:	0.01 [nsec] << TS pulse width (~20 nsec)
Number of pulses:	1000

Table 2. Fast ADC parameters

Resolution:	8, 9, 10, 11, 12, 13, 14 [bit]
Sampling Rate:	0.2, 0.5, 1, 2, 5 [GS/s]

4. Summary

We have a plan to replace the charge integrating ADC system with the fast gigasampler ADC system in the LHD Thomson scattering system to measure more accurate and reliable Thomson scattering signals.

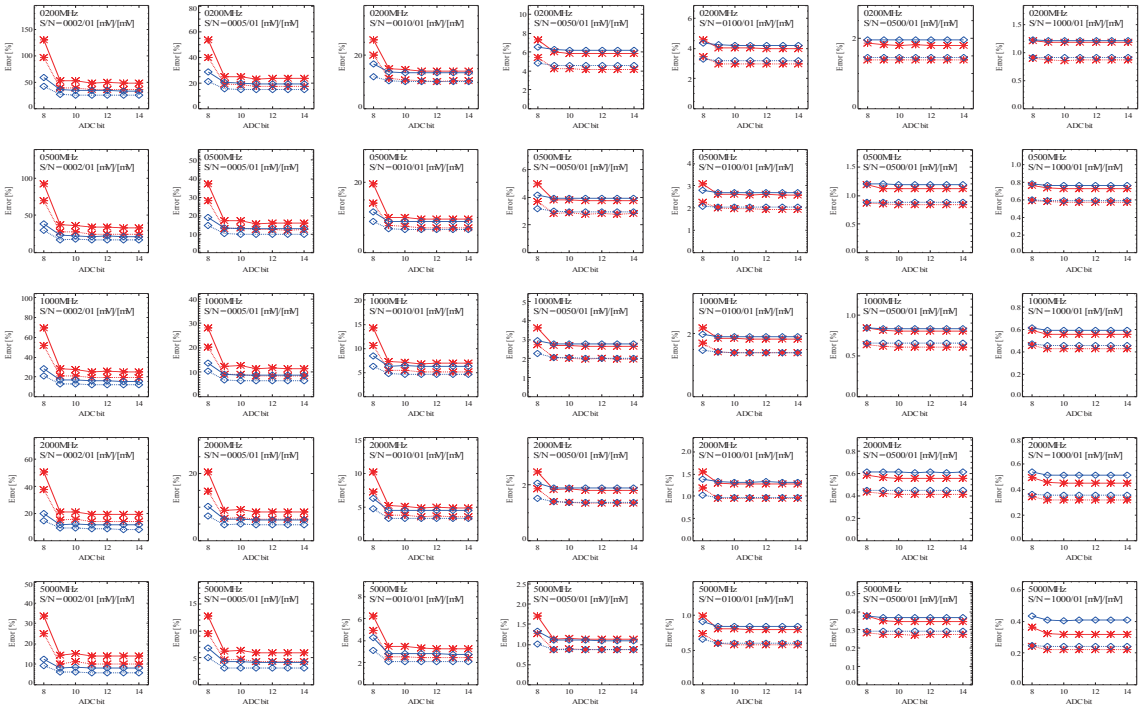

Fig.5. Summary of the results obtained from the simulation. The horizontal and vertical axes are ADC resolution and estimated error in each figure.

We have developed a simulation program to evaluate the benefit of the fast ADC system. It is found that the measurement using fast ADC system will give better results especially for low signal intensity and/or low signal-to-noise ratio cases. In addition, we tested the fast ADC in the KSTAR Thomson scattering system in the 2016 KSTAR experiment campaign, and found the fast ADC seems to work well as expected. [5]

Acknowledgements

This work was partly supported by the JSPS-NRF-NSFC A3 Foresight Program in the field of Plasma Physics (NSFC: No.11261140328, NRF: No.2012K2A2A6000443) and the LHD experiment budget (10203002ULHH005).

References

[1] I. Yamada *et al.*, Fusion Sci. Tech., **58**, 345 (2010).

[2] I. Yamada *et al.*, Rev. Sci. Instrum., **87**, 11E531 (2016).

[3] C. Liu *et al.*, JINST, **10**, C12062 (2015).

[4] K. Ohta *et al.*, Rev. Sci. Instrum., **87**, 11D617 (2016).

[5] J. H. Lee *et al.*, Rev. Sci. Instrum., **80**, 10D528 (2010).

Profile data improvement in the KSTAR Thomson scattering

Jong ha Lee[1], Seung Hun Lee[1,], K.D. Lee[1] and I.Yamada[2]

[1]National Fusion Research Institute, Gwahak-ro 169-148, Daejeon, Korea

[3]National Institute for Fusion Science, Toki 509-5292, Gifu, Japan

Abstract

Thomson scattering diagnostic data is most important in nuclear fusion machine. In KSTAR, for this reason, Thomson scattering system has been installed. From 2010 to 2014, Thomson scattering system was tested carefully in KSTAR. For example, a shutter system for vacuum window, laser beam dump, digitizer, and proto type ITER edge Thomson laser have been tested. In 2015, KSTAR installed commercial laser system for Thomson diagnostics to measured electron temperature Te and density ne profiles. However unknown noises overlapped in the Thomson signal cables continuously. Because of this, the calculation of the ne and Te was difficult. In 9th KSTAR campaign, 2016, to remove the noises we made alignment module to specific alignment and change the signal cable type to double shielded coaxial cables. Finally signal to noise ratio as increased more than 50% this decreased the error in ne and Te values. These plasma parameters measured by Thomson scattering was compared with other diagnostics. And until this the Te and ne was calculated by χ^2 method however in this year Neural Network method and Baysian method was tested to research an accuracy of these three methods. In this paper KSTAR Thomson system will describe and shows recent data.

1. Introduction

The electron density and temperature profile measurements in fusion plasmas is very important for accurate understanding of plasma behavior. As this reason, most of fusion machine installed the Thomson scattering diagnostic to measure electron temperature Te and density ne profiles. Also KSTAR installed Thomson scattering system since 2010 however most Thomson scattering systems are vertical type but KSTAR Thomson system is tangential type [1]. First two years, most of mechanical components in KSTAR Thomson system were tested such as shutter, trigger system for digitizer, polychromators and so on. After 3 years, during 2012~2014, 'proto type ITER edge Thomson laser' that made by JAEA was temporarily introduced and tested for ITER. In 2015, commercial Nd:YAG laser was set in the KSTAR for Thomson scattering system and measured Te and ne successfully. However noises form signal cable was still remains thus result of the Te, ne calculation included lots of errors until 2015. To increase the signal to noise ratios in 2016, signal cable was changed to double shielded coaxial cable, re-connect the noise cut transformer (NCT) and moreover laser beam alignment system was developed. The alignments in Thomson system is most important point to accurate measurement of Thomson signal. If alignment between collection lens and

laser beam path in vacuum vessel are slightly mismatched, the signal error was increase awfully. In this case we could not calculate exact ne, Te profiles. In KSTAR, to increase the accuracy of ne and Te values, special type of alignment system was developed which has two different type bandpass filters, APDs and four sets of optical fibers. This alignment system was tested in 2016 campaign [2]. The Thomson data was compared with other diagnostics to verification of consistency in 2015 and 2016. In this paper we will shows some Thomson data with ECE, mm- wave interferometer and FIR.

2. Data achievement and analysis

Total measuring points are 27 for KSTAR Thomson scattering system during 2015 to 2016 that means 27 polychromators are operated in plasma experiments. For the measurement, edge spatial resolution is 5mm, core resolution is over the 10mm. The polychromators have 5 channels while 4 channels are used for the ne and Te calculation remain channel used for Rayleigh calculation. Using these polychromator systems, we did a performance test of Thomson system during the KSTAR plasma experiments. First test was the measurement of the ne, Te pedestal position changes during plasma radial position shift experiments. Fig. 1 (a) is KSTAR experiment shot # 12698 in this experiments plasma position was changed on purpose. In the Fig. 1 (a), blue line at 3second indicated plasma position is goes inside in the vacuum vessel in R. After than at 6 second the plasma position goes out to the outside wall, the red line at 11 second the plasma goes inside again. On this experiment Te, ne pedestal changes flow plasma positions were measured by Thomson scattering diagnostic Fig. 1 (b). Next experiment in 2015 was a Te profile changes during ECH on-axis heating. In Fig. 2 (a) modulated ECH was injected to the on-axis of plasma that brings about change of core Te profile as Fig. 2 (b).

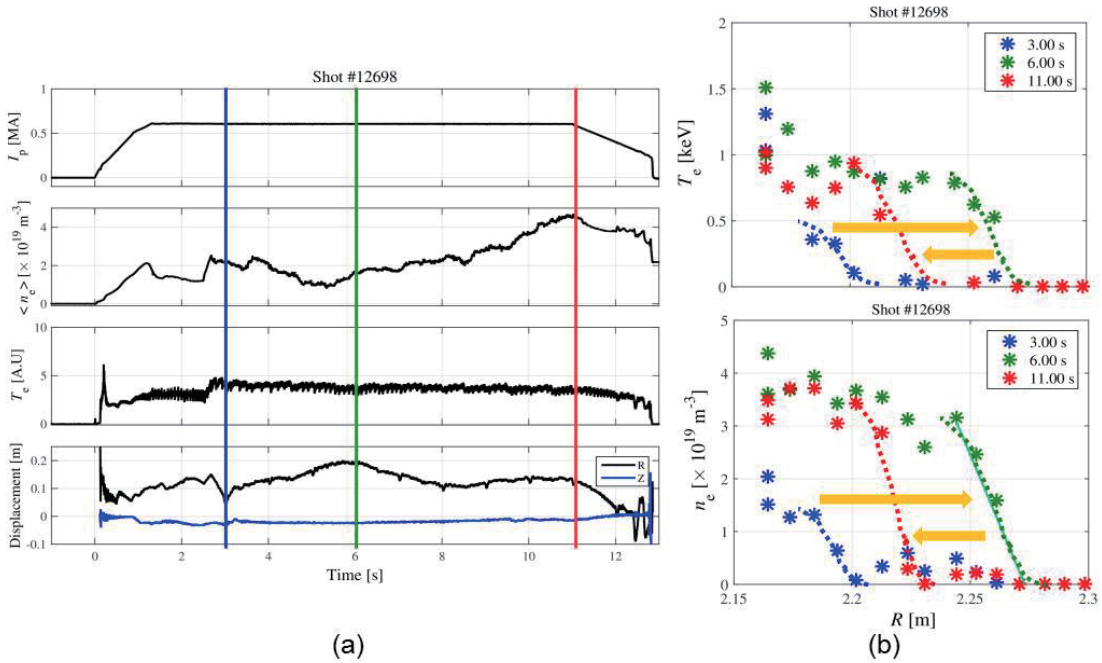

Fig. 1 Pedestal position changes by Thomson scattering measurement during the radial position shift in KSTAR shot #12698.

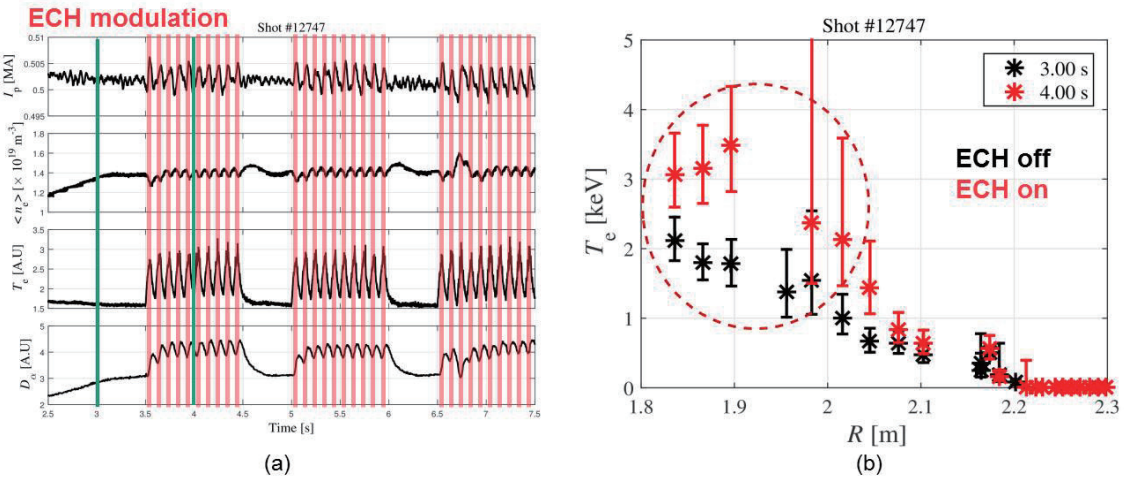

Fig. 2 Electron temperature profile changes during the ECH modulation by Thomson in KSTAR shot #12698. Clearly measured the core Te profile changes.

In 2016, Thomson signal noise was reduced ~50% than 2015 through the signal cables change to double shielded cable and using a noise cut transformer (NCT). Through this works, KSTAR Thomson profile data was upgraded as showed in Fig. 3. Fig. 3 (a) is H-mode profile and Fig. 3 (b) is L-mode profile in KSTAR plasmas. To check the consistency of diagnostic data in KSTAR we compared Thomson Te values with ECE diagnostic (Fig. 4). Fig. 4 (a) shows a Te profile between Thomson and ECE, the Thomson profile clearly restore the edge region which could not covered by ECE. And Fig. 4 (b) shows a Te in time that also good coincidence with ECE.

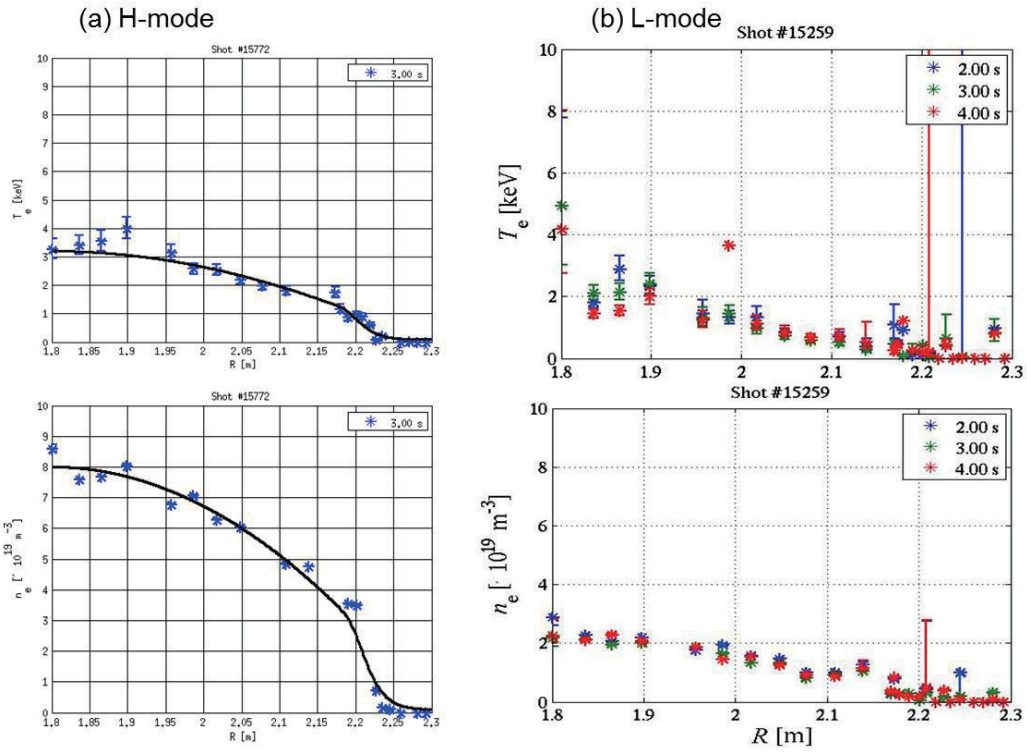

Fig. 3 (a) H-mode, (b) L-mode profiles measured by Thomson diagnostic in 2016.

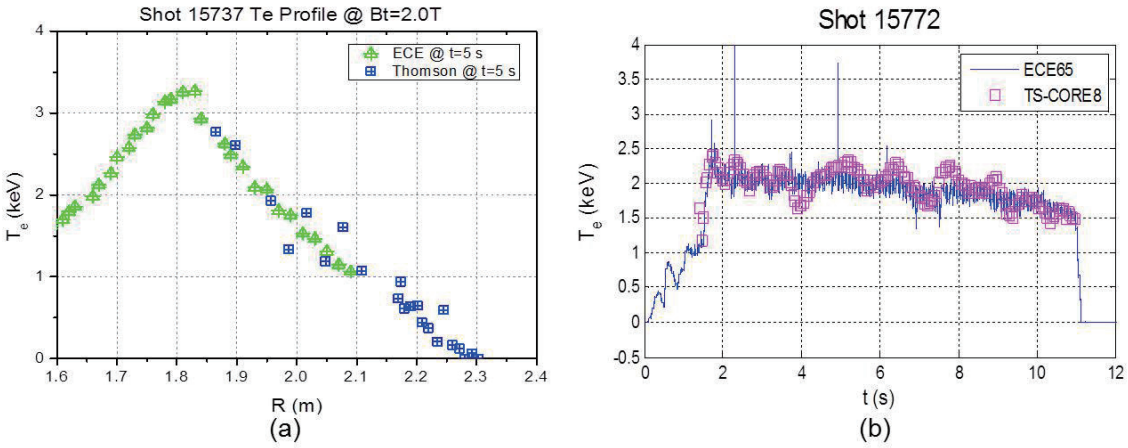

Fig. 4 Comparison Te between Thomson and ECE in KSTAR. (a) is Te profile and (b) is time trace

3. Conclusion

Performance of KSTAR Thomson scattering system is upgraded in 2016 compared to 2015. Signal noise level reduced more than 50% through development of alignment detection system and electronic works. We check the consistency of Thomson Te by comparison with ECE which gives obvious agreement in profile and time trace data. In further study we are testing a Thomson data analysis algorithm such as neural networks [3] and Bayesian [4].In this test we are comparing accuracy of these algorithm with traditional χ^2 methods.

Acknowledgements

This work was partly supported by the JSPS-NRF-NSFC A3 Foresight Program in the field of Plasma Physics (NSFC: No.11261140328, NRF: No.2012K2A2A6000443).

References

[1] Development of KSTAR Thomson scattering system, , J. H. Lee, S. T. Oh, H. M. Wi, Review of Scientific Instruments **81**, (2010) 10D528.

[2] Design of practical alignment device in KSTAR Thomson diagnostic, J. H. Lee, S. H. Lee, and I. Yamada, Review of Scientific Instruments **87**, (2016) 11E544.

[3] Development of a neural network technique for KSTAR Thomson scattering Diagnostics, Seung Hun Lee, J. H. Lee, I. Yamada, and Jae Sun Park, Review of Scientific Instruments **87**, (2016) 11E533.

[4] Signal processing of Thomson scattering data in a noisy environment in ASDEX Upgrade, B Kurzan, M Jakobi, H Murmann and ASDEX Upgrade team, Plasma Physics and controlled Fusion **46**, (2004) 299.

Effect of edge turbulence on ELM-crash suppression under $n = 1$ RMP

J. Lee[1], G.S Yun[2], M.J. Choi[3], J.M. Kwon[3] Y.M. Jeon[3], W. Lee[3], N.C. Luhmann, Jr.[4], and H.K. Park[1,3]

[1]Ulsan National Institute of Science and Technology, Ulsan 44919, Republic of Korea
[2]Pohang University of Science and Technology, Pohang 37673, Republic of Korea
[3]National Fusion Research Institute, Daejeon 34133, Republic of Korea
[4]University of California, Davis 95616, California, USA

Abstract

The effect of $n = 1$ magnetic perturbation on the edge-localized mode (ELM) and edge turbulence has been investigated by using electron cyclotron emission imaging (ECEI) system in the KSTAR. The ECEI showed that the ELM filament is sustained with substantial fluctuation in amplitude without large pedestal collapse. Correlation analysis among ECEI channels revealed that the magnetic perturbation enhances turbulent fluctuations in the edge toward the ELM-crash suppression phase. Bispectrum and velocimetry analysis of ECEI signal suggest that the turbulence involves a net radial outward energy transport and coexisting ELM filament and edge turbulence nonlinear interact with each other.

1. Introduction

The crash of edge-localized modes (ELMs) is a sudden collapse of the edge pedestal which induce relaxation of energy and particles from the confined plasma into the scrape-off layer. It is a critical issue in magnetic confined fusion device rely on H-mode plasmas, since the heat load of the ELM crash on plasma facing components can be damaged. One of promising methods to control the ELM crash is to perturb the plasma edge by applying small magnetic fields (approximately resonant with the equilibrium magnetic fields, i.e., resonant magnetic perturbation (RMP)) in the edge, thereby enhancing particle transport and keeping the edge pressure gradient below crash threshold [1, 2].

Despite successful control of the ELM crash by RMP there are still many open questions concerning the mechanism of ELM crash suppression. In this report, the change of edge transport induced by turbulence during the period of ELM-crash suppression by RMP is studied using electron cyclotron emission imaging (ECEI) system on the KSTAR.

2. Electron cyclotron emission imaging (ECEI) system on the KSTAR

The ECEI can be regarded as a microwave camera for measuring 2D electron temperature fluctuations (T_e) [3]. The KSTAR ECEI system consists of vertically aligned array of 24 antennas and each antenna is connected to heterodyne detector that resolves the radiation in 8 frequency bands. Therefore the array provides $24 \times 8 = 192$ pixels image of T_e fluctuations ($\tilde{T}_e = \delta T_e / \langle T_e \rangle$, where $\delta T_e = T_e - \langle T_e \rangle$ and $\langle T_e \rangle$ is a time average). Due to flexible local oscillator and large aperture optics system, a view position of

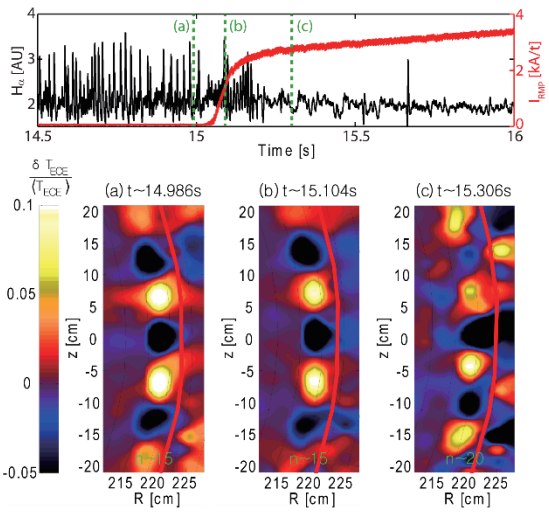

Figure 1. Time history of H_α signal with RMP coil current I_{RMP}. ECE images corresponding to (a) ELM filament before application of RMP, (b) initial phase of RMP ramp-up, (c) ELM filament in the ELM-crash suppression phase. The red line is the separatrix.

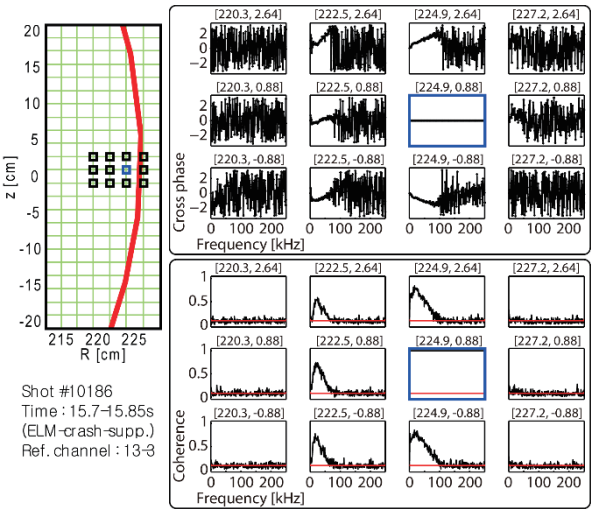

Figure 2. Cross-phase and coherence analysis among ECEI channels. The red line is separatrix position and the blue box is reference channel for correlation calculation. The red horizontal line in the coherence plot is the statistical error limit.

ECEI can be focused anywhere in poloidal cross-section with variable vertical coverage.

For the KSTAR ECEI system, the vertical channel spacing of each sample volume is in the range of $1.4-4.0$ cm And the distance between adjacent channels in the direction of major radius R is ~ 2 cm. Therefore the upper limit of the system wave number resolution is $k_\theta \leq 1.12$ cm^{-1} and $k_r \leq 0.75$ cm^{-1} at the edge.

3. Coexisting ELM filament and edge turbulence during ELM-crash suppression phase

The experiment for ELM-crash suppression [4] were configured in a lower single null, high elongation $\kappa > 1.8$ and triangularity $\delta \approx 0.5$. The plasma current is 0.5 MA, the magnetic field is 1.9 T, and the corresponding edge safety factor $q_{95} \approx 6$.

Figure 1 shows the time history of the H_α signal and ECE images of distinctive ELM filaments at different stages of $n = 1$ RMP. The ELM filament has toroidal mode number $n \approx 15$ [5] and rotates poloidally in the electron diamagnetic drift direction before applying RMP and initial ramp-up phase of RMP. Shortly after the ramp-up phase of RMP, the ELM crashes are eventually suppressed (i.e., no spikes in the H_α signal) but the ELM filaments still remains at the edge with complicated behavior; the toroidal mode number of ELM filament slightly increases and the ELM filament appears and disappears irregularly.

In order to understand the underlying physics of ELM-crash suppression, correlation analysis among ECEI channels was performed [6]. Figure 2 is example of coherence and cross-phase measurement for 4 (radial) $\times$ 3 (poloidal) ECEI channels covering 8×5 cm^2 near the separatrix during ELM-crash suppression phase. This example clearly shows the existence of broadband and low frequency coherent modes ($f < 70$ kHz) along the poloidal direction in a narrow radial zone. Figure 3a shows the dispersion relation obtained from ECEI signals in ELM-crash suppression phase. A clear dispersion relation is observed

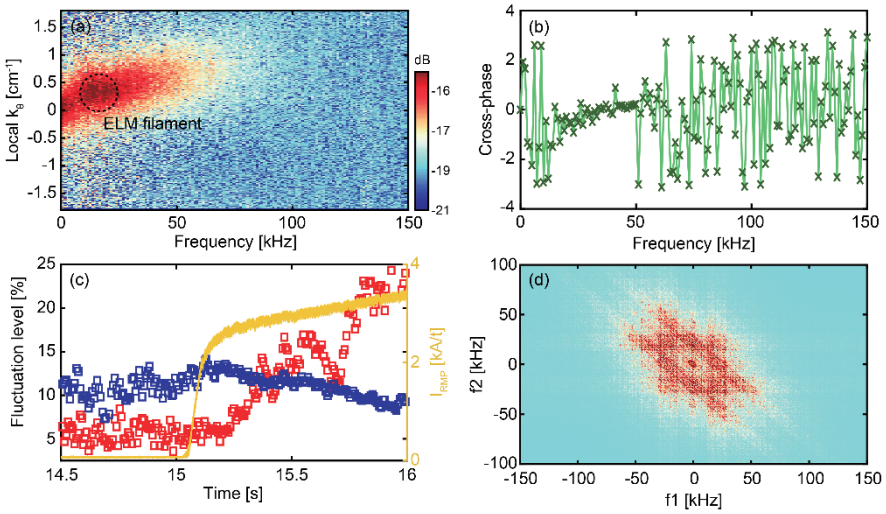

Figure 3. (a) The spectral power distribution of ECEI (ch.13-3). (b) Cross-phase between $\tilde{v}_r$ and $\tilde{T}_{\mathrm{ECE}}$ in the ELM-crash suppression phase. (c) Time series of integrated spectral powers of ELM (blue; 5-30 kHz) and turbulence (red; 30-70 kHz) with RMP coil current. (d) Auto-bispectrum estimation using a single ECEI channel (ch.13-3), located in the path of ELM filament.

over a wide range of wave numbers ($k_\theta < 1$ cm^{-1}) and frequency ($f < 70$ kHz) with the average group velocity ~ 3 km/s along the electron diamagnetic drift direction in the lab-frame. The measured wave number allows one to deduce the characteristic size of the turbulence, usually compared with the hybrid Larmor radius $\rho_s = \sqrt{2m_i T_e}/eB$ where m_i is the ion mass and e is the electric charge. In this case, $k_\theta \rho_s < 0.1$ using $\rho_s \sim 1$ mm at the edge. Kinetic ballooning modes (KBMs), microtearing modes (MTMs), resistive ballooning modes (RBMs), and ion temperature gradient (ITG) modes are of similar size ($k_\theta \rho_s \sim 0.1$ in a tokamak).

4. Interaction between ELM filament and edge turbulence

The effect of the turbulent eddies on the radial transport can be studied by measuring the phase relation between the radial velocity fluctuations ($\tilde{v}_r$) and the ECE intensity fluctuation $\tilde{T}_{\mathrm{ECE}}$. The velocimetry based on cross-correlation with time-delay estimation is applied to the ECE images to track the high speed motion of the turbulent eddies and then obtain $\tilde{v}_r$ [7]. The measured cross-phase between $\tilde{v}_r$ and $\tilde{T}_{\mathrm{ECE}}$ during ELM-crash suppression is approximately in phase in the range of $30 - 50$ kHz, suggesting the turbulent eddies cause a net radial outward energy flux $\Gamma_{\mathrm{ECE}} \propto \langle \tilde{v}_r \tilde{T}_{\mathrm{ECE}} \rangle \propto \left| \tilde{T}_{\mathrm{ECE}} \right|^2 > 0$ (Fig. 3b).

Figure 3c represents the spectral power change of ELM filament and edge turbulence with RMP current I_{RMP}. The spectral power of the turbulence ($30 - 70$ kHz) increases with I_{RMP} while the spectral power of the ELM filament ($5 - 30$ kHz) decreases. This may suggest that the RMP induces the edge turbulence and the ELM crashes are suppressed when the edge turbulence level exceeds a certain threshold.

Figure 3d is an auto-bispectrum [8] of single ECEI channel, showing the nonlinear interaction between ELM filament ($f_{\mathrm{ELM}} \sim 20$ kHz) and turbulent eddies ($30 - 70$ kHz). The bispectrum plot shows line features (vertical, horizontal, and $-45°$ lines with intercepts at $\pm f_{\mathrm{ELM}}$). Note that these lines are essential identical

by the symmetries of bispectrum. No such line features are obtained in the bispectrum of ECEI signals before the ELM-crash suppression.

The nonlinear interaction revealed by bispectrum and the opposite trends in the spectral power between ELM filament and turbulence eddies suggest that the turbulent fluctuations induced by RMP dissipate the free energy for the ELM growth.

5. Summary

The ELM-crash suppression phase under $n = 1$ RMP is characterized by the coexisting ELM filament and turbulent eddies in the edge. The measurement shows that the RMP did not completely suppress the onset of ELM filaments but instead provided a damping to balance against the instability drive. The cross-correlation technique on the ECEI signals revealed that the RMP induces the turbulence and induced turbulence has wide range of poloidal wave number $k_\theta < 1$ cm^{-1} and rotates in the electron diamagnetic drift direction. The radial velocity and ECE intensity fluctuations of these turbulent eddies are approximately in phase and thus the turbulence involves a net radial outward energy transport. The bispectrum analysis shows that the coexisting ELM filament and turbulent eddies nonlinearly interact with each other. The nonlinear interaction between ELM filament and turbulent eddies dissipates the free energy of ELM growth and that may be the key to the physics mechanism of ELM-crash suppression by $\mathrm{n} = 1$ RMP.

Acknowledgements

This work was supported by NRF-2014M1A7A1A03029865, NRF-2014M1A7AA03029881 and the U.S. DOE under contract no. DE-FG02-99ER54531, and partly supported by the JSPS-NRF-NSFC A3 Foresight Program in the field of Plasma Physics (NSFC: No.11261140328, NRF: No.2012K2A2A6000443).

References

[1] T.E. Evans, R.A. Moyer, and P. Monat, Phys. Plasmas **9** (2002) 4957.

[2] T.E. Evans, et al., Phys. Rev. Lett. **92** (2004) 235003.

[3] G.S Yun, et al., Rev. Sci. Instrum. **81** (2010) 10D930.

[4] Y.M. Jeon, et al., Phys. Rev. Lett. **109** (2012) 035004.

[5] J. Lee, et al., Rev. Sci. Instrum. **85** (2014) 063505.

[6] J. Lee, et al., Phys. Rev. Lett. **117** (2016) 075001.

[7] T. Munset, and S.J. Zweben, Rev. Sci. Instrum. **77** (2006) 103501.

[8] Y.C. Kim, et al., Phys. Fluids **23** (1980) 258.

Rapid growth of resistive interchange modes and excitation of edge localized modes (ELMs) in an H-mode Plasma of LHD

K. Toi[1], S. Ohdachi[1], K. Ogawa[1], R. Ueda[2], T. Nicolas[3], K.Y. Watanabe[1], Y. Suzuki[1], K. Tanaka[1], LHD Experiment Group[1]

[1]National Institute for Fusion Science, Toki 509-5292, Gifu, Japan

[2] Plasma research center, Tsukuba University, Tsukuba 305, Japan

[3] Ecole Polytechnique Federale de Lausanne, Switzerland

Abstract

Rapid growth of low frequency magnetic fluctuations are observed about 1 ms before an edge localized mode (ELM) event in H-mode plasmas in an outward-shifted configuration on LHD. Long ELM-free H-phases more than ~5 times of global energy confinement time are interrupted by the large amplitude ELMs with a repetition frequency typically less than 20 Hz. Magnetic fluctuations suppressed down to very low level during the ELM-free H-phase are strongly enhanced by an order of magnitude during each ELM event. The magnetic fluctuations are dominated by m=1/n=1 modes, where m and n are the poloidal and toroidal mode numbers, respectively. In the L-phase, the m=1/n=1 magnetic fluctuations are enhanced by a factor of 3 of the level of the ELM-free H-phase. In order to understand the magnetic fluctuation behaviors in the ELM free H-phase, at the ELM onset and in L-phase, the linear stability analysis of the plasmas for these three time slices has been performed against resistive interchange mode (RIC). The rapid growth of m=1/n=1 RIC can be qualitatively explained by a slight radial expansion of the edge transport barrier (ETB), of which expansion leads to an increase of the pressure gradient at the mode rational surface ι=1 in the magnetic hill region. The calculated eigenfunction of the radial displacement for the profiles simulating the ELM onset have a tearing mode character as well as interchange one, while those in the ELM-free H-phase and L-phase have typical interchange mode character.

1. Research background and objectives

Characters of ELMs and the active control are intensively studied experimentally and theoretically in many major tokamaks, because they would have strong impacts on divertor target plates in ITER like plasmas [1, 2]. The MHD instabilities triggering ELMs in tokamak plasmas through nonlinear evolution are thought to be ballooning and/or peeling (kink) modes and their combination [3,4]. The instabilities are destabilized by pressure gradients and toroidal current in ETB or pedestal region. ELMs are also observed in H-mode plasmas of stellarator/helical devices. In contrast to ELMs in tokamaks, the most likely candidate MHD instabilities triggering ELMs are thought to be resistive interchange modes (RICs) because of basically net plasma current free, i.e., in W7-AS and LHD [5-8]. Moreover, soft X-ray detector array systems in LHD revealed that the MHD modes excited in ETB region have anti-ballooning structure [9].

In LHD H-modes, two types of ELMs are observed, depending on the magnetic configurations. In so-called inward-shifted magnetic configuration, i.e., typically the magnetic axis position of the vacuum field R_{ax}=3.6 m, small and high frequency ELMs are excited immediately (less than 15 ms) after the L-H transition and cease the increase of the plasma stored energy [6,7,9]. The ELMs are typically induced by m=2/n=3 and/or m=1/n=2 magnetic fluctuations. On the other hand, in the H-modes of the outward-shifted configuration of R_{ax}=3.9 m, large amplitude ELMs are excited by m=1/n=1 magnetic fluctuations, having low repletion frequency less than 20 Hz typically. Typical time evolutions of the averaged toroidal beta value $<\beta_{dia}>$ obtained by diamagnetic measurement and the magnetic fluctuation amplitude are shown in Fig.1. The $<\beta_{dia}>$ or the plasma stored energy is decreased down to 25% by each large ELM, as seen from Fig.1. The magnetic fluctuation amplitude is enhanced by a factor of ~10 during each ELM for that in ELM-free H-phase. The amplitude in L-phase is also enhanced by a factor of ~ 3 for that in ELM free H-phase. A zoomed waveform of an ELM event is shown in Fig.2, where the poloidal magnetic probe signal starts to grow about 1 ms before the crash of the edge line-electron-density n_eL_{edge}, and about 0.2 ms later the H_α emission signal rises up drastically. In this study, the interpretation of very low level of magnetic fluctuations and the rapid growth just before an large amplitude ELM is attempted with help of linear stability analysis of RICs.

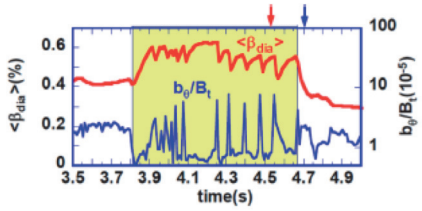

Fig.1 Time evolutions of the toroidal beta derived from the diamagnetic loop $<\beta_{dia}>$ and the poloidal magnetic fluctuation amplitude relative to the toroidal field strength b_θ/B_t in the H-mode plasma of the outward-shifted configuration. The red and blue arrows indicate the typical time slices in ELM free H-phase and L phase.

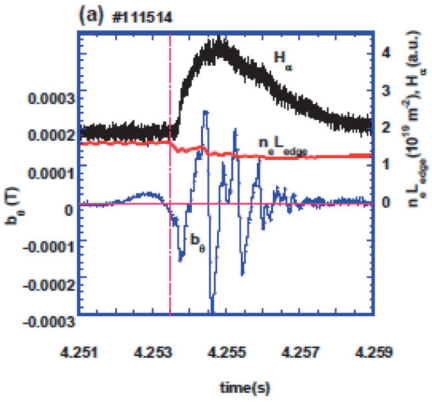

Fig.2 Zoomed waveforms of b_θ, the edge line-electron-density n_eL_{edge} and H_α emission in an ELM event.

2. Linear stability analysis of resistive interchange mode

Stability analyses against RICs of the equilibrium pressure profiles taken at the ELM-free H-phase and at L-mode after the H-L back transition are performed using two stability analysis codes [10,11]. An example of the pressure profile obtained by Thomson scattering and charge exchange recombination spectroscopy in the ELM-free H-phase is shown in Fig.3. This figure also shows a best fitted curve having the form of $P(x)$ $(=P_e+P_i)=P_{ETB}[1-\tanh(\alpha(x-x_o))] + (P_o-P_v)[1-x^{go}]^{g1}$ [12]. The parameters P_{ETB}, P_o, α, x_o and $go/g1$ stand for the pedestal pressure, the pressure at the plasma center, the steepness of the pressure gradient in the ETB, the location of the steepest pressure gradient and the parameters of the pressure profile shape near the plasma center. In this figure the radial coordinate $x=r/a$ is adopted using the effective plasma minor radius a=0.466m. Here, the lowest-order rational surface ι=1 surface locates just outside the last closed

magnetic surface (LCFS). In order to apply the linear MHD stability code to the H-mode plasma, the effective plasma radius a is expanded to place the ι=1 surface inside LCFS, so that a linear stability analysis code can be applied straightforwardly. The numerical code can calculate the growth rate and eigenfunction of RIC, where only electrical resistivity is taken into account as non-ideal effects [10]. The dependence of the growth rate on the location of the steepest pressure gradient x_o was investigated with the MHD stability code. The results are shown in Fig.4. In the H-phase, the growth rate dramatically increases when the steepest pressure gradient layer at x=x_o approaches to the ι=1 surface at x_s=0.941. In the calculation, the rotational transform profile is calculated by the MHD equilibrium calculated with the HINT code without the existence of nested magnetic surfaces [13]. The cases of x_o=0.788 and x_o=0858 simulate the situations of the ELM-free H-phase and that just prior to an ELM event. The growth rate at x_o=0858 increases an order of magnitude, compared with that at x_o=0.788. The growth rate in the L-phase shown in the arrow is by a factor of ~3 larger than that in the ELM-free H-phase. In Figs. 5 and 6, the eigenfunctions of perturbations of pressure p_1, scalar potentialϕ_1, poloidal flux ψ_1 and radial displacement ξ_r calculated by the code are shown for the ELM-free H-phase and the ELM onset, respectively. The radial profiles of equilibrium pressure and the rotational transform are shown in Fig.(a) of these figures.

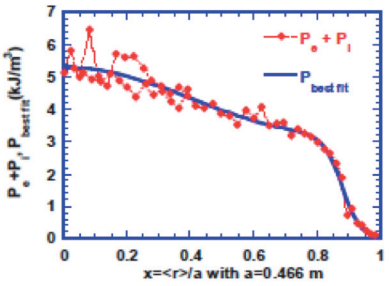

Fig.3 Pressure profile (red circles) obtained by Thomson scattering and charge exchange recombination spectroscopy at t=4.533 s in the ELM-free H-phase shown in Fig.1. The best fit curve is also shown.

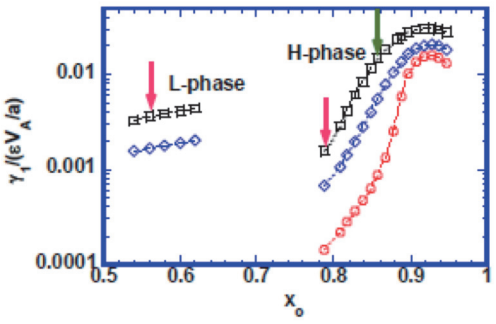

Fig.4 Dependences of the growth rates of m=1/n=1 RIC on the steep pressure gradient layer x_o for the H- and L-phases. The magenta arrows indicate the pressure profiles in the ELM-free H-phase at t=4.533s and L-phase at t=4.700 s of the H-mode shown in Fig.1. The green arrow corresponds to the case simulating the ELM onset. The growth rates for three magnetic Reynolds number S=10^5(squares), 10^6 (diamonds) and 10^8 (circles) are given.

The eigenfunctions of ϕ_1 and ξ_r in the case of the ELM onset clearly extend toward the plasma central region, while they localize strongly at the ι=1 rational surface. The eigenfunctions in the ELM-free H-phase (Fig.5) exhibit typical interchange parity having an even function at the ι=1 surface. However, the eigenfunctions for the profile simulating the ELM onset (Fig.6) tend to contain the tearing parity component having an odd function in addition to usual interchange character [12]. The eigenfunctions in the L-phase where the pressure profile has no steep pressure gradient at the ι=1 surface also have a typical interchange parity at the ι=1 surface, as seen from Fig. 7.

The large increase in the growth rate on m=1/n=1 RIC when x_o approaches x_s suggests that the large

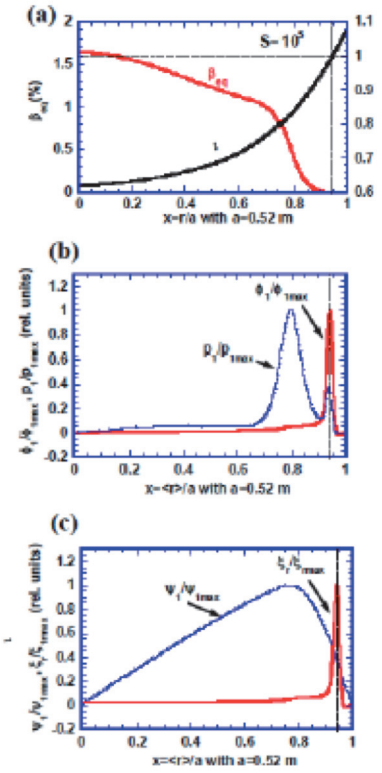

Fig.5 (a) Equilibrium profiles of pressure and the rotational transform, (b) eigenfunctions of p_l and ϕ_l, and (c) eigenfunctions of ψ_l and ξ_r in the ELM-free H-phase.

amplitude ELM observed in the H-mode of LHD would be triggered by a slight expansion of the ETB region toward the ι=1 rational surface. This seems to be consistent with the experimental observations that ELMs are often triggered suddenly without any clear increase in $<\beta_{dia}>$ from the nearly saturated value in the ELM-free H-phase. The above stability analysis of RICs was performed by using the stability analysis code where only resistivity is included as non-ideal plasma effects. In the H-mode plasma, the steep pressure gradient exists near the rational surface, so that plasma diamagnetic drift might have considerable impact on the mode stability. We investigated the effects of the diamagnetic drift effects on the RIC stability using the stability analysis code where various non-ideal

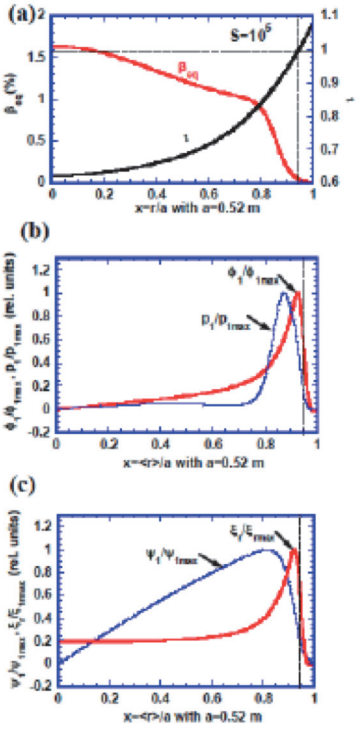

Fig.6 Equibribrium profiles and eigenfunctions in the case simulating the plasma just prior to the onset of an ELM event.

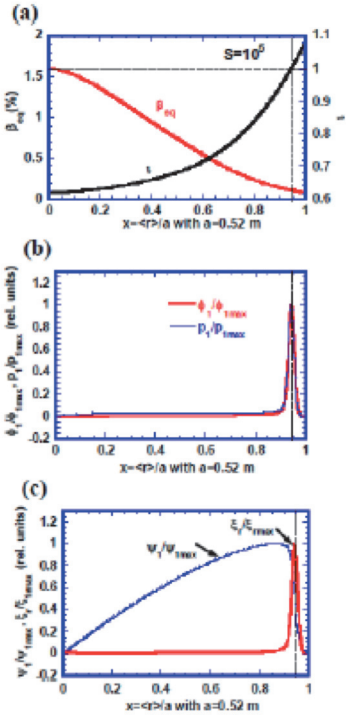

Fig.7 Equibribrium profiles and eigenfunctions in the L-phase.

effects can be included in the resistive mode stability analysis [11]. Figure 8 shows the diamagnetic effect on the RIC growth rates calculated without the diamagnetic effects. Here, the magnitudes of electron and ion diamagnetic drift frequencies are assumed to be the same. As seen from Fig.8, the diamagnetic drift effect on the growth rates is fairly weak, i.e., less than 10 % reduction except a certain range of x_o where the reduction rate reaches ~20%.

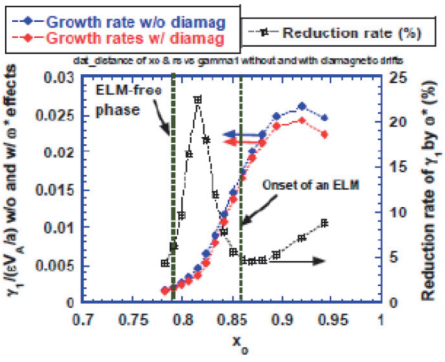

Fig.8 Effect of diamagnetic drifts on the RIC growth rates calculated without the diamagnetic effects. The figure also shows the reduction rate of the growth rate by the effects.

3. Conclusion

The linear MHD stability of the H-mode plasmas in LHD was investigated against resistive interchange modes, using two stability analysis codes. These calculations clearly indicate that the slight expansion of the size of the ETB or pedestal toward the main rational surface, i.e., the ι=1 surface may trigger a large amplitude ELM through nonlinear evolution of RICs in the H-mode plasma of LHD. The ξ_r eigenfunction calculated for the case simulating the ELM onset indicates the mixed character having tearing parity as well as interchange one, while the eigenfunctions in the ELM-free H- and L-phases have typical interchange parity.

Acknowledgements

This research is supported in part by LHD project budgets (NIFS10ULHH011, NIFS14KLPP037and NIFS12KLPP025) and the Grant-in-Aid for Scientific Research from JSPS (No. 24360386, No. 26249144, No. 26630476). It is also supported by the JSPS-NRF-NSFC A3 Foresight Program in the field of Plasma Physics (NSFC: No.11261140328, NRF: No. 2012K2A2A6000443).

References

[1] A. Loarte *et al,* Progress in the ITER physics basis chapter4 *Nucl. Fusion* **47** (2007) S203.

[2] A. Loarte *et al, Plasma Phys. Control. Fusion* **45** (2003)1549.

[3] P.B. Snyder *et al*, *Phys. Plasmas* **9** (2002) 2037.

[4] G.T.A. Huijsmans *et al, Phys. Plasmas* **22** (2015) 021805.

[5] A. Weller *et al*, *Phys. Plasmas* **8** (2001) 931.

[6] K. Toi *et al, Phys. Plasmas* **12** (2005) 020701.

[7] K. Toi *et al, Fusion Sci. Technol.* **58** (2010) 61.

[8] K. Toi *et al, Nucl. Fusion* **54** (2014) 033001.

[9] F. Watanabe *et al, Contrib. Plasma Phys.* **50** (2010) 651.

[10] R. Ueda *et al*, *Phys. Plasmas* **21** (2014) 052502.

[11] T. Nicolas and K. Ichiguchi, *Nucl. Fusion* **56** (2016) 026008

[12] K. Toi *et al*, Plasma Phys. Control. Fusion **58** (2016) 094002.

[13] Y. Suzuki *et al, Nucl. Fusion* **46** (2006) L19.

Destabilization of macro/micro-scale edge instabilities by magnetic perturbations in KSTAR

Jayhyun Kim[1], Minjun J. Choi[1], Jaehyun Lee[2], Jaemin Kwon[1], Young-Mu Jeon[1], Siwoo Yoon[1], the KSTAR team[1], and the KSTAR collaborators[2]

[1]National Fusion Research Institute, Daejeon, Republic of Korea
[2]Ulsan National University of Science and Technology, Ulsan, Republic of Korea

E-mail: jayhyunkim@nfri.re.kr

Non-axisymmetric magnetic field induced magnetic perturbation (MP) is considered to be the most likely technology to control the edge localized mode (ELM) crash, which is potentially a risk to the inner wall life of the reactor level device. However, the exact mechanism of MP is not fully understood in both ELM crash mitigation and suppression. In this study, we investigated the characteristics of macro- and micro-edge instabilities associated with MP during KSTAR ELM crash controlled discharges. The results showed that the response of macro- and micro-edge instabilities was very rapid for the applied MP, which was found to be faster than the typical edge profile changes.

1. Introduction

In an H-mode discharge, the stationary ELM-free period can be distinguished from transient ELM-free period by the presence of a regulatory mechanism to prevent the recovery of the edge profile from ELM crashes. Several transport mechanisms have been discussed as the candidates of the regulation mechanism such as edge harmonic oscillations in quiescent H-mode, weakly coherent mode in I-mode, and stochastic transport in resonant magnetic perturbation (MP)-driven ELM crash suppression.

In so-called tearing hypothesis, applied MP does not directly affect edge instability. Instead, it increases the edge transport by forming a superposition between the magnetic islands that are present on the various rational surfaces. This determined edge profile determines the nature of the edge instability. Thus, in the tearing hypothesis of ELM crash suppression, the change in edge profile must precede the change in edge instability. However, experimental studies [1, 2] and theoretical studies [3, 4] have been recently proposed / reported, in which changes in edge instability precede edge profile changes.

Here, we will discuss the characteristics of edge instability according to MP, focusing on the possibility of direct destabilization of instability in KSTAR ELM crash controlled discharges. To rule out the effects of profile changes, such as the strong density pump-out that occurs when MP is applied, we have primarily investigated the phase of deviating from ELM control with rapid turn-off of the MP. The study attempts to include both macroscopic and microscopic instabilities to explain the role of MP in both ELM crash mitigation and suppression.

2. Mitigation of ELM Crashes

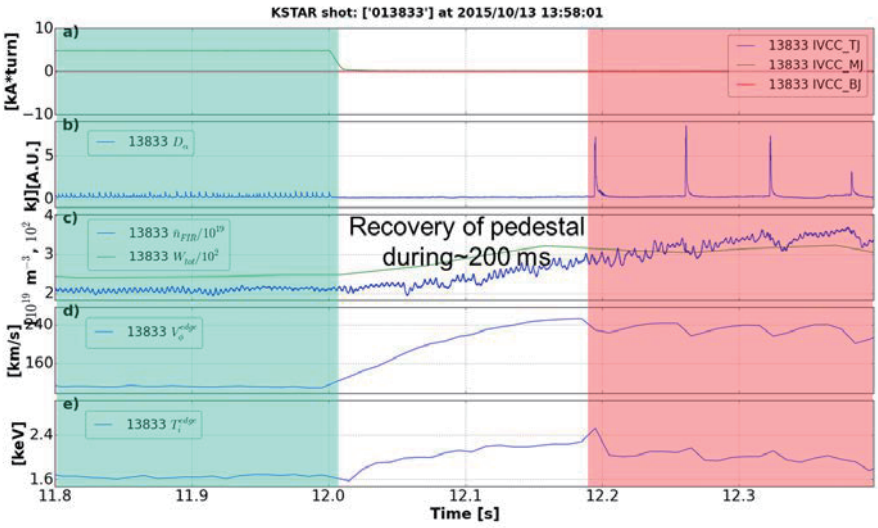

Fig. 1. Evidence of direct destabilization of macro edge instabilities by MPs in KSTAR shot no. 13833. a) Non-axisymmetric coil currents, b) Dα signal, c) line-integrated density (blue line) and stored energy (green line), d) edge rotation, and e) edge ion temperature.

Figure 1 shows the response to ELM crash with MP intensity during strongly ELM mitigated discharge. Mitigated ELM crash frequency is at least 10 times greater than natural one, but individual ELM crashes still exist on a macro scale as indicated by the Dα peak in the green shaded area. On the other hand, if the MP is turned off, the mitigated ELM crash disappears immediately. The time to turn off the MP (~ 10ms) is much shorter than the pedestal evolution time (~ 200ms) required to bring back the original ELM crash without MP effect. Therefore, it can be concluded that ELM crash occurs directly by the MP. Without MP, the peeling-ballooning (PB) mode stability criteria still remain stable due to the degraded edge pedestal.

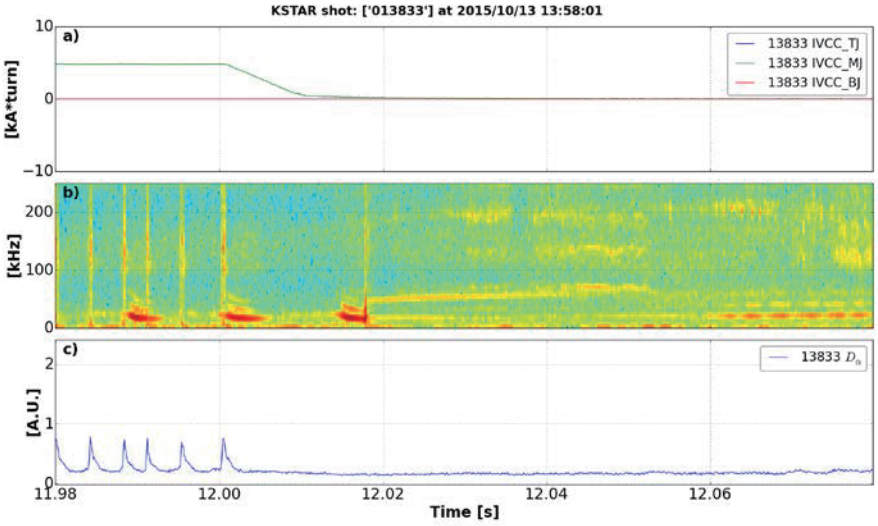

Fig. 2. Magnetic fluctuation change of ELM crash mitigated discharge in KSTAR shot no. 13833. a) Non-axisymmetric coil currents, b) spectrogram of magnetic fluctuation, and c) Dα signal.

Note that no significant change in broadband magnetic fluctuation is observed during the MP turn-off phase (t = 12.00 sec to 12.01 sec) except for the line due to an individual ELM crash in figure 2. The increase in broadband fluctuation appears to begin with the recovery of the edge pedestal.

3. Suppression of ELM Crashes

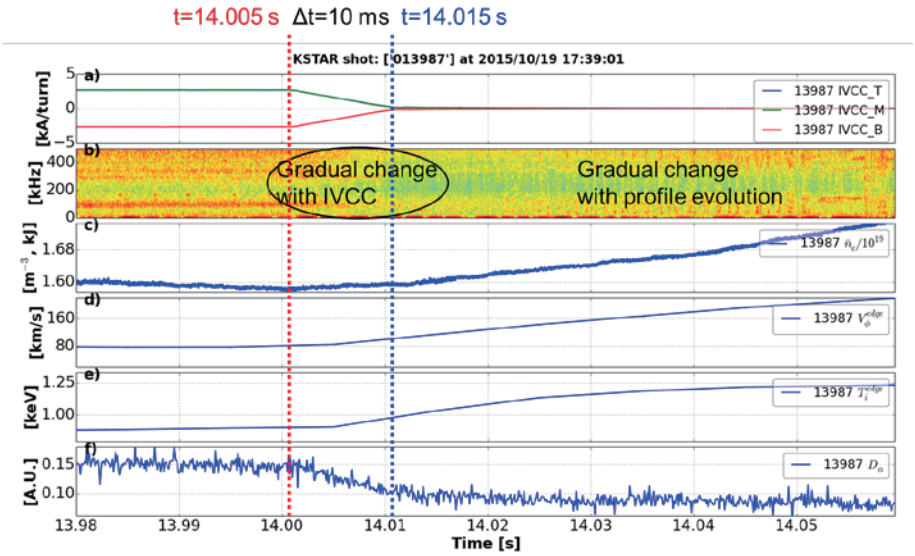

Fig. 3. Evidence of direct destabilization of micro edge instabilities by MPs with fast MP turning-off. a) Non-axisymmetric coil currents, b) spectrogram of magnetic fluctuation, c) line-integrated density, d) edge rotation, e) edge ion temperature, and f) Dα signal.

During ELM crash suppression, the Dα and magnetic fluctuation signals are responding immediately to the MP amplitude as shown in figure 3. The Dα signal (indicator of edge particle transport) shows a sudden change only when MP amplitude decreases. Subsequently, the equilibrium evolution observed at line averaged density, edge rotation and edge ion temperature progressively follows the MP intensity drop. This implies that enhanced transport induced by micro-edge instability caused by MP is responsible for keeping the edge pedestal below the ELM crash level. Analysis of edge turbulence by electron cyclotron emission image (ECEI) shows that the level of fluctuation on the low field side is significantly reduced immediately after MP is turned off as shown in figure 4. However, no significant change was detected on the high field side [5, 6]. The change in turbulence appears to be confined to a particular edge region (i.e., a particular edge channel).

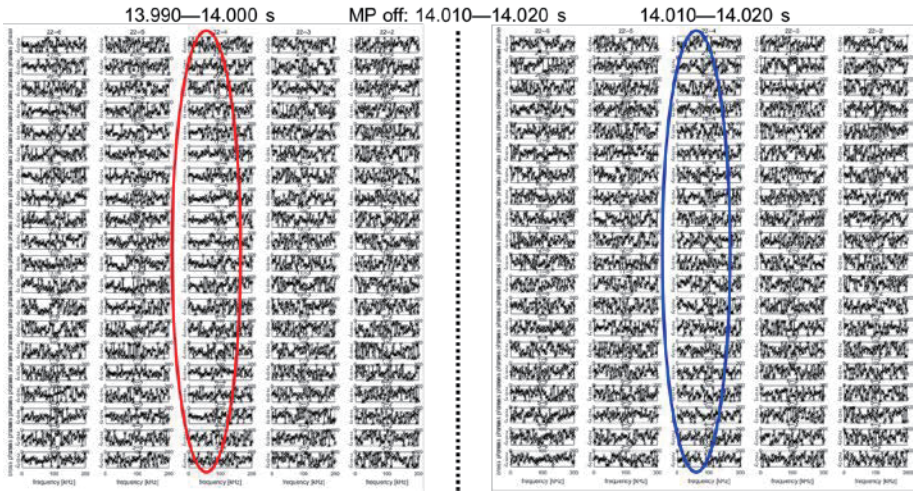

Fig. 4. Cross-phases of edge ECEI channels in KSTAR shot no. 13987 before and after the MP-turning off. Red and blue circles indicate the channels of significant change.

On the other hand, the bifurcation-like feature was observed in the magnetic fluctuation, line-integrated density, and Dα signal [6] when we slowly ramped the MP down during nearly 60 ms as shown in figure 5. Although there is a caveat in isolating the effect of pedestal evolution from the change of edge instabilities, figure 5 still represents several important aspects. Firstly, global confinements are generally governed by the MP amplitude as shown in the evolution of line-integrated density and Dα signal during t=8.01 sec ~ 8.05 sec. In addition, the bifurcation or threshold of edge instabilities intervenes the edge transport abruptly. Figure 6 depicts that the mentioned bifurcation-like feature takes place in edge localized region. The detailed analyses are still on-going with local fluctuation measurements to reveal the characteristics of MP-driven micro edge instabilities (i.e., the type of edge instability) along with bifurcation-like feature during the slow change of MPs [6].

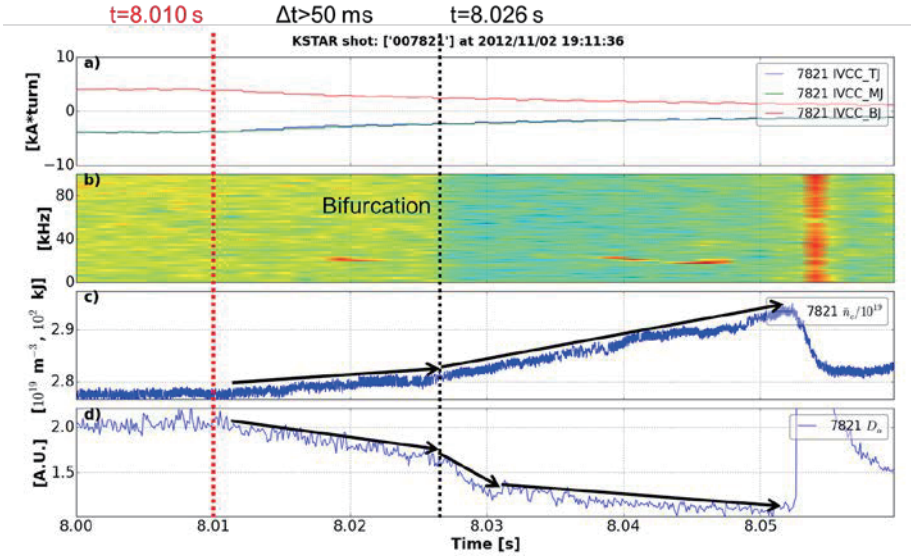

Fig. 5. Evidence of direct destabilization of micro edge instabilities by MPs with slow MP turning off. a) Non-axisymmetric coil currents, b) spectrogram of magnetic fluctuation, c) line-integrated density, and d) Dα signal.

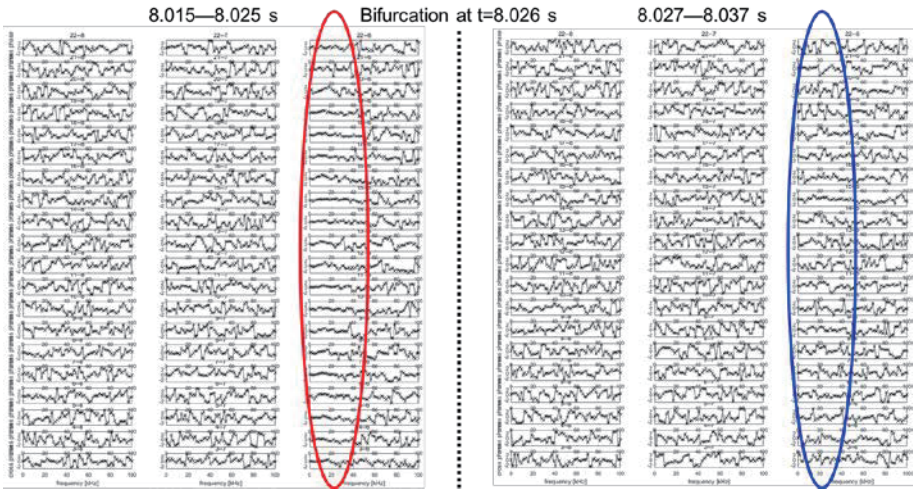

Fig. 6. Cross-phases of edge ECEI channels in KSTAR shot no. 7821 before and after the bifurcation-like feature at t=8.025 sec. Red and blue circles indicate the channels of significant change.

4. Summary and Discussion

In this study, we present evidence of direct destabilization of edge instabilities in ELM crash mitigation and suppression when MP with low n mode number (eg, n = 1 and n = 2) is applied to KSTAR H mode discharges. In fact, the edge instability characteristics are very similar in both n = 1 and n = 2 ELM crash suppression. The results of this study show that changes in edge instability precede equilibrium evolution. It is not consistent with the description of ELM crash suppression by stochastic transport, but on the other hand it shares the characteristics of bifurcation type response [6].

In order to find alternative explanations for ELM crash mitigation and suppression, it is necessary to reevaluate the stability criteria of macro- and micro-edge instabilities in the presence of MP. So far, most of the stability calculations have assumed unperturbed / undistorted equilibrium. For this reason, we plan to numerically recalculate PB mode stability in disturbed equilibrium, including mode couplings [3]. We also consider the possibility of MP-induced micro-edge instability like kinetic ballooning mode [4].

In views of meso-scale phenomena, the ELM crash suppression mechanism such as zonal flow damping by MP should not be completely excluded, but zonal flow damping has limitations in explaining the mitigated ELM crash commonly observed in various devices. For realistic applications on reactor scale devices such as ITER, an integrated picture of MP-induced ELM crash mitigation and suppression should be established.

Acknowledgements

This work was partly supported by the JSPS-NRF-NSFC A3 Foresight Program in the field of Plasma Physics (NSFC: No.11261140328, NRF: No.2012K2A2A6000443).

References

[1] S.J. Fielding et al., “ELM control in COMPASS-D”, Proceedings of 28th EPS Conference on Contr. Fusion and Plasma Phys. Funchal (2001); ECA 25A, 1825-1828 (2001).
[2] G.R. McKee et al., “Increase of turbulence and transport with resonant magnetic perturbations in ELM-suppressed plasmas on DIII-D”, Nucl. Fusion 53, 113011 (2013).
[3] C.C. Hegna, “Effects of a weakly 3-D equilibrium on ideal magnetohydrodynamic

instabilities", Phys. Plasmas 21, 072502 (2014).
[4] T.M. Bird et al., "A model for microinstability destabilization and enhanced transport in the presence of shielded 3D magnetic perturbations", Nucl. Fusion 53, 013004 (2013).
[5] C. Paz-Soldan et al., "Observation of a Multimode Plasma Response and its Relationship to Density Pumpout and Edge-Localized Mode Suppression", Phys. Rev. Lett. 114, 105001 (2015).
[6] R. Nazikian et al., "Pedestal Bifurcation and Resonant Field Penetration at the Threshold of Edge-Localized Mode Suppression in the DIII-D Tokamak", Phys. Rev. Lett. 114, 105002 (2015).

ELM study in KSTAR H-mode plasma using MHD simulation and ECEI observation

M. Kim[1], J. Lee[1], H. K. Park[1,2], G. S. Yun[3], J. E. Lee[3], W. Lee[2], S. Jardin[4], X. Q. Xu[5], M. Bécoulet[6] and KSTAR team

[1]Ulsan National Institute of Science and Technology, Ulsan 44919, Ulsan, Republic of Korea
[2]National Fusion Research Institute, Daejeon 34133, Daejeon, Republic of Korea
[3]Pohang University of Science and Technology, Pohang 37673, Gyeongbuk, Republic of Korea
[4]Princeton Plasma Physics Laboratory, Princeton 08540, NJ, USA
[5]Lawrence Livermore National Laboratory, Livermore 94550, CA, USA
[6]CEA, IRFM, Saint-Paul-Lez-Durance 13108, France

Abstract

For the robust and effective ELM-crash contorl for a steady-state operation of high-performance plasma in a fusion reactor, it is required to understand nonlinear dynamics near ELM-crash. To interpret and understand remarkable ELM observation by KSTAR ECEI systems in nonlinear phase [1, 2, 3], nonlinear MHD simulations, BOUT++, M3D-C1, and JOREK, are conducted in KSTAR H-mode plasma. Although it is hard for each code to explain all observed nonlinear ELM dynamics, the promising results are obtained; the broadband *n*-number spectrum (BOUT++), heat/particle expulsion toward SOL (M3D-C1 and JOREK) and the changes of dominant mode number during the inter-ELM-crash period (JOREK).

1. Introduction

ELM is MHD instability driven by steep pressure gradient and high current at the edge of H-mode plasmas. If the H-mode is adapted as an operation scenario for a fusion reactor, it is required to control the ELM-crash because heat and particle flux during pedestal relaxation may cause a severe damage to the machine. The KSTAR ECEI systems [4, 5] contribute to study ELM physics by visualizing ELM dynamics from initial growth to crash phase [1, 6]. In addition to that, they produce remarkable ELM observations in nonlinear phase; the rapid change of toroidal mode number [2] and simultaneous excitation of multiple modes [3] during the inter-ELM-crash period. In the previous comparative study, the observed ELM structure is compared with synthetic images based on linear ELM simulation. An excellent agreement in two images provides a confidence on the edge observation by ECEI [7]. However, it is hard to investigate nonlinear ELM dynamics using linear simulation. To interpret the observed ELM dynamics in nonlinear phase, a nonlinear simulation should be considered in the comparative study. Here the nonlinear simulation results from BOUT++ [8, 9], M3D-C1 [10] and JOREK [11] are presented and they are preliminarily compared with ECEI observations.

2. Nonlinear MHD ELM simulation in KSTAR H-mode plasma

A plasma equilibrium for nonlinear MHD simulation is reconstructed using TEQ solver in CORSICA package based on estimated p-profile and magnetic geometry information of EFIT calculation and

considering J_b from Sauter formula [12]. To determine the plasma equilibrium profile, p-profile is scanned and derived J_b is scaled so that the most unstable n-number from linear stability analysis agrees with that of observed coherent mode at the time of interest. The equilibrium shown in Fig. 1 is used as initial plasma condition for nonlinear simulation. Fig. 1(a) illustrates magnetic geometry of KSTAR discharge #7328 at t ~ 4.36 s. The characteristics of this discharge at the time of interest is following: P_{NBI} ~3 MW, I_p = 750 kA, $B_T(R_0)$ = 2.25 T and q_{95} ~ 5. Fig. 1(b) and 1(c) show selected total pressure and toroidal current density profiles on LFS mid-plane in respective. Steep pressure gradient and high edge current density are clearly shown. ECEI system clearly observes n = 8 coherent structure during quasi-stable phase (Fig. 1(d)). It means that the most unstable mode as a constraint for equilibrium reconstruction is n = 8.

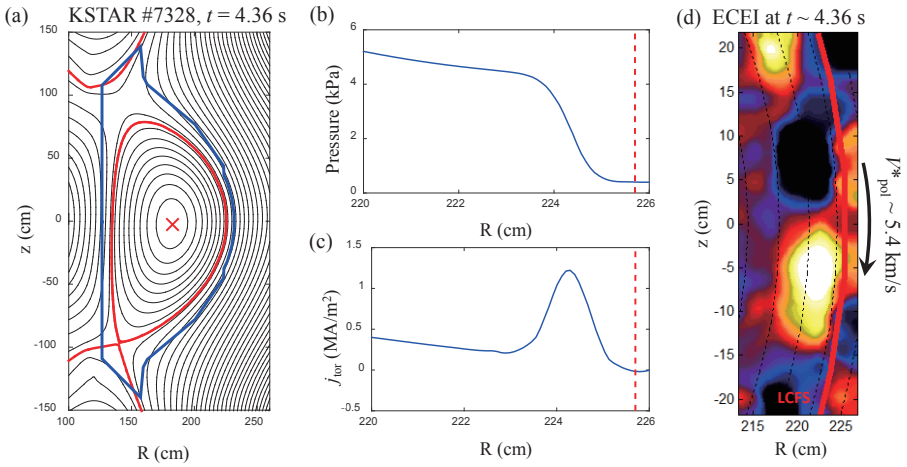

Fig. 1 (a) Reconstructed plasma equilibrium (KSTAR #7328, t = 4.36 s). Red solid line: separatrix; blue solid line: first wall. (b) Total pressure profile and (c) toroidal current density on LFS mid-plane edge. Red dotted line: separatrix location (d) ECEI observation at t ~ 4.36 s. The apparent poloidal rotation speed at LFS mid-plane V^*_{pol} is ~5.4 km/s in ion diamagnetic drift direction.

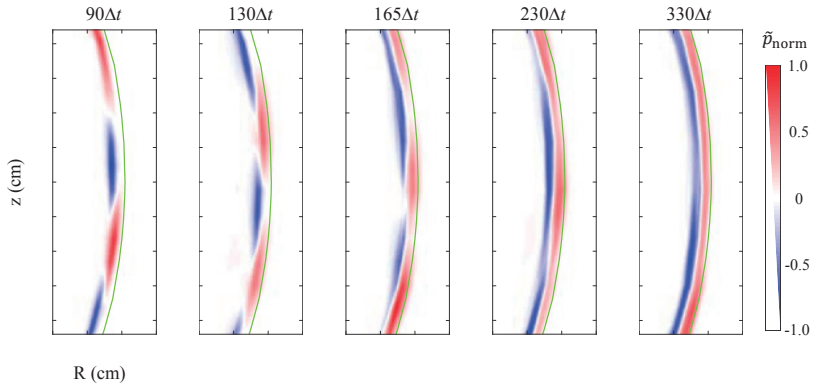

Fig. 2 Slices of 3D pressure perturbation structure on a poloidal plane at LFS edge from BOUT++. Each frame is normalized by each absolute maximum value. Green solid lines indicate LCFS.

Firstly BOUT++ nonlinear ELM simulation results are described. The 3-field model [9] is used here. Flat resistivity profile is applied. While ad-hoc hyper-resistivity and diamagnetic stabilization term are considered, net plasma rotation effect is not. n = 1, 2… 16 harmonics are included as an initial perturbation.

Fig. 2 illustrates a slices of 3D pressure perturbation structure on a poloidal plane at LFS edge. Each frame is normalized by each absolute maximum. n = 8 appears at early nonlinear phase (left three panels). Subsequently, the pressure perturbation looks as if it becomes nearly uniform in poloidal due to dominant n = 0 component.

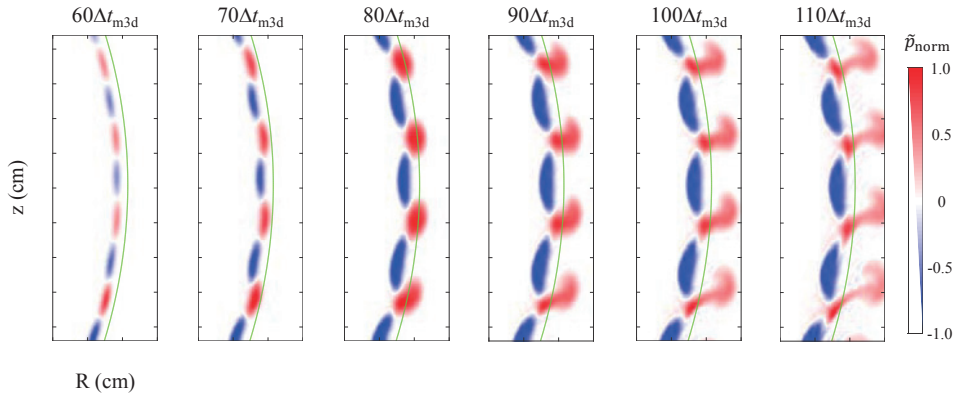

Fig. 3 Slices of 3D pressure perturbation structure on a poloidal plane at LFS edge from M3D-C1. Each frame is normalized by each absolute maximum. Green solid lines represent LCFS.

M3D-C1 is full-MHD simulation code [10]. The details of M3D-C1 formalism is explained in [10]. Here 6-field full MHD model in toroidal geometry is used. Resistivity is a flat profile in the plasma with S = 10^6 but increases to S_{vac} = 1 in the open field line (vacuum) region. Hyper-resistivity, diamagnetic effect, and plasma rotation effect are not considered in this case. Initial perturbation is set as that of BOUT++, or n = 1, 2… 16 are initialized all together. The initial conditions are not exactly same that of BOUT++. Fig. 3 shows a slice of 3D pressure perturbation on a poloidal plane at LFS edge. Each frame is normalized by each absolute maximum also. n = 16 is dominant toroidal mode number in all images in Fig. 3 because the diamagnetic stabilization effect is not taken into account. The perturbations are expelled to SOL region.

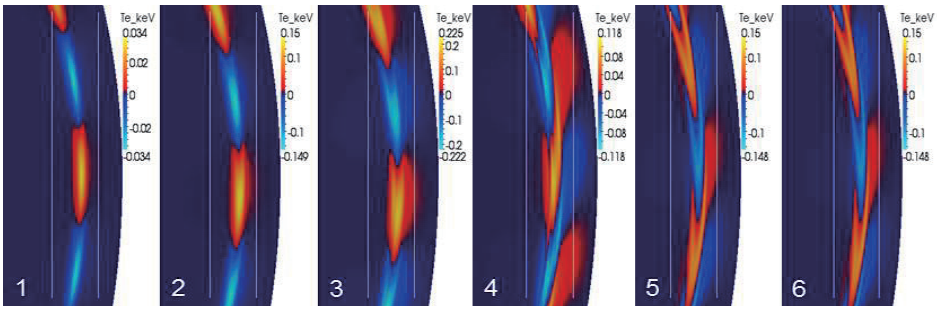

Fig. 4 T_e perturbation on a poloidal plane at LFS edge from JOREK. Each frame is separated in time by ~16.6 μs. White vertical lines indicate ECEI view window. Courtesy of M. Bécoulet [13].

JOREK is reduced resistive non-linear MHD code in full toroidal X-point geometry including separatrix and open flux surfaces [11]. Nonlinear JOREK simulation results in KSTAR geometry are described in detail [13]. Here the recent results of nonlinear simulation will be briefly summarized. Two fluid diamagnetic, neoclassical effects and plasma toroidal rotation are included in the model. In JOREK simulation with single harmonics n = 8, the apparent poloidal rotation of the mode before ELM crash is

reproduced by ~5 km/s in ion diamagnetic drift direction [13]. Fig. 4 shows T_e perturbations from JOREK nonlinear simulation in a poloidal cross-section view. On the highly non-linear phase of ELM-crash, the mode rotation decreases (frame (1)-(4) in Fig. 4) [13] and perturbation structures are expelled to the SOL which is similar to M3D-C1 results (Fig. 3).

3. Preliminary comparative study between nonlinear simulation and ECEI ELM observation

Although no codes perfectly reproduce ECEI observation near and during ELM-crash, each code can explain some parts of observation. Heat and particle transport across separatrix observed by ECEI systems [2] is reproduced by M3D-C1 (Fig. 3) and JOREK (Fig. 4). The transient disappearance of mode is probably closely related with the broadening of mode number spectrum in BOUT++. Nonlinear JOREK simulation reproduce the transition of toroidal mode number during the inter-ELM-crash period [2, 13]. To make a clear conclusion on ELM dynamics in nonlinear phase, it is required to examine the nonlinear simulation results thoroughly.

4. Summary

BOUT++, M3D-C1 and JOREK nonlinear simulation are conducted in KSTAR H-mode plasma. Even though each code has some issues to be resolved, the promising results are obtained which explain some parts of observed dynamics by KSTAR ECEI systems

Acknowledgements

This research was supported by the National R&D Program through the NRF of Korea funded by the Ministry of Science, ICT & Future Planning under contract no. 2014M1A7A1A03029865. This work was partly supported by the JSPS-NRF-NSFC A3 Foresight Program in the field of Plasma Physics (NSFC: No.11261140328, NRF: No.2012K2A2A6000443).

References

[1] G. S. Yun, W. Lee, M. J. Choi, et al., Physics of Plasmas **19** (2012) 056114.
[2] J. E. Lee, G. S. Yun, M. Kim, et al., Nuclear Fusion **55** (2015) 113035.
[3] M. Kim, J. Lee, H. K. Park, et al., Nuclear Fusion **55** (2015) 073001.
[4] G. S. Yun, W. Lee, M. J. Choi, et al., Review of Scientific Instruments **81** (2010) 10D930.
[5] G. S. Yun, W. Lee, M. J. Choi, et al., Review of Scientific Instruments **85** (2014) 11D820.
[6] G. S. Yun, W. Lee, M. J. Choi, et al., Physical Review Letters **107** (2011) 045004.
[7] M. Kim, M. J. Choi, J. Lee, et al., Nuclear Fusion **54** (2014) 093004.
[8] B. D. Dudson, M. V. Umansky, X. Q. Xu, et al., Computer Physics Communications **180** (2009) 1497.
[9] X. Q. Xu, B. D. Dudson, P. B. Snyder, et al., Nuclear Fusion **51** (2011) 103040.
[10] S. C. Jardin, N. Ferraro, J. Breslau, et al., Computational Science and Discovery **5** (2012) 014002.
[11] G. T. A. Huysmans, O. Czarny, Nuclear Fusion **47** (2007) 659.
[12] O. Sauter, C. Angioni, Y. R. Lin-Liu, Physics of Plasmas **6** (1999) 2834
[13] M. Bécoulet, M. Kim, G. S. Yun, et al., IAEA Fusion Energy Conference 2016, **TH/P1-24** (2016)

Recent progress of hydrogen isotope behavior in damaged W

Y. Oya[1], H. Fujita[1], S. Sakurada[1], Y. Uemura[1], K. Azuma[1], and Q. Zhou[2]

[1]Graduate School of Science and Technology, Shizuoka University, Shizuoka, 422-8529, Japan

[2]Faculty of Science, Shizuoka University, Shizuoka, 422-8529, Japan

Abstract

The damage distribution and thermal annealing effects on hydrogen isotope dynamics including retention, permeation were discussed. By introduction of irradiation damages, D permeation was reduced due to reduction of D diffusion path. But, the thermal annealing induced the recovery of irradiation damages and D permeation behavior was almost consistent with that for undamaged W. The damage distribution makes a large impact on D retention in damaged W. Accumulation of damages may lead to form stable trapping sites, like voids. Thermal annealing leads to growth/annihilation of damages, and the density of irradiation defects would be one of key parameters for control of aggregation or recover.

1. Introduction

Due to the high tritium solubility in graphite, tungsten (W) will be the primary plasma-facing material candidate for fusion. It is reported that lower hydrogen isotope retention and higher thermal conductivity are favorable qualities for usage of W in fusion reactor [1]. However, recent studies show that tritium dynamics will be clearly controlled by the characteristics of W material, the damage distributions introduced by neutrons and other energetic particles, history of thermal annealing and so on. In our previous studies, the D retention for 0.025 dpa neutron irradiated W was clearly enhanced and reached up to 1 at.%. In addition, the desorption temperature has shifted toward higher temperature side above 800 K, indicating that the damage distribution throughout the bulk by neutron irradiation would lead the desorption behavior. Recently, we have performed systematic D retention and permeation studies for various damage profiles in W and their recovery behavior by thermal annealing are reviewed in this paper.

2. D permeation behavior for Fe^{2+} damaged W

Fig. 1 shows the D permeabilities and diffusion coefficienets for Fe^{2+} damaged W with the damage concentration of 0.001 - 0.3 dpa. It was found that the they were reduced with increasing damage concentration due to increase of defect size or/and density. The permeability for 0.3 dpa Fe^{2+} irradiated W at 973 K was almost the same even if it was heated at 1173 K. The diffusion coefficient for 0.3 dpa Fe^{2+} irradiated W was increased because of reduction of irradiation defect density by defect aggregation. The permeabilities and diffusion coefficients for 0.001 and 0.037 dpa Fe^{2+} irradiated W were completely recovered by annealing at 1173 K (Not shown in this figures).

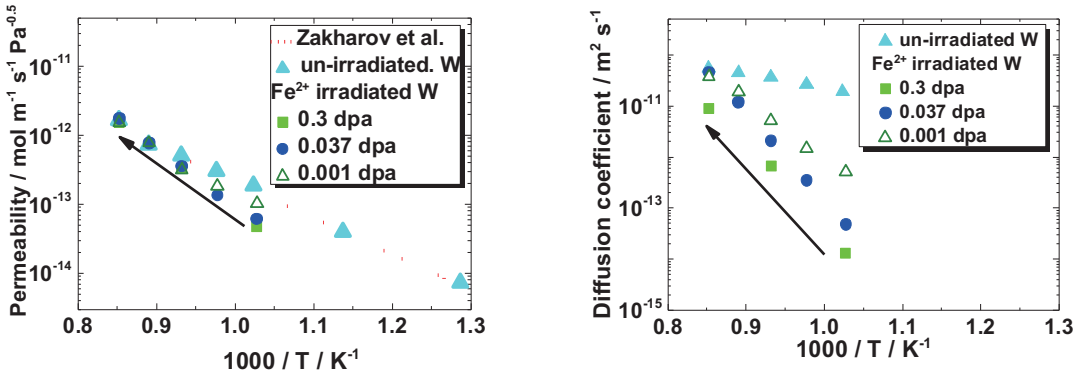

Fig. 1 D permeabilities and diffusion coefficienets for Fe^{2+} damaged W at various temperatures.

3. Damage distribution dependence on D retention in W

In our previous study, 14 MeV neutron irradiation clearly changes the D retention behavior even in the lower damage concentration due to cascade collision of energetic neutron, indicating that the control of damage distribution leads to the D retention behavior. Therefore, Fe^{2+} irradiation with the different incident energies of 0.8 MeV and 6 MeV, whose implantation depths are ~ 0.2 μm and 1.2 μm, were used to control the damage distribution. Fig. 2(a) shows the typical damage profiles by 0.8 MeV and 6 MeV Fe^{2+} irradiation in W. By changing the incident energy and ion fluence, several damage profiles can be demonstrated. The D2 TDS spectra for these damage profiles were shown in Fig. 2(b). It was found that multiple Fe^{2+} implantation with different incident energies leads to the enhancement of D trapping at lower temperature less than 600 K, although single ion implantation lead to D migration toward the depth. The D amount at Peak 4 for multiple ion implantation of (1) 0.8 MeV 0.1 dpa + 6 MeV 0.1 dpa was almost the same as that for (3) 6 MeV 0.1 dpa, indicating that D would be trapped by voids that are much more stable than monovacancies.

To confirm the hydrogen isotope distribution, DT^+ implantation was performed and β-ray Induced X-ray Spectroscopy (BIXS) was applied. Fig. 3 shows BIXS spectra for Fe^{2+} implanted W with the damage profiles of (1) 0.8 MeV 0.1 dpa + 6 MeV 0.1 dpa, (2) 0.8 MeV 0.1 dpa + 6 MeV 0.03 dpa and (3) 6 MeV

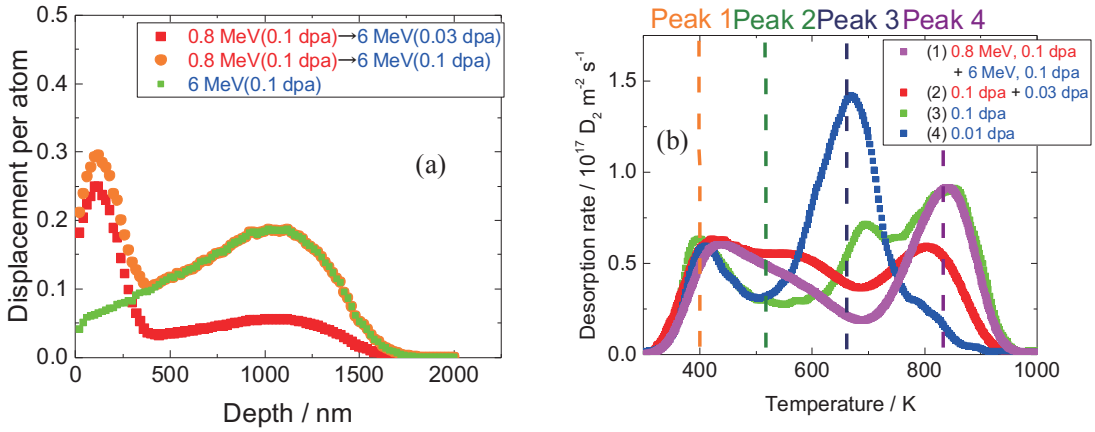

Fig 2 Damage distribution profiles by 0.8 MeV and 6 MeV Fe^{2+} irradiation in W and D_2 TDS spectra for various Fe^{2+} damaged W.

0.1 dpa, and Pure-W, respectively. There are two unique peaks located at 1.174 keV and 2.957 KeV, corresponding to W (Mα) and Ar (Kα), respectively. Ar (Kα) characteristic X-ray gives T concentration information from the surface up to the depth of ~ 50 nm, although W(Mα) gives up to the depth of 1μm [2]. Therefore, it can be found that multiple ion implantation induced T accumulation near surface region, where 0.8 MeV Fe^{2+} implantation introduced the damages, and these results were consistent with the Tritium IP images.

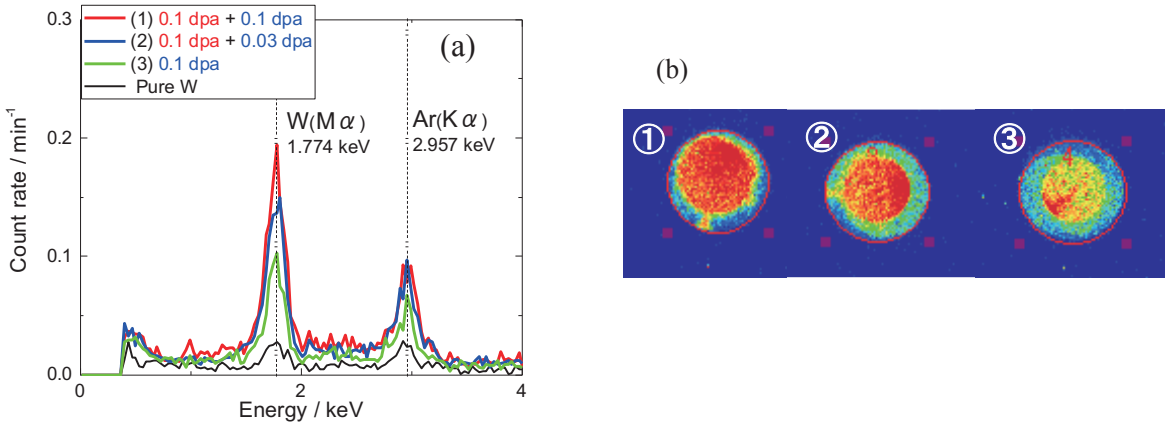

Fig. 3 (a) BIXS spectra and (b) IP images for (1) 0.8 MeV 0.1 dpa + 6 MeV 0.1 dpa, (2) 0.8 MeV 0.1 dpa + 6 MeV 0.03 dpa and (3) 6 MeV Fe^{2+} damaged W after DT^{+} implantation with the fluence of ~ 6×10^{20} DT^{+} m^{-2}.

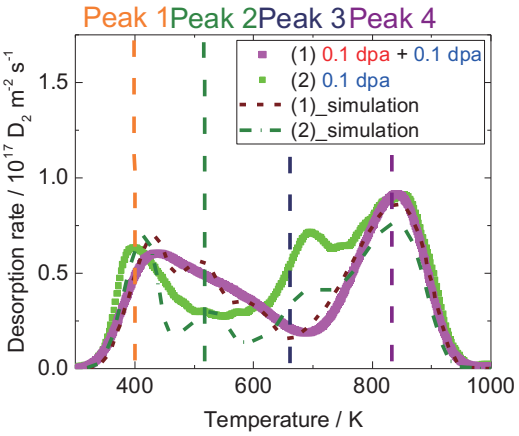

Fig. 4 Comparison of experimental results and HIDT simulation results.

Based on these experimental results, Hydrogen Isotope Diffusion and Trapping (HIDT) simulation code was applied to demonstrate the experimental results and to analyze the D distribution in W, as shown in Fig.4 [3]. This simulation also reproduces the D accumulation near surface region due to heavy damage accumulation by 0.8 MeV Fe^{2+} irradiation.

4. Thermal annealing effect on D retention in damaged W

The growth/recovery of irradiation damages is controlled by the thermal annealing. In especially. the

duration of thermal annealing would be one of key factor to determine the damage growth/recovery. Fig. 5 shows the annealing duration effect on D retention for 0.1 dpa and 1.0 dpa Fe^{2+} damaged W. For 0.1 dpa damaged W, the D retention was decreased and the shoulder of TDS spectrum at 700 K was disappeared with increasing annealing time. The vacancy clusters were completely recovered by annealing for 5 hours. The density of vacancies was decreased, but some of vacancies would remain in the damaged W even if the sample was annealed for 5 hours. For 1.0 dpa damaged W, After 0.5h annealing, Peak 3 for 1.0 dpa W was shifted to higher temperature side. By longer annealing, D trapped by voids (Peak 3) was almost disappeared. Therefore, it can be said that the thermal annealing would induce both of vacancy aggregation and recover, and the density of vacancy clearly control the growth/recover.

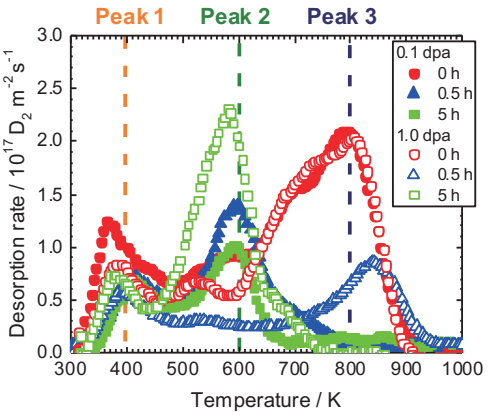

Fig. 5 D_2 TDS spectra for 0.1dpa and 1.0 dpa Fe^{2+} damaged W at 1173 K for 0 - 5 h

5. Summary

Recent progress of damage distribution and thermal annealing effects on hydrogen isotope dynamics including retention, permeation were discussed. By introduction of irradiation damages, D permeation was reduced due to reduction of D diffusion path. But, the thermal annealing induced the recovery of irradiation damages and D permeation behavior was almost consistent with that for undamaged W. The damage distribution makes a large impact on D retention in damaged W. Accumulation of damages may lead to form stable trapping sites, like voids. Thermal annealing leads to growth/annihilation of damages, and the density of irradiation defects would be one of key parameters for control of aggregation or recover.

Acknowledgements

This work was partly supported by the JSPS-NRF-NSFC A3 Foresight Program in the field of Plasma Physics (NSFC: No.11261140328, NRF: No.2012K2A2A6000443).

References

[1] Y. Ueda, et al., Phys Scr. T145 (2011) 014029.

[2] M. Matsuyama et al., J. Nucl. Mater. 307 (2002) 729.

[3] Y. Oya et al., J. Nucl. Mater. 461 (2015) 336-340.

Energetic Particle Researches in KSTAR

T.Rhee[1], J.Kim[1], J.Y.Kim[2], B.H.Park[1], Hogun Jhang[1], and KSTAR team[1]

[1]National Fusion Research Institute, Daejeon 34133, South Korea

[2]Korea University of Science and Technology, Daejeon 34113, South Korea

Abstract

Energetic particle loss by external magnetic perturbation is an important issue to design control coils of tokamaks. In this study we try to find out the basic physical mechanism of fast ion prompt loss by external magnetic perturbation. Dynamics of phase space of toroidal canonical momentum and magnetic moment is studied to describe prompt loss of fast ions deposited by neutral beam injection. Results show that toroidal canonical momentum oscillation due to drift resonance between perturbation and fast ion increases the number of lost particles.

1. Introduction

The physics of fast ions in tokamak plasmas has been widely investigated because of its importance to ion heating, which is relevant to fusion performance[1, 2]. Neutral beam injection (NBI) and ion cyclotron resonance heating (ICRH), which are auxiliary ion heating methods for current tokamaks, accelerate the ion speed from several *keV* to hundreds *keV* or *MeV*. Alpha particles are a by-product of the most promising fusion reaction between deuterium and tritium ions; they are expected to heat burning plasma and realize self-sustaining fusion machine[3, 4]. Thus, fast ion transport has been a key issue in fast ion physics.

Energetic particle loss by external magnetic perturbation is an urgent issue to design magnetic perturbation coils. One of operation scenarios for ITER is H-mode without edge localized mode (ELM). For large sized tokamak the large energy dump to plasma facing component (PFC) by ELM is not endurable. Thus ELM suppression or mitigation by external magnetization is a challenge for ITER and larger sized tokamak for ignition[5].

Meanwhile in various tokamak devices, including KSTAR, the fast ion loss detector (FILD) has been used to study fast ion transport[6-10]. A FILD measures the energetic ions bombarding a scintillator in the vicinity of a plasma facing component. It has been used to investigate fast ion loss and the correlation with magnetic perturbations like Alfvén eigenmodes[9], tearing modes[11], and external magnetic perturbations[12]. It has the benefit of enhancing the reliability of analytical predictions for the loss particle energy and pitch-angle information by allowing direct comparison with measurements.

In KSTAR, fast ion loss observed by FILD was studied in terms of prompt loss by energetic ion in the NBI heated plasma[13]. This work did not consider magnetic perturbation including toroidal field ripple and error field because intrinsic magnetic perturbation level of KSTAR is less then $\sim 10^{-4}$. They found that simple NBI deposition modeling in phase space explains the pitch angles detected by FILD. Additionally they found that fast ions deposited in the SOL are origin of high pitch angle particles detected by FILD. Thus

change of fast ion loss induced by magnetic perturbation is ready to study in KSTAR.

In this proceeding we report basic physical mechanism of increase of fast ion loss observed by FILD. In the section 2 we present modelling analysis of prompt loss and its enhancement by magnetic perturbation. Firstly, prompt loss without magnetic perturbation is modeled in the phase space. Modeling study of the effect of magnetic perturbation on prompt loss of fast ions are followed. Section 3 presents summary of this paper.

2. Result

Before entering into the analysis of experiment, we introduce modeling method which is used in the analysis. Minimal beam modeling used in Ref. [13] is adopted to calculate position and initial pitch-angle defined as $acos(v_{||}/v)$, where $v_{||}=\mathbf{v}\cdot\mathbf{B}/B$ and $v^2=\mathbf{v}\cdot\mathbf{v}$. From this modeling we calculate conserved quantities of toroidal canonical momentum $p_\phi = mv_{||}g/B - e\psi_p$ and magnetic moment $\mu \equiv \frac{1}{2B}mv_\perp^2$, where $g \equiv R_0B_0$, $\mathbf{v}_\perp \equiv \boldsymbol{v} - \boldsymbol{v}_{||}$, R_0 is the major radius, B_0 is the toroidal magnetic field strength at R_0, ψ_p is the poloidal flux, $\boldsymbol{e}$ is the unit charge, and $\boldsymbol{m}$ is the ion mass. Conserved momentum for each particle in the axisymmetric system is used to analyze observed pitch-angle by FILD probe. For the momentum varying case with magnetic perturbation, we calculate its time evolution by using guiding center motion equation (8)-(15) presented in the Ref [14].

Experimental conditions to investigate effect of magnetic perturbation on the fast ion loss are followings. Basic plasma condition is 0.5MA plasma current and 1.8T toroidal magnetic field. Error field correction coil set is prepared to generate n=1 resonant magnetic perturbation during 3s to 8s. Fast ion sources are 2 NBI ion sources of NBI1-A and NBI1-B with energy of 90keV and 80keV respectively.

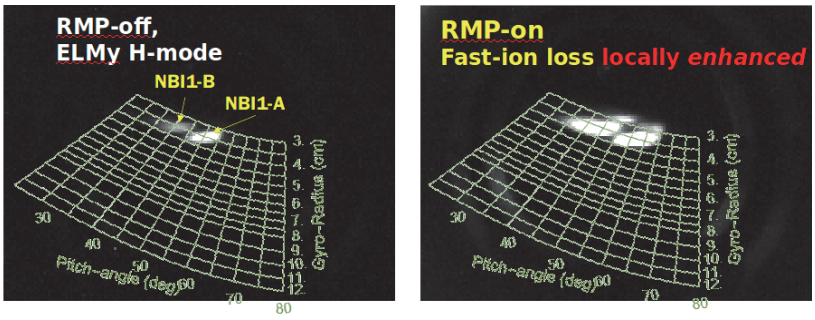

Figure 1. FILD CCD image with the pitch-angle .vs. gyro-radius map from shot #9092, t = 3.2s and 5.5s. Prompt loss spots from NBI1-A, and B are clearly shown. The pitch-angle resolution of KSTAR FILD is from maximum 0.75 at high pitch to minimum 0.9 at low pitch.

In this situation we compare FILD CCD image between with and without magnetic perturbation. Without magnetic perturbation case shows two distinguishable bright spots which lie in pitch-angle range of 35°~45° and 45°~55°. Following modeling analysis identifies that each spot is originated from NBI1-B and NBI1-A respectively.

When applying an external magnetic perturbation using in-vessel current coil, the number of fast ions detected by FILD increases. The increment is shown as being brighter in the image of FILD as presented in

the figure 1. These changes induced by magnetic perturbation happen in the time scale of μs which is much faster than the transport time scale of fast ion. Measured pitch-angles lies of 35°~50° and 50°~60°. Two features of magnetic perturbation case are broader pitch-angle range and brighter spots which mean more fast ions detection. This means that increased particles detected by FILD are originated not from core region but SOL region. Instantaneous response and unchanging pitch and energy suggest that detected particles are from the SOL region without collisions.

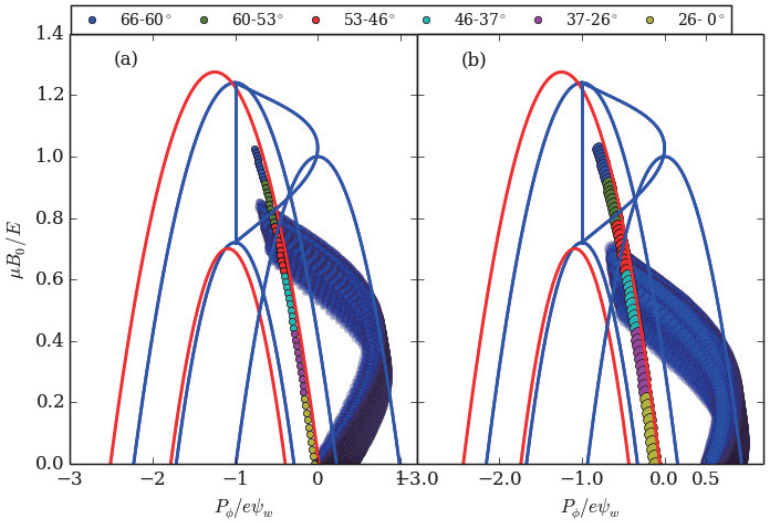

Figure 2. Normalized toroidal and magnetic moments (blue dots) of beam particles according to minimal modelling: (a) NBI1-A, (b) NBI1-B. The momentums of particles passing through the FILD position are plotted as colored circles with a black edge. The colors indicate pitch-angles as given in the legend.

Using reconstructed equilibrium fitting[15] (EFIT) and minimal beam deposition modeling we construct phase space analysis as shown in the figure 2. Figure 2.(a) plots the FILD line and NBI1-A distribution of shot #9092 at a time of 3.8s. The coloured lines and points denote the following: (1) coloured circles indicate the FILD probe with the colour representing the pitch-angle, (2) small blue circles indicate the beam distribution, and colours represent (3) the inner wall - red, (4) inner LCFS position with $Z = Z_{magnetic\ axis}$ - purple (5) magnetic centre - blue, (6) outer LCFS position with Z = 0 - green, (7) outer wall – yellowish green, and (8) maximum value - black from inside the LCFS to outside. We can determine the crossing between the beam distribution and FILD at the pitch-angle region: 45° - 55°. In the same manner, figure 2.(b) shows detectable pitch-angles by the FILD for NBI1-B of 38° – 49°. Though experimental observation and analysis has 3° difference, the model explains detected pitch-angle.

The case of magnetic perturbation is also analyzed by same manner. Perturbed magnetic field is not considered in the detected pitch calculation. Strength of perturbed magnetic field is $\sim 10^{-4}$ compared to equilibrium magnetic field thus change of toroidal canonical momentum and magnetic moment is

negligible. Pitch-angles predicted by model are not different from without magnetic perturbation case though experimental shows change of pitch-angle and brightness. Thus we study the dynamics of phase space with magnetic perturbation needs.

Time evolution of toroidal canonical momentum is calculated under magnetic perturbation. Magnetic perturbation is described by single *n=1*, *m=3* poloidal magnetic perturbation without radial dependency where *n* and *m* are toroidal and poloidal mode number. Its strength is adjusted to have $B_p/B_0 \sim 10^{-3}$ to reflect experimental magnetic perturbation level. We do not consider magnetic perturbation in the SOL.

Given magnetic perturbation generates magnetic island at the $q = 3$ flux surface drawn as red solid line in the figure 3. Its size agrees with the prediction of theory. The other islands are not shown because magnetic perturbation is not too strong to make harmonics and stochastic field lines.

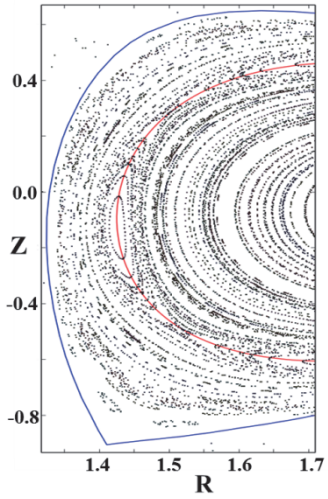

Figure 3. Field line tracing of magnetic perturbation of n=1 and m=3. Red solid line is q=3 surface.

Response of fast ions to magnetic perturbation is different from magnetic field line. We use fully passing particles with 100keV deuterium. We scatter fast ions from magnetic axis to last closed flux surface (LCFS) with random toroidal angle.

Poincare section on the poloidal plane of fast ion guiding center shows outer drift of orbit island from resonant flux surface designated by center red solid line in the figure 4 though orbit is stochastic. In addition to $q = 3$ resonant flux surface, secondary orbit islands at $q = 4$ and $q = 2$ are found and both drift to outward. The orbit in $q = 4$ surface is also stochastic due to overlap between $q = 3$ and $q = 4$ orbit islands.

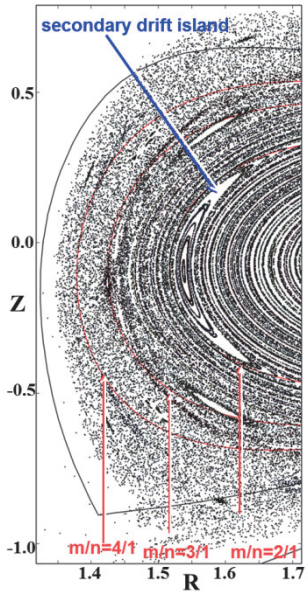

Figure 4. Poloidal Poincare section of fast ion orbit with magnetic perturbation of n=1 and m=3 mode. Red solid lines are resonant flux surface of red arrows designated with m/n mode number

Realistic case is studied with 90keV fast ions deposited by NBI1-A with shot #9092. To reduce simulation time, the particles deposited in the vicinity of FILD probe on the phase space is selected. Result is shown in the figure 5. Toroidal canonical momentum oscillates during orbit following time and cross the FILD phase space line. It means that detectable area in the phase space increase from the line to area. Thus it will be shown as brighter spot than the case of without magnetic perturbation. In this model we cannot find the increase of detectable magnetic moment.

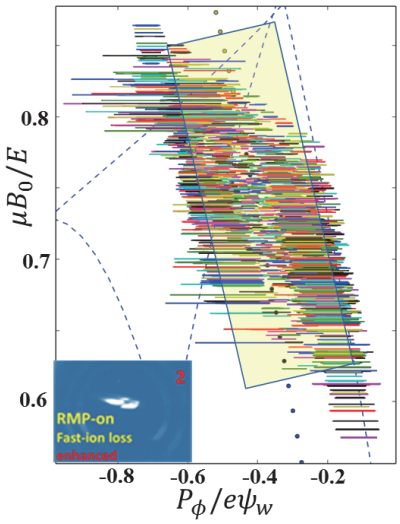

Figure 5. Time evolution of toroidal canonical moment. Each color solid line means momentum time evolution of each fast particle. Transparent yellow box shows the detectable phase space by FILD probe.

3. Summary

Fast ion loss increase by external magnetic perturbation was investigated on the momentum phase space. The comparison study between with and without magnetic perturbation was studied to figure out the features of enhanced fast ion loss by magnetic field perturbation. From this we found that perturbation makes more fast ions detection with broader pitch-angles. Toroidal canonical momentum oscillation by magnetic perturbation increases the detection by FILD as inducing intersection between the momentum line of FILD and fast ions in the phase space. Drift resonance and secondary island generation of fast ion makes large oscillation of toroidal canonical moment in the phase space.

We limited the modelling and simulation to prompt loss with single mode external magnetic perturbation. Thus, this model will be extended to include multi modes reflecting resonant magnetic field perturbation.

Acknowledgements

This work was partly supported by the JSPS-NRF-NSFC A3 Foresight Program in the field of Plasma Physics (NSFC: No.11261140328, NRF: No.2012K2A2A6000443).

References

[1] N. Gorelenkov, S. Pinches, and K. Toi, Nucl. Fusion 54 (2014) 125001.

[2] W. W. Heidbrink and G. Sadler, Nucl. Fusion 34 (1994) 535.

[3] N. Fisch and J. Rax, Phys. Rev. Lett. 69 (1992) 612.

[4] A. Bierwage, N. Aiba, and K. Shinohara, Phys. Rev. Lett. 114 (2015) 015002.

[5] T.E.Evans, R.A.Moyer, J.G.Watkins, T.H.Osborne, P.R.Thomas, M.Becoulet, J.A.Boedo, E.J.Doyle, M.E.Fenstermacher, K.H.Finken, R.J.Groebner, M.Groth, J.H.Harris, G.L.Jackson, R.J.La Haye, C.J.Lasnier, S.Masuzaki, N.Ohyabu, D.G.Pretty, H.Resmerdes, T.L.Rhodes, D.L.Rudakov, M.J.Schaffer, M.R.Wade, G.Wang, W.P.West, and L.Zeng, Nucl. Fusion 45 (2005) 595

[6] Zweben, S.J., Rev. Sci. Instrum. 57 (1986) 1774.

[7] D. S. Darrow, Rev. Sci. Instrum. 79 (2008) 023502.

[8] D. C. Pace, R. S. Granetz, R. Vieira, A. Bader, J. Bosco, D. S. Darrow, C. Fiore, J. Irby, R. R. Parker, W. Parkin, M. L. Reinke, J. L. Terry, S. M. Wolfe, S. J. Wukitch, and S. J. Zweben, Rev. Sci. Instrum. 83 (2012) 073501.

[9] M. Garcia-Munoz, I.G.J. Classen, B. Geiger, W.W. Heidbrink, M.A. Van Zeeland, S. Äkäslompolo, R. Bilato, V. Bobkov, M. Brambilla, G.D. Conway, S. da Graça, V. Igochine, Ph. Lauber, N. Luhmann, M. Maraschek, F. Meo, H. Park, M. Schneller, G. Tardini and the ASDEX Upgrade Team, Nucl. Fusion 51 (2011) 103013.

[10] J. Kim, J.Y. Kim, S. W. Yoon, M. Garcia-Munoz, M. Isobe, and W. C. Kim, Rev. Sci. Instrum. 83 (2012) 10D305.

[11] E. Poli, M. García-Muñoz, H. -U. Fahrbach, S. Günter, and ASDEX Upgrade Team, Phys. Plasmas 15 (2008) 032501.

[12] M. Garcia-Munoz, S. Äkäslompolo, O. Asunta, J. Boom, X. Chen, I.G.J. Classen, R. Dux, T.E. Evans,

S. Fietz, R.K. Fisher, C. Fuchs, B. Geiger, M. Hoelzl, V. Igochine, Y.M. Jeon, J. Kim, J.Y. Kim, B. Kurzan, N. Lazanyi, T. Lunt, R.M. McDermott, M. Nocente, D.C. Pace, T.L. Rhodes, M. Rodriguez-Ramos, K. Shinohara, W. Suttrop, M.A. Van Zeeland, E. Viezzer, M. Willensdorfer, E. Wolfrum, the ASDEX Upgrade, DIII-D and KSTAR Teams, Nucl. Fusion 53 (2013) 123008.

[13] J.Y.Kim, T.Rhee, J.Kim, S.W.Yoon, B.H.Park, M.Isobe, K.Ogawa, and W.-H.Ko, AIP Advances 6 (2016) 105013

[14] Y. Todo, Phys. Plasmas 13 (2006) 082503

[15] L.L.Lao et al., Nucl. Fusion 30 (1990) 1035.

Long-term Largescale Particle Simulations of Runaway Electron Dynamics in Tokamaks

J. Liu[1], H. Qin[1], Y. Wang[1]

[1]University of Science and Technology of China, Hefei, Anhui, China, 230026

Abstract

Fusion energy will be the ultimate clean energy source for mankind. The ITER device under construction by international partners will bring this goal one-step closer. Before constructing the first prototype fusion power plant, one of the most visible concerns that needs to be addressed is the threat of deleterious runaway electrons (REs) produced during unexpected disruptions of the fusion plasma. Massive REs can carry up to 70% of the initial plasma current in ITER, and understanding their dynamical behavior is crucial to assess the safety of ITER. However, the complex dynamics of REs in a realistic fusion reactor is almost impossible to simulate numerically because it requires efficient long-term algorithms and super-large scale computing power. In the present study, we deploy the world's fastest supercomputer, Sunway TaihuLight, and the newly developed relativistic volume-preserving algorithm 12 to carry out long-term particle simulations of 10^7 sampled REs in 6D phase space. The size of these simulations is in the range of 10^{18} particle-steps, the largest ever achieved in fusion research. Previous studies suggest that REs can be accelerated to 350MeV or higher in ITER, and randomly strike the first wall of the reactor to cause grave damage. Our simulations show that in a realistic fusion reactor, the concern of REs is not as serious as previously thought. Specifically, REs are confined much better than previously predicted and the maximum average energy is in the range of 150MeV, less than half of previous estimate. As a consequence, most of the energy carried by these electrons will be released through the benign process of synchrotron radiation without causing damage to the first wall. These simulations on Sunway TaihuLight ease the concern over REs, and give scientists more confidence in the outcome of ITER and Chinese Fusion Engineering Test Reactor (CFETR), which is the post-ITER device currently being designed.

1. Introduction

As the ITER project is making great progresses, there are still some design and operation challenges on the way to harvest fusion energy. Massive deleterious REs produced during disruption and fast shutdown become the most visible concern. It is believed that large amount of REs will be generated through avalanche multiplication in disruptions and accelerated to a high energy, and randomly strike the first wall of the reactor to cause grave damage. In ITER, REs can carry up to 70% of the initial plasma current under the large loop voltage of 1000V or higher. Under the influence of synchrotron radiation, poloidal flux variation, and magnetic field ripples, the maximum energy of each runaway electron (RE) is estimated to be 350MeV or higher in ITER. Though many important theoretical results have been achieved, the overall dynamic behavior of REs in a realistic tokamak configuration is still rather vague. To evaluate the impact of the REs on the safety of the device, a comprehensive study of statistical properties of RE dynamics is necessary.

Because REs are highly relativistic with negligible collisions, accurate descriptions for their dynamics should be based on kinetic models. Fluid descriptions, such as the Magneto-hydrodynamics model, cannot capture many important features of the REs. Unfortunately, due to extreme multi-scale and nonlinear nature of the runaway dynamics, it is difficult to accurately trace the trajectory of even one single RE in phase space for its full lifecycle, from its creation to acceleration, and to its landing on the first wall or slowing down. With highly relativistic velocities, the runaway dynamics involves many coupled characteristic timescales spanning 11 orders of magnitude. Gyro-center approximation is no longer valid for REs with high energy. Therefore, long-term simulation up to 10^{11} time steps is required to reveal the multiscale dynamics in the complex geometry. This poses a challenge for qualified numerical methods. Traditional algorithms, such as the Runge-Kutta method, cannot be applied to such long-term simulations. This is because for these algorithms, the truncation errors at different time steps accumulate coherently, and long-term numerical solutions are dominated by large numerical error, and thus not trustworthy. Efficient algorithms suitable for massively parallel supercomputers with long-term accuracy and fidelity need to be developed. On the other hand, a large number of sample points of REs in 6D phase space are required. Because the gyro-symmetry is broken with the failure of the gyro-center approximation and the toroidal symmetry is broken due to the realistic reactor configuration with the ripple field, at least ten values need to be sampled in each dimension to provide a satisfactory resolution in phase space, which means that at least 10^6 to 10^7 REs need to be sampled. The total amount of computation for one simulation study requires up to 10^{18} particle-steps, corresponding to more than 10^{21} floating-point operations, which is much larger than the largest particle simulation ever achieved in fusion research. Meanwhile, Petabyte-level high-performance storage system with large-scale parallel I/O is also necessary for handling the simulation data. These requirements on both hardware and software make a comprehensive study of REs using particle simulations almost impractical.

Recently, breakthroughs in both hardware and software enabled the first ever panoramic particle simulation of REs in a realistic fusion reactor. On the hardware side, the Sunway TaihuLight supercomputer, world's first supercomputer reaching the 100PFlops landmark, came online early 2016 at the National Supercomputing Center in Wuxi (NSCC-Wuxi). The peak performance of the Sunway TaihuLight is 125 PFlops with a Linpack rating of 93 PFlops. It is currently world's fastest supercomputer on the latest Top500 list. One major technological innovation of the Sunway TaihuLight supercomputer is its SW26010 many-core processor, which includes 4 management processing elements (MPEs) and 256 computing processing elements (CPEs). On the software side, a large-scale particle simulation code, Accurate Particle Tracer (APT), has been developed based on a series of structure-preserving geometric algorithms, such as the explicit volume-preserving algorithms and the explicit symplectic algorithms, for relativistic particles. These innovative algorithms preserve the geometric structure and energy-momentum of the relativistic dynamics and guarantee the long-term accuracy of the simulations beyond 10^{12} steps in time.

2. Long-term Largescale Particle Simulations of Runaway Electrons with Ripples

In the present work, long-term simulations on 10 million cores of Sunway TaihuLight supercomputer with the relativistic volume-preserving algorithm have been carried out using the APT code. A resolution of

10^7 in 6D phase space is used, and simulations are performed for 10^{11} steps. Statistical properties of the runaway dynamics in both the realistic ITER configuration and the ideal configuration without considering magnetic field ripples are studied for comparison.

The runaway dynamics in the ITER device is illustrated in Fig. 1a, and the evolution of density distribution of the REs in the poloidal plane is displayed in Figs. 1b-1g. Figs. 1b, 1c, and 1d shows that the REs in the ideal configuration keep drifting outwards and finally strike the first wall of the device. This is consistent with previous theories and can be explained as the effect of canonical angular momentum conservation. The loss rate of the REs is 2.6% at t=0.4s. However in the realistic configuration, the runaway beam is confined very well to the core region, and no RE is found to impact the wall, see Figs. 1e, 1f, and 1g. The runaway transit orbits shrink into the core because electrons experience an average focusing force caused by the toroidal field ripples as they travel in the toroidal direction for many turns. In this context, the toroidal ripple field behaves similarly as a periodic focusing lattice in charged particle accelerators and rings. The enhanced confinement of REs greatly reduces the risk of direct impact of the runaway beam on plasma facing components.

The average energy of the REs is plotted in Fig. 2a for both the realistic and the ideal configurations. For the ideal case (red curve), the average energy increases to the synchrotron energy limit at 320MeV. For the realistic case (blue curve), the maximum energy is reduced to the level of 150MeV due to two effects produced by the ripple field, the increased collisionless pitch-angle scattering and the harmonic resonances. The increased pitch-angle scattering results in an enhanced synchrotron radiation, as demonstrated in Fig. 2b where the ratio of total runaway radiation power in the realistic configuration to that in the ideal configuration is plotted. After 0.1s, there is a rapid increase of the ratio, which corresponds to the separation point of the two curves in Fig. 2a. After 0.3s, the ratio falls back to 1 gradually, since the average energy in both cases reach steady state and all the work by loop electric field is dissipated by radiation. The enhancement of radiation is still in effect, i.e., the 150MeV electrons in the realistic configuration radiate as much as the 320MeV electrons in the ideal configuration. The enhanced pitch-angle scattering by the ripple field is evident from the evolution of pitch-angle distribution plotted in Fig. 3. In the ideal configuration, the pitch-angle converges to an equilibrium value set by the collisionless neoclassical scattering, see Fig. 3a. The ripple field in the realistic configuration induces a much larger collisionless pitch-angle scattering effect, which is responsible for the significantly increased average and spread of the pitch-angle distribution shown in Fig. 3b.

In conclusion, large-scale long-term simulations on world's fastest computer reveal that REs in the realistic field configuration of ITER pose a much smaller threat to the device than previously predicted by overly simplified theoretical and computational models. More importantly, it is discovered that a small percentage of the 3D ripple components of the magnetic field are able to significantly reduce the RE risk for ITER. The Sunway TaihuLight supercomputer and the APT simulation code can be effectively utilized to design optimized magnetic coils to control REs for ITER and post-ITER devices, such as the CFETR.

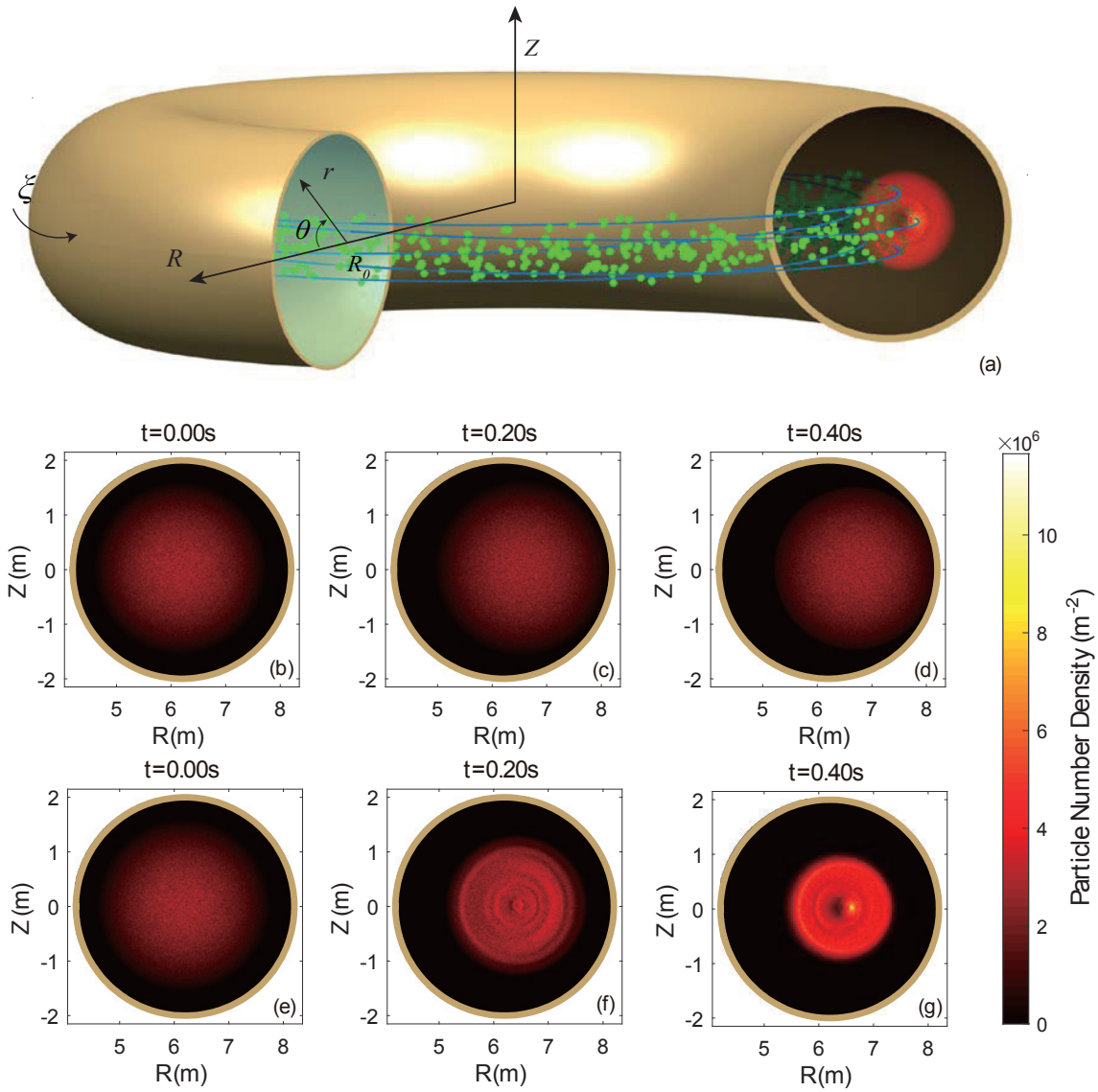

Figure 1: (a) Illustration of runaway dynamics in a tokamak and evolution of the RE distribution in a poloidal cross-section in (b)-(d) the ideal configuration and (e)-(g) the realistic configuration. The color bar indicates the number density of sampled REs within the poloidal cross-section, which are calculated using a resolution of 8mm by 8mm. In the ideal configuration, the REs drift outwards to the first wall of the device with a slightly increased spread. In the realistic configuration the REs are concentrated to the core region due to the periodic focusing effect produced by the ripple field. A ring-like pattern appears at t=0.2s. At t=0.4s, there exists a dipole structure in the center of the beam. In the ideal configuration, 0.018% of the REs strike the first wall near the position z=0m, R=8.2m at t=0.2s, and at t=0.4s the loss rate increase to 2.6%. In the contrary, there's no loss of REs in the realistic configuration. The much improved confinement in the realistic configuration enables more runaway energy released through radiation instead of direct impact on the first wall.

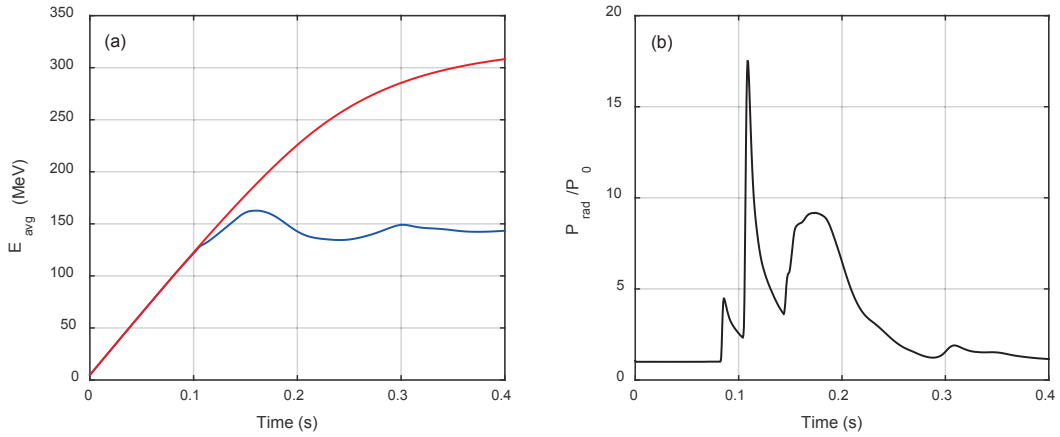

Figure 2: (a) Evolution of average runaway energy in the realistic (blue) and ideal (red) configurations. (b) Evolution of the ratio of total runaway radiation power in the realistic configuration to that in the ideal configuration. Subfigure (a) shows that the maximum runaway energy in the realistic configuration is reduced to half of that in the ideal configuration. Subfigure (b) shows the greatly enhanced radiation power induced by magnetic field ripples.

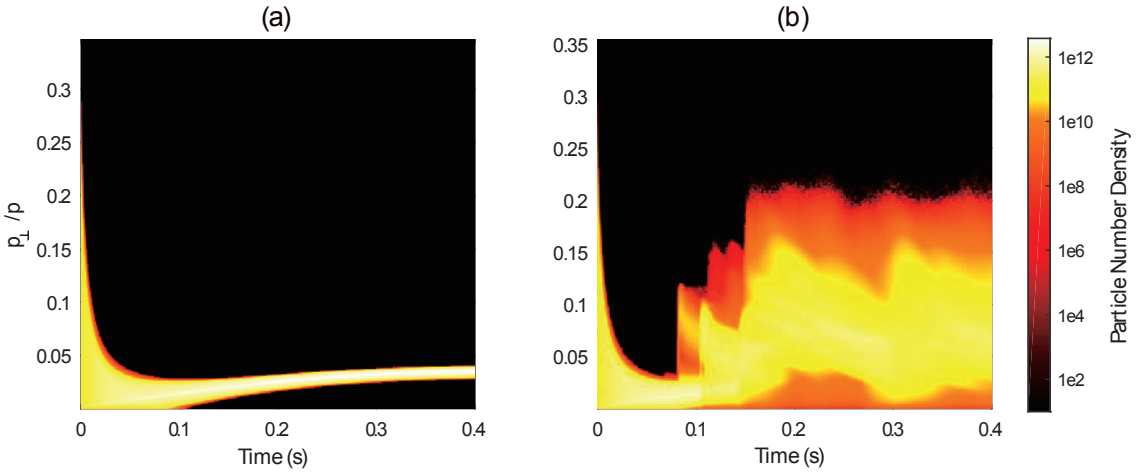

Figure 3: Evolution of the pitch-angle distribution of the REs in (a) the ideal and (b) the realistic configurations. The collisionless pitch-angle scattering due to the ripple field in the realistic configuration generates a much larger average and spread for the pitch-angle distribution.

Acknowledgements

This research was supported by National Magnetic Confinement Fusion Energy Research Project (2015GB111003, 2014GB124005), the National Natural Science Foundation of China (NSFC-11575185, 11575186, and 11305171), JSPS-NRF-NSFC A3 Foresight Program (NSFC-11261140328), and the GeoAlgorithmic Plasma Simulator (GAPS) Project

Effects of fast electrons produced in front of lower hybrid wave antenna

Nong Xiang, Binbin Lin, Jing Ou, Zongzheng Men

Institute of Plasma Physics, Chinese Academy of Sciences

Abstract

Hotspots were observed in recent EAST lower hybrid current drive experiments. It is believed that the fast electrons produced due to the interactions of electrons and high $n_{//}$ lower hybrid modes in front of the antenna are responsible to the observed hotspots. The sheath effects, however, were ignored in the previous studies. In this work, the sheath effects are discussed via one-dimensional particle-in-cell simulations. It is found that the sheath potential increases in the presence of fast electrons. As a result the ion heat flux increases and becomes comparable to the electron one. The total heat flux is much enhanced by fast electrons.

I. Introduction

In recent lower hybrid current drive experiments on EAST, hot spots are often observed as the input wave power is over 2MW [1]. It is believed that fast electrons are produced as electrons interact with the lower hybrid mode with high $n_{//}$. Then a fraction of the RF power is carried away and deposited on the walls [2]. Such enhanced heat flux loaded on the lower hybrid wave antenna guard limiters is responsible to the hot spots. The power loss and the power deposition on the walls have been reported to increase with launched power [3]. However, in these studies, the sheath effects were ignored. It is well known that a sheath decelerates electrons and accelerates ions and consequently make the heat fluxes carried by electrons and ions comparable. The presence of fast electrons not only affects the sheath dynamics and in turn alters the heat flux loaded to the walls. In this work, one-dimensional particle-in-cell simulations are performed to study the heat flux flowing to the lower hybrid wave antenna guard limiters taking the sheath effects into account.

II. Simulation model

Since electrons are well confined by magnetic fields, we use a one-dimensional model as shown in Fig.1. The plasma is confined between two conductor walls representing the wave antenna guard limiters. The size of plasma is L=0.3m. The plasma density is $n_0 = 10^{18}\mathrm{m}^{-3}$ and both electron and hydrogen ion temperature are 25ev. No source and collisions are included in the simulations. A fully kinetic model implemented in VSIM [4] is used for both electrons and ions. The grid size is chosen $dx = 0.9\lambda_D$.

III. Simulation results

Firstly we simulate the case without fast electrons. The sheath field and potential as a function of distance normalized to the Debye length are shown in Fig.2. It is verified that the plasma potential is just the floating

potential. The initial electron VDF is Maxwellian. The resulting VDF at the sheath edge and wall are shown in Fig.3. While the VDF at the sheath edge is still Maxwellian, the one at the wall is a cutoff Maxwellian.

Now we consider the VDF with fast electrons. The initial electron velocity distribution (VDF) is set with a fast electron tail due to the electron-lower hybrid wave interactions. As fast electrons are lost at the walls, the sheaths are formed which decelerate electrons so only fast electrons can arrive at the walls. Meanwhile, ions are accelerated. The field and potential of the sheath formed in front of the right wall are shown in Fig.4. It can be seen that the sheath potential is much larger than the floating potential in the absence of fast electrons.

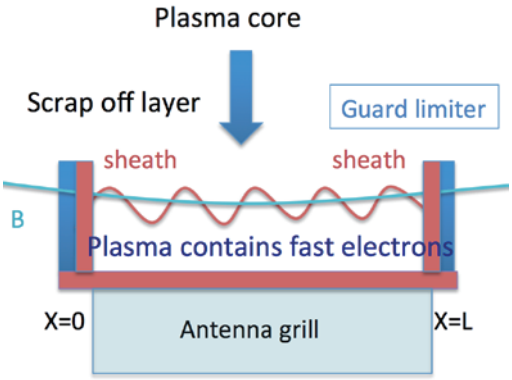

Fig.1. Schematic plot of the simulation model. The sheath in front of the right wall is considered in this work.

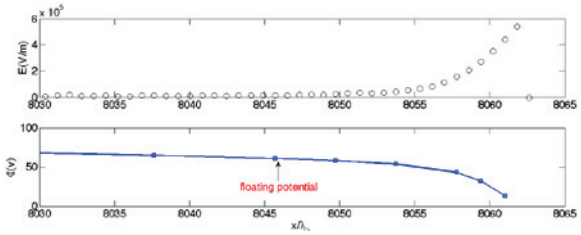

Fig.2. Sheath field (top) and potential (bottom) as a function of distance normalized to the Debye length.

The physics underlying the fact that the sheath potential is significantly enhanced is due to the enhancement of the electron flux caused by fast electrons. To reduce such flux, the sheath potential should be increased. As a result, electrons at slower velocities are expelled by the sheath field. The electron VDFs at the sheath edge and the right wall are shown in Fig.5. The electron VDF at the sheath edge has a quasi-linear plateau produced by the resonant interactions between electrons and high $n_{//}$ lower hybrid modes, which gives rise to a driven current density 26kA/m^2. The concentration of fast electron in the tail is about 3.4%. Without taking the sheath effect into account, such electron VDF results in about 200MW/m^2 heat flux at the right wall. However, due the formation of the sheath, the electrons are decelerated by the sheath field and the VDF at the wall becomes much different as shown in Fig.5. Apparently the thermal electrons cannot reach the wall and the electron flux is much reduced. Therefore the resulting electron heat flux also decreases and ion heat flux increases because of the acceleration of ions by the sheath field. The electron, ion and total heat flux as a function of the normalized distance are plotted in Fig.6. Clearly the electron heat flux decreases with the distance while the ion's increases. At the wall, they are comparable. The total heat flux at the wall is nearly 10MW/m^2, which causes unendurable heat load on the guard limiters and produces hot spots. Therefore, it is shown that the fast electrons produced by the resonant electron-wave interactions are responsible to the hot spots observed in the lower hybrid current drive experiments. The formation of the sheath can significantly reduce the electron heat flux while increasing the ion heat flux.

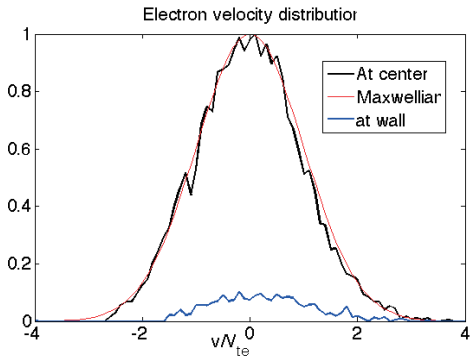

Fig.3. The electron VDF at sheath edge (black) and wall (blue).

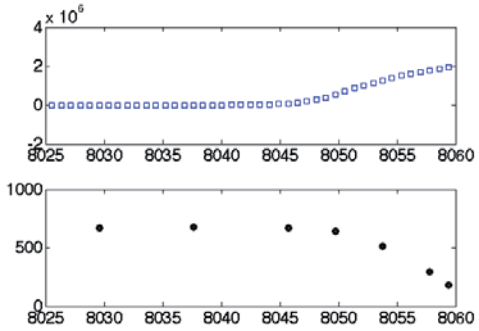

Fig.4. Sheath field (top) and potential (bottom) as a function of distance normalized to the Debye length.

To find the dependence of the heat flux to the wall on the fast electrons, we slightly change the electron VDF by increasing fast electron number and energy. Such VDF produces the current density about 37kA/m^2. The electron VDF at the sheath edge is shown in Fig.7 while the one at the right wall is shown in Fig.8. One can observe that the electrons at the wall are less than that in the previous case. Because more fast electrons with higher energy can reach the wall. The sheath field and potential are plotted in Fig.9. While the sheath field is comparable to that in the previous case, the sheath potential is much increased. As a result the sheath width also increases. Therefore the ions gain more energy while traveling to the wall. The electron, ion and total heat flux are shown in Fig.10. Once again the electron heat flux is reduced when moving to the wall while the ion heat flux increases. The total heat flux flowing to the wall is about 25MW/m^2. Apparently the heat flux to the wall is significantly increased as the number and energy of fast electrons are slightly increased.

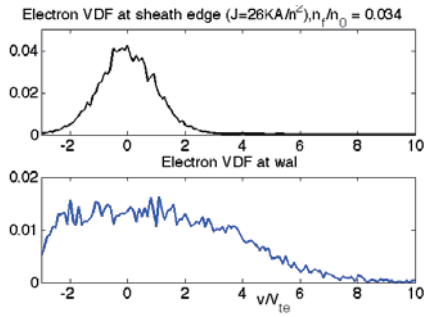

Fig.5. The electron VDF at the sheath edge (top) and right wall (bottom).

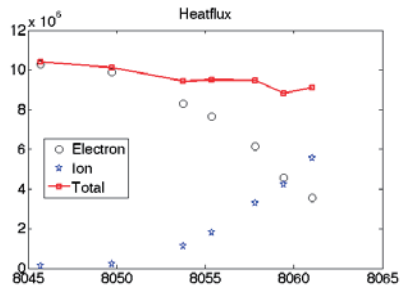

Fig.6. The electron, ion and total heat flux as a function of distance normalized to the Debye length.

In the simulations, the effects of the secondary electron emission (SEE) are not considered. It can be expected that the SEE will reduce the sheath potential, but not significantly affect the heat flux.

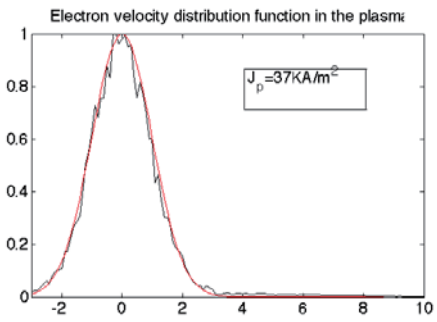

Fig.7. The electron VDF at the sheath edge, which can drive 37kA/m^2 current.

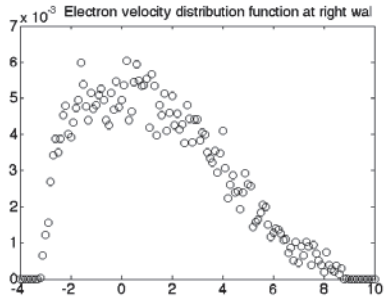

Fig.8. The electron VDF at the right wall.

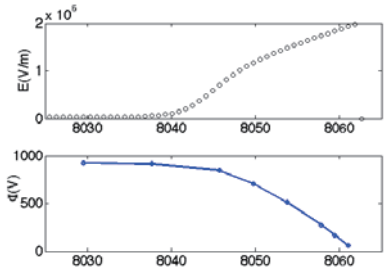

Fig.9. Sheath field and potential as a function of the normalized distance.

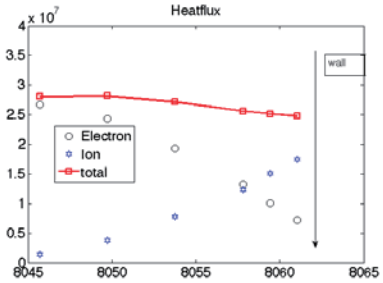

Fig.10. The electron, ion and total heat flux vs. the normalized distance.

IV. Summary

In this work, the sheath effects are discussed via one-dimensional particle-in-cell simulations. It is found that the sheath potential increases in the presence of fast electrons. As a result the ion heat flux increases and becomes comparable to the electron one. The total heat flux is much enhanced by fast electrons, which is responsible to the observed hot spots during lower hybrid current drive.

Acknowledgements

This work was partly supported by the JSPS-NRF-NSFC A3 Foresight Program in the field of Plasma Physics (NSFC: No.11261140328, NRF: No.2012K2A2A6000443).

References

[1] Y. L. Li, G.S.Xu, et al. , Phys. Plasma, 22, 022510 (2015).

[2] K.M. Rantamaki, T.J.H. Pattikangas, et al., Nucl. Fusion, **40,** 1477 (2000).

[3] J. Mailoux, et al., J. Nucl. Mater., **241-243,** 745 (1997).

[4] C.Nieter and J.R.Cary, J. Comput. Phys., 196, 448 (2004).

Influence of energetic ions on neoclassical tearing modes

Huishan Cai[1]

[1]University of Science and Technology of China, Hefei, Anhui 230026, P. R. China

Abstract

In addition to their effect on the linear stability of tearing modes, energetic particles can influence the nonlinear evolution of a magnetic island through an uncompensated cross field current due to the effect of charge separation when the orbit width of an energetic particle is much larger than the island width. The corresponding return parallel current may compensate the loss of bootstrap current in the magnetic island. This nonlinear effect depends on the island's propagation frequency (the rotation frequency of the island relative to the plasma), the density gradient of energetic ions and magnetic shear. If the island's propagation frequency is positive, the effect of the uncompensated current plays a stable role on neoclassical tearing modes. When the magnetic shear is sufficiently small, this effect becomes significant and can partially cancel or even overcome the destabilizing effect of the perturbed bootstrap current. In ITER this provides a possibility of using energetic ions to suppress the neoclassical tearing mode for the steady state and hybrid scenarios with weak magnetic shear.

1. Introduction

Neoclassical tearing modes (NTMs) have been observed in major tokamaks, and they can negatively and significantly impact the performance of magnetically confined plasmas[1-4]. These modes are driven by the perturbed helical bootstrap current due to the pressure flattening across the island. They can increase the local radial transport, degrade plasma confinement and even lead to the disruption in high β plasma, resulting in a limit on maximum achievable β[5]. Thus, understanding the physics of NTMs in tokamak plasmas is one of the critical problems of present and future devices for achieving steady-state and high confinement plasmas, such as International Thermonuclear Experimental Reactor (ITER)[6]. To achieve high β and steady operation plasmas, scenarios with a weak magnetic shear configuration were proposed and successfully realized in some large tokamaks[7]. Hence, it is important to explore the physics of NTMs in the operation scenarios with weak magnetic shear configuration.

Energetic particles are inevitably produced in burning plasma or during auxiliary heating (such as neutral beam injection) in tokamak. They can interact with plasma instabilities effectively. Much work has been devoted to investigating the interaction between energetic particles and ideal MHD instabilities[8-11], such as the internal kink and Alfven eigenmodes. However, the study on the interaction between energetic particles and resistive instabilities of m>1 modes (such as NTMs) has just begun. Recently, the effective interaction between NTMs (including tearing modes) and energetic ions has been shown in some

experiments and theories[12-23]. The redistribution and loss of energetic ions due to NTM and beam ion effects on NTM onset threshold during neutral beam injection (NBI) have been observed in the experiments[12-15]. In DIII-D[14], it was shown that the onset threshold increases with co-injected beam. Hegna et. al.[17] showed that energetic ions can stabilize nonlinear tearing modes by the perturbed beam ion parallel current in the island region. This beam ion parallel current is due to the deformation of particle distribution function by the magnetic island. However, this stabilizing effect is expected to be small when the orbit width of energetic ions is much larger than island width because the responses of energetic ions to perturbation in the island region is weakened by orbit averaging. In this case, energetic ions can affect the linear stability of tearing modes through their interaction with tearing modes in the outer region[18-21,23]. Furthermore, Mirnov et. al.[24] recently pointed out that the effects of energetic ions in the inner region of linear tearing modes can not be neglected even when their orbit width is large for a RFP plasma. It was shown that an uncompensated cross field current is produced due to the charge separation effect, and the effect of this uncompensated current is stabilizing for linear tearing modes. The uncompensated current comes from a net ExB current because the beam ion ExB current is significantly reduced by orbit averaging effect in the limit of large orbit width. In this work, we investigate the effect of the uncompensated current on the nonlinear evolution of NTM. We will show that the effect is significant when magnetic shear is weak and is stabilizing when the mode frequency is positive in plasma frame.

2. Influence of energetic ions on NTM

The detailed calculation can be referred to the paper [25]. By a series of derivation, we can obtain the evolution of NTMs including energetic ions, as

$$\frac{8\pi}{\eta c^2} I_1 \frac{dw}{dt} = \Delta' + \Delta'_b + \Delta'_\pi + \Delta'_u \tag{1}$$

where $\Delta'_b, \Delta'_\pi, \Delta'_u$ result from the contribution of bootstrap current, neoclassical polarization current and uncompensated cross field current, respectively, as

$$\Delta'_b = G_1 \sqrt{\varepsilon_s} \frac{r_s}{sL_n} \frac{\beta_{\theta i}}{w}, \tag{2}$$

$$\Delta'_\pi = -1.64 \varepsilon_s^{3/2} G_2 \frac{r_s^2}{s^2 L_n^2} \frac{\rho_{\theta i}^2}{w^2} \frac{\beta_{\theta i}}{w} \frac{\omega'(\omega' - \omega_{*i})}{\omega_{*i}^2}, \tag{3}$$

$$\Delta'_u = -G_3 \frac{r_s^2}{s^2 L_n^2} \frac{\beta_{\theta i}}{w} \frac{\omega'}{\omega_{*i}} \frac{L_{ni}}{L_{nh}} \frac{n_h}{n_i}. \tag{4}$$

Here, the numerical coefficients $I_1 \sim 0.83, G_1 \sim 2.31, G_2 \sim 1.42, G_3 \sim 1.58,$ ω_{*i} is the ion diamagnetic current, L_{ni}, L_{nh} are the scale lengths of ion density and energetic ion density, respectively. ω' is determined by the torque balance, which is still an open debate. Here, it is needed to point out that the contributions of energetic ions are reflected in both Δ'_u and the stability criterion Δ' (one can refer the detail in **Ref**.[19]. From Eq.(4), it can be seen that the effect of uncompensated cross field current from energetic ions depends on the magnetic shear, propagation frequency of the island and the density gradients

of ions and energetic ions at resonance surface. It plays a stable role for $\omega' > 0$ if density gradients of ions and energetic ions at resonance surface have the same sign. This is different from the effect of neoclassical polarization current, which is stabilizing for $\omega' < 0$ or $\omega' > \omega_{*_i}$. Although the density of energetic ions is much smaller than the ion density, Δ'_u may become significant for weak magnetic shear, like in one of the scenarios of high β and steady state and hybrid operations in ITER[26] and some large tokamaks[7], where a lot of steady operation discharges have been realized with a zero or weak magnetic shear configuration. For weak magnetic shear, the effect of uncompensated cross field current from energetic ions can be comparable with the contribution of the perturbed bootstrap current, and would enhance the onset threshold of NTMs or suppress the NTMs. For the typical tokamak like JT-60U, the main parameters $R_0 \sim 3.2, a \sim 0.8,$ and the energetic ion density can be up to $0.02n_i$ during neutral beam injection[30]. Given $\omega' \sim \omega_{*_i}$, $\varepsilon_s \sim 1/8$, $L_h \sim 0.16m$, $L_{ni} \sim 0.7m$, the ratio of $|\Delta'_u / \Delta'_b|$ against n_h / n_i is shown in **Fig**.1. From **Fig**.1, it can be seen that $|\Delta'_u / \Delta'_b|$ increases with n_h / n_i increasing or s decreasing. For the weak magnetic shear and large fraction of energetic ion density, $|\Delta'_u| \sim |\Delta'_b|$, even $|\Delta'_u| > |\Delta'_b|$. Namely, the contribution of uncompensated cross field current from energetic ions becomes significant, and its stabilizing effect can partially cancel or overcome the destabilizing effect of the perturbed bootstrap current. Then, NTMs will be suppressed.

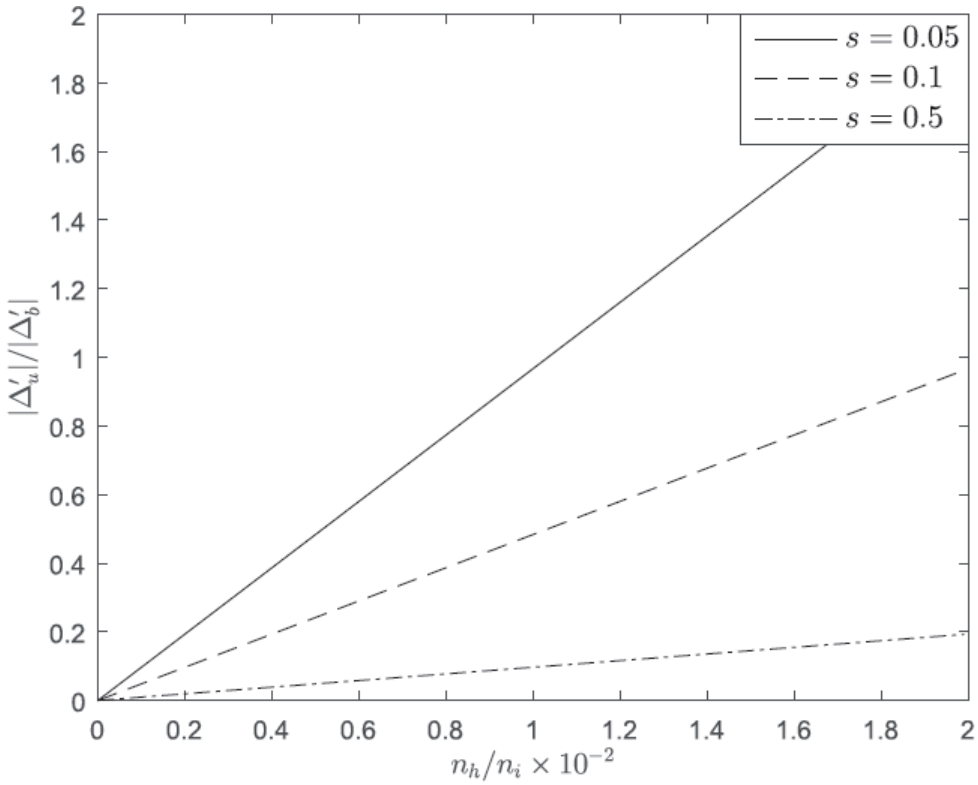

Figure 1. The ratio between the contributions of uncompensated cross field current due to energetic ions and bootstrap current, $|\Delta'_u|/|\Delta'_b|$, against the fraction of energetic ion density n_h/n_i with different values of magnetic shear $s = 0.05,\ 0.1,\ 0.5$.

Acknowledgements

This work was partly supported by the JSPS-NRF-NSFC A3 Foresight Program in the field of Plasma Physics (NSFC: No.11261140328, NRF: No.2012K2A2A6000443).

References

[1] [1] Chang Z., Callen J.D., Fredrickson E.D., Budny R.V., Hegna C.C., McGuire K.M., Zarnstorff M.C. and TFTR Group 1995 Phys. Rev. Lett. 74 4663

[2] Sauter O. et al 1998 Phys. Plasmas 4 1654

[3] Maraschek M., Sauter O., Günter S., Zohm H. and ASDEX Upgrade Team 2003 Plasma Phys. Control. Fusion 45 1369

[4] Buttery R.J., Hender T.C., Howell D.F., La Haye R.J., Sauter O., Testa D. and Contributors to the EFDA-JET Workprogramme 2003 Nucl. Fusion 43 69

[5] Hender T.C. et al 2004 Nucl. Fusion 44 788

[6] Hender T.C. et al 2007 Progress in the ITER physics basis, chapter 3: MHD stability, operational limits and disruptions Nucl. Fusion 47 s128

[7] Oyama N. and the JT-60 Team 2009 Nucl. Fusion 49 104007

[8] Chen L., White R.B. and Rosenbluth M.N. 1984 Phys. Rev. Lett. 52 1122

[9] Porcelli F. 1991 Plasma Phys. Control. Fusion 33 1601

[10] Liu Y. 2010 Nucl. Fusion 50 095008

[11] Hao G.Z., Wang A.K., Liu Y.Q. and Qiu X.M. 2011 Phys. Rev. Lett. 107 015001

[12] Poli E. et al 2008 Phys. Plasmas 15 032501

[13] García-Mu 駑 z M. et al 2009 Nucl. Fusion 49 085014

[14] Buttery R.J. et al 2008 Phys. Plasmas 15 056115

[15] Fietz S., Maraschek M., Zohm H., Reich M., Barrera L., McDermott R.M. and the ASDEX Upgrade Team 2013 Plasma Phys. Control. Fusion 55 085010

[16] Marchenko V.S. and Lutsenko V.V. 2001 Phys. Plasmas 8 4834

[17] Hegna C.C. and Bhattacharjee A. 1989 Phys. Rev. Lett. 63 2056

[18] Takahashi R., Brennan D.P. and Kim C.C. 2009 Phys. Rev. Lett. 102 135001

[19] Cai H., Wang S., Xu Y., Cao J. and Li D. 2011 Phys. Rev. Lett. 106 075002

[20] Cai H. and Fu G. 2012 Phys. Plasmas 19 072506

[21] Cai H., Lin L., Ding W., Anderson J.K. and Brower D.L. 2015
Plasma Phys. Control. Fusion 57 025021

[22] Li E., Hu L., Lin S., Shen B., Liu Y. and HT-7 Team 2014 Nucl. Fusion 54 042001

[23] Liu Y., Hastie R.J. and Hender T.C. 2012 Phys. Plasmas 19 092510

[24] Mirnov V.V., Ebrahimi F., Kim C.C., King J.R., Miller M.C., Reusch J.A., Sarff J.S., Schnack D.D., Sovinec C.R. and Tharp T.D. 2010 Fusion Energy (Proc. 23rd Int. Conf. Daejeon, 2010) (Vienna: IAEA) CD-ROM file THS/P5-11 www-naweb.iaea.org/napc/physics/FEC/FEC2010/index.htm

[25] Cai H, Nucl. Fusion 56, 126016(2016)

[26] Gormezano C. et al 2007 Progress in the ITER physics basis, chapter 6: steady state operation Nucl. Fusion 47 S285–336

Program of 10th A3 Workshop

(Nov. 22-25, 2016, Grabel Hotel Jeju, Jeju, Korea)

November 21, 2016 (Monday)
Registration: 15:00-21:00
Welcome Reception 18:00 – 20:00, *Banquet Hall B (B1F)*

November 22, 2016 (Tuesday)
Banquet Hall A (1F)

Opening Session	08:30	Yeong-Kook OH (NFRI)	Opening & Announcement
	08:40	Keeman KIM (NFRI)	Welcome speech
Session 1 (Category: I) Chair: Y. Kishimoto	09:00	Baonian WAN (ASIPP)	(Inv) Overview of EAST experiments on the development of high-xperformance steady-state scenario
	09:30	Yeong-Kook OH (NFRI)	(Inv) Recent experimental results and plan of KSTAR for high performance steady state operation
	10:00	Akihiko ISAYAMA (QST)	(Inv) Status of the JT-60SA project
Coffee Break 10:30-10:50			
Session 2 (Category: I) Chair: Y.K. Oh	10:50	Yasuaki KISHIMOTO (Kyoto Univ.)	(Inv) Characteristics of turbulent transport in flux-driven toroidal plasmas
	11:20	Si-Woo YOON (NFRI)	Operational boundary of high-beta long-pulse discharges at KSTAR
	11:40	Jinil CHUNG (NFRI)	Internal transport barrier formation in KSTAR: Initial observations with L-mode discharges
Group Photo & Lunch Break 12:00-14:00			
Session 3 (Category: II-b & III) Chair: J.G. Kwak	14:00	Liqun HU (ASIPP)	Recent study of internal kink mode instability on EAST tokamak
	14:20	Jianyuan XIAO (USTC)	High-order Non-canonical symplectic Particle-in-cell method for Vlasov-Maxwell systems
	14:40	Won-Ha KO (NFRI)	The Effect of non-axisymmetric magnetic fields on the LH transition and rotation in KSTAR
	15:00	Minyou YE (USTC)	Design of Ultra-fast Charge eXchange Recombination Spectroscopy diagnostic in EAST tokamak
Coffee Break 15:20-15:40			
Session 4 (Category: I) Chair: L.Q. Hu	15:40	Bojiang DING (ASIPP)	Recent LH and EC wave experiments in EAST
	16:00	Sangwook JUNG (NFRI)	Current status and plan of KSTAR NBI system
	16:20	Hyun-Seok KIM (NFRI)	Responses of safety factor profile against external heating and current drive scenarios
	16:40	Bingjia XIAO (ASIPP)	Plasma control for advanced EAST scenario
	17:00	Sang Hee HAHN (NFRI)	Measuring and extending vertical stabilization controllability of KSTAR
	17:20		Open discussion & Announcement

November 23, 2016 (Wednesday) *Banquet Hall A (1F)*			
Session 5 (Category: II-a) Chair: B.J. Xiao	08:30	Shigeru MORITA (NIFS)	Preliminary result of cross-field impurity transport study in stochastic magnetic field layer of LHD
	08:50	Tetsutarou OISHI (NIFS)	Impact of impurity flow on the impurity transport in the edge stochastic magnetic field layer of LHD
	09:10	Mamoru SHOJI (NIFS)	Simulation analysis of the dust shielding effect by the ergodic layer in long pulse plasma discharges in LHD
	09:30	Fuqiong WANG (Dong Hua Univ.)	SOLPS modelling on the radiative divertor operation for EAST
	09:50	Naoko ASHIKAWA (NIFS)	Hydrogen isotope retention on deposited W materials exposed to plasmas in KSTAR and EAST
Coffee Break 10:10 – 10:20			
Session 6 (Category: II-a & III) Chair: S. Morita	10:20	Jong-Gu KWAK (NFRI)	Neutron measurement at KSTAR
	10:40	Takahiro BANDO (Sokendai)	Analysis of MHD phenomena just after hydrogen pellet injections in LHD
	11:00	Eunnam BANG (NFRI)	Analysis of deposition inside the gap of castellated tungsten blocks of different shapes
	11:20	Shuyu DAI (DLUT)	Kinetic modelling of material erosion and impurity transport in edge
	11:40	Shifeng MAO (USTC)	Study of the Effect of Magnetic Expansion in Snowflake Divertor on Impurity Screening
	12:00	Taisuke KOBAYASHI (Sokendai)	Relation between magnetic structure and emission of hydrogen and carbon in divertor region of LHD
			Open discussion & Announcement
Lunch 12:30-13:20			
Session 7 Discussions on A3 program Chair: Y.K. Oh L.Q. Hu S. Morita	13:30-17:00 Discussions on next seminar and workshop plans Education of young scientists Discussion on coordinator meeting Discussion on annual report of A3 collaboration Discussion on web site of A3 collaboration Discussions on machine operation schedules Discussions on new toroidal devices		

November 24, 2016 (Thursday) *Banquet Hall A (1F)*			
Session 9 (Category: II-a & II-b) Chair: K. Toi	08:30	Hyeon Keo PARK (UNIST/NFRI)	(Inv) New physics from 2D microwave imaging systems in KSTAR
	09:00	Hao WANG (NIFS)	Nonlinear simulations of energetic particle driven geodesic acoustic mode in 3-dimensional LHD equilibrium
	09:20	Minho KIM (POSTECH)	Fast RF diagnostics for ion cyclotron harmonic waves and whistler waves in KSTAR
	09:40	Woochang LEE (NFRI)	Measurement and characterization of Turbulent fluctuations in KSTAR plasmas
	10:00	Yi YU (USTC)	Cooperative research of spectroscopy diagnostics in HL-2A tokamak
Coffee Break 10:20 - 10:40			
Session 10 (Category: II-a & II-b) Chair: N. Xiang	10:40	Chu ZHOU (USTC)	The application of microwave diagnostics on EAST tokamak
	11:00	Seong-Heon SEO (NFRI)	Introduction of KSTAR reflectometer for density profile measurement
	11:20	Ichihiro YAMADA (NIFS)	Fast ADC system for Thomson scattering diagnostics
	11:40	Jong-Ha LEE (NFRI)	Profile data achievement in the KSTAR Thomson scattering system
Lunch Break 12:00 - 13:30			
Session 11 (Category: II-b) Chair: H.K. Park	13:30	YoungMu JEON (NFRI)	Progress highlights of ELM-RMP experiments in KSTAR
	13:50	Jaehyun LEE (UNIST)	Effect of edge turbulence on ELM-crash-suppression under n=1 RMP
	14:10	Kazuo TOI (NIFS)	Rapid growth of resistive interchange modes and excitation of edge localized mode (ELM) in an H-mode Plasma of LHD
	14:30	Jayhyun KIM (NFRI)	Destabilization of macro/micro edge instabilities by magnetic perturbations in KSTAR
	14:50	Minwoo KIM (UNIST)	ELM study in KSTAR H-mode plasma using MHD simulation and ECEI observation
Coffee Break 15:10 – 15:30			
Session 12 (Category: III) Chair: A. Isayama	15:30	Yasuhisa OYA (Shizuoka Univ.)	Recent progress of hydrogen isotope behavior in damaged W
	15:50	Tongnyeol RHEE (NFRI)	Energetic particle research in KSTAR
	16:10	Jian LIU (USTC)	Long-term Largescale Particle Simulations of Runaway Electron Dynamics in Tokamaks
	16:30	Nong XIANG (ASIPP)	Effects of fast electrons produced in front of lower hybrid antenna on EAST
	16:50	Huishan CAI (USTC)	Influence of energetic ions on neoclassical tearing modes
	17:10		Open discussion & Announcement

November 25, 2016 (Friday)	
Session 12 Discussions on A3 collaboration Chair: Y.K. Oh S. Morita L.Q. Hu	09:00-12:00 Plenary meeting on future collaboration at each category for A3 Foresight Program on Critical Physics Issues Specific to Steady State Sustainment of High-Performance Plasmas **Category I:** Steady state sustainment of magnetic configurations (Current drive and profile control) **Category II:** Edge and divertor plasma control Category IIa: Transport of edge and divertor plasmas Category IIb: Stability of edge plasma **Category III:** Confinement of alpha particles .(Interaction of energetic particle and bulk plasma) **Category IV:** Theory and simulation 13:30-17:00 Individual discussion on personnel exchange Individual discussion on hardware construction and operation of diagnostics and heating devices Individual discussion on device operation and machine time Discussion on overall report of 5-year A3 program Discussions on on-going and future studies in A3 collaboration Discussions with PHD students, Post-doctoral researchers and young scientists Discussion on post-A3 program

(END)

Participants of the 10th A3 Workshop in Jeju

NO.	Affiliation & Name			Title	M/F	e-mail
1	NFRI	고원하	Won-Ha KO	Dr.	F	whko@nfri.re.kr
2	NFRI	곽종구	Jong-Gu KWAK	Dr.	M	jgkwak@nfri.re.kr
3	NFRI	김기만	Keeman KIM	Dr.	M	kkeeman@nfri.re.kr
4	NFRI	김재현	Jayhyun KIM	Dr.	M	jayhyunkim@nfri.re.kr
5	NFRI	김현석	Hyun-Seok KIM	Dr.	M	hskim0618@nfri.re.kr
6	NFRI	방은남	Eun-nam BANG	Ms.	F	Bang14@nfri.re.kr
7	NFRI	서성헌	Seong-Heon SEO	Dr.	M	shseo@nfri.re.kr
8	NFRI	오노영	Noh-Yeong OH	Ms.	F	ony55@nfri.re.kr
9	NFRI	오영국	Yeong-Kook OH	Dr.	M	ykoh@nfri.re.kr
10	NFRI	윤석인	Seok-In YOON	Mr.	M	siyoon@nfri.re.kr
11	NFRI	윤시우	Si-Woo YOON	Dr.	M	swyoon@nfri.re.kr
12	NFRI	이동렬	Tongnyeol RHEE	Dr.	M	trhee@nfri.re.kr
13	NFRI	이우창	Woochang LEE	Dr.	M	wclee@nfri.re.kr
14	NFRI	이종하	Jong-Ha LEE	Dr.	M	jhlee@nfri.re.kr
15	NFRI	전영무	YoungMu JEON	Dr.	M	ymjeon@nfri.re.kr
16	NFRI	정진일	Jinil CHUNG	Dr.	M	jinil@nfri.re.kr
17	NFRI	정상욱	Sangwook JUNG	Dr.	M	woogijung@nfri.re.kr
18	NFRI	한상희	Sang Hee HAHN	Dr.	F	hahn76@nfri.re.kr
19	UNIST/NFRI	박현거	Hyeon Keo PARK	Prof.	M	hyeonpark@unist.ac.kr
20	UNIST	김민우	Minwoo KIM	Dr.	M	minwookim@unist.ac.kr
21	UNIST	이재현	Jaehyun LEE	Dr.	M	jaehyun@unist.ac.kr
22	POSTECH	김민호	Minho KIM	M.	M	kmh415@postech.ac.kr
23	ASIPP	万宝年	Baonian WAN	Prof.	M	bnwan@ipp.ac.cn
24	ASIPP	肖炳甲	Bingjia XIAO	Prof.	M	bjxiao@ipp.ac.cn
25	ASIPP	丁伯江	Bojiang DING	Prof.	M	bjding@ipp.ac.cn
26	ASIPP	胡立群	Liqun HU	Prof.	M	lqhu@ipp.ac.cn
27	ASIPP	项 农	Nong XIANG	Prof.	M	xiangn@ipp.ac.cn
28	ASIPP	席莹琨	Yingkun XI	Ms.	F	xiyingkun@ipp.ac.cn
29	Dong Hua Univ.	王福琼	Fuqiong WANG	Dr.	F	wangfq@dhu.edu.cn
30	USTC	周楚	Chu ZHOU	Dr.	M	zhouchu@ustc.edu.cn
31	USTC	蔡辉山	Huishan CAI	Dr.	M	hscai@mail.ustc.edu.cn
32	USTC	刘 健	Jian LIU	Dr.	M	jliuphy@ustc.edu.cn
33	USTC	肖建元	Jianyuan XIAO	Mr.	M	xiaojy@mail.ustc.edu.cn
34	USTC	叶民友	Minyou YE	Prof.	M	yemy@ustc.edu.cn
35	USTC	毛世峰	Shifeng MAO	Dr.	M	sfmao@ustc.edu.cn
36	USTC	余 羿	Yi YU	Dr.	M	yuyi@ustc.edu.cn
37	DLUT	戴舒宇	Shuyu DAI	Dr.	M	daishuyu@dlut.edu.cn
38	Kyoto Univ.	岸本泰明	Yasuaki KISHIMOTO	Dr.	M	kishimoto@energy.kyoto-u.ac.jp
39	NIFS	迫千尋	Chihiro SAKO	Mr.	M	sako.chihiro@nifs.ac.jp
40	NIFS	王灝	Hao WANG	Dr.	M	wang.hao@nifs.ac.jp
41	NIFS	山田一博	Ichihiro YAMADA	Dr.	M	yamadai@nifs.ac.jp
42	NIFS	東井和夫	Kazuo TOI	Dr.	M	toi@nifs.ac.jp
43	NIFS	庄司主	Mamoru SHOJI	Dr.	M	shoji@nifs.ac.jp
44	NIFS	芦川直子	Naoko ASHIKAWA	Dr.	F	ashikawa@nifs.ac.jp
45	NIFS	森田繁	Shigeru MORITA	Dr.	M	morita@nifs.ac.jp
46	NIFS	大石鉄太郎	Tetsutarou OISHI	Dr.	M	oishi@nifs.ac.jp
47	NIFS	神谷良志夫	Yoshio KAMIYA	Mr.	M	kamiya.yoshio@nifs.ac.jp
48	QST	諫山明彦	Akihiko ISAYAMA	Dr.	M	isayama.akihiko@qst.go.jp
49	Shizuoka Univ.	大矢恭久	Yasuhisa OYA	Dr.	M	syoya@ipc.shizuoka.ac.jp
50	Sokendai	小林汰輔	Taisuke KOBAYASHI	Mr.	M	kobayashi.taisuke@nifs.ac.jp
51	Sokendai	坂東隆宏	Takahiro BANDO	Mr.	M	bando.takahiro@nifs.ac.jp